Technical University of Denmark

DTU

The Formation of Aerosol Particles during Combustion of Biomass and Waste

Zeuthen, Frederik Jacob; Livbjerg, Hans; Glarborg, Peter; Jappe Frandsen, Flemming

Publication date:
2007

Link back to DTU Orbit

DTU Library
Technical Information Center of Denmark

Ph.D. Thesis

THE FORMATION OF AEROSOL PARTICLES DURING COMBUSTION OF BIOMASS AND WASTE
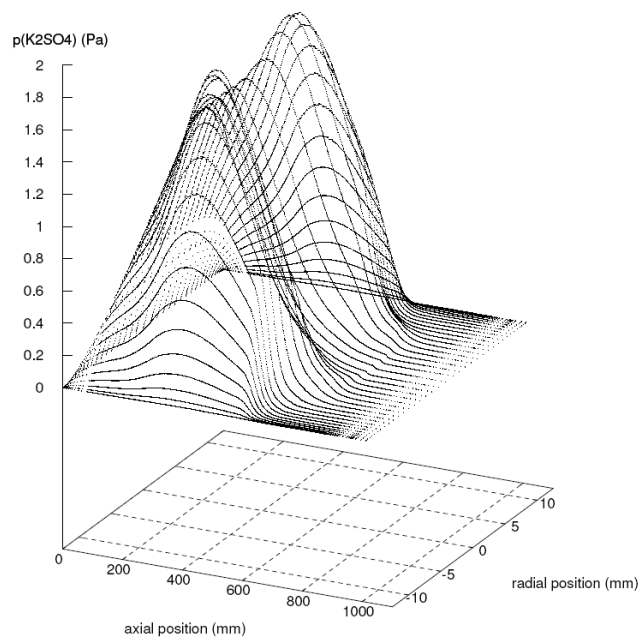
Jacob Hjerrild Zeuthen

The Aerosol Laboratory

Department of Chemical Engineering

Technical University of Denmark

Kgs. Lyngby 2007

Figure on title page: *Simulated partial vapor pressure of $K_2SO_{4(g)}$ as a function of axial and radial position in the Laminar Flow Aerosol Condenser. The simulation of the aerosol formation is performed with a reacting flow containing the gaseous components KCl, SO_2, H_2O, and O_2. Figure from Chapter 3.*

PREFACE

This dissertation is a partial fulfillment of the requirements for the Ph.D. degree. The work has been carried out in The Aerosol Laboratory, Department of Chemical Engineering at the Technical University of Denmark (DTU) from October 2003 to February 2007. The main and co-supervisors on the project were Prof. Hans Livbjerg, Dr. Peter Glarborg, and Dr. Flemming Jappe Frandsen. I would like to express my sincere gratitude to Hans Livbjerg for guiding me through these three years of research. Also thanks to Peter Glarborg, Flemming Jappe Frandsen, and Peter Arendt Jensen for fruitful discussions and useful suggestions. I would like to thank Anne Juul Pedersen, Ayten Yilmaz, and Lusi Hindiyarti in the CHEC Research Center for a rewarding collaboration.

During the project I have received technical assistance from a lot of people. I want to thank Bente Beckerslev for help in the laboratory and during the full-scale measuring campaign at Avedøre Power Station. Thank you to the workshop at the department for help with design of new probes and for implementing changes in the laboratory setup. Thank you to Flemming Grumsen, Inger Søndergaard, and Laila Leth at the Department of Manufacturing for carrying out the electron microscopy, to Edith Thomsen at Ensted Power Plant for carrying out the ICP-OES analysis, and to Ellen ter Haar Hansen at Vattenfall A/S for the chemical analysis by ion chromatography.
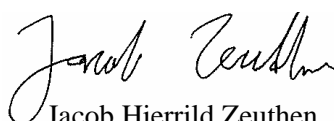
I want to thank the people from DONG Energy A/S, RISØ, Vølund, I/S FASAN, and Institute for Environment and Resources at DTU who participated in the measuring campaigns at Avedøre Power Station and at FASAN Waste Incinerator.

Thank you to my colleagues in The Aerosol Laboratory and in the CHEC Research Center for providing a pleasant working environment during my study.

Part of the research was done at The Technical Research Center of Finland (VTT) in September – November 2005 under guidance of Dr. Jouni Pyykönen and Prof. Jorma Jokiniemi. I would like to thank my two supervisors for a warm welcome and for good and patient assistance during the work with aerosol simulations. Thank you to everyone at the Aerosol Technology Group at VTT for making me and my family feel welcome in Helsinki.

Finally I want to thank my friends and family and especially Louise and Adam for their constant love and support.

Jacob Hjerrild Zeuthen
Kgs. Lyngby, Denmark
February 2007.

SUMMARY

This thesis describes the formation of aerosol particles during combustion of biomass and waste. The thesis contains five chapters:

Chapter 1. A general introduction to the topic is given in this chapter.

Chapter 2. The formation of aerosol particles is investigated by studying condensation of alkali salts from synthetic flue gasses in a laboratory tubular furnace. In this so-called laminar flow aerosol condenser-furnace gaseous alkali chlorides are mixed with sulphur dioxide, water vapor, and oxygen. At high temperatures the alkali chloride reacts with sulphur dioxide to form alkali sulphate. During subsequent cooling of the synthetic flue gas the chlorides and sulphates condense either as deposits on walls or on other particles or directly from the gas phase by homogeneous nucleation. It is investigated whether the homogeneous nucleation is caused by condensation of gaseous alkali sulphate. So far there is no consensus on the mechanism behind the nucleation in the literature. Using a specially designed high-temperature impactor probe to sample aerosols of pure alkali sulphate formed by gas phase sulphation of alkali chloride, it was possible to confirm the hypothesis that gaseous sulphates are responsible for the initial particle formation.

Investigations of the influence of the chemical composition of the flue gas on the particle size distribution and chemical composition of the aerosols show that the number concentration of particles depends only on the concentration of sulphur dioxide and oxygen. This confirms that the rate limiting step of the sulphation reaction is the oxidation of sulphur dioxide to sulphur trioxide. It is also found that the concentration of alkali chloride has a considerable influence on the mass-based size distribution. The chemical composition has a major effect on the final size distribution of the aerosol. Particle size distributions are determined using low-pressure cascade impactor and scanning mobility particle sizer. Chemical composition is determined using energy dispersive x-ray spectroscopy or ion chromatography.

Experiments with varying cooling rate and the residence time at high temperature show that the particle size distribution can be greatly affected by changes in these operational parameters of the combustor. However, the gas composition is the most important parameter. Thus, laboratory investigations suggest that fuel composition and the release of alkali metals, chlorine, and sulphur are the key parameters to reduce aerosol emissions.

Experiments with alkali chloride sulphation in a synthetic gas containing seed particles show that the formation of sulphate is increased when seed particles are present. This indicates that the surface of the seed particles acts as a heterogeneous catalyst for the oxidation of sulphur dioxide.

Chapter 3. A previously developed computer code for simulation of one-component nucleation of particles in a cylindrical laminar flow is extended to include a homogeneous gas phase reaction

to produce gaseous alkali sulphate. The model uses classical nucleation theory to calculate the rate of formation of new particles. The surface tension of the particles is corrected for curvature dependence. The non-linear second-order partial differential equations describing mass and energy conservation and the particle growth by diffusional controlled condensation are solved using the method of orthogonal collocation. A rate expression is fitted to experimental data from an independent source and used in the model. Assuming that particles are formed by homogeneous nucleation of alkali sulphate and subsequently heterogeneous condensation of alkali chloride, the particle size distribution of an aerosol is simulated. The total number concentration of particles is fitted to experimental data by adjusting the curvature dependence of the surface tension. The value of this so-called Tolman correction coefficient obtained through this fit is in good agreement with the value suggested by molecular dynamics simulation in the literature. Good agreement between the simulated particle size distribution and the experimental data suggests that the assumed formation mechanism is correct.

Chapter 4. The formation of during full-scale combustion of wheat straw is investigated in a 100 MW grate-fired boiler. The aerosol particles are sampled with an ejector-dilution probe and the size distribution and the chemical composition of particles is characterized by use of a low-pressure cascade impactor and electron diffraction X-ray spectroscopy. The particles are sampled before the flue gas cleaning. The results from the full-scale experiments show that it is indeed possible to reduce the aerosol formation by adding alkali-binding sorbents to the boiler. It is also shown that increasing the combustion temperature increases the mass load of particles. A value of $PM_{2.5}$ for the aerosols of 390±66 mg/m^3 is found when no sorbents are added. This is reduced as much as 70% when sorbents are added. The particles are composed mainly of the potassium salts of chloride and sulphate. In some cases phosphates are also present in high amounts. Analysis of the gas and particle compositions from the experiments suggests that the chemical composition of the cooled flue gas can be described by the equilibrium between chloride and sulphate at 812 °C. This indicates that the reactions taking place at high temperatures are quenched when the flue gas is cooled.

Chapter 5. Aerosols from incineration of waste are investigated during full-scale combustion of municipal waste in a 22 MW grate-fired unit. The aerosol mass load is lower than in biomass combustion. A value for $PM_{2.5}$ of 252±21 mg/m^3 is found when a base-load waste mixed of 80% household waste and 20% small combustibles is incinerated. The mass-based size distribution is rather constant even when applying significant changes to the composition of the fuel and to the operational conditions of the combustor. The number concentration of particles, determined by a scanning mobility particle sizer, fluctuates more. This may be caused by nucleation of new particles by heavy metal inclusions in the fuel. The release of these heavy metals is not uniform and the total number concentration may fluctuate for this reason. During incineration of base load waste the total number concentration is $(43±10) \cdot 10^6/cm^3$. This concentration increases considerably when applying changes in the operational parameters. The particles are composed mainly of the alkali salts of chlorine, sulphate, and phosphate, and of lead and zinc. A large number of heavy metals are also present in the particles in smaller concentrations. The number concentration of particles in the flue gas before and after the flue gas cleaning is used to determine the penetration through this. The total penetration is 0.11% with a maximum at 30 nm and one at 500 nm.

The five chapters are followed by final conclusions, references, and appendices.

RESUMÉ (SUMMARY IN DANISH)

Denne afhandling beskriver dannelsen af aerosolpartikler ved afbrænding af biomasse og affald. Afhandlingen indeholder fem kapitler:

Kapitel 1. En generel indledning til emnet er givet i dette kapitel.

Kapitel 2. Dannelsen af aerosolpartikler er undersøgt ved at kondensere alkalisalte fra en syntetisk røggas i en rørreaktor. I denne såkaldte laminart flow aerosol kondensations-ovn blandes gasformigt alkaliklorid med svovldioxid, vanddamp og oxygen. Alkalikloridet reagerer med svovldioxid og danner alkalisulfat ved høj temperatur. Under den efterfølgende afkøling af den syntetiske røggas kondenserer klorider og sulfater til fast fase på enten rørvæggene eller på andre partikler, eller ved direkte fra gasfasen at danne nye partikler ved homogen nukleering. Det er undersøgt om partikeldannelsen er forårsaget af homogen nukleering af gasformigt alkalisulfat. Hidtil har der ikke været enighed omkring dannelsesmekanismen i literaturen. Aerosoler af rent alkalisulfat dannet fra gasfase-sulfatisering af alkaliklorid er blevet opsamlet direkte ved høj temperatur ved hjælp af en specialdesignet impaktor-sonde. Det har således været muligt at påvise, at dannelse af partikler ved homogen nukleering af gasformigt alkalisulfat er mulig.

Undersøgelser af indflydelsen af den kemiske sammensætning i den syntetiske røggas for den dannede aerosols størrelsesfordeling og kemiske sammensætning viser, at antalskoncentrationen af partikler kun afhænger af koncentrationen af svovldioxid og oxygen. Dette bekræfter, at det hastighedsbegrænsende trin i sulfatiseringsreaktionen er oxideringen af svovldioxid til svovltrioxid. Koncentrationen af alkaliklorid har en afgørende indflydelse på den masse-baserede størrelsesfordeling af aerosolen. Ændringerne i den kemiske sammensætning har en afgørende effekt på egenskaberne for den dannede aerosol. Partikel-størrelsesfordelinger bestemmes ved brug af lavtryks kaskade-impaktor og scanning mobility particle sizer. Den kemiske sammensætning bestemmes ved brug af energi dispersiv røntgen-spektroskopi eller ved ion-kromatografi.

Forsøg med varierende afkølingshastighed og opholdstid ved høj temperatur viser, at partiklernes størrelsesfordeling kan påvirkes betydeligt ved ændringer i disse driftsparametre for forbrændingsenheden. Gassammensætningen er dog den vigtigste parameter og laboratorieundersøgelserne indikerer, at brændselssammensætningen, samt frigivelsen af alkali, klor og svovl ved forbrændingen, er nøgleparametrene for at reducere aerosolemissioner.

Eksperimenter med sulfatisering af alkaliklorid i en syntetisk røggas indeholdende kim-partikler er udført, og det er fundet, at dannelsen af sulfat øges, når kim-partikler er tilstede. Dette indikerer, at overfladen af kim-partiklerne fungerer som en heterogen katalysator for oxidationen af svovldioxid.

Kapitel 3. En tidligere udviklet computermodel til simulering af 1-komponent nukleering af partikler i et cylindrisk, laminart flow er blevet videreudviklet til at inkludere dannelsen af gasformig alkalisulfat ved en homogen gasfasereaktion. Modellen anvender klassisk

nukleeringsteori til at beregne nukleeringshastigheden for dannelsen af nye partikler. Ikke-lineære andenordens partielle differentialligninger som beskriver masse og energi-bevarelse, samt partikelvækst ved diffusiv kontrolleret kondensation, løses ved hjælp af metoden ortogonal kollokation. Et hastighedsudtryk er fittet til eksperimentielle data fra en uafhængig kilde og bruges i modellen. Under antagelse af, at partiklerne dannes ved homogen nukleering af gasformigt alkalisulfat og efterfølgende heterogen kondensering af alkaliklorid simuleres partikelstørrelsesfordelingen for den dannede aerosol. Antalskoncentrationen for de dannede partikler er fittet til eksperimentielle data ved at variere partiklernes overfladespændings afhængighed af overfladekrumningen. Værdien af den såkaldte Tolman korrektionsfaktor, som opnås ved dette fit, er i god overensstemmelse med den værdi som foreslås på baggrund af molekyle-dynamiske simuleringer i literaturen. En god overensstemmelse mellem den eksperimentielle og den simulerede partikelstørrelsesfordeling giver anledning til at tro, at den antagede dannelsesmekanisme er korrekt.

Kapitel 4. Dannelsen af aerosoler er undersøgt under fuldskala-forbrænding af hvede halm i en 100 MW ristefyret forbrændingsenhed. Aerosolpartiklerne er opsamlet med en ejektor-fortyndings sonde, mens størrelsesfordeling og kemisk sammensætning er karakteriseret ved brug af en lavtryks kaskade-impaktor og energi dispersiv røntgen-spektroskopi. Partiklerne opsamles før røggasrensningen. Resultaterne fra disse eksperimenter viser, at det er muligt at reducere aerosoldannelsen ved at tilsætte alkali-bindende additiver til forbrændingskammeret. Det er også vist, at masse-koncentrationen af partikler øges, når temperaturen i forbrændingskammeret øges. En værdi for $PM_{2.5}$ på 390 ± 66 mg/m^3 er bestemt under drift uden tilsætning af additiver. Denne bliver reduceret med op til 70% ved tilsætning af additiver under forsøgene. Partiklernes kemiske sammensætning udgøres primært af kaliumsalte af klorid og sulfat. I visse tilfælde er fosfat også tilstede i betydelige mængder. Analyse af gasfasens og partiklernes sammensætning indikerer, at den kemiske sammensætning af den afkølede røggas kan beskrives ved den kemiske ligevægt mellem klorid og sulfat ved 812°C. Dette afspejler, at reaktionerne, der finder sted ved høj temperatur, bliver kinetisk fastfrossede, når røggassen afkøles.

Kapitel 5. Aerosoler fra affaldsforbrænding er undersøgt under fuldskala afbrænding af husholdnningsaffald i et 22 MW ristefyret anlæg. Massekoncentrationen af aerosolen er lavere end i biomasse-afbrænding. En værdi for $PM_{2.5}$ på 252 ± 21 mg/m^3 bestemmes ved afbrænding af et reference-affald bestående af 80% husholdningsaffald og 20% småt brændbart. Den massebaserede størrelsesfordeling er forholdsvis konstant, selv når der påføres betydelige ændringer i sammensætningen af brændslet og i driftsparametrene for anlægget. Antals-koncentrationen, bestemt ved brug af en scanning mobility particle sizer, fluktuerer mere. Dette kan skyldes, at nukleering af nye partikler kan forårsages af frigivne inklusioner af tungmetaller fra brænslet. Frigivelsen af disse foregår ikke jævnt, og dette kan være årsagen til ændringerne over tid. Under afbrænding af reference-affaldet bestemmes den totale antalskoncentration til $(43\pm10)\cdot10^6$/cm^3. Denne koncentration øges betydeligt under de påførte ændringer i driftsparametre. Partiklerne består primært af alkalisaltene af klorid, sulfat og fosfat, samt af bly og zink. Et stort antal af tungmetaller er også tilstede i partiklerne i mindre koncentrationer. Antalskoncentrationen af partikler i røggassen er målt før og efter røggasrensningen og penetrationen gennem denne er bestemt. Den totale penetration er 0.11% med et maksimum ved 30 nm og et ved 500 nm.

De fem kapitler efterfølges af en sammenfattende konklusion, referencer og bilag.

TABLE OF CONTENTS

LIST OF SYMBOLS

Latin Letters

C_c	Cunningham slip correction factor	[-]
C_1	Temperature-dependent constant in rate expression	[mole/(m^3·s)]
C_2	Temperature-dependent constant in rate expression	[-]
D_A	Binary diffusion coefficient for component A	[m^2/s]
D_p	Particle diameter	[m]
E	Electrical field	[V/m]
E_a	Activation energy	[kJ/mole]
G	Gibbs free energy	[kJ/mole]
G	Mass flow rate	[kg/(m^2·s)]
ΔH_c	Heat of condensation	[kJ/mole]
J	Homogeneous nucleation rate	[1/(m^3·s)]
K	Reaction constant	[1/s]
k	Heat conductivity	[W/(m ·K)]
k_B	Boltzmanns constant ($k_B = 1.38065…·10^{-23}$ J/K)	[J/K]
Kn	Knudsen number	[-]
L	Length	[m]
M	Molar mass	[kg/mole]
N	Particle number concentration	[1/m^3]
N_a	Avogadro's number ($N_a = 6.02214…·10^{23}$ 1/mole	[1/mole]
n_p	Number of elemental charges on particle	[-]
p	Pressure	[Pa]
Q	Flow	[m^3/s]
r	Reaction rate	[mole/(m^3·s)]
R_g	Gas constant ($R_g = 8.31447…$ J/(mole ·K))	[J/(mole·K)]
R_p	Particle radius	[m]
s	Source term	[mole/(m^3·s)]
S	Saturation	[-]
St	Stokes number	[-]
T	Temperature	[K]
t	Time	[s]
U	Electrical potential	[V]
v	Molecular volume	[m^3]
W	Mass fraction	[%]
y	Mole fraction	[-]
X	Conversion	[-]
Z	Element number	[-]
z	Axial coordinate	[m]
Z_p	Electrical mobility of particle	[m^2/(V·s)]

Greek Letters

σ	Surface tension	[N/m]
λ	Mean free path	[m]
λ	Wave length	[nm]
μ	Viscosity	[kg/(m·s)]
φ	Size distribution density function	[#/m³/m]
δ	Dirac delta function	[-]
ρ	Density (ρ_g for gas density and ρ_p for particle density)	[g/cm³]
π	Pi ($\pi = 3.14159\ldots$)	[-]
α	Median of the log-normal distribution	[-]
β	Standard deviation in the log-normal distribution	[-]
θ	Scaling factor for the log-normal distribution	[mg/m³]
σ_i	Tolman length of the ith component	[m]
μ_i	Chemical potential of the ith component	[J/mole]
η	Sticking coefficient	[-]

Abbreviations

BPR	Back Pressure Regulator
CFD	Computational Fluid Dynamics
CO	Critical Orifice
CPC	Condensational Particle Counter
DMA	Differential Mobility Analyzer
EDS	Electron Diffraction X-ray Spectroscopy (EDX by some authors)
GF-AAS	Graphite Furnace Atomic Absorption Spectroscopy
GMD	Geometric Mean Diameter
ICP-OES	Induced Coupled Plasma Optical Emission Spectroscopy
LFAC	Laminar Flow Aerosol Condenser
LPI	Low-Pressure (cascade) Impactor
PFAC	Plug Flow Aerosol Condenser
PM_x	Particulate Matter (mass concentration with $D_{ae} < x$ µm)
PSD	Particle Size Distribution
SEM	Scanning Electron Microscope
SMPS	Scanning Mobility Particle Sizer
TEM	Transition Electron Microscope

Subscripts

ae	Aerodynamic
g	Gas
i	Component *i*
p	Particle
w	Wall property

Superscripts

*	Saturation
o	Standard state

x

CHAPTER 1 INTRODUCTION

This chapter gives an introduction to combustion of biomass and waste, to aerosols in general, and to aerosols from combustion of biomass and waste.

1. 1 Biomass combustion

Combustion of biomass is one of the oldest means of energy production in house holds. In recent years the concern for global warming has increased the focus on biomass combustion. Biomass is considered a CO_2-neutral fuel because the uptake of atmospheric CO_2 by photosynthesis during growth is equal to the release during combustion.

Utilization of biomass in large scale energy production as a mean to replace oil and coal is in principle very simple but has in practice proved troublesome (e.g. Bain *et al.*, 1998). Biofuels are characterized by low heating values, high moisture content, and a low ash content (e.g. Baxter *et al.*, 1998; Jenkins *et al.*, 1998). The ash, however, is characterized by a large amount of alkali salts, which will evaporate to some degree during combustion depending on the combustion conditions (Baxter *et al.*, 1998). Potassium is a macronutrient for plants and is usually found in biomass fuels in concentrations around 1% on dry weight (Jenkins *et al.*, 1998). The name potassium comes from *pot-ash* – since it was first discovered in ash from wood combustion. The type of biomass used for energy production varies regionally, but all are characterized by high contents of alkali chlorides and the problems related to their utilization are the same. Some examples are paper pulp (Mikkanen *et al.*, 2001), olive residues (Jimenez and Ballester, 2004), wood pellets (Johansson *et al.*, 2003) and straw (Christensen and Livbjerg, 1996). While the presence of alkali is found in all kinds of biomass fuels, the amounts of chlorine and sulphur depend on the type of fuel. These are very low in e.g. wood and bark, while straw and paper pulp contains considerable amounts. A common biomass fuel in Denmark is straw. In Table 1 the typical compositions of straw and straw-ash are given.

Deposits containing alkali chloride are highly corrosive (Michelsen *et al.*, 1998; Obernberger *et al.*, 1997; Henderson *et al.*, 2006; Miles *et al.*, 1996). The chloride selectively attacks the chromium of the alloys (Nielsen, 1998a). Alkali metals combine with alumino silicates in deposits and lower the melting point of these, which in some cases lead to formation of a corrosive melt. By lowering the melting point of the deposits the alkalis also enhance slagging (Heinzel *et al.*, 1998). Corrosion is favored by high temperatures, and the temperature of

superheaters in biomass combustion therefore has to be lowered compared with coal combustion (Bain *et al*., 1998; Frandsen, 2005; Bryers, 1996). The lower steam temperature limits the overall electrical efficiency of power plants used for biomass combustion. One way of combining a low metal temperature in the biomass boiler and still maintain an improved electrical efficiency is to keep a low steam temperature at the outlet from a biomass fired boiler and increase the temperature further in a second coal-fired unit (Nielsen, 1998a).

Table 1: *Chemical composition of straw (wheat and rye) as reported by Obernberger et al. (2006), Dayton et al. (1999), and Christensen et al. (1998). Ash composition is from van Loo (2002). The ash content of the fuel is determined by ISO 1171 (1997) at 550 °C. The element content in the fuel is on a dry, ash-free basis*

Parameter	Unit (dry basis)	Fuel composition	Ash composition
Ash	w/w %	5.0-12	-
Moisture	w/w %	13-16	
C	w/w %	42-49	
O	w/w %	39-43	
H	w/w %	5.1-6.3	
K	w/w %	0.4-2.1	10-16
Si	w/w %	1.0	16-30
N	w/w %	0.5-0.7	
Ca	w/w %	0.4	4.5-8.0
Cl	w/w %	0.1-2.0	
S	w/w %	0.09-0.12	
Mg	w/w %	0.07	1.1-2.7
Na	w/w %	0.01-0.09	0.2-1.0
P	mg/kg	1000	
Fe	mg/kg	100	
Al	mg/kg	50	
Zn	mg/kg	10	60-90
Cr	mg/kg	10	
F	mg/kg	5	
V	mg/kg	3	
Cu	mg/kg	2	
Ni	mg/kg	1	
Pb	mg/kg	0.5	
Cd	mg/kg	0.1	0.1-0.9
As	mg/kg	<0.1	
Hg	mg/kg	0.02	

The formation of corrosive deposits is the main problem in biomass combustion from an economic point of view. Another important problem is a high degree of formation of sub-micrometer aerosol particles. Handling and transportation of the fuel, high moisture content, and the technical design of combustors are other important limitations to biomass combustion. In most large scale combustors the fuel is combusted on a grate (Stoker grate), in fluidized bed or by suspension firing (Bain *et al*., 1998). Underfeed Stokers are not suitable for ash-rich fuels due to the formation of ash layers on the surface of the fuel bed which can cause irregular breakthroughs of the gas and combustion air resulting in increased emissions (Obernberger *et al*., 2006). For straw combustion the grate-fired boilers are mainly used. This type of combustor is illustrated in Figure 1. The main problems for the combustion process are illustrated.
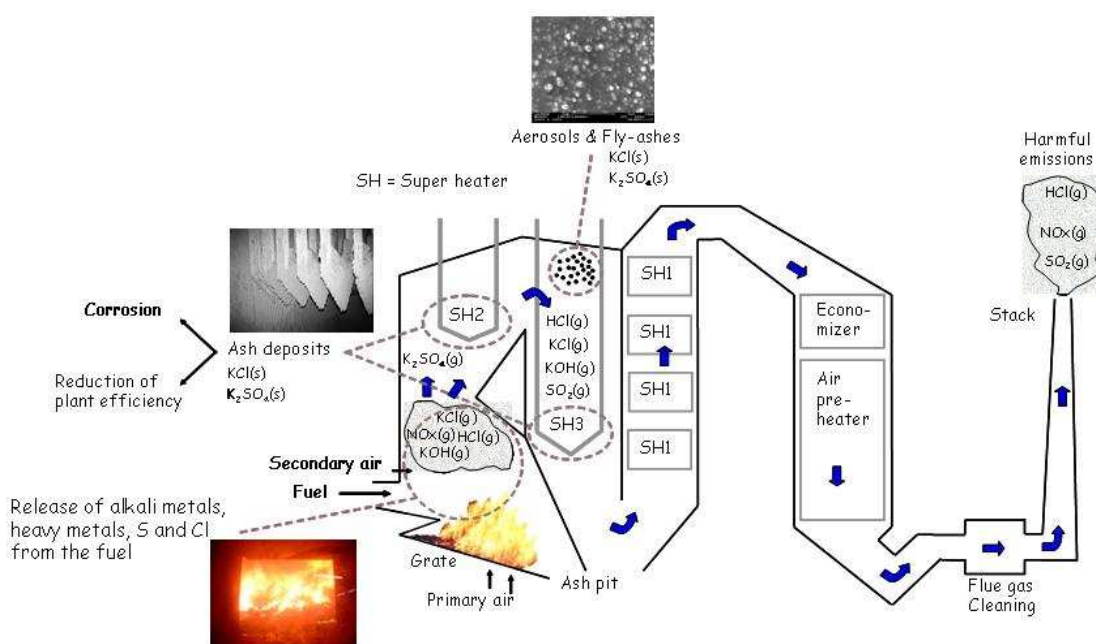
Figure 1. *Illustration of typical grate-fired combustor for biomass combustion. The specific problems related to biomass combustion are pointed out: Alkali metal release in the combustion zone, formation of corrosive deposits on super-heaters, formation of aerosols, and release of harmful emissions through the stack.*

In large scale biomass combustion the flue gases are most often cleaned. The oxides from sulphur and nitrogen are sometimes removed and particulate matter is removed by cyclones, filters or electrostatic precipitators. In small scale combustors like wood stoves, household pellet burners etc., the flue gases are generally not cleaned.

In Denmark biomass combustion is an important part of the energy production. Approximately 70% of the sustainable energy is produced by combustion of biomass and waste (Ministry of Transport and Energy, 2006). Wood, waste, and straw account for the majority, while gasified biomass only gives a small contribution. Between 1980 and 2004 the energy production from combustion of biomass and waste was tripled. The total energy production from combustion of these fuels in Denmark is shown in Figure 2.

The use of energy from biomass combustion in Europe is planned to double from 2002 to 2010 (Danish Energy Authority, 2006). Thus, solving the technical problems related to this technology becomes even more important.

The release of alkali, chlorine, and sulphur to the gas phase from the fuel during combustion depends on the temperature of the combustion zone and on the type of biomass fuel (Dayton *et al.*, 1999). The inorganic constituents of the fuel can be bonded as chelates and cat-ions on oxygen containing groups on the fuel (hydroxyl-, carboxyl-, ether-, and ketone-groups) (Baxter, 1993). In fuels with a high O:C ratio the number of these groups is generally high and the release of inorganics is therefore high. As much as 95% (w/w) of the inorganics in the fuel can be released during pyrolysis (Baxter, 1993). Potassium is released as $KCl_{(g)}$ when the fuel contains high amounts of chlorine (straw and grasses) and as KOH from feedstock that are high in alkali metals and low in chlorine (wood etc.) (Dayton and Milne, 1996).

3
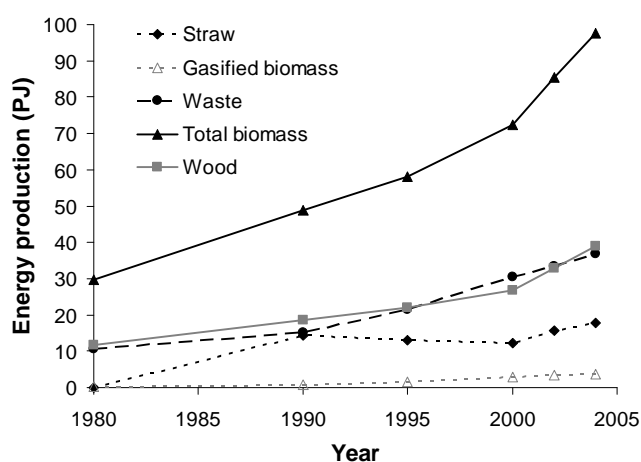
Figure 2. *Energy production from biomass and waste combustion in Denmark 1980-2004. The data for wood combustion is a sum of waste wood, wood chips and wood logs (Ministry of Transport and Energy, 2006).*

The release also depends on the composition of the fuel ash. A high Si content will limit the release of potassium. At 1150°C between 50 and 90% of the potassium from straw is released while chlorine is completely vaporized at this high temperature (Knudsen *et al.*, 2004b). Approximately 85% (w/w) of the sulphur in straw is released at 950°C (Knudsen *et al.*, 2004a). Secondary reactions between char and chlorine or sulphur may be important. The char can capture the gaseous components HCl and SO_2 to significant extent (Knudsen *et al.*, 2005b).

1. 2   Waste combustion

Combustion of waste is an important technology in modern society. In most waste incinerators the waste is combusted on a moving grate with primary air introduced through the grate and secondary air introduced well above the grate to minimize the formation of nitrous oxides. Slags from waste contain high amounts of heavy metals and the washing out of these after deposition is a major problem (Pedersen *et al.*, 2005). As for biomass combustion, a high chlorine release from the waste during combustion is also a limitation for the steam temperature in waste incinerators (Miltner *et al.*, 2006). Due to the very inhomogeneous nature of waste it is difficult to give a general chemical composition of the fuel as it is done for straw in the previous section.

The incineration of waste is an option for reducing the amount of waste to be land-filled, while recovering its energy content for generation of electricity and district heating. The technology also allows waste hygienization (Sabbas *et al.*, 2003). However, municipal waste incinerators have had a bad reputation due to the emission of toxic combustion byproducts as polychlorinated dibenzo-p-dioxins and polychlorinated dibenzofurans (PCDD/Fs) (Oh *et al.*, 2006), polycyclic aromatic hydrocarbons (PAH) (Zimmermann *et al.*, 2000), heavy metals (Riber *et al.*, 2005; Chang *et al.*, 2000; Yoo *et al.*, 2002), and aerosols (Maguhn *et al.*, 2003). Large efforts have been made to reduce toxic emissions from municipal waste incinerators and many incinerators are nowadays equipped with emission reducing devices such as wet-scrubbers, baghouse filters, absorbers or electrostatic precipitators. Filters and electrostatic precipitators are extremely

effective in decreasing the particulate content of the flue gas when considering the total mass. However, fine particles will always penetrate most cleaning devises to some extent. The retention for sub-micrometer particles in various cleaning technologies are not very well characterized. Some studies have shown that the precipitation minima is in the 0.1-1 µm range for electrostatic precipitators (Huang and Chen, 2002; Nielsen *et al*., 2002) and for fibrous filters (Jiang *et al*., 2006; Kim *et al*., 2006).

In 2004, the total reported waste production in Denmark amounted 13,400,000 tonnes, of which 26% was incinerated, and an additional 1% was left in temporary storage to be incinerated later (Danish Ministry of the Environment, 2006b). The incineration of waste was distributed between 32 waste-to-energy plants located in different cities all over Denmark. Of the 26% (3,400,000 tonnes) of the waste, which was incinerated, 55% came from household waste, 25% came from the service sector (institutions, trade and offices etc.), 8% from industry (manufacturing residues, packaging, plastic, paper, etc.), 2% from building and construction, and 10% from waste water treatment plants (The Danish Environmental Protection Agency, 2004). The Danish strategy for waste management is still to increase recycling and on the same time to reduce the volume of land-filled waste, in order to avoid loss of resources. The recycling aim for 2008 is 65% (w/w) and the aim for land-filling is a maximum of 9%. The 2008 aim for incineration is 26% (The Danish Environmental Protection Agency, 2004).

1.3   Aerosols

A number of definitions of aerosols are found in the literature. The general and simplest definition describes an aerosol as a suspension of particles or droplets in a gas (Friedlander, 2000). Some of the early scientific publications regarding aerosols were related to the formation of sodium/plutonium droplets in the hypothetical case of an accident in a fast breeder reactor for nuclear power generation (e.g. Kawahara, 1977). Aerosols are generally unstable. Particles can settle by gravitation or other transport mechanisms as diffusion, thermophoresis or electrical migration. Collision of particles can cause formation of larger aggregates and thus reduce number concentrations. Droplets can evaporate or grow depending on vapor pressure and finally new particles or droplets can form by homogeneous nucleation. Typical sizes are in the range 0.01 to 20 µm. Smaller particles will often collide and form aggregates due to Brownian motion and larger particles will settle due to the gravitational force. Many authors define particles with aerodynamic diameters below 2.5 µm as fine particles and larger particles as coarse particles. The aerodynamic diameter is the diameter of a unit density sphere with a mass equal to the mass of the particle. Particles formed by nucleation processes are generally fine while particles formed by mechanical processes are coarse. The ratio between surface area of a particle and its volume increases when the diameter decreases: $4\pi \cdot R_p^2/(4/3\pi \cdot R_p^3) \propto R_p^{-1}$. This gives some important properties of materials formed by aerosol processes. Aerosol techniques are used to produce powders used as strengtheners in composite materials (aerosols, carbon black) and to a minor extent to form catalysts, ceramic membranes, and other advanced materials. In energy production by combustion technologies the aerosols are important as they improve the heat transfer from combusted gases to the cooling surfaces by radiation (Lind *et al*., 2006).

The behavior of aerosols is important in the environment and in relation to public health. The concern for particulate matter in the atmosphere has increased in recent years. Major sources of

airborne particles are traffic, wood stoves, power plants, and natural sources (e.g. dust, sea salt, and volcanic dust) (Friedlander, 2000). The use of fireworks also contributes considerably to formation of fine particles. A 6-times increase of the background $PM_{2.5}$ in Beijing during a spring festival has been reported (Wang *et al.*, 2007). Recent studies have shown that fine particles, defined as those less than 2.5 µm diameter, have a greater impact on visibility, health, and water droplet nucleation than larger particles. Moreover, the extended time fine particles spend in the atmosphere makes them more difficult to control than larger particles. Accordingly, a new particulate matter standard, based on an aerodynamic diameter below 2.5 µm, has been proposed in the US (U.S.Environmental Protection Agency, 2006).

1. 3. 1   Health effects

Some epidemiological evidence correlates the increase in PM mass concentrations with cardiopulmonary disease (Pope *et al.*, 1999) and mortality (Anderson *et al.*, 1996; Dockery *et al.*, 1993; Delfino *et al.*, 2005; Fernandez *et al.*, 2005; Maynard and Maynard, 2002; Pope *et al.*, 2002). No specific particle property or component responsible for the toxicological effects has yet been identified. However, the importance of particle properties other than mass concentration, such as chemical composition, particle size, and number concentration, have been emphasized (Harrison and Yin, 2000; Lighty *et al.*, 2000a). In general, epidemiological studies are difficult to make because the actual exposures are mixtures of different pollutants. The measured effects on human health are influenced by the various pollutants and it is difficult to define the effect caused by particulate pollution (Brunekreef *et al.*, 1995). Most studies are based on hospital records.

1. 3. 2   Environmental effects

Anthropogenic-derived atmospheric aerosols are important for the climate on a global and regional scale. Aerosols have an important effect on global warming (Charlson and Wigley, 1994; Charlson *et al.*, 1992). Sulphate aerosols can cool the climate in two basic ways: Either directly, under clear sky conditions, by reflecting some of the incoming solar radiation, or indirectly, by increasing the reflectivity of clouds (Charlson *et al.*, 1992). The cooling effect caused by sulphate particles is of comparable magnitude to the heating caused by green house gases. Carbonaceous aerosols absorb sunlight and thus reduce the sunlight reaching the surface of the earth. However, the low frequency radiation from the surface of the earth is also absorbed when passing the carbonaceous aerosols in the atmosphere. Depending on the conditions this can cause a heating effect on the climate (Ramanathan *et al.*, 2001). In general, the cooling effect is dominant in the day time, while the heating effect of carbonaceous aerosol is dominant during the night.

1. 4   Combustion aerosols

Combustion is one of the major sources of anthropogenic aerosol formation. Three main types of particles are formed in a combustion process. Fine particles are formed by evaporation and re-condensing of non-combustible inclusions in the fuel. Also, the formation of soot during fuel-rich

combustion causes formation of fine carbonaceous particles. Finally coarse particles are formed by non-combusted material from the fuel. These particles are most often composed of non-combustible material. The particle size distributions of aerosols from combustion of solid fuels are often bimodal due to the formation of fine and coarse particles (Nielsen *et al.*, 2002; Jimenez and Ballester, 2006).

Coarse particles are larger than 1 μm and they essentially retain the inorganic matter properties of the original fuel (Jimenez and Ballester, 2006). The particles are often melted when the fuel is combusted and thus the structure is compact. Some studies indicate that the mass of coarse particles is linearly dependent on the inorganic content in the fuel (Wiinikka and Gebart, 2005).

Soot is formed in fuel-rich hydrocarbon flames by reactions between hydrocarbon gases under combustion conditions (Skjøth-Rasmussen *et al*., 2004). It is formed by very small primary particles with diameters of 1-2 nm that are agglomerated to larger aggregates of 10-30 primary particles (Bockhorn, 1994). The primary particles are formed by formation and stacking of polyaromatic hydrocarbons (PAH) as shown in Figure 3.
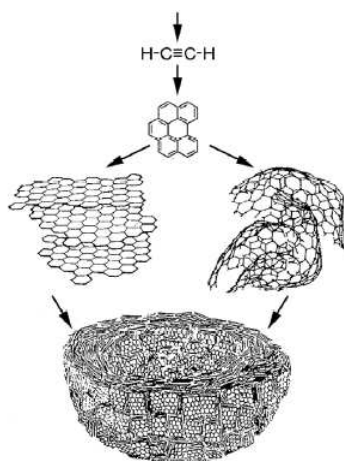
Figure 3. *Main steps in soot formation (Diesel Particulate Filter Manufacturers Task Force, 2000).*

In general the amount of carbonaceous material can be substantially reduced relatively easy by primary measures that facilitate increased combustion efficiency.

The aerosol formation from coal combustion has been studied intensively over the years. Full-scale measurements have been carried out (McCain *et al*., 1975; Kauppinen *et al*., 1990; Nielsen *et al*., 2002) as well as laboratory studies (Flagan and Taylor, 1981; Quann *et al*., 1990). The mechanism of aerosol formation during combustion of coal is well established. Locally reducing conditions within the burning, porous char particle will favor release of gaseous SiO at high temperature. When the SiO is oxidized SiO_2 with very low vapor pressure condenses directly from the gas phase by homogeneous nucleation and particles of very small size are formed in high number concentrations (Quann *et al.*, 1990; Quann and Sarofim, 1982; Sarofim *et al.*, 1977). Similar reduction/volatilization/reoxidation sequence might occur for other metal oxides.

Particle formation is practically unavoidable during combustion of solid and liquid fuels, where non-combustibles from the fuel will evaporate during combustion and re-condense when the combusted gas is cooled. When the temperature is reduced the saturation of the released non-

combustible components will increase and condensation will cause formation of particles and/or deposits on existing surfaces. The amount and properties of the non-combustible fraction of the fuel is very different between different types of fuels.

Biomass and waste are examples of solid fuels with a high amount of non-combustible inorganics, which can be released during combustion.

1. 4. 1   Aerosols from biomass combustion

Due to the increased interest for biomass fuels in recent years, combustion aerosols from utilization of these have been studied. Biomass fuels are all characterized by a high content of alkali chlorides. Sulphur, phosphorous, and carbonates are found in various amounts in these fuels. The three main routes for particle formation mentioned previously are all present in biomass combustion processes. An overview of the particle formation is given in Figure 4. The devolatilization is the release of combustible gases from the fuel caused by heating of the fuel. When the volatiles are released the char will begin burning. During the char-combustion the inorganic inclusions are partly vaporized and the fraction which is not vaporized will melt and form small spherical ash inclusions. The vaporized inclusions will condense on surfaces or as new particles when the temperature is decreased or if they react chemically to form compounds with lower saturation vapor pressures. The resulting particle size distribution is bimodal with one peak originating from the non-vaporized inclusions in the fuel and one resulting from the homogeneous nucleation of vaporized inclusions. Some of the typical components for the ash inclusions in biomass fuels are shown in Figure 4.

.

Figure 4. *Main mechanisms for formation of particles during biomass combustion. Figure from van Loo and Koopejan (2002).*

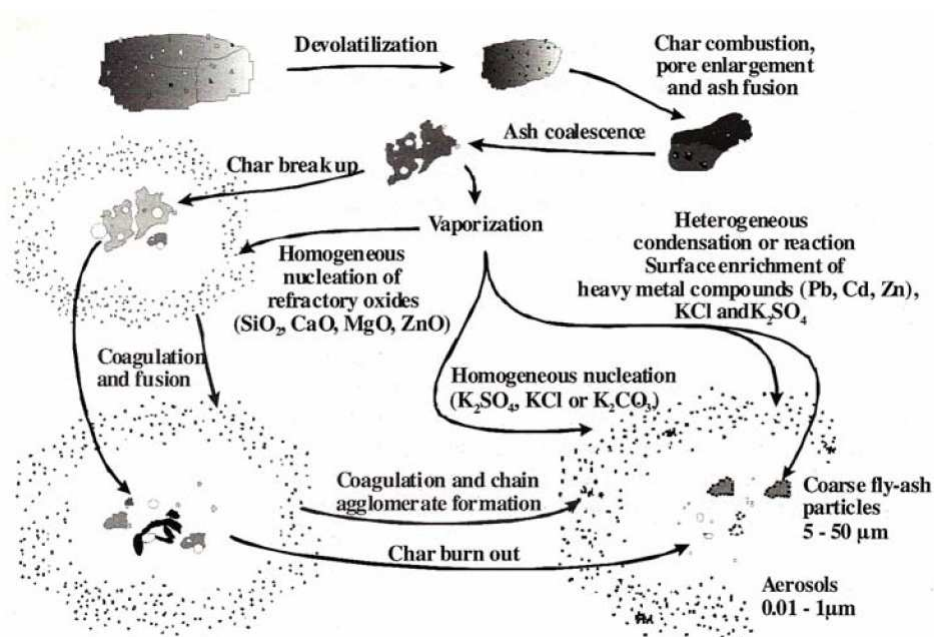Thorough analyses of biomass fuel compositions are given in the literature (e.g. Baxter *et al.*, 1998; Jenkins *et al.*, 1998; Dayton *et al.*, 1999; Jimenez and Ballester, 2006; Turn *et al.*, 1997). The alkali content of wheat straw is high compared to most biomass fuels (>1 kg alkali/GJ) (Jenkins *et al.*, 1998; Turn *et al.*, 1997). The alkali content of the fuel correlates well with the mass concentration of sub-micrometer particles (Christensen *et al*., 1998). The content of salt in the straw varies with use of fertilizer and with weather conditions before harvesting (Sander, 1997; Olsson *et al.*, 1997). The presence of chlorine in the fuel will facilitate volatilization of alkali metals and other metals (Baxter *et al*., 1998; Miller *et al*., 2003; Lind *et al*., 2006). Washing of straw, called fuel-leaching, will reduce the salt content and minimize deposit and aerosol formation, but unfortunately, this is not practically feasible (Jenkins *et al*., 1996; Dayton *et al*., 1999; Knudsen *et al.*, 1998)

Laboratory studies of the particle formation have been made (e.g. Jensen *et al.*, 2000; Jimenez and Ballester, 2004; Jimenez and Ballester, 2005b; Jimenez and Ballester, 2006), full-scale experiments have been performed (e.g. Christensen and Livbjerg, 1996; Valmari *et al.*, 1998; Pagels *et al.*, 2003; Nielsen, 2001; Wiinikka and Gebart, 2005; Johansson *et al.*, 2003), and computational models have been developed (e.g. Pyykönen and Jokiniemi, 2000; Jensen *et al.*, 2000; Christensen and Livbjerg, 2000; Joller *et al.*, 2005; Glarborg and Marshall, 2005; Jokiniemi *et al.*, 1994). The kinetics in the flue gas prior to particle formation have been simulated by detailed kinetics by Glarborg and Marshall (2005) and by Hindiyarti (2007). The mechanisms leading to aerosol formation are not perfectly understood as discussed in Section 1.4.3.

The fine particles generated in biomass combustion are characterized mainly by the elements potassium, sodium, chlorine, and sulphur (e.g. Christensen and Livbjerg, 1996; Nielsen, 2001; Yamasoe *et al.*, 2000; Skrifvars *et al.*, 1998)). In many cases phosphorous is also an important element in the particle composition. Excess potassium can also be bound as K_2CO_3 (Valmari *et al.*, 1998). This compound is condensed heterogeneously (Steinberg and Schofield, 2002; Joller *et al*., 2005). If trace elements such as cadmium, lead, and zinc are present in the fuel, they can be volatilized during combustion in all types of combustion devices and be found as condensed species in the fine particles (Obernberger, 1998; Lind *et al*., 1999; Obernberger *et al*., 1997). The mass load of the fine particles only accounts for a small fraction of the total fly ash. For biomass combustion this fraction is reported as 3-10% (Jimenez and Ballester, 2006) or 34-54% (Nielsen, 2001). However, the number-based size distribution for the aerosol (fine and coarse particles) is always dominated by the fine mode.

Due to the high surface area of the finest particles, components condensing at low temperatures will be dominant in the finest particles. The high volatility of elements like Cd, Zn, and Pb will cause these elements to be enriched in the fine particles when condensing at low temperatures (Obernberger *et al*., 2006).

1. 4. 2   Aerosols from waste combustion

The main environmental concern for waste incineration is the leaching of hazardous elements from the solid residues. However, the combustion aerosols that penetrate the flue gas cleaning devices are also important since they emit to the atmosphere. The particles pose a health problem as discussed in Section 1.3.1. The presence of heavy metals in particles from waste combustion cause an additional problem to the PM_x value. The toxic heavy metals are condensed in the fine

particles and can be inhaled and deposited directly in the lung. The heavy metals are extremely harmful in the human body (Lighty *et al.*, 2000b). Particulate matter from municipal waste incinerator stacks contain high amounts of the heavy metals Fe, Zn, Mg, Mn, Cu, Ni, Pb, Cr, Hg, and Cd (Mateu *et al*., 1999; Yoo *et al*., 2002; Thipse *et al*., 2002).

Particle formation during combustion of waste is dominated by the same main particle formation routes as in biomass combustion. Thus, the overview given in Figure 4 is valid for this type of combustion though less is known about how the nucleation during waste incineration is initiated. The variety of the fuel composition is much greater for waste. Also, in waste, large non-combustible inclusions in the fuel (e.g. large metal parts, ceramics, etc.) are dropped from the grate and contribute to the slag-formation. Some studies reveal that the particles formed in waste combustion are composed mainly of alkali chlorides (Yoo *et al.*, 2002; Mateu *et al.*, 1999).

The literature on fine particles from waste combustion is quite limited. Due to the large variations in fuel chemistry and the presence of a large number of heavy metals, realistic small-scale experiments are difficult to perform in the laboratory.

1. 4. 3   Mechanism for aerosol formation

The fine particles formed by biomass combustion are condensed from volatile vapors. The mechanisms and the sequence of condensation are still not resolved. In one suggested mechanism, potassium reacts with sulphur in the gas phase to form gaseous potassium sulphate. The overall sulphation reactions for the most important potassium components at combustion temperatures (>900°C), KCl and KOH, are given by (e.g. Valmari, 2000):

$$2KCl_{(g)} + SO_{2(g)} + H_2O_{(g)} + \tfrac{1}{2}O_{2(g)} \xrightarrow{\ high\ temperature\ } K_2SO_{4(g)} + 2HCl_{(g)} \qquad (1)$$

$$2KOH_{(g)} + SO_{2(g)} + \tfrac{1}{2}O_{2(g)} \xrightarrow{\ high\ temperature\ } K_2SO_{4(g)} + H_2O_{(g)} \qquad (2)$$
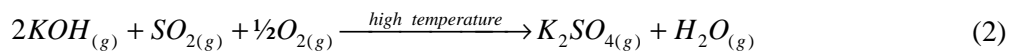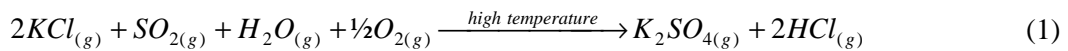
Due to the presence of high amounts of chlorine in most biomass combustion processes the potassium is mainly present as chloride after its release and reaction (1) is dominating. The reaction has been proposed in several studies (Jokiniemi *et al.*, 1994; Christensen, 1995; Valmari *et al.*, 1998). Christensen (1995) suggested that the reaction is kinetically limited by the oxidation of SO_2 to SO_3. In this case reaction (1) can be divided into two important reactions:

$$SO_{2(g)} + \tfrac{1}{2}O_{2(g)} \xrightarrow{\ high\ temperature\ } SO_{3(g)} \qquad (3)$$

$$2KCl_{(g)} + SO_{3(g)} + H_2O_{(g)} \xrightarrow{\ very\ fast\ } K_2SO_{4(g)} + 2HCl_{(g)} \qquad (4)$$
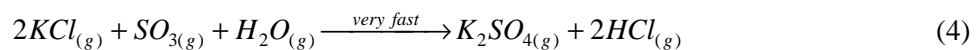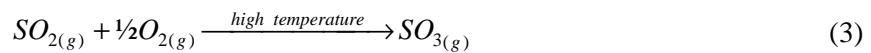
However, some authors disagree that the extremely low vapor pressure of gaseous sulphate can account for sufficient presence of gaseous sulphate in the nucleation process (Steinberg and Schofield, 1990; Steinberg and Schofield, 2002; Schofield, 2003). Their main point of concern regarding the homogeneous formation of sulphate is that this reaction is kinetically very demanding. They propose a mechanism which includes different radicals that needs to combine in order to allow this homogeneous formation of sulphate. In the homogeneous mechanism

proposed by Glarborg and Marshall (2005) the formation of sulphate is not limited by these radical combinations and a much faster reaction is proposed. The heterogeneous formation of K_2SO_4 has been shown to be rather fast at any surface and for this reason they doubt that the homogeneous reaction will occur (Steinberg and Schofield, 1996; Steinberg and Schofield, 2002; Schofield, 2003). They propose that the seeds for forming aerosols are already present in the flue gases when sulphate is formed at high temperatures. Several studies do give reason to doubt that this is the governing mechanism: The particle number concentrations found after the condensation of sulphate is order of magnitudes higher than the number concentrations observed in the hot flue gas (Jimenez and Ballester, 2004). It was shown by Jensen *et al.* (2000) that the formation of particles by KCl in a laboratory furnace was easy to suppress. However, when SO_2 was added in addition to KCl, O_2, and H_2O it was impossible to suppress the nucleation of new particles. In addition, Jimenez and Ballester (2004) and Valmari (2000) reported that particles sampled from flue gases at high temperatures are composed of almost pure potassium sulphate with no traces of condensed chlorine. This, however, does not prove that seed of other components cannot be formed before the alkali sulphate is condensed.

If K_2SO_4 is not the nucleating component, a third component in the post-combustion gases must nucleate. For some types of biomass combustion seeds of CaO have been observed (Nussbaumer and Hasler, 1999). These are mainly found during combustion of wood bark. Ca is not present in all biomass fuels (Obernberger *et al.*, 2006) and cannot explain the high number concentrations found in combustion of all kinds of biomass fuels. The nucleation could also be caused by alkali phosphates. The kinetic limitations for forming the phosphates homogeneously are probably similar to the ones for sulphates and phosphorous is not found in all biomass fuels (Obernberger *et al.*, 2006; Turn *et al.*, 1997).

If the sulphate is nucleating, the above mentioned homogeneous reactions are followed by the following condensation reactions:

$$K_2SO_{4(g)} \xrightarrow{\text{homogeneous nucleation during cooling}} K_2SO_{4(s)} \tag{5}$$

$$KCl_{(g)} \xrightarrow{\text{heterogeneouss nucleation on } K_2SO_4\text{-seeds during cooling}} KCl_{(s)} \tag{6}$$
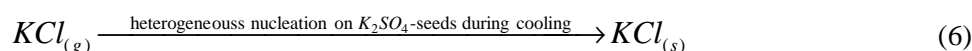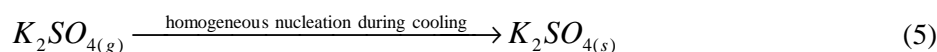
The mechanism for the particle formation is important if the process is to be modeled correctly and if means to reduce particle formation are to be developed.

It is also possible that heterogeneous reactions influence the formation of aerosol particles. The reactions may influence the heterogeneous growth as well as heterogeneous catalysis of gas phase reactions. The catalytic effect on the gas composition may be an important part of the homogeneous nucleation processes leading to formation of new particles.

1.5   Reduction of particle emissions

Particle emissions can be reduced either by reducing particle formation from combustion sources or by cleaning of flue gases. The reduction of particle formation is obtained by control of the combustion parameters or by reducing inorganic contents of the fuel. For wood combustion Nussbaumer (2003) has reported a reduction in fine particle mass concentration by a factor of 5

by reducing primary air in a laboratory reactor. This huge reduction was not observed in the field measurements described in Chapter 5 but it might be an option for reduction of particulate pollution from wood stoves. Reduction of particulate pollution from diesel engines is possible to some extent by optimizing engine design (Spencer *et al*., 2006) and high efficiency removal of particles from cars is possible by filters (Ntziachristos *et al*., 2005). High amounts of aerosol particles are formed in large scale combustion facilities. However, most plants are nowadays equipped with high efficiency particle removal devices. Reduction of particle formation is obtained by using fuels with low alkali contents (as described in this thesis) or by co-firing alkali-containing fuels with coal. In this case the alkali metals will react with alumina and silicates and the formation of fine particles by alkali sulphates and chlorides is reduced (Heinzel *et al*., 1998; Nussbaumer, 2003; Jimenez and Ballester, 2005a). Addition of biomass to coal combustion has a number of advantages, as for example reduction of NO_x and SO_x emissions, but the ash can not be used in cement production due to the presence of potassium (Pedersen *et al*., 1996). Addition of sorbents is another possibility to reduce particle formation as described in Chapter 4.

1. 5. 1   Removal of aerosols

Flue gases from power plants are most often cleaned for particulate matter by cyclones, baghouse filters or electrostatic precipitators. Modern filter technologies are very effective in cleaning coarse particles from the flue gas. However, the fine particles are difficult to remove. These fine particles have very low particle masses and it is difficult to separate them by inertia as in cyclones. The very fine particles have high diffusion coefficients and these will to a high degree deposit by particle diffusion. Different studies have reported a maximum in particle penetration through electrostatic precipitators in the diameter interval from 0.1 to 1.0 μm (Nielsen *et al.*, 2002; Huang and Chen, 2002; McElroy *et al.*, 1982). The degree of penetration is determined by the design of the electrostatic precipitator and the applied voltage. At normal running conditions a penetration maximum at ~200-800 nm is 5-6% by mass (Nielsen *et al*., 2002; Huang and Chen, 2002). The efficiency for baghouse filters is similar to that of an electrostatic precipitator and a maximum penetration is observed at 100-500 nm for filters (Jiang *et al*., 2006; Kim *et al*., 2006).

1. 6   Deposit formation

The deposit formation during combustion of waste and biomass fuels is a major problem. Deposits are formed by fly ash deposition and condensation of volatiles. The deposits are difficult to remove and they have a higher density than deposits generated by combustion of subbituminous or higher rank coals. This is caused by the high amount of inorganic species vaporized during the combustion and thereby a higher degree of the deposits is formed by condensation. Potassium will deposit mainly as chloride in straw-fired boilers (Nielsen, 1998a). If the content of sulphur in the flue gas is high, the composition of deposited potassium salts changes in favor of more potassium sulphate. The coarse particles from the fuel are deposited on the super heater tubes by impaction. These will mainly be found on the upwind side of the super heater tubes. The chlorides and sulphates may condense directly on the super heater tubes. The chlorides can react to form sulphate after deposition. However, this reaction is rather slow (Iisa *et*

al., 1999) and the composition is mainly determined on the rate of deposition of the two alkali components. Thus, the aerosol dynamics play an important role in the understanding of deposit formation during biomass combustion. While coarse particles deposit by impaction on the upwind side of the super heater tubes, aerosol particles are also deposited on the sides of the tubes (Nielsen, 1998a). This is due to thermophoretic and diffusional transport of the aerosol particles.

1. 7   Motivation

The growing importance of alternative energy sources will increase the focus on combustion of renewable fuels in the future. The increased use of biomass and waste combustion will cause increased emissions of fine particulate matter if the formation of aerosols is not reduced from the present level. At the same time the growing understanding of the damaging health effects of particulate matter will lead to a public demand that aerosol emissions are low. An example of the increased concern for particulate matter emissions is the formulation of new guidelines for use of candle lights in private homes etc. (Danish Ministry of the Environment, 2006a).

Some sources of particulate pollution will be reduced by means of separation processes. Two examples of reductions which are being implemented at the moment are the use of filters for diesel vehicles and the introduction of new and more efficient wood stoves.

In most large scale combustion plants flue gas cleaning devices are installed. These can be improved to increase the efficiency of the cleaning of fine particles to some degree. However, several studies have shown that a small fraction of the particles will always penetrate the flue gas cleaning. Reducing the formation of the particle formation is an option to improve the emissions from large scale combustion sources.

Improving the understanding of the mechanisms leading to particle formation in combustion processes is a key measure to reduce emissions. The increasing use of biomass fuels and waste as a source to generate energy gives motivation to study the aerosol formation in these combustion processes. The study needs to focus on the following aspects of the particle formation:

The mechanism for the formation of aerosol particles: How does the particles form and which chemical reactions are important in the formation process?

Measures to reduce the formation of aerosolparticles. How does operational parameters affect the formation of particles and is it possible to change these in order to reduce the formation? Is it possible to affect the chemistry in the flue gasses to reduce particulate formation? Is this done by obtaining a specific composition of the fuel or can sorbents be used to change the flue gas composition after release of volatile components from the fuel?

Is it possible to predict the extent of particle formation and the properties of the resulting particle size distribution by means of computational methods?

In this thesis it is aimed to answer some of these questions.

CHAPTER 2   LAMINAR FLOW AEROSOL CONDENSER

This chapter describes the study of aerosol formation in a laboratory reactor. It is aimed to reveal the mechanism for aerosol formation during biomass combustion by experiments with a synthetic flue gas. The laboratory setup is described and the results obtained are presented and discussed.[1]

2. 1   Introduction to the experimental setup

The laminar flow aerosol condenser (LFAC) is a tubular furnace in which a synthetic flue gas, fed in laminar flow, is preheated and subsequently cooled. The total length of the furnace is 200 cm and the temperature is controlled by 9 axial zones with separately controlled heating. The inner diameter of the furnace is 25 mm. The length of the heated section of the furnace is 173 cm. Alkali chlorides and hydroxides are fed in controlled amounts by an inert gas flowing through a bed of porous pellets impregnated with the salt or hydroxide of interest. The saturator pellets are placed in an alumina tube coaxially inside the first part of the furnace. The temperature in this zone is kept constant and by controlling the temperature and flow of inert gas that passes the pellets the desired concentration is obtained in the furnace. It is assumed that the vapor pressure above the pellets reaches the level of saturation before the end of the saturator. This assumption was tested by using different amounts of pellets in the saturator and verified that the concentration did not increase when adding more pellets. The saturator was modeled by Nielsen (1998b) and it was found that the gas was saturated well before leaving the saturator. On the outside of the saturator it is possible to introduce other gases to the furnace. The gas from the saturator mixes with the gas from this parallel feeding by radial diffusion. A parabolic laminar flow profile is obtained shortly after the mixing. In Appendix B the extreme case of 100% feeding through the saturator is illustrated and it is found that after 10 cm the parabolic profile is obtained. Gasses of main interest are oxygen, water, and sulphur dioxide. The filler-gas is nitrogen. The cooling of the synthetic flue gas results in an increased saturation of the condensable components as the gas flows through the furnace. As a result of the cooling or due to chemical reactions the gas becomes super-saturated and condensation on the furnace walls will result. If the gas becomes sufficiently super-saturated condensing will occur and new particles are formed

---

[1] The results from Chapter 2 and 3 are used in a publication under preparation: 'The Formation Mechanism for Aerosol Particles during the Combustion of Biomass'

directly in the gas phase by homogeneous nucleation. By adjusting the chemical composition, the temperature, and the flow field to the conditions found in post-combustion gasses in biomass combustion the laminar flow aerosol condenser can be used to investigate the particle formation mechanisms governing these processes. The LFAC with the setup used to prepare the gasses and to characterize the aerosols is shown in Figure 5. The setup is equipped with a line for introduction of seed particles to the furnace. These seed particles are formed in an atomizer and subsequently dried in two diffusion dryers. The flow can be diluted with nitrogen after the atomizer. The flow of seed-aerosol is controlled by controlling the pressure drop through one or more capillary tubes. The pressure is controlled by a Back Pressure Regulator (BPR) which is a column of water with an open-end tube emerged to a water level corresponding to the pressure of interest. If no seed particles are introduced the flow is controlled by a rotameter. Parallel to the saturator a feeding gas containing H_2O, O_2, SO_2, and N_2 is introduced. The concentrations of water and oxygen are controlled by passing a gas flow of technical clean air (21% O_2 in pure N_2) through a packed column with demineralized water in counter-current flow. The water saturation is controlled by adjusting the water temperature and assuming 100% saturation in the gas outlet. The line from the water saturator to the furnace inlet is heated to ~120°C to avoid condensation.
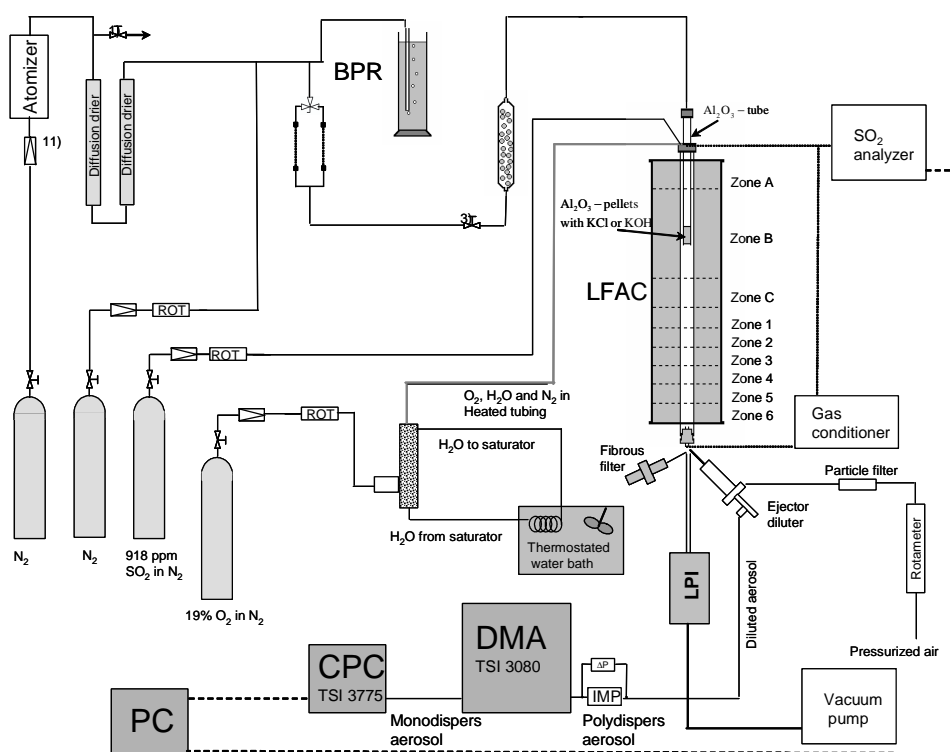
Figure 5. *Laboratory setup for the laminar flow aerosol condenser (LFAC).*

The laminar flow aerosol condenser can be operated either in vertical or horizontal position. The vertical position is used to obtain a symmetrical flow field while the horizontal position is necessary when running experiments with introduction of long probes to the furnace. In practice the results obtained from similar runs with the two different positions were similar and for this reason many experiments are performed in the horizontal position. To introduce probes to the furnace while avoiding contact between the cold probe and the hot furnace wall, a sledge was

specially designed to operate a wide variety of probes in the horizontal position.[2] The laminar flow aerosol condenser is shown in Figure 6 in horizontal position, with the probe-sledge attached, and in vertical position.
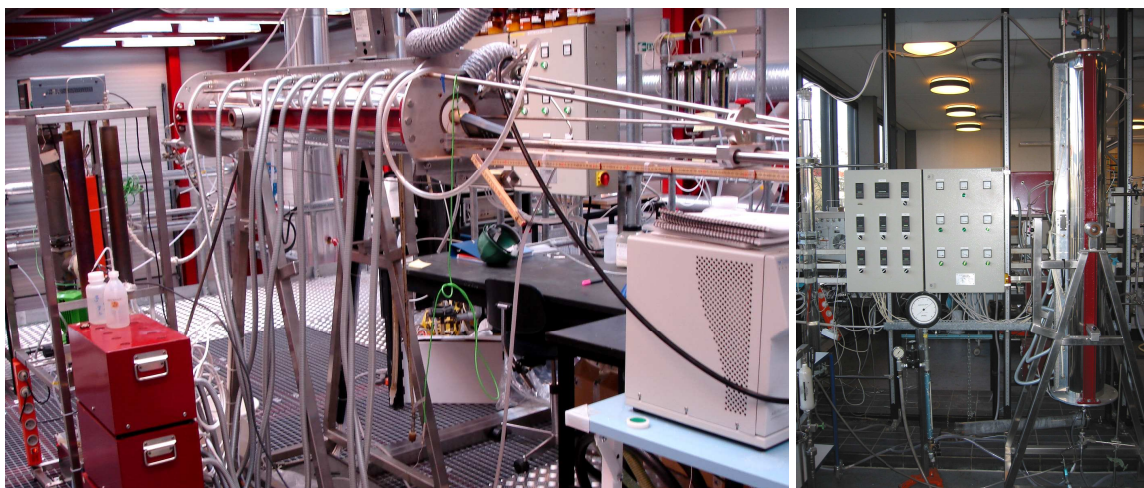
Figure 6. *Laminar flow aerosol condenser (LFAC). Left: The furnace is shown in horizontal position. The diffusion dryers and the water saturator are seen in the left side of the picture. The sledge for introduction of probes is attached on the outlet-side of the furnace. The ejector-diluter is seen above the outlet of the LFAC and a tube connects it to the SMPS. Right: Vertical positioning of the furnace. Left from the furnace the temperature-control board is seen. The setup in the two pictures is placed in two different laboratories.*

The cooling rate in the flue gas when passing the super heater tubes in grate-fired boilers is approximately 500 K/s according to Christensen (1995). For this reason the reference temperature profile was chosen in a way that allowed particles to form with a cooling rate close to this. The reference temperature profile for the reactor is shown in Figure 7. The wall temperature is measured using a long probe equipped with a nickel/nickel-chromium thermo-element (type K), which is insulated to the sides. The thermo-element is pressed against the reactor wall and kept steady until a constant temperature is observed. The plug flow residence time of the gas from the mixing point to the peak temperature point is 0.5 s and the residence time from the peak temperature point to the reactor outlet is approximately 3 s with this temperature profile (as shown later in Figure 22 on page 33). The measured temperature profiles are very similar to the profiles obtained by linear interpolation between the set-points of the temperature controllers. For this reason the profiles were not measured for all different runs. In some cases this was obtained by interpolations from set-point temperatures. The center-line temperature in the furnace, as calculated by the computer model MONAERO (described in Chapter 3), is shown in Figure 7. The temperature difference from the wall to the center of the furnace is approximately 100-125°C when the flow rate is 3500 mL/min (20°C, 1 atm). The same result was obtained by computational fluid dynamics simulations and it was found that the effect of radiation on the centerline temperature was negligible for the relevant gas compositions. The conditions described above gives a radial temperature gradient, which is approximately 10 times larger than the axial temperature gradient.

---

[2] The sledge was made by Henning Koldbech in the workshop of the Department of Chemical Engineering.
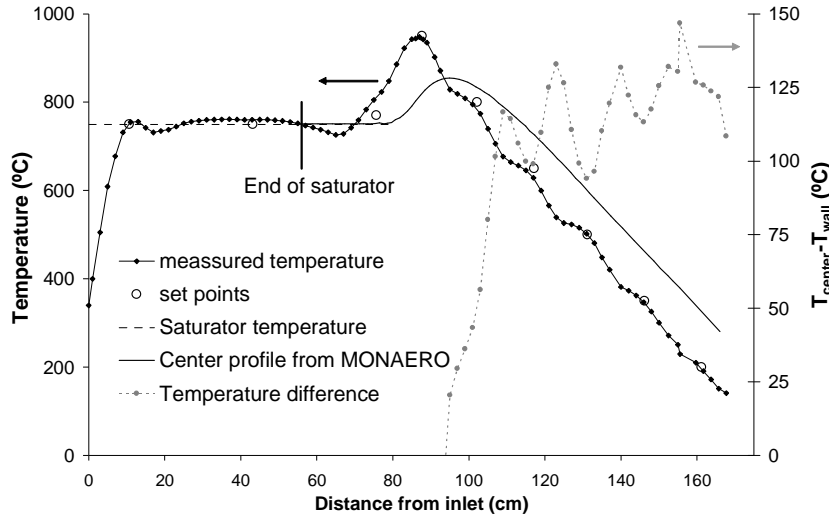
Figure 7. *'Reference' temperature profile used in most experiments with the LFAC. The inlet is here defined as the point where the heating sections begin. The end of the saturator is placed 56 cm from this inlet and the peak temperature is positioned 87 cm from the inlet. The center-line profile is calculated by the computer model MONAERO using the gas properties of pure nitrogen and neglecting radiation. The temperature difference between center and wall in the LFAC is shown on a separate axis.*

2. 2   Characterization of aerosol particles

The instruments used in the laboratory are described in the following. Many of the instruments, were also used in the field measurements, as described in Chapter 4 and 5.

2. 2. 1   Scanning mobility particle sizer

The scanning mobility particle sizer (SMPS) is an instrument for measuring particle size distributions based on the number of particles. The system consists of an electrostatic classifier and a condensational particle counter (CPC). The electrostatic classifier charges the particles and introduces the aerosol in a well defined flow into a differential mobility analyzer (DMA). In the DMA the charged particles are separated by their mobile diameter. The electrical mobility, Z_p, is given by (Baron and Willeke, 2005):

$$Z_p = \frac{U_p}{E} = \frac{n_p \cdot e \cdot C_c(D_p)}{3\pi \cdot \mu \cdot D_p} \tag{7}$$

where $e = 1.602176\ldots\cdot 10^{-19}$C is the charge of a single electron, n_p is the number of charges, and $C_c(D_p)$ is the Cunningham slip correction factor given by (Friedlander, 2000):

$$C_c(D_p) = 1 + \frac{2\lambda}{D_p}\left(A_1 + A_2 \exp\left\{\frac{-A_3 D_p}{\lambda}\right\}\right) \tag{8}$$

$$\lambda = \frac{\mu}{\rho_g}\sqrt{\frac{\pi \cdot M_g}{2R_g T}} \tag{9}$$

18

with $A_1 = 2.5140$, $A_2 = 0.800$, and $A_3 = 0.55$. The Cunningham slip correction factor becomes important, when the particle diameter is of the same order of magnitude as the mean free path of the surrounding gas. In this case the drag on the particle is lower than the one calculated by continuum mechanics (Seinfeld, 1986). In the DMA the aerosol is introduced in a laminar flow close to the wall of a cylinder. In the core of the aerosol flow a laminar flow of particle-free gas is introduced and in the center of the cylinder a rod is placed. By applying a voltage to the center rod the charged particles are moved in radial direction by an electrical force. The DMA is designed so that only particles with a specific diameter will leave the DMA. The ratio between aerosol flow and sheath air flow is typically fixed at 1:10. The diameter of the particles leaving the DMA depends on the voltage applied to the instrument and it is given by (Pagels, 2005):

$$D_p = \frac{2n \cdot e \cdot U \cdot L \cdot C_c(D_p)}{3\mu \cdot Q_s \ln(R_2 / R_1)} \tag{10}$$

where n is the number of elemental charges, e, on the particle, U is the potential of the center rod, L is the length of the DMA, $C_c(D_p)$ is the slip correction, μ is the gas viscosity, and Q_s is the flow of dilution air in the DMA. R_2 is the radius of the outer cylinder wall and R_1 of the center rod. The particle separation principle in the DMA is illustrated in Figure 8. The monodisperse aerosol leaving the DMA enters the condensational particle counter (CPC) and the particles are enlarged by condensation of *n*-butanol. The enlarged droplets are counted in a laser. The DMA and the CPC are connected to a computer and the particle size distribution is scanned by changing the voltage in the DMA.
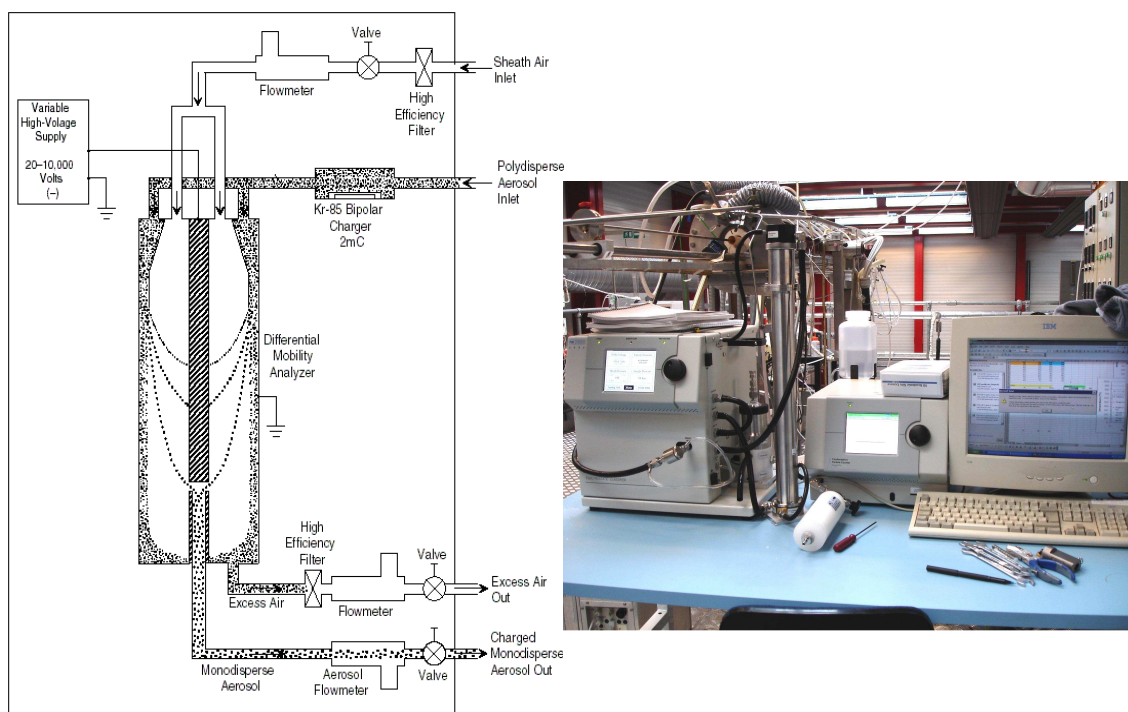
Figure 8. *Left: Illustration of the differential mobility analyzer (DMA). The aerosol is introduced in a laminar flow parallel to the walls of the cylinder. Particle-free gas is introduced with the same velocity in the core. In the center of the cylinder a rod with an applied voltage is placed. After charging in a neutralizer (Bipolar charger) the particles are separated in the electrical field due to their mobile diameter. Figure from www.tsi.com Right: The scanning mobility particle sizer used in this chapter (SMPS).*

In this study two different SMPS systems are used. In the full-scale measurements in Chapter 4 and 5 a TSI 3071 electrostatic classifier with a TSI 3010 CPC is used, while a newer system containing a TSI 3080 electrostatic classifier with a TSI 3775 CPC is used in the laboratory measurements in this chapter and in Chapter 4. The latter is equipped with either a TSI 3085 nano-DMA or a TSI 3081 long-DMA (the system is shown in Figure 6 with the long-DMA applied). The range of particle diameters depends on the geometry of the DMA and the flow rates of aerosol and sheath air as given by equation (10). The lower limit of the CPC does also limit the diameter range of the SMPS system in some cases. By using a nano-DMA with a sheath air flow of 15 L/min the instrument can scan from 2 to 150 nm while the range is from 14 to 800 nm with the long-DMA and a flow of 3 L/min.

2. 2. 2 Cascade impactor (LPI)

An impactor is an instrument, which separates particles according to their inertia by impaction. The impactor directs a jet of the investigated aerosol through a nozzle and against a flat impactor plate perpendicular to the direction of the flow. Particles with inertia too high to follow the stream lines of the gas will collide with the plate. The principle is shown in Figure 9. The impactor separates particles from the aerosol by their aerodynamic diameters. The aerosol particles are separated with a certain cut-off aerodynamic diameter. This cut-off diameter can be varied by changing the aerosol velocity. In the cascade impactor a number of impactors are connected in series and the cut-off diameter is stepped down in every stage by increasing the linear gas velocity and by decreasing the pressure. The aerosol is thereby classified in a number of size classes. In a low-pressure impactor (LPI) the gas flow is driven by a vacuum on the downstream side of the instrument. The flow in the last stage is controlled by critical nozzles. This ensures a fixed flow through the LPI if an aerosol with constant pressure and temperature is measured.

The Stokes number for the particles at the cut-diameter is the same for all stages ($St_{cut} = 0.22$). This is given by (Friedlander, 2000):

$$St = \frac{D_p^2 \rho_p C_c(D_P) u}{18 \mu \cdot d} \tag{11}$$

where ρ_p is the particle density, u is the average gas velocity, d is the diameter of the impactor nozzle, $C_c(D_p)$ is the Cunningham slip correction factor, and μ is gas viscosity. The slip correction increases with decreasing particle diameter. For this reason it is possible to measure smaller particles when decreasing the pressure.

The collected particles on the impactor plates can be quantified gravimetrically or electrically (the instrument is then called an electrical impactor, ELPI). In the first method a thin foil of alumina is placed on the impactor plate and the weight of particles is determined by weighing the foil with and without deposits. This method is used here and samples are weighed twice before and after sampling using a Satrorius M5D-000V001 microbalance. The used instrument is a Berner-type low-pressure cascade impactor with a range in aerodynamic diameters from 0.030 to 12.7 µm. The range given by the manufacturer, Hauke GmbH, is 0.018-16 µm. The impactor has been subject to a detailed investigation of the pressure drop across each stage and a subsequent calculation of the actual cut-diameters in a study by Steffensen (1998), hence the values from this study are used in this work. In an ideal impactor the efficiency curve describing the collection

efficiency as a function of the particle diameter will be a step-function. For a real impactor the curve deviates from the ideal case as seen in Figure 9. No correction for this is necessary according to Hillamo and Kauppinen (1991). The foils and the dissembled impactor are also shown in Figure 9.
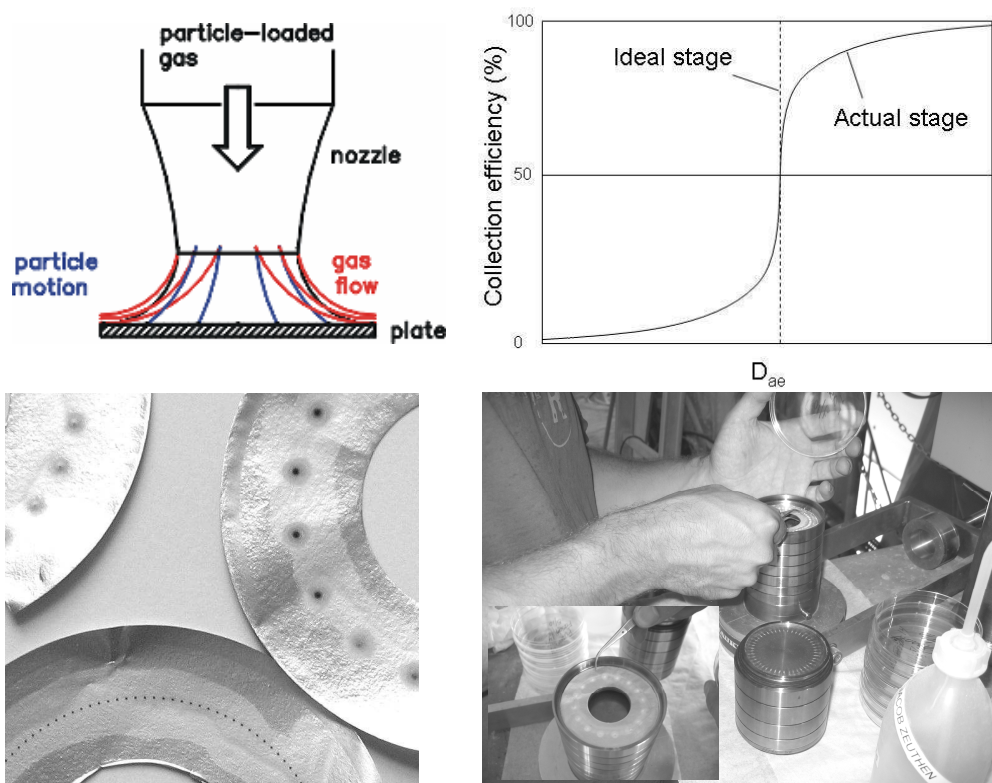
Figure 9. *Principle for impaction of particles in a LPI. Top-left: The stream lines for the gas are not followed by the particles in the aerosol. These impact and form deposits if their aerodynamic diameter is too high. Top-right: The efficiency of an impactor stage. The aerodynamic cut-diameter is defined as the diameter with 50% collection efficiency. Bottom-left: Foils from different stages with grease and particle deposits. The fine particles are black (soot) while the coarser particles are white (salt) in this case. Bottom-right: Dissembling of the cascade impactor.*

Impactors have the advantage of being simple, both in construction and operation, and are therefore widely used. However, it is difficult to sample very small particles accurately due to their low mass and to particle bounce at high gas velocities. The particle bounce is minimized by applying a thin layer of Apiezon H vacuum grease to the alumina foils (applied as a 2.5% (w/w) solution in Toluene and dried for 2 hours at 140°C). The LPI is cleaned with ethanol and pressurized air between every measurement.

2. 2. 3   Electron microscopy

In electron microscopy the light beam from optical microscopy is replaced by a beam of electrons (Baron and Willeke, 2005). The monochromatic electron beam is focused using metal aperatures

and magnetic lenses. When the electrons hit the sample they may be transmitted through the sample. These electrons are used in a transition electron microscope (TEM). In this microscope a very high resolution of the sample morphology is obtained. Electrons can also reflect from the sample by backscattering or as auger electrons or secondary electrons. These electrons are used in a scanning electron microscope (SEM). This instrument is well suited for topographic studies of surfaces. When the sample is bombarded with electrons the atoms are exited to higher energy levels. As the electrons fall back to their non-excited state an X-ray is emitted. The wave lengths are characteristic for the specific atom and by measuring these it is possible to obtain (local) chemical analysis in the microscope. This technique is called energy dispersive X-ray spectroscopy (EDS) and is available in both SEM and TEM microscopes. The chemical compositions measured by EDS are normalized to the elements included in the analysis. Elements with atom numbers smaller than $Z = 11$ (Na) are not included and when analyzing deposits on impactor foils Al is not included, because the signal from the foils is dominating. The mass-based composition is given by:

$$W_i = \frac{m_i}{\sum_j m_j} \cdot 100\% \tag{12}$$

The accuracy of EDS is ± 1% and concentrations below 1% are generally not reliable. Particles are sampled for TEM analysis by inserting a small grid of Cu coated with a thin layer of carbon into the particle-laden gas. The particles deposit by diffusion. Since the diffusion of particles is very size dependent the size distribution of the particles on the grid is not representative of the distribution in the gas. This can be improved to some extent by cooling the grid and thereby allowing particle transport by thermophoresis.

2. 2. 4   Ion chromatography

Ion chromatography is based on liquid chromatography and uses ion-exchange resins to separate atomic or molecular ions based on their interaction with the resin (Ewing, 1985). Its greatest utility is for analysis of anions for which there are no other rapid analytical methods. It is also commonly used for cations and biochemical species such as amino acids and proteins. Most ion-exchange separations are done with pumps and metal columns. The method is very precise and anions can be quantified on a ppb-level.

2. 2. 5   Ejector-diluter

The ejector-diluter is a simple instrument for diluting gases. The sample gas is withdrawn through a capillary. On the downstream side of the capillary a flow of dilution gas is directed along the flow direction of the sample on the outer side of the capillary. This creates a vacuum causing the sample to flow into the ejector probe. The dilution serves a three-fold purpose. The dilution and simultaneous cooling of the aerosol quenches coagulation of the aerosol particles. The dilution lowers the dew point of the aerosol and finally the lowering of the mass concentration of the aerosol enables longer sampling times for cascade impactors and ensures single-counting of particles in condensational particle counters. The ejector principle is illustrated in Figure 10.
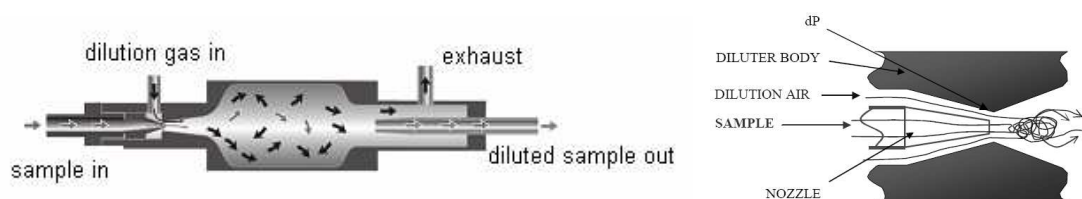
Figure 10. *Principle of an ejector-diluter. The sample is withdrawn through a capillary by a vacuum created by an ejector pump. Turbulence on the downstream side of the capillary outlet ensures thorough mixing. Figures from www.dekati.com*

Different ejectors are used in the laboratory and in the field measurements (the latter is described in Chapter 4 and 5). The dilution ratios in the two are similar (5-200) and was set at approximately 10 in most experiments.

If the ejector is placed with the capillary orthogonal to the sample gas flow the inertia of the large particles will cause a pre-separation before the aerosol enters the ejector. The size-dependent sampling efficiency of this virtual impactor prefilter is calculated by (Vincent, 1989):

$$\text{Efficiency} = \frac{1}{1 + 4\chi \cdot St\sqrt{U/U_t}} \tag{13}$$

where the Stokes number is given by equation (11), $\chi = 2.1$ is an empirical constant (U is the velocity of the sample gas and U_t is the gas velocity in the ejector capillary. The efficiency is the fraction of particles that are sampled to the probe. For large particles the Stokes number is large and the efficiency is therefore low.

2. 2. 6   Gas analyzer

CO_2 and SO_2 concentrations were measured by gas analyzers of the type Rosemount NGA2000. The measurement principle is based on the molecule-specific absorption of bands of infrared radiation. The absorbed wave lengths are characteristic for the individual gases. The instrument used here can specifically measure carbon dioxide, nitrogen oxide, and sulphur dioxide. The analyzer is calibrated with a zero-gas and a span-gas before each series of measurements.

2. 2. 7   ICP-OES and GF-AAS

Induced coupled plasma optical emission spectroscopy (ICP-OES) is a wet chemical analysis for the detection of single elements (Ewing, 1985). The sample is digested in strong acids (HF and HNO_3) and nebulized into a high-temperature argon plasma where the sample dissociates into free excited atoms. When the atoms relax to their normal state they emit radiation that is characteristic for the single elements, and by a quantitative measurement of this by photo multipliers the composition of the sample is determined. The sample can be analyzed for a number of 30-40 elements with high accuracy simultaneously (Baron and Willeke, 2005).

Graphite furnace atomic absorption spectroscopy (GF-AAS) is based on the phenomenon that free atoms will absorb light at frequencies characteristic of the element of interest (Ewing, 1985). Within certain limits, the amount of light absorbed can be linearly correlated to the concentration

of analyte present. Free atoms of most elements can be produced from samples by the application of high temperatures. In GF-AAS, samples are deposited in a small graphite tube, which is then heated to vaporize and atomize the analyte. Concentrations in the ppb range can be detected. Radiation from a cathodic lamp is absorbed by the sample and the concentration of the element of interest can be determined. The wave length of the radiation needed for specific elements vary and different bulbs are needed (λ: 180-900 nm), hence the method rather time consuming.

2. 3 Results and discussion

This section describes the experimental investigation of aerosol formation during cooling of a synthetic flue gas simulating the flue gas cooling during combustion of biomass. The laminar flow aerosol condenser is used in all the experiments. Aerosol formation by homogeneous nucleation from vapors of pure alkali chloride or from reacting gases containing alkali chloride, sulphur dioxide, water vapor, and oxygen is investigated.

2. 3. 1 Nucleation of pure KCl

The nucleation of pure KCl vapors in the laminar flow aerosol condenser has previously been studied by Nielsen (1998b) and by Jensen *et al.* (2000) by using the same furnace as described in this chapter. However, the setup used in connection with the furnace has been almost completely rebuild. To test the new setup of the furnace some of the results from Jensen *et al.* (2000) have been verified in this study. Some new results with pure KCl condensation have also been obtained. The influence of flow rate through the furnace was investigated. The homogeneous nucleation of pure KCl vapors in a seed-free carrier gas was investigated at different flow rates with a fixed temperature profile. Figure 11 shows the particle size distributions from experiments with a carrier gas flow rate from 1000 to 4000 mL/min (20°C and 1 atm). The saturator temperature was constant and the concentration of KCl in the feed was 364 ppm. This reflects the problem of dimensioning the cross-sectional area of the flue gas ducts in the cooling sections of a power plant. A smaller area will cause the same flue gas to cool faster by increasing the flow rate.
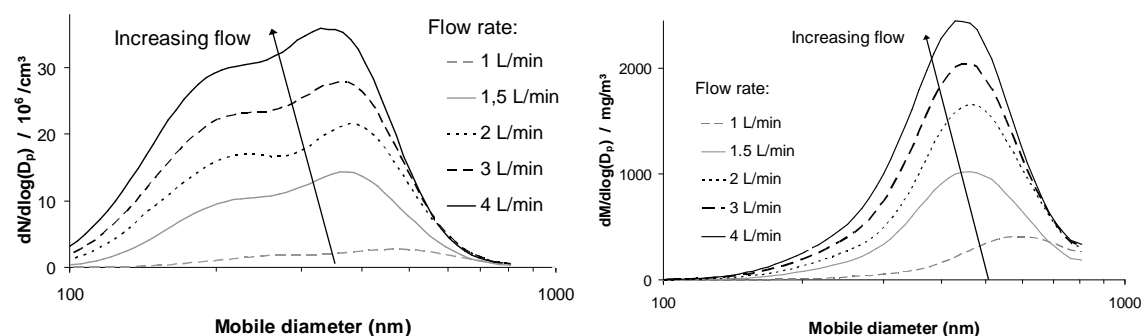
Figure 11. *Number and mass-based size distributions from runs with a pure KCl and different flow rates. The concentration of KCl is 364 ppm. Each distribution represents an average of 3-6 SMPS scans.*

It was observed that the average diameter of the particles decreases when increasing the flow rate. The number and mass concentrations increased with higher flow rates. Increasing the flow rate decreased the wall deposition in the furnace. The wall deposition was calculated for all flow rates by assuming that all KCl vapors from the feed gas are recovered either in the particles or in the wall deposits. The mass concentration of particles was obtained by integration of the mass-based size distributions in Figure 11.

In Figure 12 the mass concentrations of the aerosols are plotted against the residence time in the LFAC. The mass concentrations are each based on 5-8 SMPS scans and bars represent the standard deviation between these. The residence time is calculated based on a furnace length of 1200 mm for a hot flue gas at 800°C. The wall deposition of KCl depends almost linearly on the residence time in the furnace. Extrapolation of the results suggests that no wall deposition will occur at infinitely high flow rates. The experiments were simulated by the computer model MONAERO as described in Chapter 3.
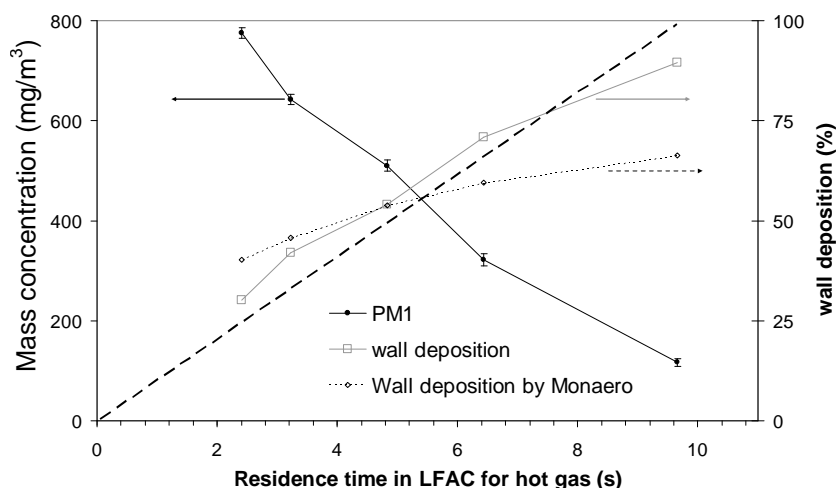
Figure 12. *The mass concentrations of KCl particles as a function of residence time in the LFAC. The temperature profile and the inlet concentration of $KCl_{(g)}$ are the same in all runs (364 ppm). The wall depositions obtained from experimental results and from model results are shown on a separate axis.*

Experiments with different inlet concentrations of $KCl_{(g)}$ were also carried out. The flow rate was 3500 mL/min and the temperature profile was the reference profile shown in Figure 7. The resulting particle size distributions for inlet concentrations in the range from 104 to 364 ppm KCl are shown in Figure 13.

The total number and mass concentrations obtained by integration of the particle size distributions in Figure 13 are plotted as a function of the inlet KCl concentration in Figure 14. The total outlet mass concentration indicates that a maximum level was obtained when increasing the inlet concentration. A higher inlet concentration will cause super-saturation to occur at higher temperature and due to the higher diffusivity of the condensing component at high temperature this will cause higher wall condensation by diffusion and lower particle number concentrations.
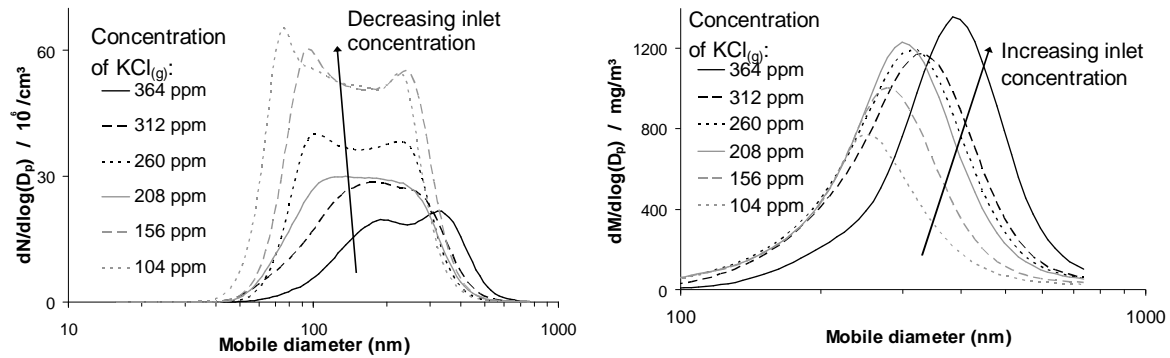
Figure 13. *Number and mass-based size distributions from runs with pure KCl and different inlet concentrations of KCl in the range 104-364 ppm. Each distribution represents an average of several SMPS scans (12-18). The mass-based distributions are calculated from the number-based ones by assuming spherical particles with a constant density of 2 g/cm³.*
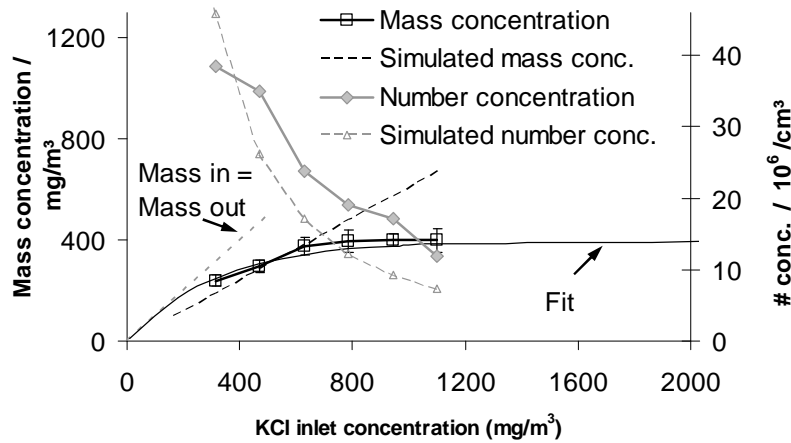
Figure 14. *Integrated properties of particle size distributions from experiments with homogeneous nucleation of KCl with varying inlet concentration. The standard deviations represented by the error bars are based on 12-18 measurements.*

The outlet mass concentration for this series of experiments can be fitted with a simple saturation expression:

$$c(KCl_{out}) = 398 \tfrac{mg}{m^3} \cdot \left(1 - \exp\left\{ -\frac{c(KCl_{in})}{320 \tfrac{g}{m^3}} \right\} \right) \tag{14}$$

The fit is shown in Figure 14 and simulations of the total number and mass concentrations by MONAERO are also shown. These are described later in Chapter 3. The decrease in number concentration when increasing the inlet vapor pressure of KCl has been observed previously by Jensen *et al.* (2000).

2. 3. 2   Influence of chemical composition

The influence of the chemical composition in flue gases from biomass combustion on the particle size distribution and chemical composition of the particles was investigated in the laminar flow aerosol condenser. The overall reaction for the sulphation of potassium is given by equation (1) and (2). The influence of changing the concentration of reactants in the overall reaction was investigated. A reference run with a synthetic flue gas containing 200 ppm KCl, 50 ppm SO_2, 5% O_2 and 5% H_2O was made. These concentrations are typical in the flue gas from straw combustion according to Christensen *et al.* (1998). The concentrations of the reactants in the reference run were changed and the resulting size distributions were compared to the reference case. The temperature profile in all runs was as in Figure 7 and the total gas flow was 3500 mL/min.

In Table 2 the concentrations of the 4 reactants in the experiments are given.

Table 2. *Inlet concentrations for the LFAC experiments with varying chemical composition*

Run	c(KCl) (ppm)	c(SO_2) (ppm)	c(H_2O) (%)	c(O_2) (%)
Reference	200	50	5	5
High SO_2	200	500	5	5
No SO_2	200	0	5	5
High O_2	200	50	5	8
Low O_2	200	50	5	2
High KCl	300	50	5	5

The furnace was thoroughly cleaned before every run. If experiments without sulphur are carried out without proper cleaning after a run with sulphur the results are affected by this. After the furnace has been thermally equilibrated for several hours the gas flows were adjusted and a steady particle size distribution was obtained after a few minutes. The measurements with the cascade impactor were carried out ~3 times for each run and the SMPS measurements were carried out several times (~6-25 scans for each run). In a few measurements the result deviated considerably from the repeated runs. These were not used in the average distributions. All size distributions from LPI, which are included in the average particle size distributions, are shown in Appendix A.

The mass-based size distributions from LPI measurements, and based on SMPS data for the number-based particle size distributions, are shown in the following three figures. In Figure 15 the reference run (50 ppm SO_2) is compared to the run with a higher concentration of SO_2 (500 ppm SO_2) and with the run without SO_2. In Figure 16 the reference run (5% O_2) is compared to a run with higher O_2 concentration (8% O_2) and one with a lower O_2 concentration (2% O_2). In Figure 17 the reference run (200 ppm KCl) is compared to a run with an increased level of KCl (300 ppm KCl).
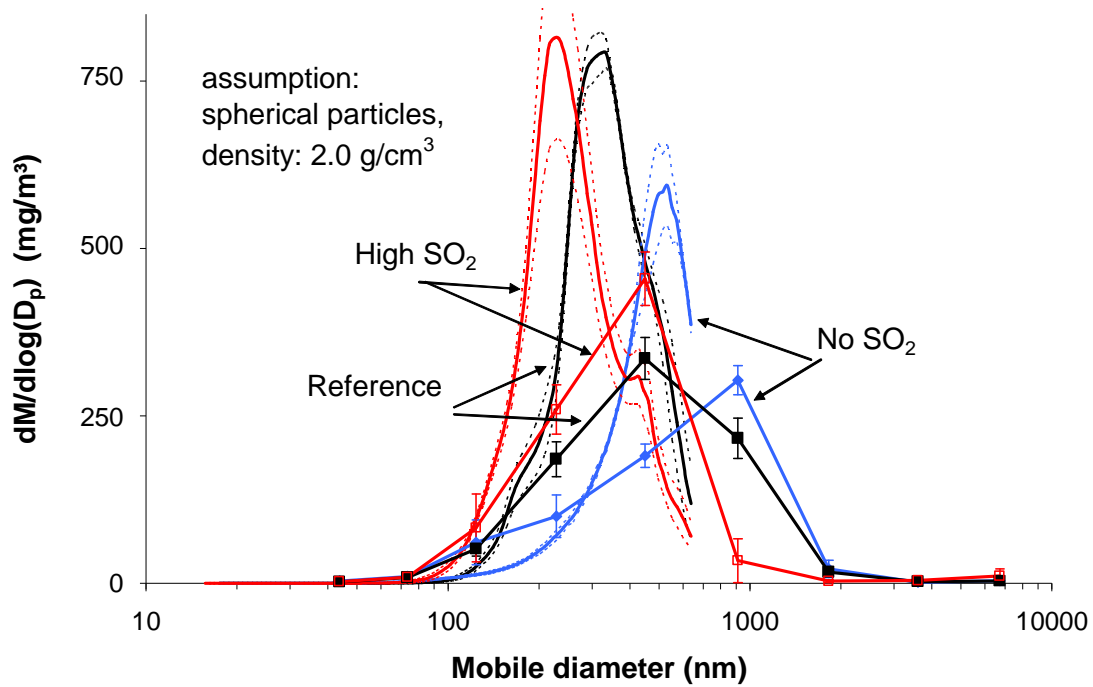
Figure 15. *Mass-based particle size distributions for experiments in the laminar flow aerosol condenser with varying concentration of SO_2 (0, 50, and 500 ppm). The curves obtained from the LPI are shown with standard deviations between 2-4 repetitive measurements represented by error bars. On the curves obtained by SMPS the standard deviation between measurements is represented by dotted lines.*
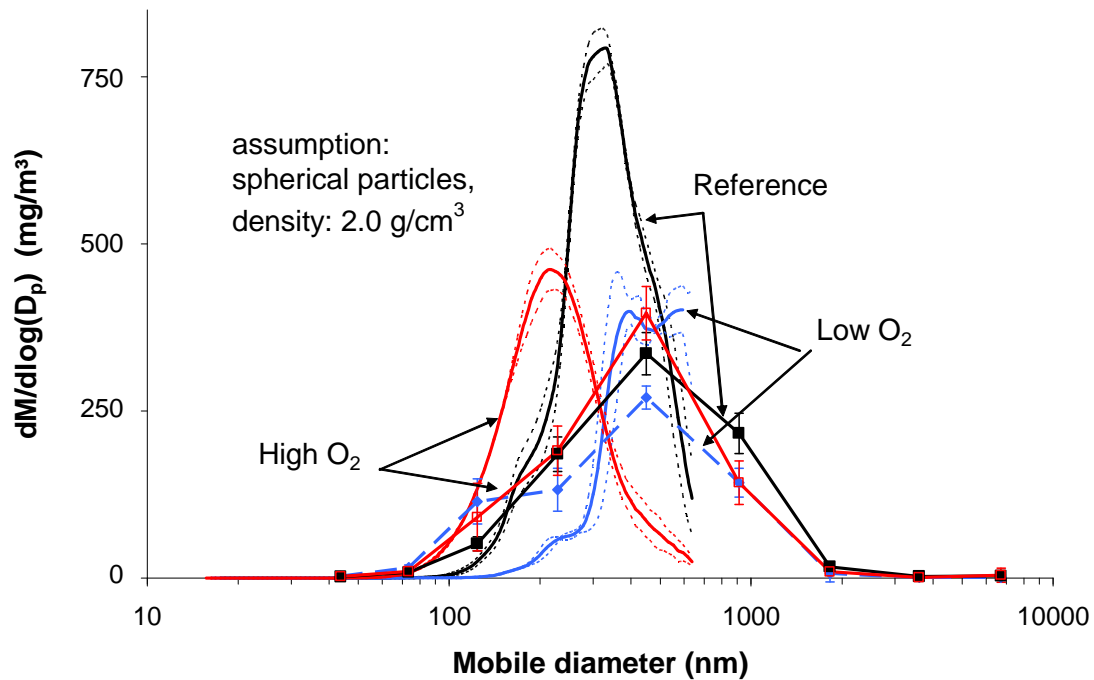
Figure 16. *Mass-based particle size distributions for experiments in the laminar flow aerosol condenser with varying concentration of O_2 (2, 5, and 8%). The standard deviations between measurements are represented by error bars and dotted lines.*

28
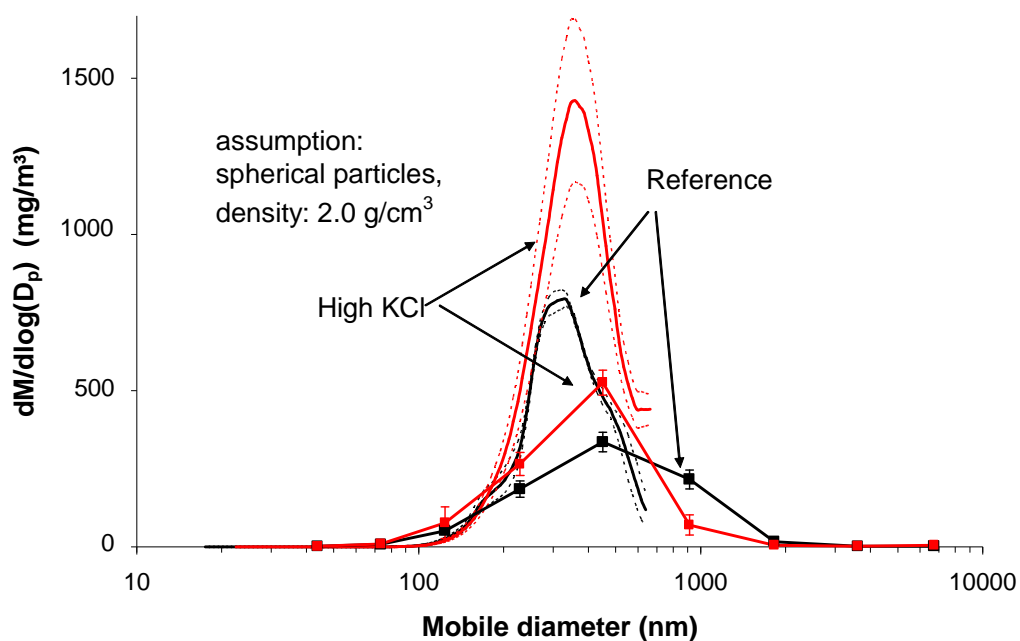
Figure 17. *Mass-based particle size distributions for experiments with varying KCl concentration in the laminar flow aerosol condenser (200 and 300 ppm). The standard deviations between measurements are represented by error bars and dotted lines.*

The number-based size distributions obtained by SMPS from all six runs are shown in Figure 18.
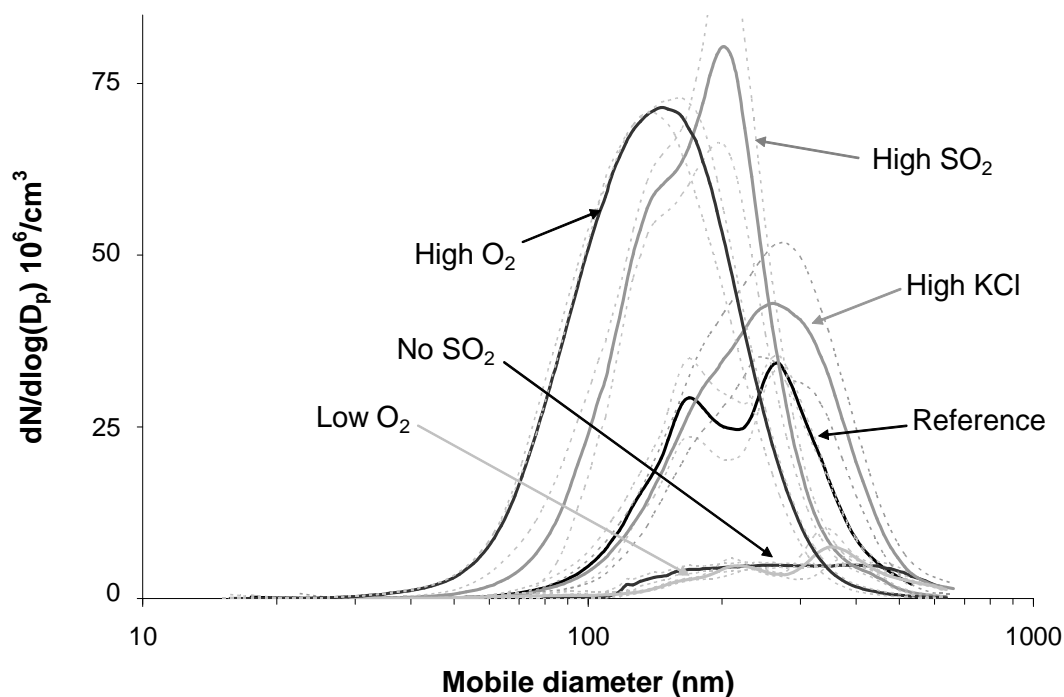
Figure 18. *Number-based size distributions from experiments with variations in the feed composition. The standard deviations are based on 6-25 measurements. The standard deviations between measurements are represented by dotted lines.*

Significant differences in the particle number concentration were observed when changing the concentration of SO_2 or O_2. The mass-based size distributions obtained from measurements with LPI did not resemble distributions based on measurements with SMPS well. The properties of the number- and mass-based size distributions are shown in Table 3.

Table 3. *Properties of the particle size distributions from sulphation of different alkali sources. The experimental conditions are shown in Table 2 and the distributions are shown in Figure 17-18. The properties are derived from the SMPS data, except for the mass concentration, which is derived from LPI and SMPS data. All GMD-values are based on mobile diameters*

Run:	Number concentration 10^6/cm^3	Mass concentration (LPI / SMPS) mg/m^3	Geometric mean diameter (number) nm	Geometric mean diameter (mass, LPI / SMPS) nm
Reference	14.7 ± 1.9	234 / 278	203	393 / 309
No SO$_2$	3.0 ± 0.48	209 / 142	155	456 / 427
High SO$_2$	29.2 ± 4.8	196 / 283	145	305 / 243
Low O$_2$	2.8 ± 0.63	176 / 132	290	321 / 412
High O$_2$	32.1 ± 1.7	221 / 184	140	341 / 216
High KCl	18.3 ± 4.1	275 / 501	249	319 / 363

The increase in number concentration when increasing the concentrations of SO_2 and O_2 is probably caused by increased levels of SO_3 and thereby increased formation of K_2SO_4. Thus, a higher concentration of gaseous K_2SO_4 increases the number of particles formed and thereby decreases the average particle size. This can seem somehow contradictory to the findings for nucleation of pure KCl. In this case increasing inlet concentration to the furnace resulted in a decrease of the number of particles formed while the average particle size was increased. This can be explained by formation of particles as the chemical reaction proceeds to form more gaseous K_2SO_4. Thus, the increased levels of the reactants in reaction (3) will increase the rate of formation of SO_3, but in addition to this the formation will also occur in a longer section of the LFAC. This will result in a higher number concentration of particles when the formation of K_2SO_4 is increased.

The shape of the number-based particle size distribution is bimodal in some cases. This is probably caused by nucleation in different regions of the LFAC. The mass-based particle size distributions are all mono-modal. Most of the distributions can be represented well with a log-normal distribution given by:

$$\frac{dM}{d\log(D_p)} = f(D_p, \alpha, \beta, \theta) = \frac{\theta}{(D_p/\mu m)\beta\sqrt{2\pi}} \exp\left(-\frac{1}{2}\left(\frac{\ln(D_p/\mu m) - \alpha}{\beta}\right)^2\right) \qquad (15)$$

where α is the mean, β is the standard deviation, and θ is a scaling factor. The parameters for the fitted log-normal distribution describing the mass-based size distribution from the reference run are: α = -0.45 and β = -0.65 and θ = 260 mg/m^3. The mean of the log-normal distribution is given by: $D_{p, mean}$ = exp(-0.45)×1μm×(1000 nm/1μm) = 638 nm. The mass-based size distribution of the reference experiment is shown together with the fitted log-normal distribution in Figure 19.
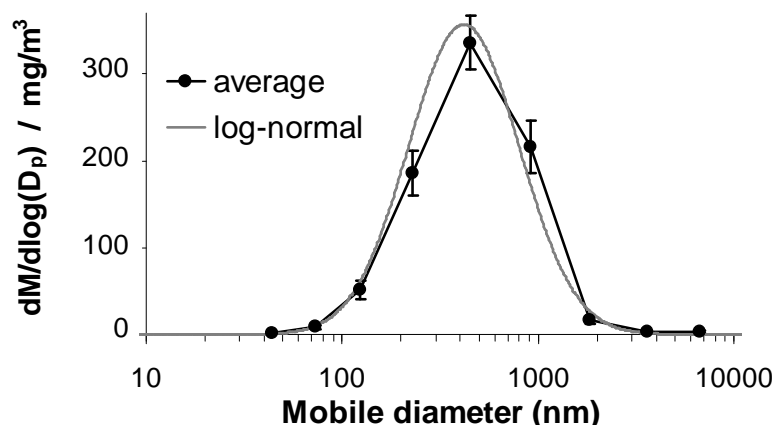
Figure 19. *Mass-based particle size distributions for experiment with 200 ppm KCl, 50 ppm SO_2, 5% H_2O, and 5% O_2. The distribution obtained from cascade impactor and by a fit with a log-normal fit to the experimental data are shown. The standard deviation represented by the error bars is based on 3 measurements.*

2. 3. 3   Composition of particles

The impactor foils from the runs with variation in inlet composition have been analyzed for chemical composition by EDS. The content of sulphate in the particles in the different runs are compared in Figure 20.
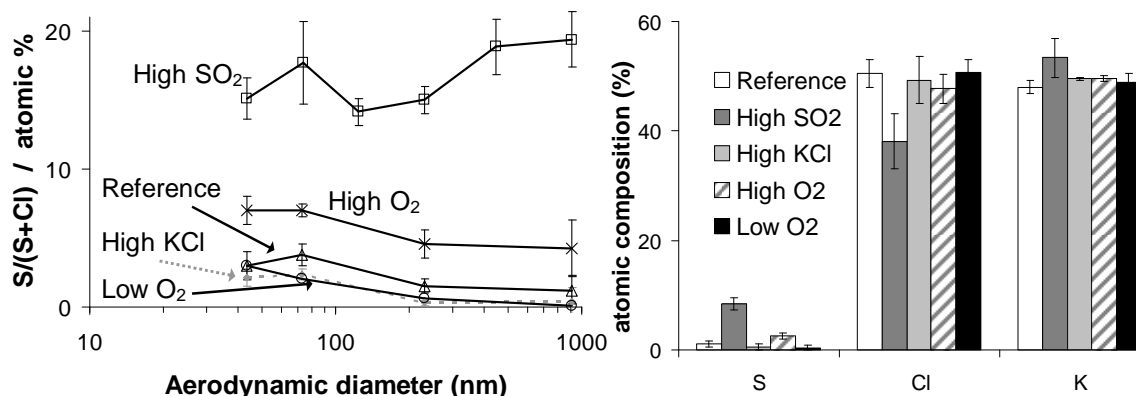
Figure 20. *Sulphur content in particles deposited in the cascade impactor during experiments with variations in chemical composition of the inlet gas. The error bars represent the standard deviation between 2-3 measurements. The elemental composition was determined by EDS. The standard deviation of the total composition represents the deviation between deposits from one set of impactor foils.*

The content of sulphur in the particles from one impactor measurement was largely independent of particle sizes. The particles from experiments with increased inlet concentrations of SO_2 or O_2 had a higher sulphur content. This indicates that the sulphation reaction was faster in these runs. The sulphur content in the runs with low concentration of O_2 indicates that the sulphation reaction

in these runs was slower. The lower sulphur content in the run with increased concentration of KCl was caused by an increased level of KCl in the particles relative to the level of K_2SO_4. The consistency of the data was checked by comparing the amount of positive and negative charges from potassium, chlorine, and sulphur. If the index $n(K)/(2n(S)+n(Cl))$ is different from unity it either indicates that the particles contain other components or that the measurements are not consistent. The index is often shown in the literature with values close to one for the smallest particles and lower values for larger particles (e.g. Lind *et al.*, 2006). The content of potassium should be 50% or higher on an atomic scale. If the content of K_2SO_4 is high the atomic content of potassium will be higher. The potassium content and the ratio between cations and anions are plotted in Figure 21.
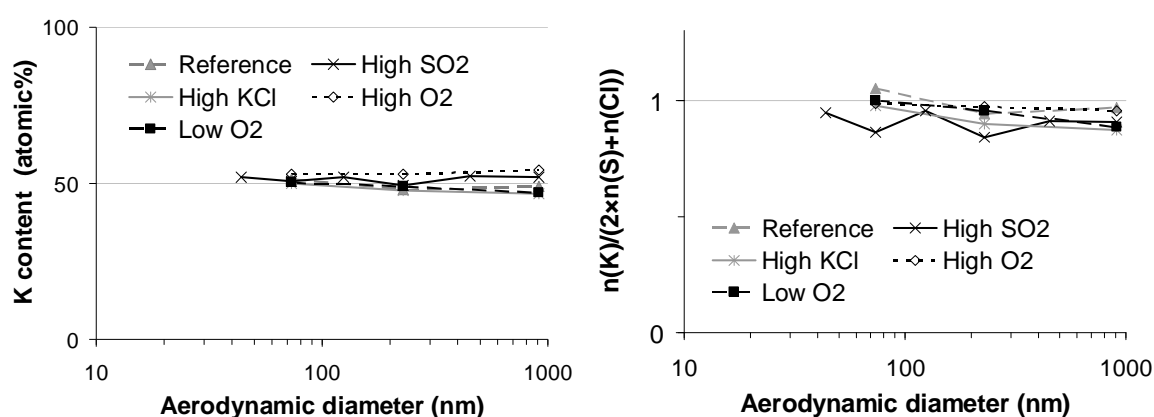
Figure 21. *Plots to test if EDS measurements are reliable. Left: Elemental content of potassium. Right: The ratio between amounts of cations and anions.*

The EDS data are in good agreement with the expectations for particles of pure KCl and K_2SO_4, because the potassium content is close to 50% in all deposits and the index describing the number of anions and cations from these two salts is close to unity. The observations for the sulphur content agreed well with the changes in the particle size distribution for the aerosols during the experiments. A higher sulphur content in the particles corresponds well with a higher number of particles and smaller diameters of the particles. This suggests that a higher degree of sulphation will form a larger number of particles. The condensation of approximately the same mass of chloride on this increased number of particles will result in a lower average particle diameter.

2. 3. 4   Effect of cooling rate on aerosol formation

To study the effect of cooling rate a number of experiments with different temperature profiles were made. A series of runs with two different SO_2 concentrations and three different temperature profiles was performed. The average cooling rate in axial direction is calculated for each profile as function of the axial position in the furnace, and the time-scales for each curve are shown in Figure 22. The residence time decreased considerably when the cooling rate was decreased. Thus, besides the influence on the particle dynamics by faster cooling, the change in cooling rate might also affect the extent of reaction by changing the residence time in the furnace.
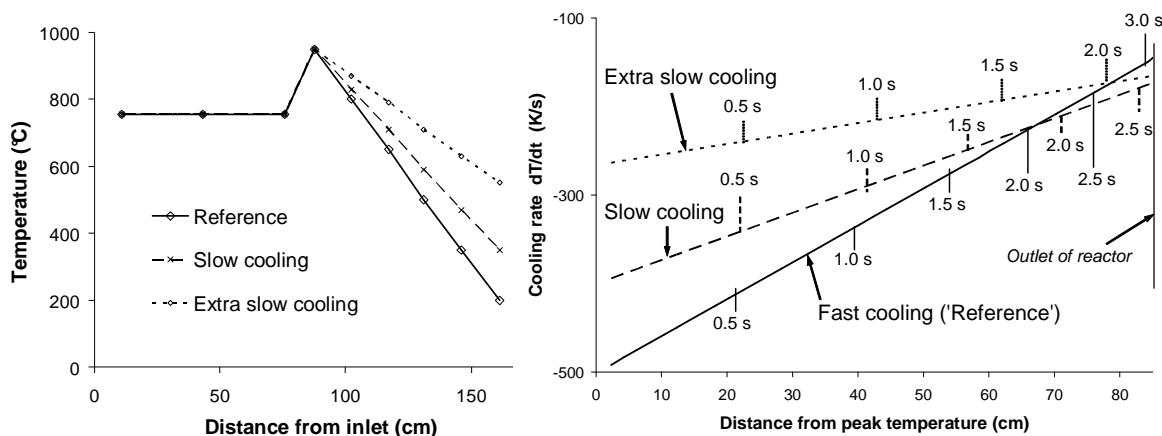
Figure 22. *Temperature profiles used to investigate the effect of cooling rate. In the right figure the average cooling rate of the gas is shown as a function of the axial distance from the location of the peak temperature in the furnace (all the profiles are chosen with constant dT/dz). The residence time of the gas in the cooling section of the furnace is depicted on the curves.*

The number-based size distributions from runs with different cooling rates and 0 or 50 ppm SO_2 are shown in Figure 23.

When decreasing the cooling rate, the number and mass of particles were decreased. The lower mass concentration of the effluent particles is caused by an increased deposition on the walls. When the condensable vapors are lost to the walls the super-saturation is decreased and the homogeneous nucleation is delayed to occur at lower gas temperatures. The saturation ratio does not reach as high a value as it does when the cooling rate is decreased. This leads to a lower nucleation rate and thereby a lower number concentration.
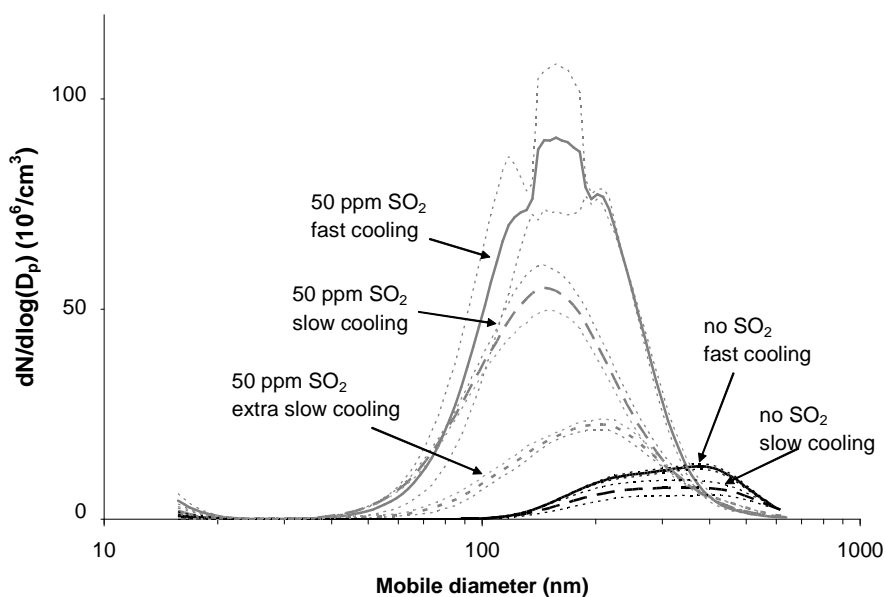
Figure 23. *Particle size distribution for aerosols formed with two or three different cooling rates and with and without a 50 ppm partial pressure of SO_2. The standard deviations between 5-10 measurements are represented by dotted lines.*

33

The difference between the particle size distribution with and without SO_2 in the gas is due to the formation of potassium sulphate seeds as discussed in the previous section. The effect of decreasing the rate of cooling is qualitatively the same for pure KCl and for KCl + SO_2. If sulphation is increased when the cooling rate is decreased, this would increase the nucleation rate. However, the effect is not observed in the results. Decreasing the cooling rate is an option for reducing number and mass concentrations of sub-micrometer particles. The effect might be even more pronounced when seed particles are present, since these provide a large surface area for heterogeneous condensation. This suggests an easy approach to reduce particle loads from industrial boilers. The coarse particles, which can be separated from the flue gas subsequently, will provide the surface area for heterogeneous condensation.

2. 3. 5   Seed particle experiments

The introduction of seed particles to the furnace introduces a larger surface area available for heterogeneous reactions and heterogeneous condensation. Thus at some critical number concentration of seed particles, the homogeneous nucleation might be suppressed, because heterogeneous condensation becomes sufficiently fast to keep the super-saturation low. Jensen *et al.* (2000) showed that the nucleation of alkali chlorides was suppressed at total number concentrations as low as $5 \cdot 10^4$ #/cm³. The introduction of seeds has been used here to investigate whether the surface of K_2SO_4 functions as a catalyst for SO_2 oxidation. Seeds of potassium sulphate were formed in an aerosol atomizer (TSI 9306a Six-Jet Atomizer). The seeds are formed when the water content was evaporated from droplets of aqueous potassium sulphate, sprayed from a number of jets. To dry the droplets the aerosol was led through two laminar diffusion dryers. The flow of seed gas was controlled by using a back-pressure regulator (BPR). To ensure that a similar flow in the runs with no seed particles was obtained, the same flow regulation was also used in these runs in this series of experiments. Thus, pure nitrogen was led through the capillaries and the pressure was controlled by the back pressure regulator in the experiments without seed particles. The setup is shown in Figure 5 on page 16. The concentration of seed particles was measured in the outlet of the LFAC in a run with a cold furnace.

The experimental conditions and the observed number and mass concentrations are shown in Table 4. The particle size distributions from the experiments are shown in Figure 24.

Table 4. *Experimental conditions and results from investigation of influence from seed particles. In all runs the gas also contains 5% O_2 and 5% H_2O. The GMD-values are mobile geometric mean diameters based on the SMPS measurements.*

Run	Composition	# conc. (10^6/cm³)	$PM_{0.8}$ (mg/m³)	GMD (nm)
No seeds	Pure KCl	0.27	10.6	216
	KCl + 50 ppm SO_2	1.87	11.7	148
Seeds in hot furnace	Pure KCl	0.079	13.0	617
	KCl + 50 ppm SO_2	2.28	12.6	198
Pure seeds	Seeds of K_2SO_4	0.086	0.157	88
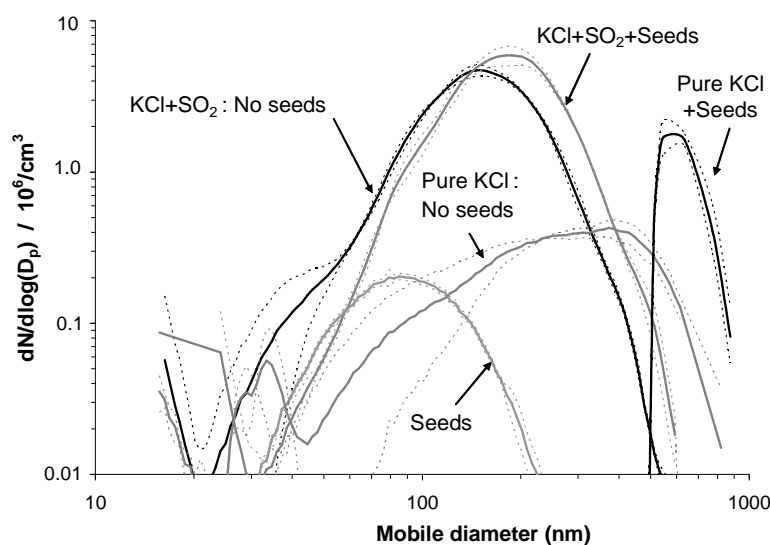
Figure 24. *Particle size distributions from experiments with addition of seeds of potassium sulphate. Note the logarithmic axis. The properties of the particle size distributions are shown in Table 4. Four experiments are conducted under similar flow and temperature conditions. These are with and without 50 ppm SO_2 and with and without seed particles in a concentration of $9 \cdot 10^4 \#/cm^3$. The distribution for the experiment with inlet seed particles and no KCl, conducted in a cold furnace, is also shown ('seeds').*

Homogeneous nucleation of K_2SO_4 in the furnace could not be suppressed by introducing seeds in the highest possible number concentration ($\sim 1 \cdot 10^6$ #/cm^3). The homogeneous nucleation of pure KCl was easily suppressed. The particles were enlarged considerably in these runs and mass concentrations similar to or higher than the runs with pure KCl without seeds were found. The higher mass concentration is possibly caused by a reduction in wall condensation when a new surface area is available on the seed particles. When KCl was introduced in the furnace the seed particles were enlarged, with the geometric mean diameter increasing from 88 to 617 nm, while the number concentration was almost unchanged (Figure 24). The distribution of particle sizes is narrowed as the particles grow by heterogeneous nucleation because the condensation takes place on the surface of the particles. The larger surface area of the smallest particles will favor condensation on these and thus the distribution is narrowed while the particles grow.

When KCl was introduced without seed particles the mass concentration of the aerosol was slightly lower than when seeds are present (10.6 and 13.0 mg/m^3). This is probably because the heterogeneous nucleation on the seed particles reduce the loss of chloride to the reactor walls. The number concentration for the particles formed by homogeneous nucleation of KCl was considerably lower than the number concentration in the experiments with formation of sulphate particles. This is also seen on Figure 24.

The results from nucleation of pure KCl are not surprising. However, an interesting change in the particle size distribution was observed when seed particles are added in runs with sulphate nucleation. The average particle diameter and the number concentration of the particles increased when seeds were present. This suggests that the oxidation of SO_2 increased and more gaseous sulphate was available for nucleation. The experiments described in this section suggest that the presence of seed particles in a flue gas will catalyze sulphation of alkali vapors while homogeneous nucleation of alkali chlorides is suppressed. The number and the size of particles increased when adding seed particles to the furnace under conditions allowing formation of potassium sulphate. The results were very clear and the increase must be caused by increased

oxidation of SO_2. Some of the formed SO_3 must be able to leave the surface of the seed particle before the sulphate is formed, because the number of particles is increased.

2. 3. 6   KOH sulphation

Equilibrium calculations suggest that alkali metals in flue gases from biomass combustion are present as chlorides and hydroxides at high temperatures (e.g. Baxter *et al.*, 1998). However, there are no studies available concerning the formation of aerosols from K_2SO_4 formed by direct reaction with KOH. According to Steinberg and Schofield (1990) the kinetics of NaOH and KOH sulphation are not well known. Therefore, the sulphation of potassium in the form of hydroxides is investigated in the following.

The potassium hydroxide was fed to the LFAC by the saturator in a similar way as the chlorides. The saturation vapor pressure of the hydroxide was considerably higher than for the chloride (as seen in Appendix C) and the temperature of the saturator was considerably lowered. It was assumed that the inert gas that passes through the bed of pellets impregnated with KOH is fully saturated. The handling of the hydroxide in the reactor has proved more difficult, because the alumina tubes seem to break easier when exposed to the hot basic flue gases. The idea with the experiments was to expose the same amount of potassium to sulphation under similar conditions, with potassium is bound as chloride and hydroxide respectively, and compare the results from the experiments. If the rate of formation for gaseous K_2SO_4 is controlled only by the rate of oxidation of SO_2, the change of potassium source should not change the particle dynamics. That is, the number concentration of particles should be independent of the carrier of alkali as it was also shown to be independent of the alkali concentration. In Figure 25 the mass-based size distribution from sulphation of 200 ppm KOH with 500 ppm SO_2 (20 minutes sampling time) is compared to the distributions found when introducing 200 ppm KCl or NaCl to the same conditions.
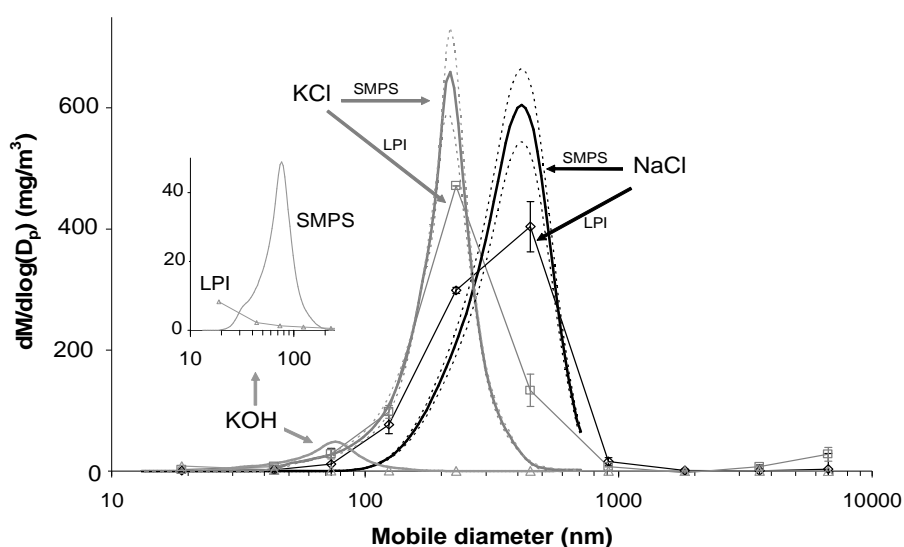
Figure 25. *The particle size distributions for sulphation of 200 ppm alkali from three different sources: KCl, KOH, and NaCl (500 ppm SO_2, 10% O_2, and 5% H_2O). The small insert is an enlargement of the particle size distribution by LPI and SMPS for KOH. The standard deviation is not shown for the curves from the sulphation of KOH, because the deviation is huge and depends on the time of the measurement.*

It was observed that the mass of particles that leaves the reactor in the KOH experiment is considerably lower than the mass of particles in the chloride experiments. The distributions were obtained with SMPS and LPI. The LPI measurements from the runs with KOH hardly showed any mass deposition. The mass concentration of particles during a run with KOH sulphation was very unstable and never reached a true steady state. The results from LPI and SMPS measurements are shown for all three alkali sources (Figure 25). For the two chloride sources the data from SMPS and LPI agreed very well, while the results in the case of KOH sulphation changed with time as discussed later. The number and mass concentrations and the geometric mean diameter based on number and mass are summarized in Table 5. The difference in number concentration between the experiments with sulphation of KCl and NaCl is caused by the different physical properties of K_2SO_4 and Na_2SO_4. A chemical analysis of the deposits from the hydroxide sulphation showed that the deposits in the impactor consist of pure potassium sulphate.

The aerosol characteristics in the experiments with hydroxide sulphation are very different from the ones from sulphation of chlorides. The number concentration was almost constant over time, and the number concentration is equal to the one observed when introducing the potassium as a chloride (within the standard deviation). This supports the theory that the formation of potassium sulphate depends only on the SO_2 oxidation. However, the particles became larger with time and therefore the mass concentration increased over time. This behavior is not seen for the chlorides. If no sulphur is added the mass concentration of the KOH-aerosol decreased with time.

It is difficult to interpret the results with unstable mass concentration obtained with the sulphation of KOH, which were verified in a number of repetitive experiments. The deviation between the repetitive runs with similar conditions was considerably larger than the deviation between similar repetitive runs with chloride sulphation.

Table 5. *Properties of the particle size distributions from sulphation of different alkali sources. The distributions are shown in Figure 25. The properties are derived from the SMPS data, except for the mass concentration and the mass-based GMD, which are derived from LPI and SMPS data*

Alkali source:	Number concentration $10^6/cm^3$	Mass concentration (LPI / SMPS) mg/m^3	Geometric mean diameter (number) nm	Geometric mean diameter (mass, LPI / SMPS) nm
KOH	54.0 ± 18.8	4.3 / 15	44	154 / 71
KCl	37.3 ± 9.1	203 / 166	103	364 / 199
NaCl	7.97 ± 2.1	225 / 218	215	439 / 362

Mass-based size distributions from runs with hydroxide introduced with and without SO_2 are shown in Figure 26. Arrows indicate the development of the distributions over time.
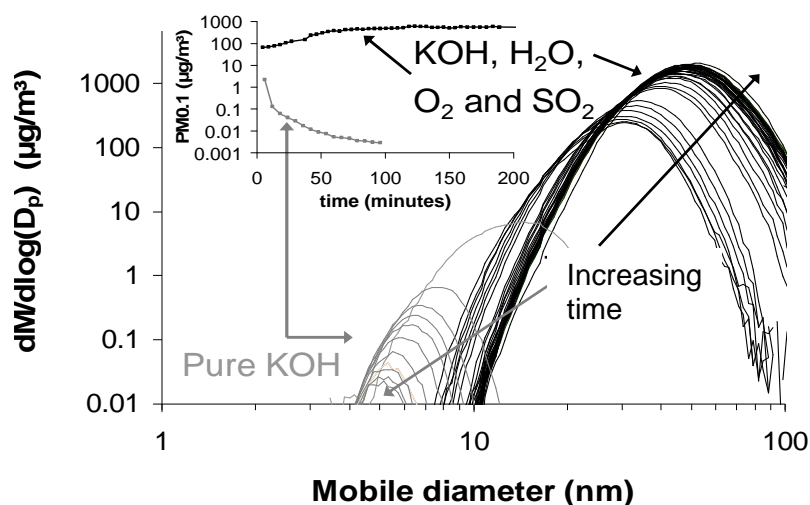
Figure 26. *Mass-based particle size distributions illustrating the unsteady aerosol formation of pure KOH and of K$_2$SO$_4$ formed by sulphation of KOH. The distribution changes with time when 200 ppm KOH is introduced at constant levels in a fresh reactor (5% H$_2$O, 5% O$_2$). The mass concentration of the sulphate particles increases until a level is reached where the concentration is almost constant. When SO$_2$ is not supplied the opposed trend is found. The mass concentration decreases with time until a constant level is reached. The PM$_{0.1}$ values obtained by integration of the curves as a function of time are also shown.*

Replacing the alumina tube in the furnace with quartz did not have any effect on the results when SO$_2$ was added. If pure KOH was introduced the decrease of mass concentration over time was reduced by approximately 40% when using quartz as wall material. This also depended on the extent of cleaning of the tube before the experiments. The flushing water from rinsing of the furnace tube after an experiment was analyzed. The water did not show any increase in pH as expected if KOH was deposited by simple condensation. This indicates that a reaction with the wall took place. The mass concentration of the aerosol was very low compared to the experiments with KCl sulphation. The difference in the molar mass for the two components did not account for this large difference (M_{KCl} = 74.45 g/mole and M_{KOH} = 56.11 g/mole). The highest possible wall deposition during the experiments is obtained when no particles are formed. To find this maximal wall deposition by diffusion a computational fluid dynamics (CFD) simulation of the wall deposition was made using the commercial computer code Fluent. The physical constants used for the simulations are given in Appendix C. The computational fluid dynamics simulation solves differential equations describing mass and energy conservation using a finite volume method. The volume of interest is described by applying a fine computational grid and the boundary conditions describing the problem. No further introduction to the use of CFD is given here. The results are shown in Figure 27.

The cup-mix mass concentrations predicted by the CFD simulations without aerosol dynamics are 55.0 mg/m^3 (18.4 ppm) for KCl and 31.2 mg/m^3 (13.8 ppm) for KOH. The mass concentration of aerosol in the run with KCl sulphation was 203 mg/m^3 (from the LPI measurement). This is well above the value predicted by CFD without aerosol dynamics, which is expected, because the aerosol particles decrease the wall deposition. For KOH, however, the mass concentration of the aerosol was 4.3 mg/m^3 (from the LPI measurement), which is much lower than the value 31.2 mg/m^3 predicted by CFD without aerosol dynamics. This either means that the mass concentration of KOH available for aerosol formation is lower than predicted by CFD, or that the mass was lost after the particle formation. To investigate if the difference could be caused by a

reaction between KOH and the walls of the reactor a simulation with a boundary condition specifying zero concentration on the reactor walls was made. This simulation predicted an outlet mass concentration of 4.5 mg/m^3 (2.0 ppm KOH). This agrees better with the measured mass concentration of particles (4.3 mg/m^3 with LPI and 15 mg/m^3 by SMPS). However, the boundary condition of 100% reaction at the entire wall surface might not be fulfilled, because this requires an infinitely high reaction rate even at the lower temperatures. If this is the case the mass available for particle formation must be higher.
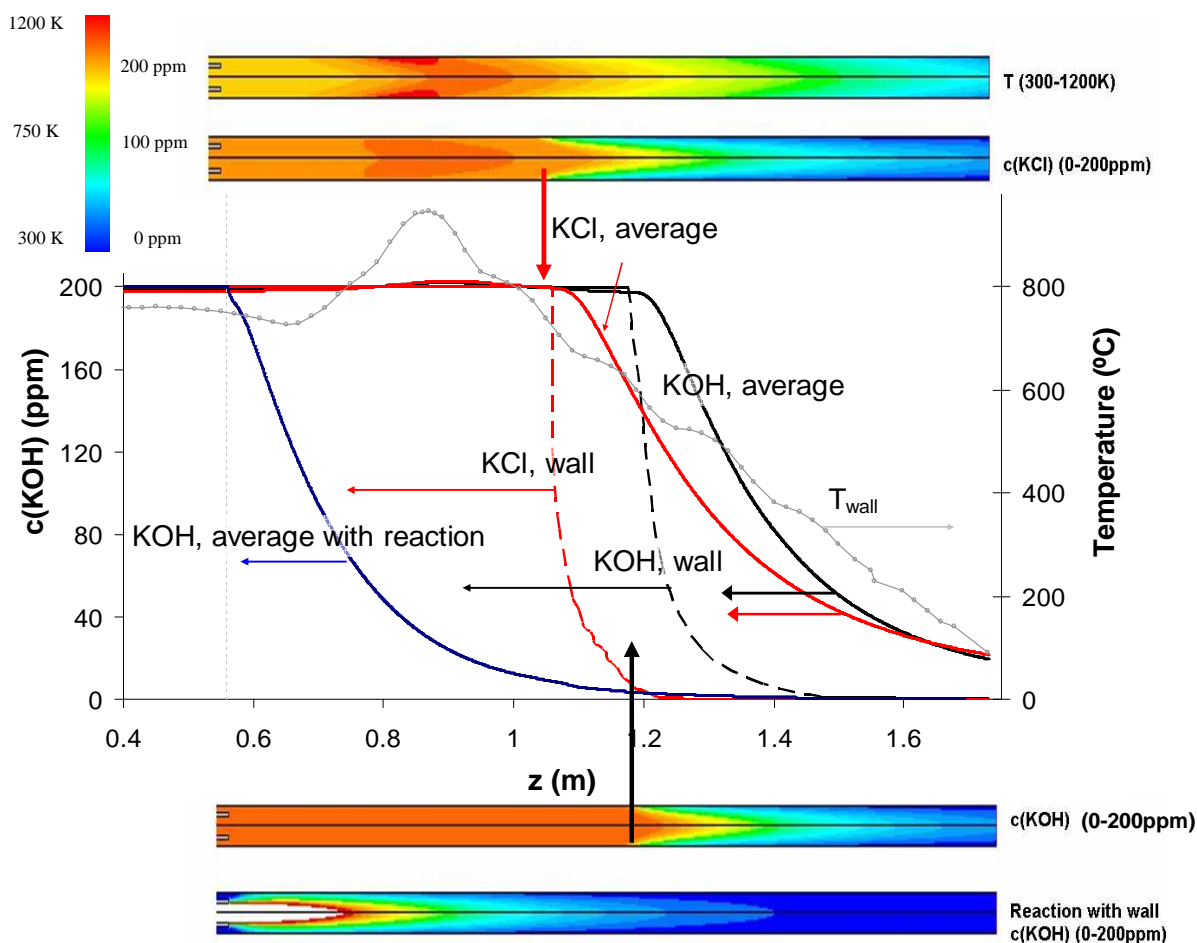
Figure 27. *Concentration of KOH and KCl at different locations in the LFAC calculated by FLUENT. For both components 200 ppm is introduced in the inlet. The mass-flow averaged partial pressures of KCl and KOH are plotted. The maximal wall concentration is the saturation pressure of KCl or KOH at the wall temperature. The temperature profile is shown together with the concentrations. The colored contour plots show the temperature profile and the concentrations of KCl and KOH when accumulation by condensation at the walls is assumed. For KOH a profile is also shown for the case where 100% reaction takes place at the reactor walls (c(KOH)$_{wall}$=0). In this case all the KOH is introduced through the saturator. The vertical dotted line indicate the end of the saturator.*

The effect of changing the concentration of SO$_2$ on the aerosol formation was studied for the sulphation of KOH. Three runs with SO$_2$ concentrations of 0, 50, and 500 ppm were made and compared to experiments with KCl sulphation using the same concentrations of SO$_2$. The

number-based particle size distributions are shown as averages of several SMPS measurements in Figure 28.
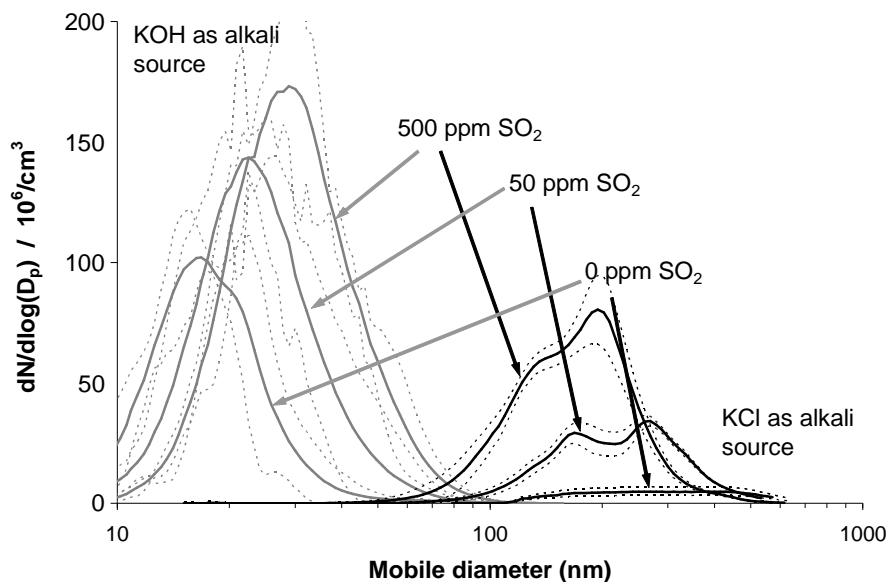
Figure 28. *Number-based size distributions from experiments with sulphation of 200 ppm K bound as KOH or KCl with addition of different amounts of SO$_2$.*

While the number concentration increased with the concentration of SO$_2$ in the sulphation of both KCl and KOH an increase in particle size was observed only for the sulphation of KOH. For the sulphation of KCl the mass concentration was found to be almost constant over time. In this case the majority of the particle mass is the KCl that condensed in the sulphate particles. Thus, a higher number of particles will distribute the same mass of KCl on more particles and thus decrease the geometric mean diameter of the aerosol, because less chloride is condensed on each particle. In the case of KOH the particles were formed by pure K$_2$SO$_4$ as shown by EDS. In this case the more K$_2$SO$_4$ formed by chemical reaction by the higher concentration of SO$_2$ will cause an increase in mass concentration. The mass concentration of particles increased considerably as shown by the mass-based size distributions obtained from the SMPS data. The distributions are shown in Figure 29 and the properties of the aerosols based on the data from Figure 28 and 29 are shown in Table 6.

The number concentrations for the experiments with KOH and KCl sulphation are not similar for these experiments.

The experiments with sulphation of hydroxide agreed well with the conception that aerosol formation during biomass combustion is initiated by oxidation of SO$_2$ and followed by a fast reaction between SO$_3$ and alkali metal. The condensation of chlorine takes place after the formation of the sulphate nucleus. It is plausible that hydroxide reacted with the alumina tubes and that only a very small amount was available for condensation on the aerosol particles. Particles from experiments with sulphation of KOH were composed of pure K$_2$SO$_4$. Based on the composition of the particles, which resembled that of pure K$_2$SO$_4$, there was no indication of subsequent condensation of KOH on the particles. No explanation for this can be offered, since the particle number concentration did not seem to depend on the concentration of KOH.
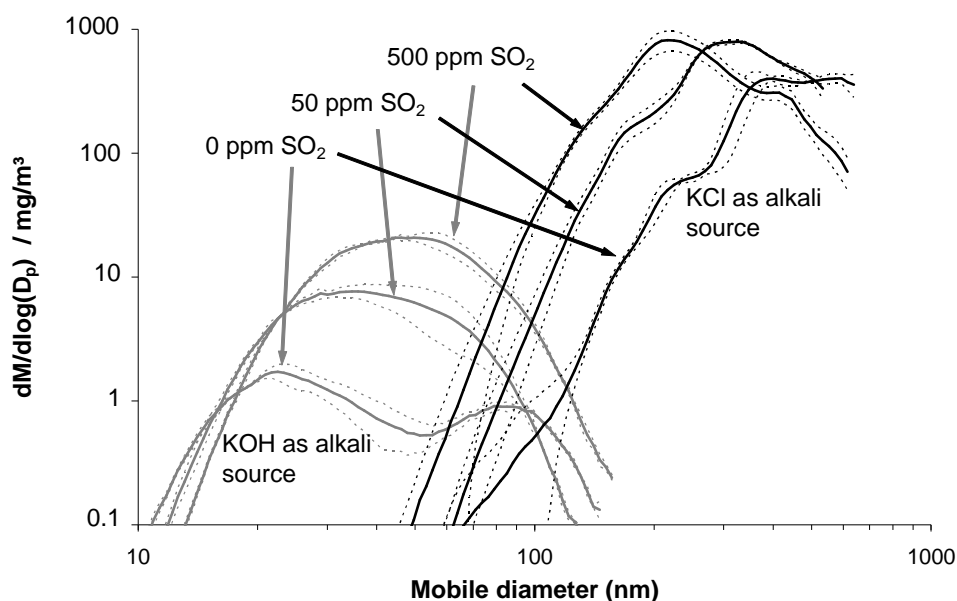
Figure 29. *Mass-based size distributions from experiments with sulphation of 200 ppm K bound as KOH or KCl with addition of different amounts of SO₂. The distributions are obtained by transforming the number-based size distributions shown in Figure 28.*

Table 6. *Properties of the particle size distributions from sulphation of different alkali sources. The particle size distributions are shown in Figure 28 (number) and Figure 29 (mass). The properties are derived from the SMPS data. The GMD-values are based on mobile diameters*

Potassium source and $p(SO_2)$:		Number concentration $10^6/cm^3$	Mass concentration (SMPS) mg/m^3	Geometric mean diameter (number) nm	Geometric mean diameter (mass) Nm
KCl	0 ppm	2.97	198	278	418
	50 ppm	14.0	278	217	313
	500 ppm	29.3	328	169	255
KOH	0 ppm	36.4	1.0	17	36
	50 ppm	54.0	3.9	23	38
	500 ppm	69.9	9.8	29	46

2. 3. 7   Particle sampling at high temperature

It was desired to investigate if particles of alkali sulphates can be formed directly from the gas phase of a synthetic flue gas. Due to the large difference between equilibrium vapor pressure of KCl and K_2SO_4 (these are shown in Appendix C), the sulphate can be sampled at high temperatures without condensation of chloride. In the following, experiments to prove the existence of sulphate particles at high temperatures are described. In order to sample particles at high temperatures a new probe of quartz was designed.[3] A 20 mm glass tube is closed in one end

---

3 Three probes were designed as the handling of these in the hot furnace without breakage proved difficult. The probes were made by Jan Patrick Scholer at the Department of Chemistry, DTU.

by a porous plate of quartz crystals (porosity number 3), spacers of silica glass are placed on the outside of the probe for centering the probe in the tubular furnace (see Figure 30) A quartz filter is placed on the porous plate before each run and a vacuum is applied inside the glass probe. The filter was placed in the LFAC before heating to the temperature profile of interest. When the LFAC was thermally equilibrated a synthetic flue gas was introduced and the vacuum was applied inside the probe. The filter was placed upstream from the point where KCl was saturated during cooling. By this qualitative experiment it was tested whether particles were formed before KCl was condensed. Deposits were observed on the filters at temperatures above 850°C. The concentration of KCl was 200 ppm and saturation was reached when cooling to 726°C. This means that K_2SO_4 can form before KCl was condensed. A SEM micrograph of the deposits from a sample obtained at 800 °C is shown in Figure 30. In this case the filter was quench-cooled.
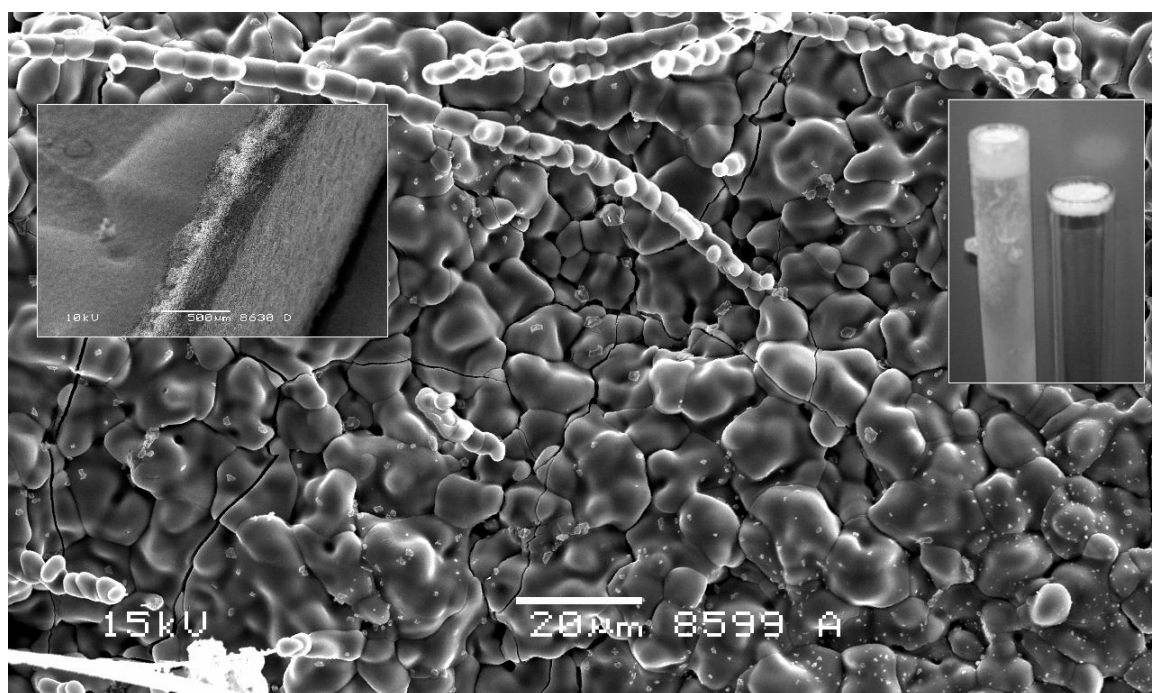
Figure 30. *SEM micrograph showing filter deposits from sampling at 800°C. The deposits are large flakes of K_2SO_4. The inserts show the filter from the side and the probes of quartz. The filter is cooled in liquid nitrogen and broken in two pieces to get a well-defined cut without compressing the filter. The deposit is the thin white layer on top of the filter. The small particles found on top of the larger deposits were only observed if the filter was quench-cooled.*

The appearance of the deposits was the same regardless of the sampling temperature (above KCl saturation) and the concentrations of KCl and SO_2. The deposits were analyzed by EDS and the elemental composition was that of pure potassium sulphate in all cases. The signal for chlorine was below the detection limit of 1%.

The experiment does not prove that sulphate can form homogeneously. The appearance of the deposit indicates that the sulphate is possibly formed heterogeneously on the filter and later on the surface of the sulphate deposit. Interestingly, this suggests an auto-catalytic effect where the surface of the formed solid sulphate catalyze the formation of more sulphate from SO_2, KCl, and O_2 in the flue gas by a surface reaction. The kinetics for the homogeneous sulphation of

potassium suggests a much lower conversion of SO_2 than those found in the laboratory (Hindiyarti, 2007). Thus, if the surface of K_2SO_4 particles can catalyze the oxidation of SO_2, the low conversion predicted by the homogeneous gas phase kinetics might be explained by this catalytic effect.

It is possible that an aerosol of sulphate particles was formed upstream from the filter and sulphate particles were deposited on the filter (or on the deposit) and due to the high temperature the particles were later sintered together to the observed flakes of sulphate. When the probe was cooled with the furnace (several hours) only large flakes of sulphate were found on the filter. To see if this sintering could be quenched the probe was extracted very fast in some runs by use of a sledge specially designed for this purpose (shown in Figure 6). The quench-cooled filter did indeed show small particles on top of the sulphate flakes. However, it was not possible to determine if these small particles are composed of K_2SO_4.

2. 3. 8 High temperature impactor

Since the filter-probe approach did not manage to prove the existence of sulphate particles at high temperatures a new probe was designed. This probe is basically a one-step impactor with a low cut-diameter, designed for use at high temperatures.[4] If particles exist in the gas surrounding the impactor, the impaction of these will create a well defined deposit, whereas a deposit formation by heterogeneous reactions on the probe surface will create a deposit covering all parts on the probe exposed to the gas.

The probe was designed with a cut-diameter of 4 nm. The design is derived in the following. It was assumed that the particle density is 2.0 g/cm³ and that the gas temperature is 900°C. The temperature-dependent mean free path of the gas can be obtained by (Willeke, 1976):

$$\lambda(T) = \lambda_0 \left(\frac{T}{T_0} \right) \left(\frac{p_0}{p} \right) \left(\frac{1 + 110.4\,\text{K}/T_0}{1 + 110.4\,\text{K}/T} \right) \tag{16}$$

with $\lambda_0 = 0.0673\ \mu m$, $T_0 = 296$ K, and $p_0 = 101325$ Pa. At 900°C this gives a mean free path for the gas of 3.347 μm at atmospheric pressure. The viscosity of nitrogen is $\mu = 4.5 \cdot 10^{-5}$ kg/(m·s) at this temperature (LMNO Engineering, 2003). The Cunningham slip correction for a 4 nm particle is given by equation (8) (page 18):

$$C_c = 1 + \frac{3.347\,\mu m}{0.004\,\mu m} \left(2.5140 + 0.800 \cdot \exp\left\{ -\frac{0.55 \cdot 0.004\,\mu m}{3.347\,\mu m} \right\} \right) = 2770 \tag{17}$$

The Stokes diameter for 50% collection efficiency is 0.22 (Hillamo and Kauppinen, 1991). The width of the impactor nozzle is found by using the definition of the Stokes number given in equation (11):

$$W = \frac{2000\,\text{kg/m}^3 \cdot 2770 \cdot 698.42\,\text{m/s} \cdot (4 \cdot 10^{-9}\,\text{m})^2}{18 \cdot 4.5 \cdot 10^{-5}\,\text{kg/(m·s)} \cdot 0.22} = 0.35\,\text{mm} \tag{18}$$

---

[4] The probe was made by Henning Koldbech in the workshop of the Department of Chemical Engineering. The probe was redesigned a few times before successful measurements could be made under the very corrosive conditions found in the LFAC.

The length of the impactor nozzle is $3.4 \times W = 1.2$ mm as recommended by Parker and Calvert (1981). The impactor nozzle and the impactor plate were constructed in platinum. The measured pressure in the impactor was ~150 mbar, which is sufficient to ensure sonic flow. The high temperature impactor is shown in Figure 31.
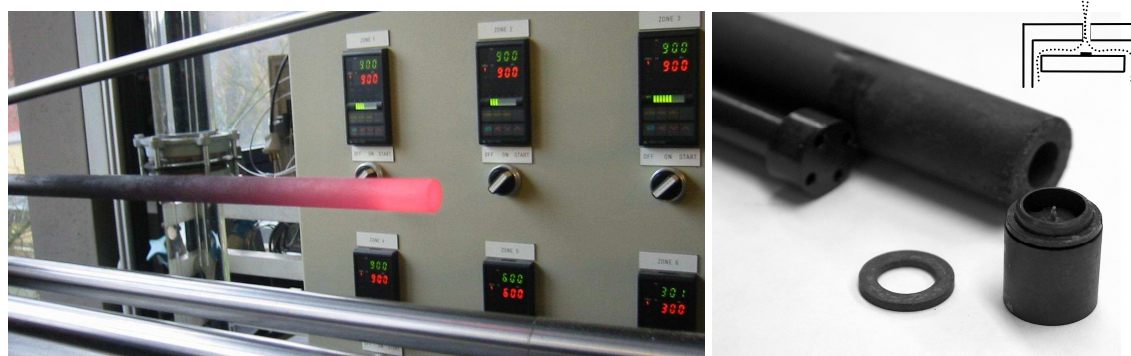
Figure 31. *Left: High temperature impactor after fast withdrawal from the furnace by using the horizontal probe-sledge. Right: Dissembled impactor. The large deposit on this picture is KCl from sampling at 700 °C.*

The impactor was inserted into the LFAC during runs with constant temperature for 30-120 minutes. Several runs with the furnace kept at constant temperatures at 800°C and 850°C were made and the deposits on the impactor platinum plate were analyzed with SEM and EDS. The concentration of potassium (as KCl or KOH) in the feed gas was 200 ppm and the vapor pressure of SO_2 was 100 ppm in all runs (5% H_2O and 5% O_2). Two SEM micrographs from the sampling during experiments with sulphation of KCl are shown in Figure 32. The compositions of the deposits are shown in Figure 32. The build-up of particle deposits on the impactor plate was approximately equally fast when using KOH and KCl as the alkali source. Unfortunately it was not possible to develop the probe for the quantitative analysis of particles. The probe had to be constructed by heavy parts of platinum in order to withstand the corrosive gas attack.
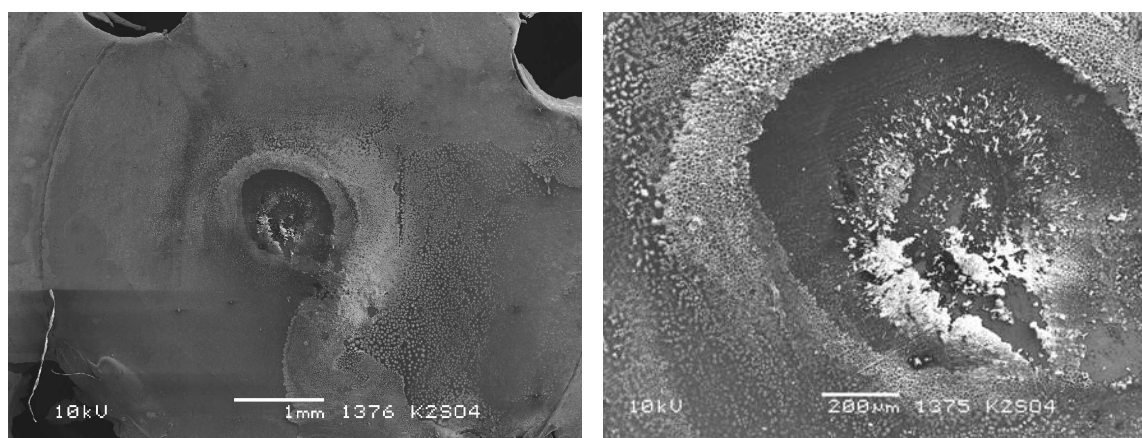
Figure 32. *SEM micrographs of deposit on impactor plate in the high temperature impactor. The deposit is from a run with sulphation of KCl.*

The chemical composition of the deposits from the high temperature impactor are shown in Figure 33. The composition from the experiments with sulphation of chloride and hydroxide are shown together with the composition of pure alkali sulphate. The EDS spectrum for the analysis of a deposit from an experiment with sulphation of KCl at 850°C is also shown. The deposits were well defined in the center of the impactor plate. This is caused by particulate depositions from the impinging jet on the plate.
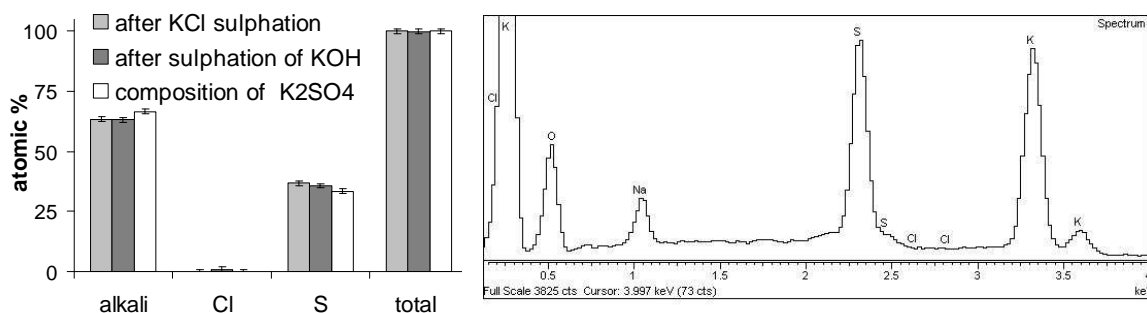
Figure 33. *Left: Composition of particles sampled at 850 ℃. The compositions of the deposits from runs with sulphation of KCl and KOH are compared to the composition of pure K_2SO_4. The compositions are converted to an O-free basis. The error bars represent the expected uncertainty of the analysis method. Right: Example of EDS spectrum for deposit from the KCl-sulphation run.*

The compositions of the two deposits are very similar to that of pure K_2SO_4. The uncertainty of EDS is +/- 1% as indicated by the error bars in the figure. The measured content of chlorine was close to zero and well below the uncertainty-limit of the measurements. The experiments with the high temperature impactor clearly proved that particles can be formed from gaseous K_2SO_4. The deposits found in the high temperature impactor can only be formed by sampling of particles. The deposits were sampled at 800-850°C and EDS revealed that their composition was that of pure K_2SO_4. No other explanation can be given for the formation of these deposits than the formation of gaseous sulphate and homogeneous nucleation of new particles by this component.

2. 3. 9   Morphology of particles

The morphology of the aerosol particles generated in the laminar flow aerosol condenser has been investigated by scanning electron microscopy (SEM). Three samples were analyzed: Particles from an experiment with 200 ppm KCl, 5% H_2O, and 5% O_2 cooled by applying the temperature profile shown in Figure 7 and a flow of 3500 mL/min, particles from a similar experiment with addition of 150 ppm SO_2, and particles from sulphation of 200 ppm KOH with 200 ppm SO_2, 5% H_2O, and 5% O_2. The SEM-images are shown in Figure 34.

The morphology of the particles generated from condensation of potassium chloride is very compact and in most cases dominated by the cubic crystalline structure of KCl. The particles from the experiment with sulphation of chloride were more spherical and some of them were also aggregates of 2-6 primary particles. The primary particles were considerably smaller than the compact particles of pure KCl. The particles from sulphation of KOH were small and dense

45

spheres. The particles were not agglomerates and the deviation between the mass-based particle size distributions by LPI and SMPS for these particles cannot be explained by the presence of agglomerates. The particle sizes observed on the SEM micrographs correspond well to the particle sizes measured by SMPS.
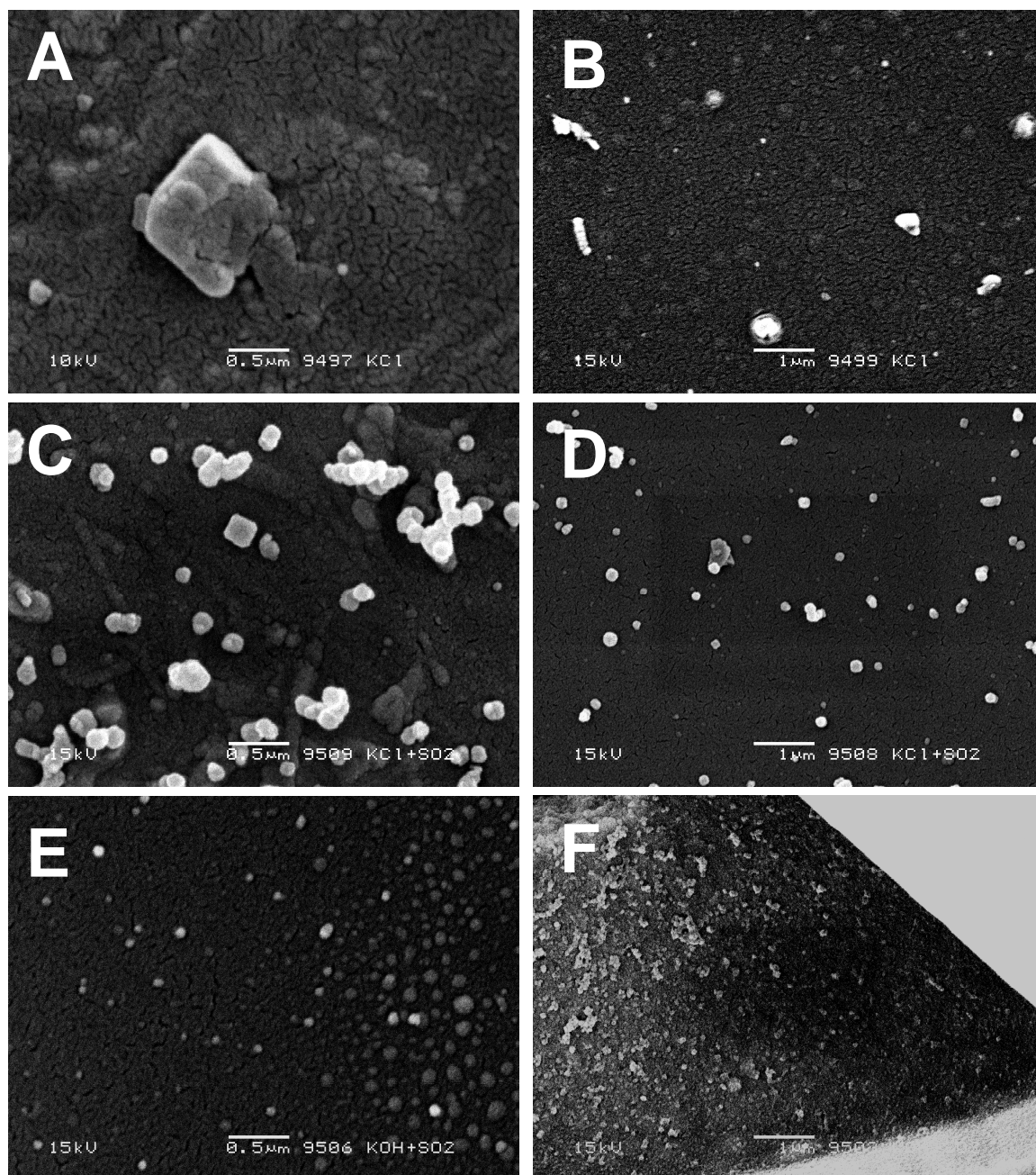
Figure 34. *Scanning electron microscopy images of aerosol particles sampled from the laminar flow aerosol condenser. Images of three samples are shown: Particles of pure KCl (A+B), particles of KCl and K$_2$SO$_4$ from experiment with sulphation of KCl (C+D), and particles of pure K$_2$SO$_4$ from experiment with sulphation of KOH (E+F).*

2. 4 Chemical equilibrium calculations

A theoretical study of the gas composition in the LFAC under the assumption of simultaneous chemical and phase equilibrium at the peak temperature in the furnace provides useful elucidation of the mechanisms for aerosol formation, although such calculations ignore kinetic and diffusional effects that may delay the actual attainment of equilibrium. For this purpose a routine by Michelsen (1989) called CREAC2 is used. The routine calculates the chemical equilibrium by minimizing the total Gibbs energy of a multi-component, multi-phase mixture at constant pressure and temperature. If n_{ik} and μ_{ik} are the number of moles and the chemical potential of component i in phase k, the function to be minimized in a system of n_c components and n_f phases is given by:

$$G = \sum_{i=1}^{n_c} \sum_{k=1}^{n_f} n_{ik} \mu_{ik} \tag{19}$$

The equation is solved with the following constraints:

$$\sum_{i=1}^{n_c} \gamma_{ji} \sum_{k=1}^{n_f} n_{ik} = e_j, \quad j = 1, 2, \ldots n_e \tag{20}$$

$$n_{ik} \geq 0 \quad i = 1, 2, \ldots, n_c \qquad k = 1, 2, \ldots, n_f \tag{21}$$

where γ_{ij} is the number of atoms of element j in one molecule of component i and e_j the total number of atoms of element j. n_f is the number of phases. Ideal conditions are assumed for the gas ($k = 1$) and the chemical potential is given by:

$$\mu_{il} = \mu_{il}^o + R_g T \ln(y_{il}) \tag{22}$$

where μ_{il}^o is the free energy of the pure component at the given pressure and temperature and y_{il} is the mole fraction. The elements included in the calculation are: K, Cl, S, O, H, and N_2 and the possible components are (n_c=22):

> KCl, K_2SO_4, $(KCl)_2$, K, KOH, $(KOH)_2$, KH, SO_2, SO_3, H_2SO_4,
> HS, H_2S, Cl, Cl_2, HCl, H, H_2, O, O_2, OH, H_2O, N_2
> $\tag{23}$
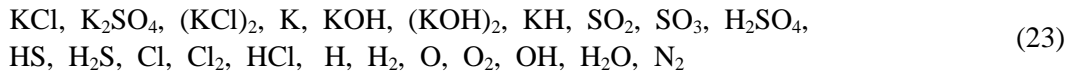
The standard values of the heat of formation and the coefficients for the temperature-dependent heat capacity, necessary for the calculation of μ_{il}^o are taken from Knacke *et al.* (1991). Equation (19) is minimized to its global minimum. The parameters used to calculate the chemical potentials of the components are given in Appendix C. The equilibrium concentration of the sulphur-containing component in a gas composed of 100 ppm KCl, 100 ppm SO_2, 5% O_2, and 5% H_2O is shown in Figure 35 together with the composition when no KCl is present.

At high temperatures sulphur is mainly found as SO_2. As the temperature is decreased SO_2 is oxidized. However, the oxidation reactions are kinetically limited at low temperatures and typically the equilibrium composition is not obtained.
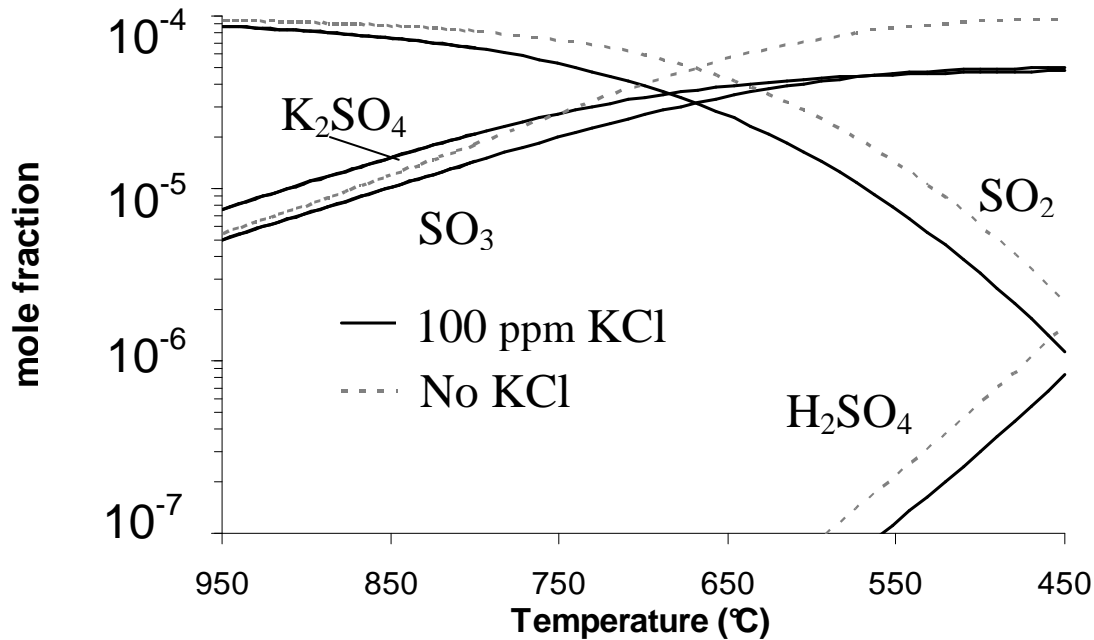
Figure 35. *Equilibrium composition of sulphur containing species in the LFAC flue gas during cooling from 950°C. The composition of the feed gas is 100 ppm SO₂, 5% O₂, and 5% H₂O. The equilibrium is shown with and without addition of 100 ppm KCl. The values on the temperature axis are in reverse order.*

2. 4. 1   SO₂ conversion in the LFAC

To investigate the conversion of SO_2 in the laminar flow aerosol condenser the furnace was equipped with a gas analyzer. The analyzer was connected to the inlet and outlet of the furnace as seen in Figure 5 (page 16). The conversion of SO_2 was calculated based on the SO_2 concentrations in the inlet and outlet of the furnace. Conversion was measured by running experiments with different SO_2 concentrations (temperature profile as in Figure 7) and with different peak temperatures (similar to the profiles shown in Figure 36). Experiments were made with and without addition of KCl to the furnace. In both cases the conversion of SO_2 is given by the oxidation reaction:

$$SO_2 + \frac{1}{2}O_2 \leftrightarrow SO_3 \qquad \text{with} \qquad X_{SO_2} = 1 - \frac{c(SO_2)_{outlet}}{c(SO_2)_{inlet}} \qquad (24)$$
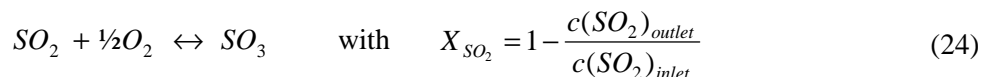
Unfortunately, the conversions measured by this approach were too high. The outlet concentration of SO_2 was lower than predicted by the equilibrium calculation. This is probably due to loss of SO_2 in the wet gas-conditioning unit (if chemical equilibrium is to account for the measured concentrations this should be established at very low temperatures). However, qualitatively the results are interesting, because the conversion showed a maximum between 800 and 900°C which indicates that the reaction is favored at these temperatures. The conversion based on gas measurements is shown in Figure 37. The series of experiments were repeated with sampling of particles on a fibrous filter. By analyzing the deposits on the filters an accurate conversion of SO_2 was determined based on the product of the reaction with SO_2. The filter

48

deposits were dissolved and analyzed for Cl^- and SO_4^{2-} by ion chromatography.[5] The sulphur content in the particles is plotted together with the equilibrium conversion of SO_2 in Figure 38.
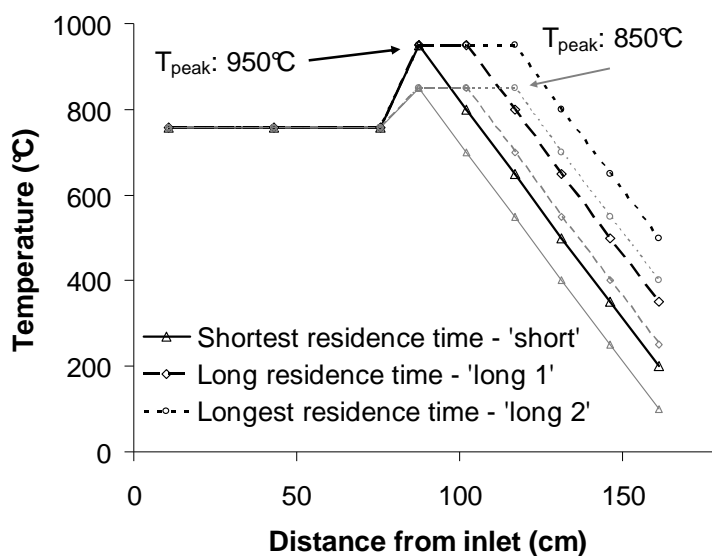
Figure 36. *Temperature profiles used to investigate the effect of cooling rate. For clarity the figure only shows two peak temperatures as an example. However, runs with many different peak temperatures were made. The profile labeled 'short' with a peak temperature of 950°C corresponds to the reference profile in Figure 7.*
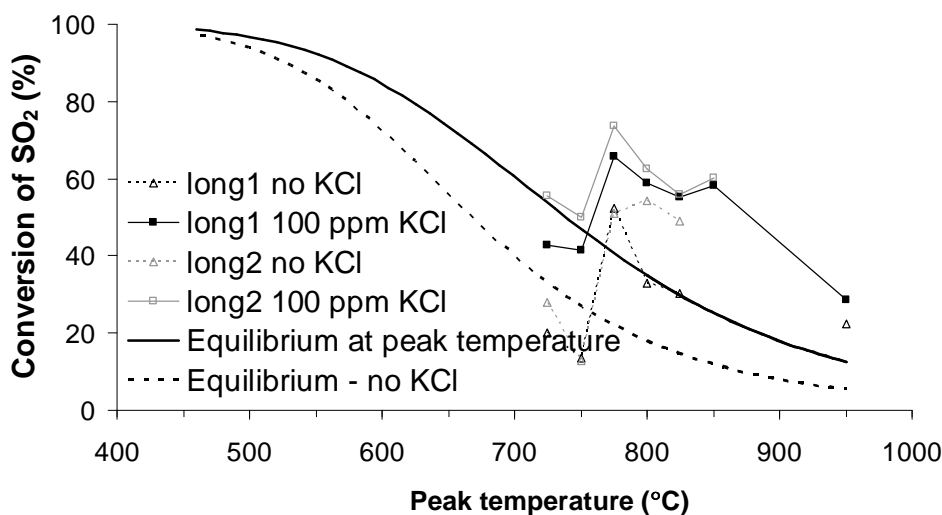
Figure 37. *Conversion of SO_2 in the LFAC during series with different peak temperatures. The cooling rate and the inlet composition are fixed. The conversions are very high and above the conversions suggested by equilibrium calculations.*

---

[5] The samples were analyzed with ion chromatography by Ellen ter Haar Hansen at Amager Power Station, Vattenfall, A/S.
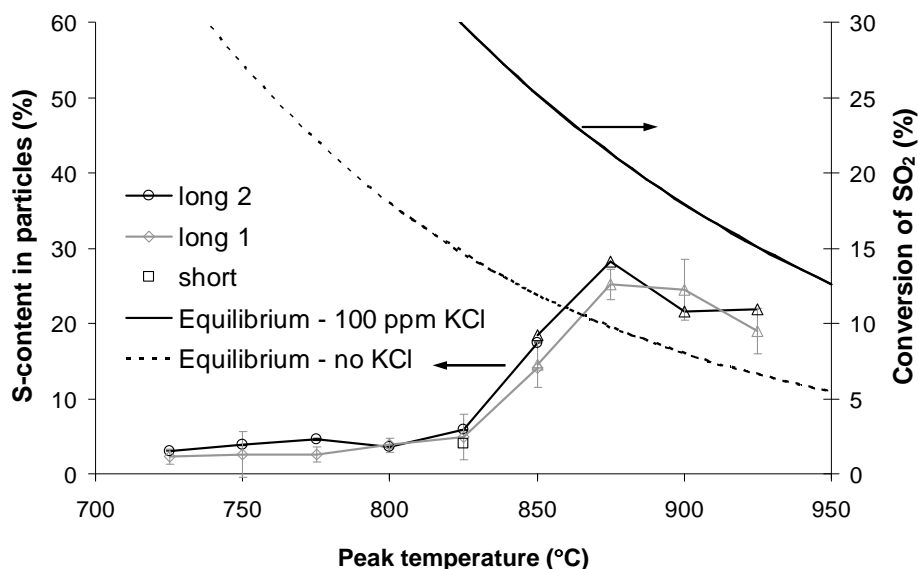
Figure 38. *Sulphur content in particles as function of the peak temperature in the LFAC. In all runs 100 ppm KCl and 100 ppm SO$_2$ are introduced and the same axial cooling rate at the wall is applied. The residence time at the peak temperature is changed in the 3 series ('Short'<'Long 1'<'Long 2'). Particle composition is measured by ion chromatography. The equilibrium conversion of SO$_2$ calculated by CREAC2 is shown for the system with and without KCl in the gas phase. The conversions are calculated based on the equilibrium concentrations of SO$_2$ shown in Figure 35.*

The 'Long 2' series, with the longest residence time, is based on a single set of runs, while the 'Long 1' series measurements are based on 2-4 set of runs. The two series with different residence times are surprisingly similar. Because of the kinetic limitation at low temperatures, it is expected that a longer residence time would cause the system to approach equilibrium better than at the shorter residence times, but this is not evident from the two data series. The data showed a peak in sulphur conversion at 875°C, which is in good agreement with the findings from the gas analysis. The sulphur content of particles from runs at high temperatures showed a decrease with increasing peak temperature, which is qualitatively similar to the one predicted by the equilibrium calculations. However, the equilibrium conversion predicted by calculations with the same inlet concentration of KCl as in the experiments over-predict the conversion. The same calculations without including KCl predict a conversion that is too low. This shows that some of the KCl was condensed on the reactor walls and hence it was not available for particle formation.

For the experiments in the temperature range 725 to 875°C, particle size distributions were measured using SMPS (equipped with the TSI 3081 long-DMA). These showed a considerably difference between experiments with different residence times at the lowest peak temperatures. When increasing the residence time the total number concentration was increased if the peak temperature was low. At high temperatures the particle size distribution was almost identical for experiments with different residence times. The total number concentration at different temperatures through the two series 'Long 1' and 'Long 2' are shown in Figure 39.
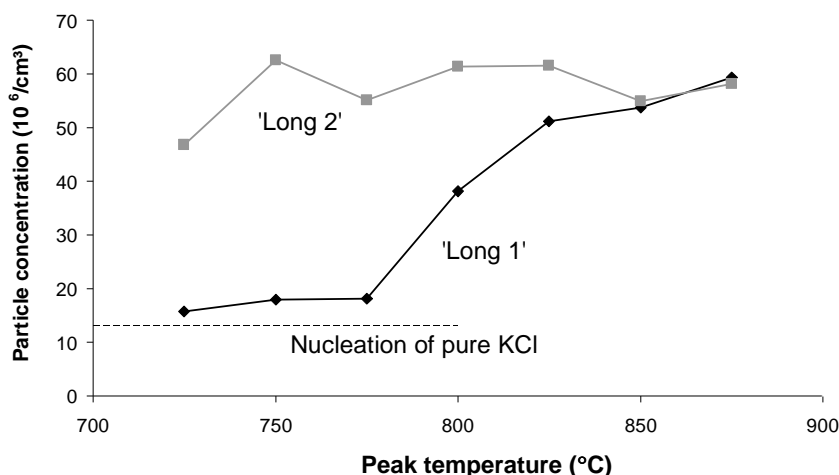
Figure 39. *Total number concentration of particles in experiments with different peak temperatures and constant cooling rate. Two different residence times at the peak temperature are investigated. In 'Long 2' the residence time at this temperature is longer than for 'Long 1'.*

The change in residence time had no influence on the size distribution when the peak temperature is 850°C or above. This indicates that an equilibrium conversion of sulphur was obtained at the peak temperature. The number concentration of particles in the 'Long 2' series was rather constant when the peak temperature was increased. The particle size distributions for the two residence time series are shown for the peak temperature 725°C in Figure 40 and for 850°C in Figure 41.
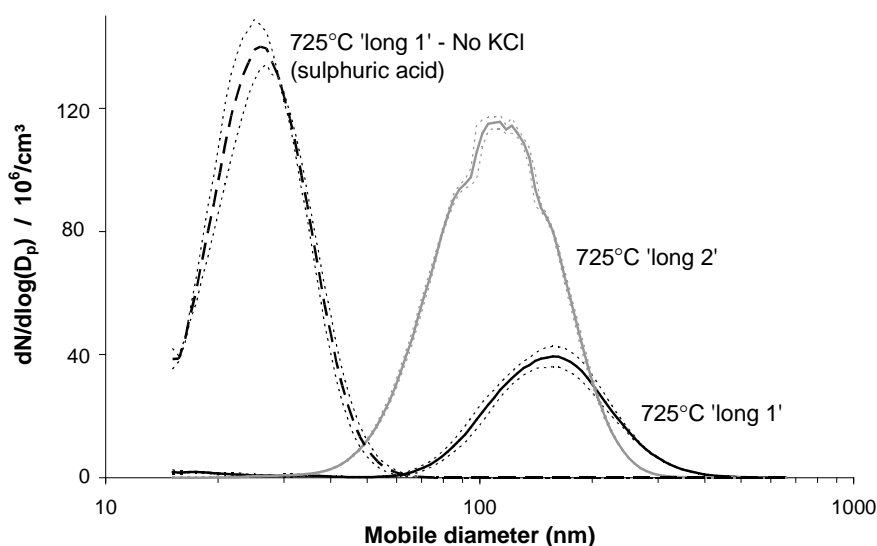
Figure 40. *Number-based size distributions for 'Long 1' and 'Long 2' experiments at 725°C. With the longest residence time the number of particles is considerably higher and the particles are smaller, which indicates a higher conversion of SO_2. The particle size distribution for an experiment where no KCl is fed is also shown. The small particles (droplets) observed in this case are formed by homogeneous nucleation of sulphuric acid at low temperature. The standard deviations shown by the dotted lines represent the variation over several runs.*

51

In Figure 40 the size distribution from a run without addition of KCl is also shown. When no potassium is available the SO_3 reacts with H_2O to form gaseous sulphuric acid (Simonsen, 1993):

$$H_2O_{(g)} + SO_{3(g)} \xrightarrow{\sim 200°C} H_2SO_{4(g)} \xrightarrow{nucleation} H_2SO_{4(l)} \tag{25}$$
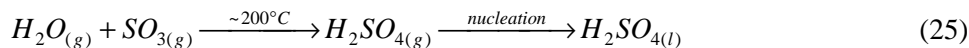
The sulphuric acid forms droplets by homogeneous nucleation. These fine droplets have diameters below 50 nm.
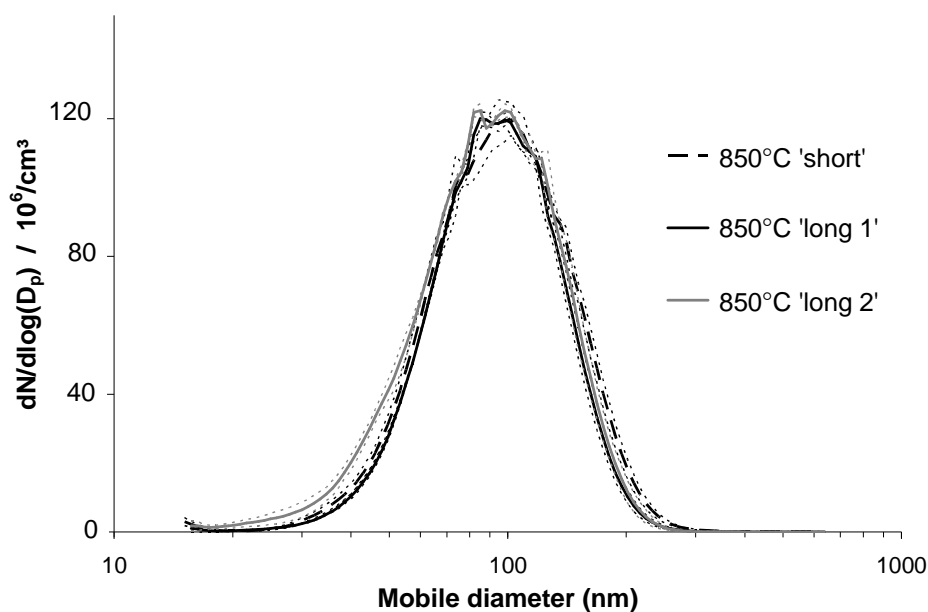
Figure 41. *Number-based size distributions for different residence times at the peak temperature 850 °C. The particle size distributions are identical within the standard deviation of the average particle size distributions based on 10-15 SMPS scans.*

The effect of S:K ratio in the inlet gas was investigated in a series of experiments with a constant temperature profile ('950°C, short' – as in Figure 7). Two series of experiments were made with $c(SO_2)$ between 50 and 800 ppm; one with 5% O_2 and 5% H_2O without KCl and one with 100 ppm KCl added. The concentration of SO_2 in the gas was used to determine the conversion. The conversion in the experiments are shown in Figure 42.

The equilibrium conversion for the peak temperature in the absence of KCl was 13% (see Figure 38). When KCl was present the conversion depended on the concentration of SO_2. The equilibrium conversion approached the one for the experiment without KCl when the S:K ratio became very high. The equilibrium conversion for the SO_2 concentrations used here were between 5 and 13%. The measured conversions were very much higher than the equilibrium concentrations. This was probably due to loss of SO_2 in the gas conditioner as mentioned previously.
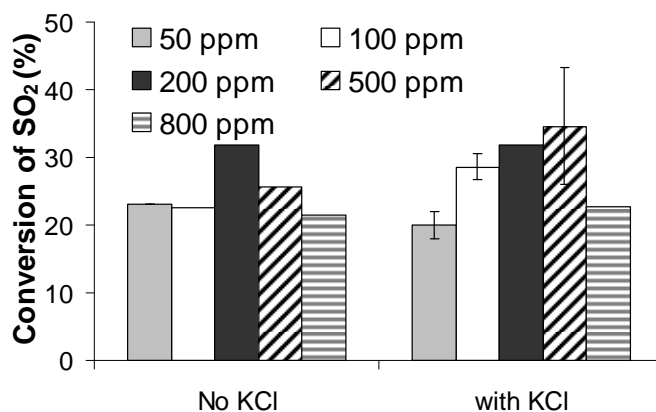
Figure 42. *Conversion of SO$_2$ in the LFAC during experiments with different amounts of SO$_2$. Results from runs with and without 100 ppm KCl are shown.*

The conversion was independent of the concentration of SO$_2$ and did not change considerably upon addition of 100 ppm KCl. This indicates that the conversion of SO$_2$ is only dependent on the oxidation of SO$_2$ to SO$_3$. Since the conversion is independent of the inlet concentration of SO$_2$ it is a first order reaction. A catalytic effect of the reactor wall on the oxidation might influence the results. Results from aerosol formation in experiments with the alumina reactor wall replaced by a quartz tube indicated that the conversion of SO$_2$ was lower. Thus, the alumina might catalyze the reaction better than quartz.

2. 5   Conclusion

The formation of aerosol particles from cooling of a synthetic flue gas, with a composition similar to the post-combustion flue gases found in straw-fired boilers has been studied in a tubular furnace. Particles were formed by nucleation of pure alkali chloride or by nucleation of alkali sulphate from a reacting flow containing alkali chloride, sulphur dioxide, oxygen, and water vapor. The influence of the chemical composition of the feed gas on the particle size distribution and on the chemical composition of the particles was investigated. The number of particles formed in the nucleation increased considerably when SO$_2$ was added to the synthetic flue gas. This proves that the nucleation is caused by formation of gaseous alkali sulphate and subsequent homogeneous nucleation of this component. The number concentration did only depend on the concentration of SO$_2$ and O$_2$, while the concentration of alkali chloride did only change the mass concentration of the aerosol. This indicates that the limiting step for the kinetics of sulphate formation is the oxidation of SO$_2$. However, if no alkali chloride was present, the number concentration was very high due to the formation of aerosol droplets of sulphuric acid at low temperatures.

The influence of operational parameters on the particle size distribution was investigated. Decreasing the cooling rate decreased the number and mass concentration of particles. The

particle size distribution of the aerosols was independent of the residence of the synthetic flue gas at the peak temperature when the temperature was 850°C or higher. At lower peak temperatures the number of particles formed decreased when decreasing the peak temperature while keeping the cooling rate constant. This indicates that less sulphate was formed and thus that the sulphation became kinetically limited. Ion chromatography showed that the sulphur content increased with temperature until a maximum was reached at 875°C, above this point the sulphate content was determined by chemical equilibrium.

Particles of alkali sulphate were sampled directly from a hot synthetic flue gas by an impactor probe. These experiments provide very solid proof that gaseous sulphate is formed.

Experiments with introduction of alkali metal as a hydroxide were conducted. The number concentration of particles was independent on whether alkali was introduced as chloride or hydroxide. The mass concentration of particles from runs with sulphation of hydroxide was extremely low and changed with time. Calculations by computational fluid dynamics indicated that the hydroxide reacted with the walls of the furnace.

Experiments with introduction of seed particles in the synthetic flue gas showed that nucleation of pure alkali chloride was suppressed while the seeds did not suppress homogeneous nucleation when alkali sulphate was formed. The formation of sulphate was increased when the seeds were added which indicates that the surface of the seed particles acts as a heterogeneous catalyst for the SO_2 oxidation.

CHAPTER 3   SIMULATION OF SULPHATE NUCLEATION

In this chapter simulations of aerosol formation in the laminar flow aerosol condenser by homogeneous nucleation of KCl or K_2SO_4 are described. The model includes the formation of gaseous sulphate by a homogeneous gas phase reaction. It is aimed to prove the formation mechanism suggested in Chapter 2 by simulations. An introduction to the model is given and results are discussed.

3. 1   Introduction

The aerosol formation in biomass combustion has been subject to some interesting studies.

Jokiniemi *et al.* (1994) have developed a one-dimensional model for formation of particles of KCl and K_2SO_4. The model, termed the Aerosol Behavior in Combustion model (ABC-code), is based on the general dynamic equation with solution of homogeneous nucleation, heterogeneous condensation, and coagulation. It assumes turbulent flow and the aerosol particles are divided into size classes for resolving the number-based particle size distribution. Chemical equilibrium and reaction kinetics are taken into account in the model.

Christensen (1995) and Christensen *et al.* (1998) have developed a one-dimensional model for formation of particles by nucleation of KCl and K_2SO_4. The model, termed the Plug Flow Aerosol Condenser (PFAC), assumes chemical equilibrium between KCl, SO_2, HCl, H_2O, O_2, and K_2SO_4 at high temperatures. At lower temperatures the oxidation of SO_2 to SO_3 is assumed to be rate limiting. The model assumes that the rate depends on the difference between the actual and the equilibrium concentration of SO_2. The model allows the presence of seeds in the combustion gasses and it accounts for coagulation and settling. The chemical equilibria are calculated by a Gibbs free energy minimization method developed by Michelsen (1989).

Joller *et al.* (2005) have recently developed a novel one-dimensional model with chemical equilibrium at high temperatures and oxidation of SO_2 as the limiting step. The model was used to simulate particle size distributions from aerosols during full-scale combustion of waste wood. The model was able to estimate the content of heavy metals in the particles. The model uses the commercial packages Chemsheet and FactSage to calculate the chemical equilibrium.

Pyykönen (2002) and Pyykönen and Jokiniemi (2000) have developed a model for computational fluid dynamics-based simulation of one-component nucleation in laminar flows and applied it to KCl nucleation in tubular furnaces. The model, termed the Stream Tube model, is based on the

general dynamic equation with discrimination of the size distribution in a number of size classes. The model is based on post processing of flow simulations from CFD simulations. Stream lines are extracted from the CFD solution and aerosol dynamics are applied along these streamlines including mass exchange between neighboring streamlines.

The Plug Flow Aerosol Condenser model by Christensen (1995) and the Stream Tube model by Pyykönen (2002) are compared by simulation of the same single component experimental data in Appendix B. The models show quite similar results for a 1-dimensional simulation.

3. 2   Aerosol formation in the LFAC

A model for the formation of particles or droplets in a laminar cylindrical flow containing one or more condensable components has been derived previously by Simonsen and Livbjerg (1992) and Simonsen (1993). The model was applied to systems containing sulphuric acid and water in a cylindrical geometry with cooling of the gas by the walls of the cylinder. The model was later applied to simulate particle formation of pure alkali chlorides by Nielsen (1998b) and Jensen *et al.* (2000). Here, the model is applied to the reacting system containing potassium chloride, sulphur dioxide, oxygen, and water. The model is used in a 2-step simulation as described in the following sections. It is assumed that only potassium sulphate nucleates and that chloride condenses on the seeds formed by the sulphate. A fit to experimental data from homogeneous gas phase chemistry for the sulphation reaction is included. Furthermore, the model is tested on data with nucleation of pure KCl.

3. 2. 1   Introduction to model

The model is based on partial differential equations describing momentum, mass, and energy conservation. The aerosol dynamics are described by using an aerosol population balance model. The model is designed for cylindrical geometry and the notation is based on cylindrical coordinates. The model is based on the following assumptions:

> - *The particles are perfectly wetted by the gaseous components*
> - *The effect of gravity is negligible*
> - *Particles move only by convection following the gas flow*
> - *Coagulation of particles is neglected*
> - *The LFAC is operated in steady state*
> - *The pressure is constant in the furnace*
> - *The particles are spherical*

In the following sections the governing equations for the model are presented for condensation of a single component, *A*. A more thorough introduction to the model is given by Simonsen (1993). The FORTRAN code, including the extensions described later in this chapter, is given in Appendix D. The assumption that coagulation does not influence the results considerably was justified by simulations with the one-dimensional models (stream tube model and PFAC) with coagulation included. The maximal effect of the coagulation on the total particle number concentration during runs with nucleation of KCl was les than 10%.

56

3. 2. 2   Transport equations

The flow in the cylinder is laminar, but due to cooling of the gas the linear gas velocity profile will deviate from the parabolic profile found at isothermal conditions. The actual flow profile is approximated by a parabolic profile for the mass flow, G, given by:

$$G(r) = 2G_0 \left(1 - \left(\frac{r}{R} \right)^2 \right)$$
(26)

where G_0 is the average mass velocity, r is the radial coordinate, and R is the radius of the cylinder. The dynamics of particle change is only affected by axial convective particle transport, birth of new particles by homogeneous nucleation, and growth of particles by heterogeneous condensation of vapors. Particle coagulation and particle transport by Brownian diffusion and thermophoresis are neglected for the experimental conditions investigated. In the continuity equations for mass and energy it is assumed that the flow is laminar and that axial diffusion and energy conduction can be neglected. The equations are given by:

$$\frac{1}{p_t} \frac{\partial p_A}{\partial z} = \frac{M_g}{G \cdot p_t r} \frac{\partial}{\partial r} \left(r \cdot D_A C_t \frac{\partial p_A}{\partial r} \right) - \frac{M_g s_A}{G} - \gamma \cdot r_A$$
(27)

$$\frac{\partial T}{\partial z} = \frac{1}{G \cdot C_p r} \frac{\partial}{\partial r} \left(r \cdot k \frac{\partial T}{\partial r} \right) - \frac{\Delta H_c s_A^{\#}}{G \cdot C_p}$$
(28)

where A is the condensing component, D_A is the binary diffusion coefficient, s_A is the source term describing the rate of gas-to-particle conversion (mole/s/m^3), γ is a constant, ΔH_c is the heat of condensation, and k is the thermal conductivity of the gas.

3. 2. 3   Aerosol population balance

The population balance in cylindrical coordinates for particles with particle radius r_p and with coagulation neglected is given by (Friedlander, 2000):

$$\frac{\partial}{\partial z} (v_z \varphi) + \frac{\partial}{\partial r_p} \left(I_{r_p} \varphi \right) - J\delta\left(r_p - r_p^{\ *} \right) = 0$$
(29)

where φ is the size distribution density function depending on r_p, r, and z. The function is defined such that $\varphi(r_p, r, z) \cdot \Delta r_p$ is the number concentration of particles with a particle radius in the range $(r_p; r_p + \Delta r_p)$. I_{r_p} is the local growth rate of particles and J is the rate of homogeneous nucleation. δ is the Dirac delta function given by:

$$\int_\alpha^\beta \delta\left(r_p - r_p^{\ *} \right) = \begin{cases} 1 & \text{if} \quad \alpha < r_p - r_p^{\ *} < \beta \\ 0 & \text{else} \end{cases}$$
(30)

with the dimension $[1/r_p]$. The radial growth rate is given by a steady state Maxwellian flux expression:

$$I_{r_p} = \left(\frac{\partial r_p}{\partial t}\right)_{particle} = F(Kn)\frac{D_A M_A}{RT\rho_s r_p}\left(p_A - p_A{}^*\right) \tag{31}$$

where Kn is the Knudsen number and $F(Kn)$ is the correction of the diffusion for non-continuum mechanics given by the Dahneke equation as (Seinfeld, 1986):

$$F(Kn) = \frac{1+Kn}{1+2Kn(1+Kn)/\eta_A} \qquad Kn = \frac{2D_A}{r_p}\sqrt{\frac{\pi M_A}{8RT}} \tag{32}$$

η_A is the sticking coefficient for A. This represents the probability that a molecule sticks to the particle when it collides on the surface and is assumed to be unity in the simulations. $F(Kn)$ approaches unity when the Knudsen number becomes very small. Thus, no correction is applied for large particles, while the correction limits the growth rate for smaller particles. $Kn < 0.1$ is called the continuum regime, $Kn > 10$ is called the Knudsen regime and the interval $0.1 < Kn < 10$ the transition regime.

3. 2. 4   Homogeneous nucleation

The nucleation step involves the transformation of vapor-monomers to clusters by a series of reversible steps. The clusters will persist and grow when the Gibbs free energy change accompanying the phase transformation is negative (Seinfeld and Pandis, 1998). The critical cluster size is the boundary between incipient particles, which are stable and can continue to grow and unstable clusters, which redisperse into the gas phase. The equilibrium vapor pressure over the small clusters is extremely high due to the Kelvin effect. For a particle of pure component A the increase in saturation vapor pressure due to this effect is given by (Atkins, 1998):

$$\frac{p_{A,curved}^*}{p_{A,flat}^*} = \exp\left(\frac{2\sigma_A M_A}{r_p RT\rho_A}\right) \tag{33}$$

The convex curvature of the surface makes it easier for molecules to escape the surface and thus a higher vapor pressure is needed to stabilize the particle or droplet. The Gibbs free energy for the formation of a single particle of n components with n_i molecules of the ith component and the surface tension σ_i is given by (Seinfeld, 1986):

$$\Delta G = \sum_{i=1}^{n} n_i k_B T \ln(S_i) + \pi \cdot d_p^2 \sigma_i \tag{34}$$

where S_i is the saturation of the ith component given by:

$$S_i = \frac{p_i}{p_i^*(T)} \tag{35}$$

where p_i is the vapor pressure and $p_i^*(T)$ is the temperature-dependent saturation pressure.

The surface tension of component A is corrected for curvature-dependence with the Tolman length, δ_A. The correction decreases the surface tension of small particles and is given by (Vogelsberger, 1980):

$$\sigma_A = \frac{\sigma_{\infty,A}}{1 + 4 \cdot \delta_A / d_{p,A}} \tag{36}$$

The Tolman correction does also affect the change in Gibbs free energy, which for the formation of a cluster of q_A molecules becomes (Christensen, 1995):

$$\Delta G_A = -q_A k_b T \ln(S_A) + \frac{K_2 q_A}{K_1 q_A^{1/3} + 2\delta_A} \tag{37}$$

$$K_1 = \left(\frac{3 v_{m,A}}{4\pi}\right)^{1/3} \quad \text{and} \quad K_2 = 3\sigma_{\infty,A} \cdot v_{m,A} \tag{38}$$

where $v_{m,A} = M_A/(\rho_{p,A} N_a)$ is the molecular volume for the condensed component A. The homogeneous nucleation rate is given by a product of three terms (Seinfeld, 1986):

$$J_A = C_A^* \cdot Z_A \cdot N_A^e \tag{39}$$

where C_A^* is the growth rate (molecules/s) of the critical cluster and is given by (Seinfeld, 1986):

$$C_A^* = \frac{\pi \cdot d_p^{*2} p_A}{k_B T} \sqrt{\frac{R_g T}{2\pi \cdot M_A}} \tag{40}$$

Z_A is the Zeldovich factor. It accounts for the fact that the pseudo steady state cluster concentration differs from the equilibrium cluster concentration. When the Tolman correction is taken into account this is given by (Christensen, 1995):

$$Z_A = \sqrt{\left(-\frac{1}{2\pi \cdot k_B T}\left(\frac{d^2 \Delta G_A}{dq_A^2}\right)_{q^*}\right)} = \sqrt{\left(-\frac{K_1 K_2}{9\pi \cdot k_B T} \cdot \frac{K_1 q_A^{*-1/3} + 4\delta_A q_A^{*-2/3}}{(K_1 q_A^{*1/3} + 2\delta_A)^3}\right)} \tag{41}$$

with K_1 and K_2 given by equation (38). The equilibrium cluster concentration follows the Boltzmann distribution and is given by (Christensen, 1995):

$$N_A^e(q_A) = N_A(1)\exp\left(-\frac{\Delta G_A}{k_B T}\right) = \frac{p_A}{k_B \cdot T} S_A^q \cdot \exp\left(-\frac{K_2 q_A}{k_B T(K_1 q_A^{1/3} + 2\delta_A)}\right) \tag{42}$$

The diameter of the critical cluster is:

$$d_p^* = \frac{1}{K_3}\left(1 - 4 \cdot K_3 \cdot \delta_A\right) + \sqrt{4 \cdot K_3 \cdot \delta_A + 1} \quad \text{with} \quad K_3 = \frac{k_B T \ln(S_A)}{2\sigma_{\infty,A} \cdot v_{m,A}} \tag{43}$$

and the number of molecules A in the critical cluster is given by:

$$q_A^* = \frac{\pi \cdot d_p^{*3}}{6 \cdot v_{m,A}} \tag{44}$$

For extremely high values of the saturation ratio, the collision of two molecules can form a stable cluster. In this case homogeneous nucleation is called collision limited, because the rate is limited by the rate of molecular collisions. Component A is either KCl or K_2SO_4 in the simulations presented in the following. For the simulation of particle formation by condensation of KCl the above equations are corrected for the presence of dimers as shown by Christensen (1995). Coagulation is not included in the simulations due to the short residence time of particles between the homogeneous nucleation zone, the sampling, and dilution by the ejector-diluter. To simulate particle formation from K_2SO_4 the computer program was extended with the chemical rate expression presented in the following section.

3. 2. 5 Rate expression for SO₂ conversion used in the model

A rate expression for the formation of gaseous potassium sulphate is used in the model. The rate expression is first order with respect to the SO_2 concentration. In order to account for the reverse reaction a thermodynamic limitation was included in the expression. The rate expression is validated against experimental data for the homogeneous gas phase reaction of potassium sulphation. Experimental data for the gas phase conversion of SO_2 to SO_3 has been provided by Lusi Hindiyarti. The data was obtained by introducing a gas containing known concentrations of O_2, SO_2, SO_3, H_2O water to an isothermal tubular furnace and then measure the concentration of SO_2 in the inlet and outlet gas while applying different temperatures to the reactor. The data are shown in Appendix A. Unfortunately, the concentration of SO_3 used in the inlet of the furnace was rather high and the dissociation of SO_3 is dominating in some of the data. The experimental data show a decreasing conversion with temperature at high temperatures. This indicates that the conversion is limited by equilibrium at high temperatures. The same experimental set of data was modeled with a more detailed kinetic model by Yilmaz *et al.* (2006). The reaction rate used in the model was assumed to be a first order reaction in SO_2 partial pressure and follow an expression given by:

$$r_{K_2SO_4} = -r_{SO_2} = k_{SO_2}(T)c(SO_2)\left(1 - \frac{Q}{K_{eq}}\right) \tag{45}$$

The term Q/K_{eq} is an indicator of the deviation from the equilibrium composition. Q is given by (e.g. Muller, 1994):

$$Q = \frac{p(SO_3)}{p(O_2)^{\frac{1}{2}} p(SO_2)} = \frac{p(SO_2)_0 X_{SO_2}}{p(O_2)^{\frac{1}{2}} p(SO_2)_0 (1 - X_{SO_2})} = \frac{X_{SO_2}}{p(O_2)^{\frac{1}{2}} (1 - X_{SO_2})} \tag{46}$$

A temperature-dependent equilibrium constant for the reaction is applied. The expression is suggested by Appl and Neth (1979):

$$\log_{10} K_{eq} = \left(\frac{4956K}{T} - 4.678\right)\left[\text{bar}^{-\frac{1}{2}}\right] \tag{47}$$

In Figure 43 the equilibrium constant is compared to *Q,* based on the experimental data, at different temperatures. Good agreement is observed at high temperatures indicating that chemical equilibrium is established in these experiments.

Fitting an expression of the type $K = \exp(A/T\text{-}B)$ to the experimental data at high temperatures to obtain a temperature-dependent equilibrium constant instead of using the one found in the literature gave similar results for the K_2SO_4 formation in the final simulations.
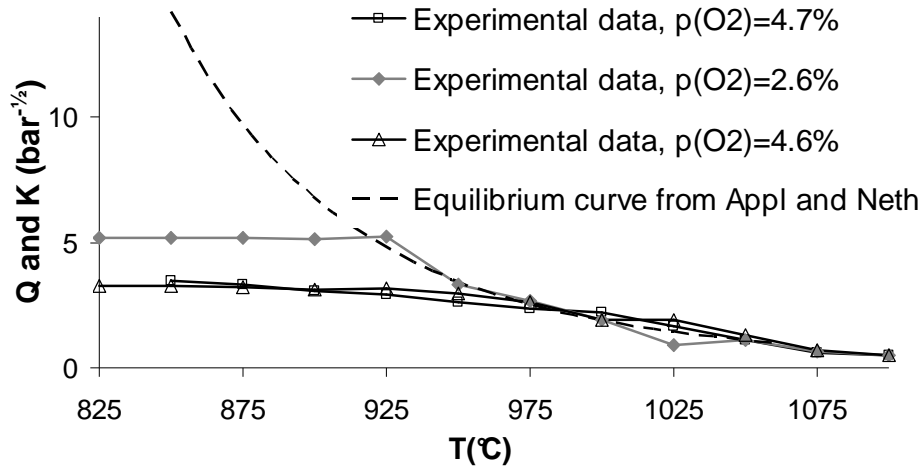
Figure 43. *Experimental values of Q for the oxidation of SO_2. At high temperatures the reaction is at equilibrium and the values of Q are equal to the value of the temperature-dependent equilibrium constant.*

The reaction rate is given by equation (45):

$$r_{K_2SO_4} = -r_{SO_2} = k_{SO_2} \exp\left\{-\frac{E_a}{R}\cdot\frac{1}{T}\right\} c(SO_2)\left(1-\left[\frac{p(SO_3)}{p(O_2)^{\frac{1}{2}}\, p(SO_2)\cdot K_{eq}}\right]\right)$$

$$= C_1(T)\{1-X_{SO_2}\}\left(1-C_2(p(O_2),T)\cdot\frac{X_{SO_2}}{1-X_{SO_2}}\right) = C_1\left(1-X_{SO_2}-C_2\cdot X_{SO_2}\right) \tag{48}$$

where C_1 and C_2 are given by:

$$C_1(T) = k_{SO_2}\exp\left\{-\frac{E_a}{R}\cdot\frac{1}{T}\right\} c(SO_2)_0 \quad \text{and} \quad C_2(p(O_2),T) = \frac{1}{p(O_2)^{\frac{1}{2}} K_{eq}(T)} \tag{49}$$

The dimension for the reaction rate is $[\,r_{K_2SO_4}\,] = \frac{\text{mole}}{\text{s}\cdot\text{m}^3}$

The flow in the homogeneous gas phase reactor is assumed to be plug flow. The design equation for a plug flow reactor is introduced. By integration of the rate expression the following expression for the reactor volume is obtained:

$$V = \dot{n}(SO_2)_0 \int_{X_{SO_2,in}}^{X_{SO_2,out}} \frac{1}{-r_{SO_2}} dX'_{SO_2} = \frac{p(SO_2)_0 \cdot \dot{V}/(RT)}{\tau \cdot K_1(T)\{K_2(p(O_2),T)+1\}} \ln\left|\{K_2(T)+1\}X'_{SO_2}-1\right| \Bigg|_{X_{SO_2,in}}^{X_{SO_2,out}} \quad (50)$$

The reactor volume is known and the only unknown parameters are k_{SO_2} and E_a. These are found by a least square fit of the calculated reactor volume. Reasonable fit of two data series with different oxygen levels are obtained with the parameters $k_{SO_2} = 69\frac{1}{s}$ and $E_a = 63\frac{kJ}{mole}$ (Figure 44).
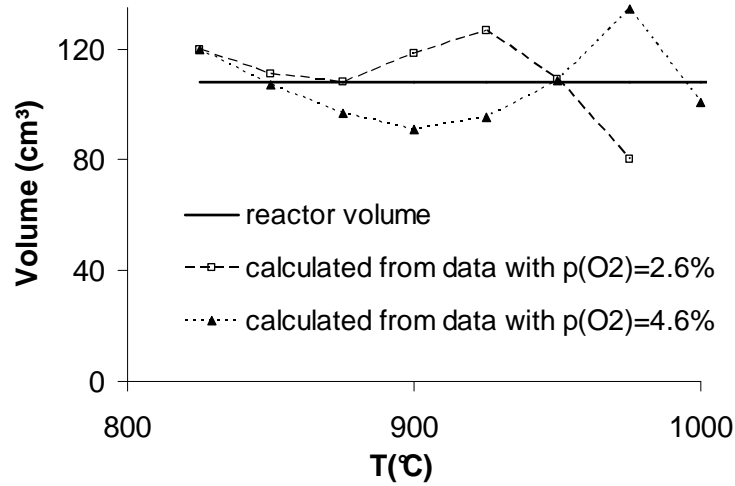
Figure 44. *Reactor volume determined by fitted rate expression and equation (50) .*

The parameters obtained by fitting the plug-flow reactor model to the data are used in the calculation of sulphate formation in the computer code. The reaction rates with a fixed value of either the inlet pressure of SO_2 or of the conversion are shown in Figure 45 and 46.

The rate shows a maximum in the range ~800-1000°C, which is in good agreement with the experimental results in Chapter 2. The rate expression is introduced in the laminar flow model by introducing a new source term, $s_{reaction}$, into the total mass balance. The total mass balance for component A is then:

$$\frac{1}{r}\frac{\partial}{\partial r}\left(-r \cdot c \cdot D_A \frac{\partial y_A}{\partial r} + r \cdot y_A c \cdot v_r\right) + \frac{\partial}{\partial z}(y_A c \cdot v_z) = -s_{A,\ growth} - s_{A,\ nucleation} + s_{reaction} \quad (51)$$

where the rates of particle growth, $s_{A,growth}$, and nucleation, $s_{A,nucleation}$, (mole/m³/s) are given by:

$$s_{A,\ growth} = \int_0^\infty \varphi \cdot v_z \frac{\partial}{\partial z}\left(\frac{4\pi \cdot r_p^3}{3}\frac{\rho_A}{M_A}\right)da \quad (52)$$

$$s_{A,\ nucleation} = \left(\frac{4\pi \cdot r_p^3}{3}\frac{\rho_A}{M_A}\right)J_A \quad (53)$$

The implementation of the rate expression in the original computer code MONAERO is shown in Appendix D. The code is called K2SO4_AERO_REACTION.
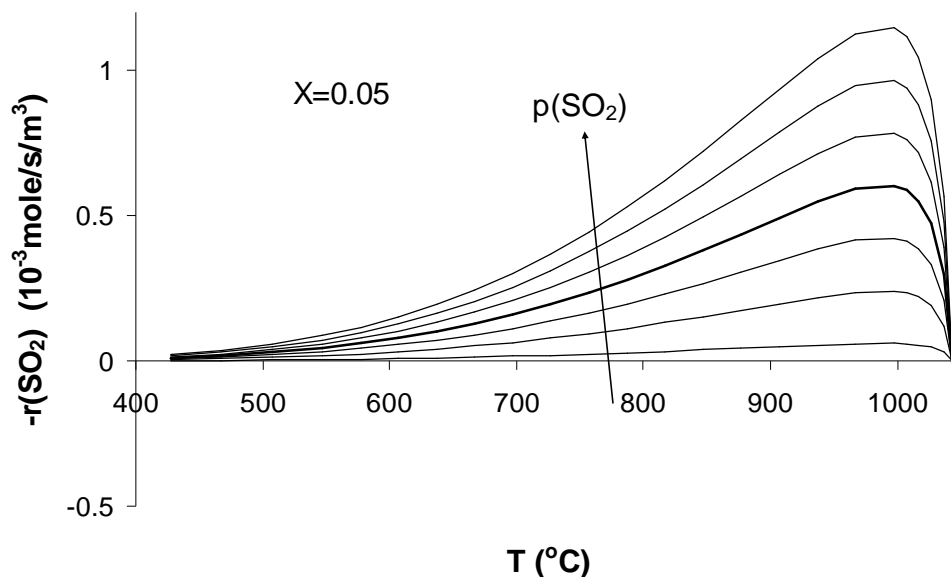
Figure 45. *The reaction rate as function of temperature for different SO_2 vapor pressures (5-95 Pa) and a fixed conversion X=0.05.*
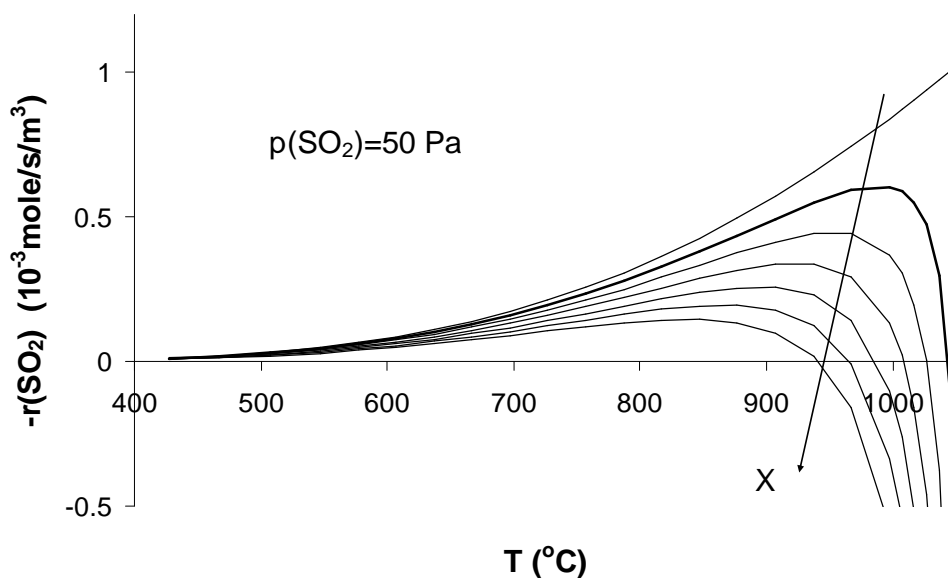
Figure 46. *The reaction rate as function of temperature for different values of the SO_2 conversion (0-0.3) and an inlet SO_2 vapor pressure of 50 Pa. For high conversions and high temperatures the reaction is reversed. This is because the reaction is exothermic.*

3. 2. 6   Numerical solution

The equations given in the previous sections are solved using the approximation of constant mass velocity in the computer code MONAERO by Simonsen (1993). The non-linear second order differential equations in the mathematical model are transformed to a set of ordinary differential equations by discretization of the radial cylindrical coordinate using orthogonal collocation (Villadsen and Michelsen, 1978). The particle size distribution is solved using a sectional method. The particles are divided into a number of size classes of uniform particle properties. The code uses the so-called moving sectional method (Gelbard, 1990). The equations are integrated in axial steps using a third order semi-implicit Runge-Kutta method. In each step the rate of homogeneous nucleation is calculated and new size sections are added. It is tested how the solution depends on the number of collocation points and the minimal step length and the integration parameters are chosen in a way that ensures a solution, which is independent of these.

If the model is used to simulate reaction and condensation of a reacting flow with high concentration of SO_2 the relative decrease in SO_2 will be negligible. In this case the concentration can be assumed constant and an extra dependent variable can be avoided in the computer code.

3. 3   Simulation results

The results from the simulations are divided in two parts; verification of the MONAERO code with monomer/dimer nucleation of $KCl/(KCl)_2$ as implemented by Nielsen (1998b), and a 2-step simulation of aerosol formation in a reacting flow with formation of K_2SO_4.

3. 3. 1   Nucleation of pure KCl

The results from simulations of pure KCl are based on the parameters determined by Jensen *et al.* (2000). The dependence on curvature of the surface tension is corrected with the Tolman length $\delta_{KCl} = 1.0 \cdot 10^{-10}$m. For the diffusion coefficient an average value for monomers and dimers determined by the Chapmann-Enskog equation is used with an additional parameter fitted to experimental data from the LFAC. The diffusivity is thus given by:

$$D_{KCl} = Q \cdot A \cdot T^B = 1.15 \cdot 1.632 \cdot 10^{-10} \tfrac{m^2}{s} \cdot (T/K)^{1.88} \tag{54}$$

For further details on the physical properties for KCl used in the simulations see Appendix C. Simulations are performed to analyze experiments with different inlet concentrations and different flow rates. The data presented below are from a series of experiments and simulations with a feed of 200 ppm KCl in the LFAC, a temperature profile as the one shown in Figure 7, and with different flow rates through the reactor. The number-based particle size distributions obtained in the LFAC are compared to the ones obtained by simulations with MONAERO in Figure 47. An increase in the flow rate increases the cooling rate while decreasing the residence time. The average diameter of the particles is decreased and the number concentration is increased when increasing the flow rate.
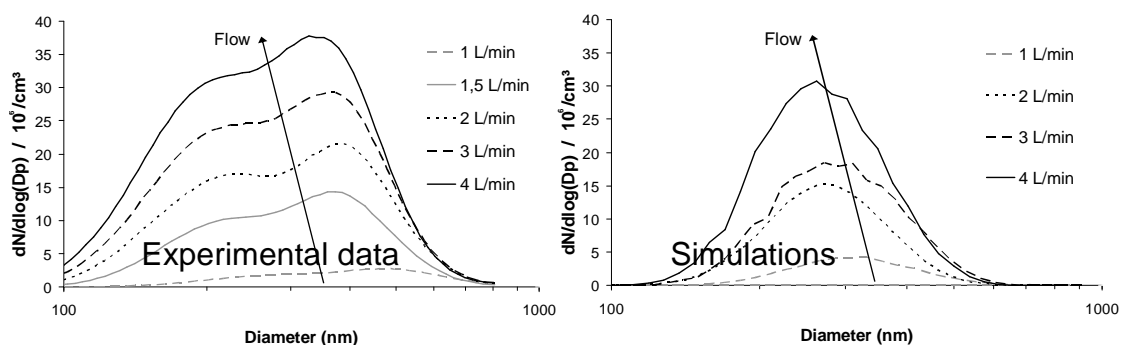
Figure 47. *Experimental data and simulations of KCl-nucleation in the LFAC with different total flow through the reactor. The physical parameters and the Tolman correction are as determined for KCl by Jensen et al. (2000).*

Simulations resulted in lower particle number concentrations than the experimentally observed values. A better agreement between the experimental results and the simulations exists when mass-based size distributions are calculated based on the number-based particle size distribution. The wall depositions from experiments and simulations are shown in Figure 12. The simulation predicted the data well when the flow rate is close to the value used by Jensen *et al.*, in the experiments where the parameters for the diffusion coefficient and the Tolman coefficient were estimated (3500 mL/min). An under-prediction of the wall deposition is simulated at lower flow rates.

The model was applied to simulate the total number concentrations for the experiments with different inlet concentrations of KCl. The results are shown in Figure 14 on page 26. The number concentration decreases with increasing inlet vapor pressure of KCl as observed previously by Jensen *et al.* (2000).

3. 3. 2   Nucleation of K₂SO₄ and condensation of KCl

To investigate whether the formation of aerosols in post-combustion gases from biomass combustion can be described by homogeneous nucleation of potassium sulphate and subsequently heterogeneous nucleation of potassium chloride, the formation process is simulated by a 2-step procedure. The first step is the formation of gaseous K_2SO_4 followed by homogeneous nucleation of this component. In the second step, the resulting particle size distribution from step 1 is introduced as seed particles to a reactor containing KCl and this component is condensed on the seeds. Thus, the model assumes that the condensation of sulphate is completed, when the temperature becomes sufficiently low for the condensation of chloride.

The experiment called 'High SO₂' in Chapter 3 was chosen for the simulation due to the relatively small change in the SO₂ concentration in this experiment, and therefore it is reasonable to assume a constant concentration of SO₂ in the reactor. The conditions for the experiment are:

> *Inlet concentrations: 200 ppm KCl, 500 ppm SO₂, 5% H₂O, and 5% O₂*
> *Temperature profile: The 'Reference' profile (shown in Figure 7)*
> *Flow rate: 3500 L/min at 20 °C and 1 atm.*

The concentration of SO_2 exceeds the concentration of KCl, and the assumption that all SO_3 will react immediately to form K_2SO_4 is only valid if the SO_2 conversion is below 20% (corresponding to 100% sulphate content in the particles). The analysis of impactor samples from this experiment showed a sulphate content around 20% on an atomic basis corresponding to approximately 35% sulphate in the particles on a weight basis.

The sulphate concentration in the inlet of the furnace is zero. Sulphate is formed by the kinetics described in Section 3.2.5. The parameters for the kinetic expression in equation (48) obtained by fitting of experimental data, the Tolman coefficient, and the inlet vapor pressure of SO_2 are:

$$k_{SO_2} = 69 \ 1/s, \quad E_a = 63000 \ \text{J/mol}, \quad p(SO_2) = 50 \ \text{Pa}, \quad \text{and} \quad \delta_{K_2SO_4} = 0.95 \cdot 10^{-10} \ \text{m}.$$

The 2-step procedure for aerosol formation is compared to experimental data and to a simulation with pure KCl as illustrated in Figure 48. The comparison between nucleation of pure KCl and K_2SO_4 formed by reaction in step 1 is used to determine the compound which nucleates first.
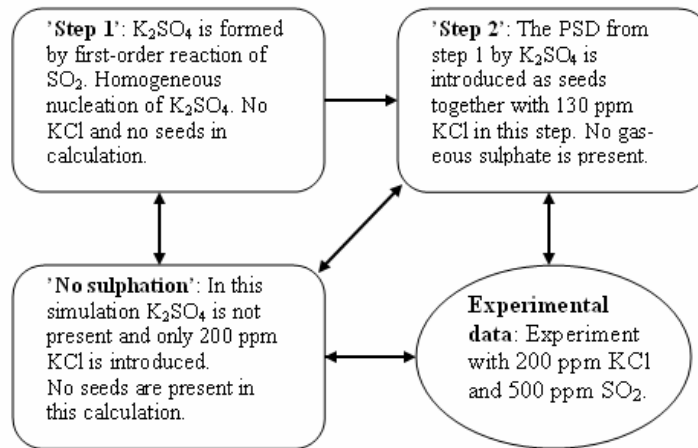
Figure 48. *Procedure for evaluating the 2-step procedure for simulation of aerosol formation. The vapor pressure of KCl in step 2 is adjusted for the amount of K used in step 1.*

In step 1 the vapor pressure of K_2SO_4 in the furnace is determined by the reaction of SO_2, loss to the walls and condensation on particles. In step 2 the vapor pressure of KCl can be adjusted for the amount of potassium used to form sulphate in step 1. The temperature profile used in the simulations and the vapor pressure of gaseous potassium sulphate is shown as function of radial and axial position in the furnace in Figure 49.

The vapor pressure of K_2SO_4 increases immediately after the saturator, where SO_2 and KCl are mixed, and a maximum is reached rather quickly. After the maximum of approximately 20 ppm, the vapor pressure decreases to very low values. This is caused by formation of very high numbers of new particles by homogeneous nucleation of K_2SO_4. The formed particles provide a very large surface area for subsequent heterogeneous nucleation. After the particles have been formed, more K_2SO_4 is formed, but the diffusion to the surface of the existing particles is sufficiently fast to remove all the formed sulphate. A part of the formed sulphate is also lost to the walls of the furnace. This is evident by a parabolic shape of the vapor pressure profile established prior to the particle formation.
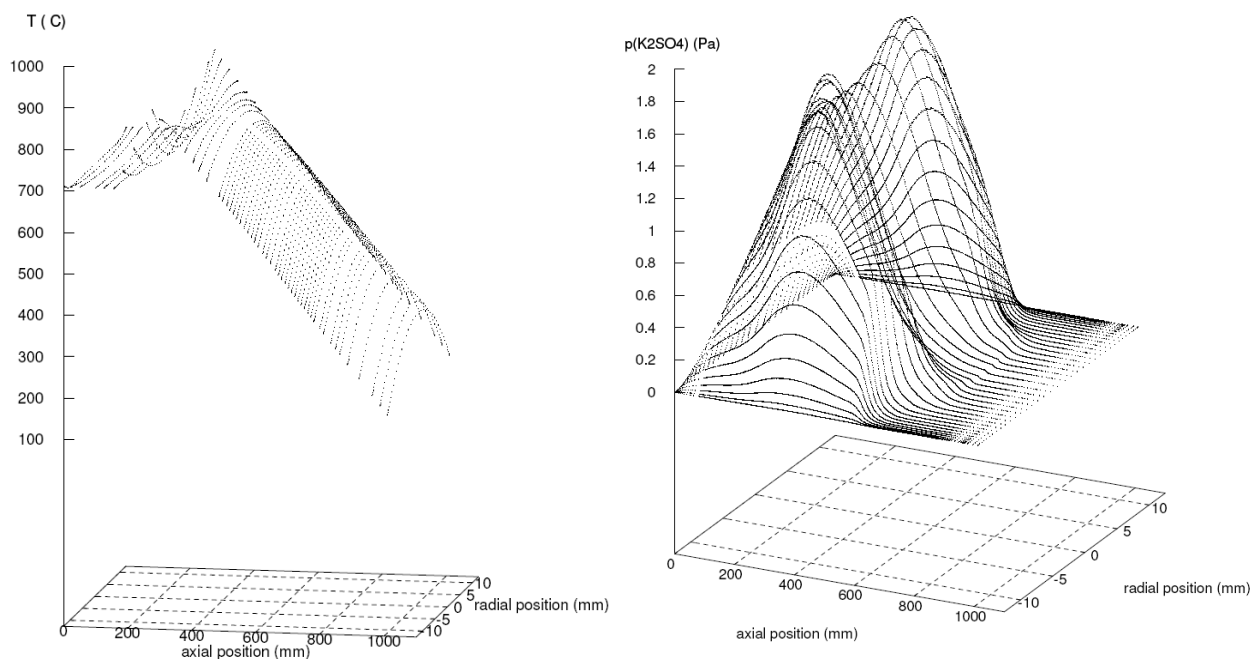
Figure 49. *The calculated temperature profile and the vapor pressure of gaseous K_2SO_4 in the LFAC during step 1. In this step gaseous sulphate formed by a homogeneous gas phase reaction and subsequently forms new particles are created by homogeneous nucleation.*

The nucleation rate of K_2SO_4 in step 1 is shown in Figure 50 together with the nucleation rate of KCl in the simulation where only KCl is condensed.
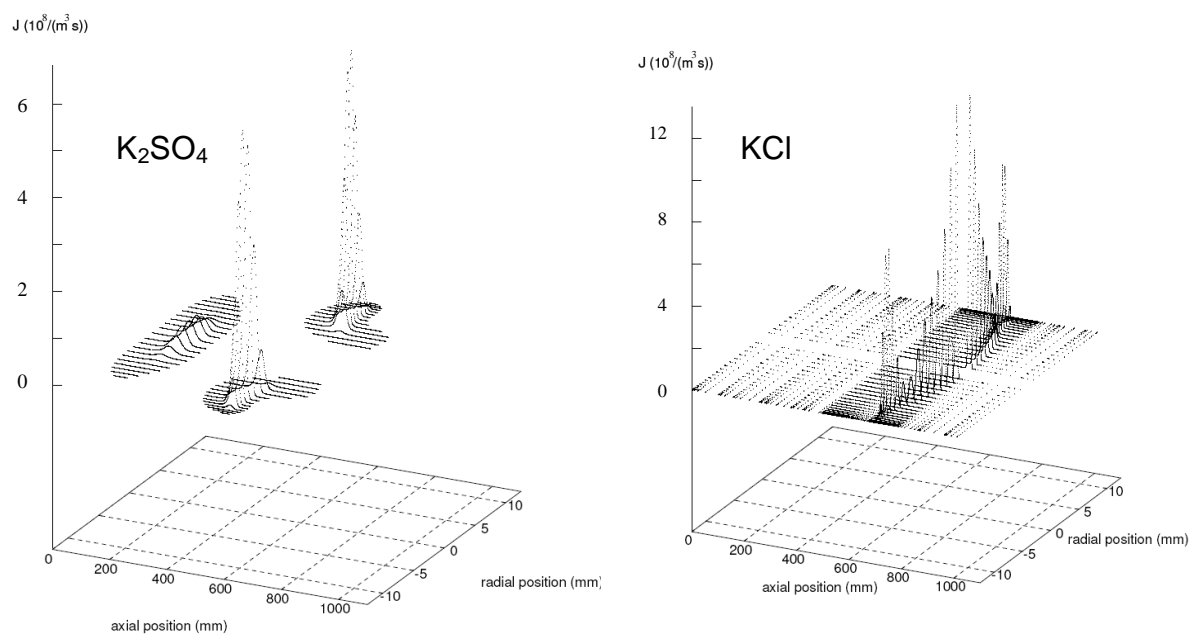
Figure 50. *The rate of homogeneous nucleation in the LFAC during nucleation of K_2SO_4 in the first step of the 2-step procedure and of KCl in the simulation of pure KCl condensation.*

The nucleation of pure KCl takes place much further downstream in the furnace than the nucleation of K_2SO_4 in step 1. This means that if a mixture of the two components is cooled, sulphate will nucleate first and suppress the homogeneous nucleation of KCl. Clearly, the locations of the two nucleation fronts are dependent on the concentrations of the two components. The concentration of sulphate depends on the reaction rate. The accuracy of this reaction rate may be low due to lack of experimental data for the reaction at low temperatures. However, the simulations clearly show that sulphate nucleation will occur prior to condensation of KCl even if the kinetic parameters are not very accurately determined. The simulations still show that the formation of sulphate seeds occur prior to condensation of KCl when the reaction rate is decreased ten times simultaneously with a ten times increase in the concentration of KCl. The saturation of the condensing component in the two cases is very different. The saturation increases until the location of the nucleation front in both cases. However, for K_2SO_4, a super-saturation of several thousands is reached, while for KCl this ratio stays below 50 in all simulations. This is due to the very different equilibrium vapor pressures and surface tensions of the two components and because sulphate is formed at the same time as it is consumed during the particle formation. In this case this causes the high super-saturation to be maintained for a longer time.

The vapor pressure of KCl in step 2 is compared to the case with nucleation of pure KCl in Figure 51. It is seen that the vapor pressure begins to decrease at approximately the same location in the furnace. However, when no seed particles are present, the decrease is considerably enhanced at some point, caused by the sudden formation of new particles. In the case shown here, the vapor pressure of KCl in the input to the simulation has not been reduced to compensate for the use of K in the potassium sulphate formation. If this correction is applied the decrease of vapor pressure will begin further downstream in the furnace but the difference between the case with and without seeds will be qualitatively similar to the cases shown here.
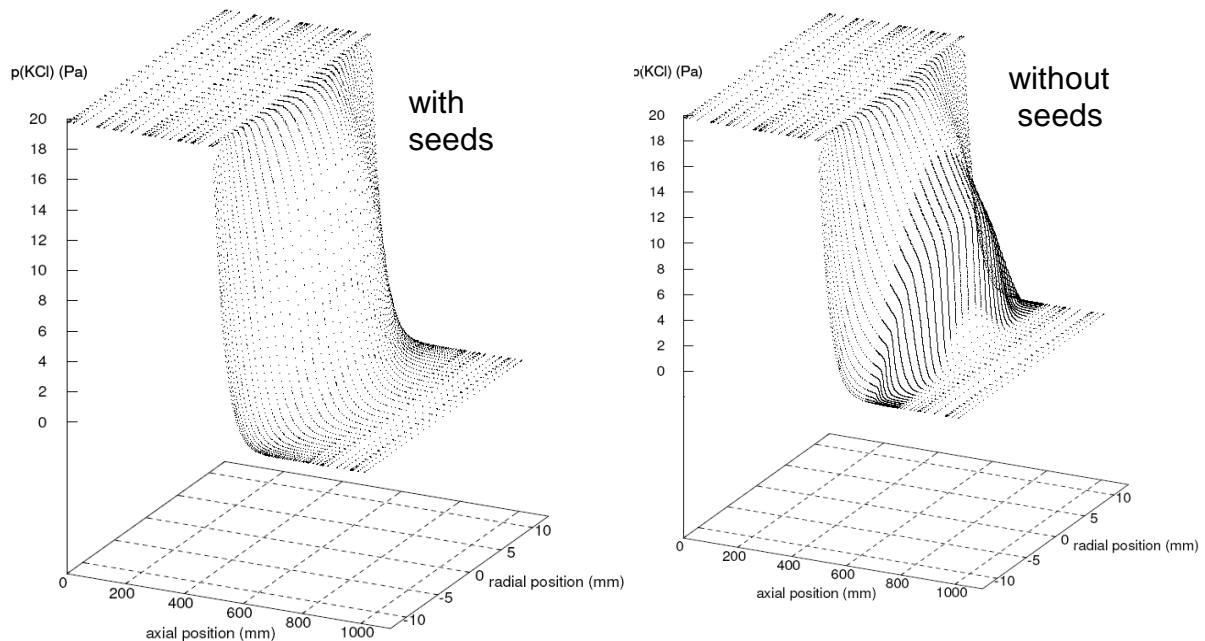
Figure 51. *The vapor pressure of KCl in the LFAC during condensation in the simulation, step 2, with sulphate seeds, and during the run with nucleation of pure KCl. The potassium concentration is not corrected for the amount of potassium that is used during the formation of potassium sulphate.*

The particle size distribution from experimental data is compared to the particle size distributions obtained by the 2-step simulation and by the simulation of pure KCl nucleation. The number-based particle size distributions are shown in Figure 52 and the calculated mass-based particle size distributions are shown in Figure 53.
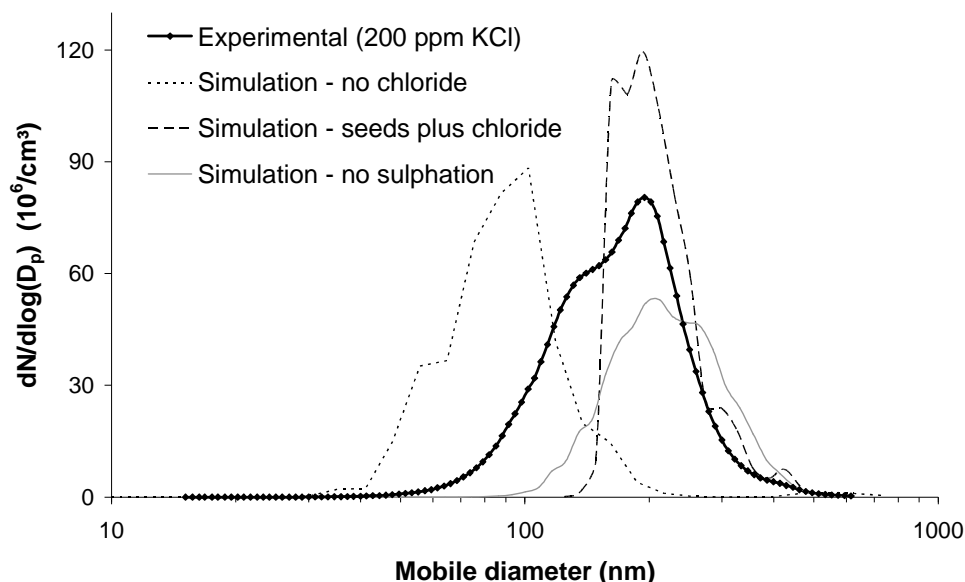
Figure 52. *Number-based particle size distribution for experiment with aerosol formation from a gas containing 200 ppm KCl and 500 ppm SO_2 (5% O_2, 5% H_2O, and N_2 as filler-gas). The experimental data are shown together with simulations with the 2-step procedure and with pure KCl condensation.*
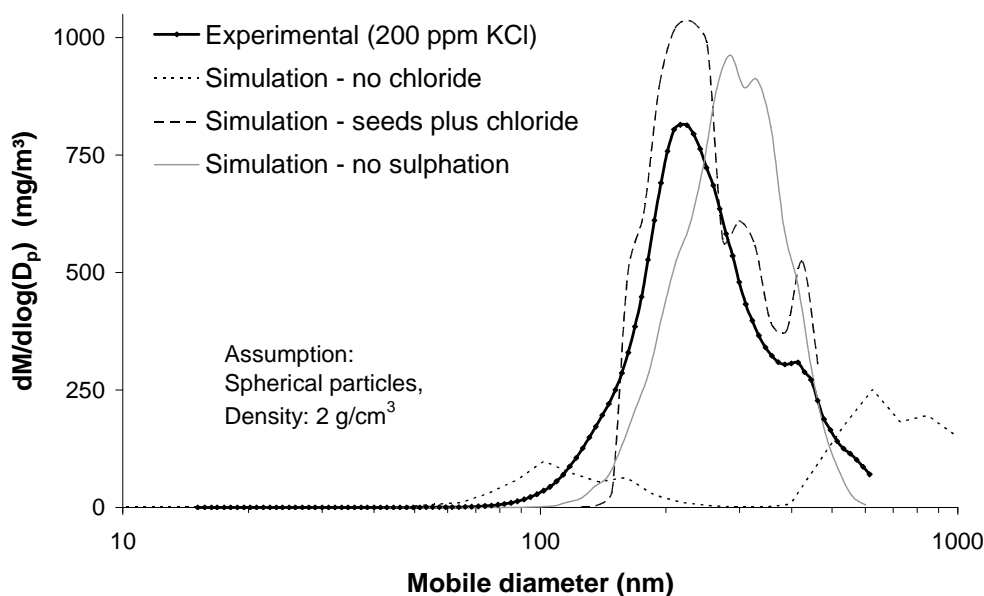
Figure 53. *Mass-based particle size distribution from experiment with aerosol formation from a gas containing 200 ppm KCl and 500 ppm SO_2 (5% O_2, 5% H_2O, and N_2 as filler-gas). The experimental data are shown together with simulations with the 2-step procedure and with pure KCl condensation. All curves are obtained by conversion of the number-based distributions in Figure 52 assuming spherical particles with constant density.*

The particle size distribution for the particles formed in step 1 is dominated by very fine particles with mobile diameters below 100 nm. The size distribution shown here is bimodal due to the formation of particles in two separate axial locations in the furnace. The nucleation of particles in the early part of the reactor, before the gas is heated, is avoided if a slightly lower value of the Tolman correction is used. However, the change in the final particle distribution after the 2-step simulation is insignificant.

The final particle size distributions from the 2-step simulation procedure agree very well with the experimentally obtained data. It must be emphasized that the only parameter in the model that has not been predicted independently of the results is the fit of the total number concentration in step 1 by changing the Tolman coefficient. The simulation does not include the heterogeneous conversion of SO_2 that was suggested in Chapter 2. The size distribution of the particles is in good agreement with the experimental results. However, the total sulphate content of the particles is slightly lower than the experimental value. This could be due to a heterogeneous reaction that is not included in the simulation.

The results from the simulation of pure KCl nucleation do not describe the experimental results for the run with sulphation well. The predicted number concentration is too low and the particle diameters are over-predicted.

The simulations of sulphate nucleation with experimentally based kinetics for the SO_2 oxidation proves that it is indeed possible that the particle formation occurs by this mechanism.

3. 3. 3   Sensitivity analysis for the 2-step simulation

The sensitivity of the simulations to the estimated parameters of the kinetic expression k and E_a, the SO_2 pressure, and the Tolman length, δ, is investigated. These parameters are varied by ±10% and the effect on the total number concentration of the sulphate particles is investigated. In Figure 54 the number concentrations are normalized with the concentration when the simulation parameters are: $k = 69$ 1/s, $E_a = 63000$ J/mol, $p(SO_2) = 50$ Pa, and $\delta = 0.95 \cdot 10^{-10}$ m. The parameters are also normalized to these reference values.

It is seen that the number concentration increases with the rate constant and the SO_2 vapor pressure. The relative increase is the same for the two parameters. This is because the backward reaction is practically zero under the given conditions and the rate of sulphate formation is therefore almost directly proportional to the SO_2 concentration.

The number concentration is very sensitive to the Tolman length, because the nucleation rate is heavily dependent on the surface tension of the condensing component. The Tolman coefficient of K_2SO_4 is not known from experimental results. However, Haye and Bruin (1994) have suggested a dimensionless Tolman coefficient, based on molecular dynamics simulations of 0.2 as adequate for so-called Lennard Jones liquids. The dimensionless Tolman length is given by:

$$\kappa(K_2SO_4) = \delta_{K_2SO_4} / \sigma_{LJ, K_2SO_4} \tag{55}$$

where $\sigma_{LJ, K_2SO_4} = 1.222 \cdot v_{m, K_2SO_4}^{1/3} = 1.222 \cdot \left(93.18 \frac{cm^3}{mole}\right)^{1/3} = 5.54 \cdot 10^{-10}$ m (Bird $et\ al.$, 1960). For the Tolman length, obtained by fitting the number concentration, this gives a dimensionless Tolman length of 0.17, which is in good agreement with the value suggested by molecular dynamics

simulations. The total number concentration decreases with increasing activation energy of the SO_2 oxidation.
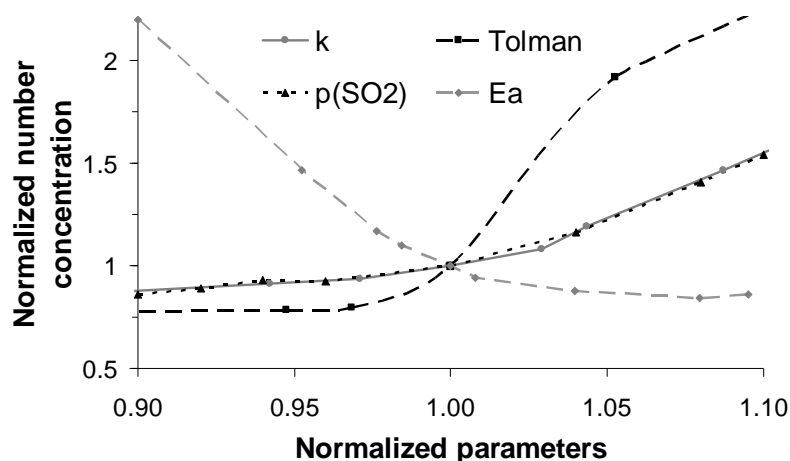
Figure 54. *The relative effect on the total number concentration of changing the simulation parameters from the applied values by 10%. The used values (corresponding to 1.0 at the abscissa axis) are k = 69 1/s, E_a = 63 kJ/mol, $p(SO_2)$ = 50 Pa (500 ppm), and δ = 0.95·10^{-10} m.*

3. 3. 4 Suppression of the homogeneous nucleation

The homogeneous nucleation of KCl is easily suppressed by introducing seed particles in the LFAC as described by Jensen *et al.* (2000). However, when SO_2 is added to KCl the nucleation is not suppressed when adding seed particles from the six-jet atomizer. The highest possible seed particle concentration is $5·10^4$-$2·10^5$#/cm^3. The possibility of suppressing the sulphate nucleation is tested here in the 'Step 1' simulation with addition of seed particles of various particle number concentrations. 500 ppm SO_2 is added and the parameters and temperature profile for the LFAC are as described above. It is found that a complete suppression of homogeneous nucleation is obtained when adding a seed aerosol containing $> 2.2·10^6$ #/cm^3. This is well above the highest number concentration that was added from the atomizer in the experiments and the number is therefore not experimentally verified. The limit for the suppression depends on the choice of Tolman coefficient. In any case the concentration is well above the $5·10^4$-$2·10^5$ #/cm^3 required to suppress nucleation of alkali chlorides (Jensen *et al.*, 2000). The simulated outlet number concentrations at different inlet number concentrations are shown in Figure 55. The measured number concentration without seed particles and the concentration when no homogeneous nucleation occurs are shown by dotted lines.

The shape of the curve is very similar to the ones presented for KCl (Jensen *et al.*, 2000) and for H_2SO_4 (Simonsen, 1993). However, the minimal seed concentration required to suppress the nucleation of K_2SO_4 is considerably higher than for the previously investigated components.
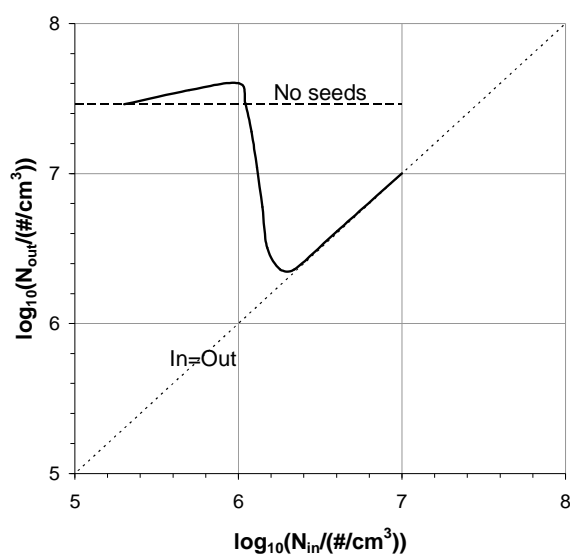
Figure 55. *Particle number concentration in the LFAC-outlet with different inlet concentrations of seed particles. Gas composition, flow rate and temperature profile are fixed.*

3. 4   Conclusion

Aerosol formation in the laminar flow aerosol condenser has been simulated for single component aerosol formation by KCl. The numerical simulation agrees satisfactorily with the experimental observations and provide an insight into the details of the mechanisms of gas-to-particle transformations. The simulation was used to analyze experimental data theoretically with a model based on realistic parameters. The model includes loses to the reactor walls, homogeneous nucleation, and heterogeneous condensation. The model does not take coagulation and particle diffusion into account. Initial estimation proved that these phenomena can be neglected.

The single component model was extended with a simple kinetic model to predict the formation of gaseous potassium sulphate. The model was adapted to experimental data by fitting the number concentration with the Tolman correction factor. A reasonable value of the Tolman coefficient was obtained. The particle size distributions obtained were in good agreement with the expectation that small seeds of sulphate particles are formed and later grow by heterogeneous condensation of chlorides. The chloride was condensed in a separate simulation and the final size distribution from this 2-step procedure agreed well with the experimental data. The mass content of sulphur in the final particles was somewhat lower than suggested by the experimental results. This is probably due to the usage of homogeneous gas phase chemistry data to determine the conversion of SO_2. The surface of the particles probably acts as a catalyst to further oxidation of sulphur. Simulations show that the sulphate nucleation can be suppressed by adding seed particles in a concentration higher than $2.2 \cdot 10^6$ #/cm^3, which is considerably higher than the concentration needed to suppress nucleation of KCl.

Comparison of the axial position of the nucleation front of the sulphate nucleation with the nucleation front from a simulation of pure KCl nucleation under similar conditions showed very clearly that initial nucleation of particles in post-combustion gases with a content of sulphur is by potassium sulphate. This agrees well with the results found in Chapter 2.

CHAPTER 4   FULL–SCALE COMBUSTION OF STRAW

This chapter covers the results obtained during a full-scale measuring campaign at Avedøre Power Plant in Copenhagen, from 23 November to 7 December 2004. The project was funded by PSO grant 1202. The chapter was used as a draft for the publication:[6]

Jacob H. Zeuthen, Peter A. Jensen, Jørgen P. Jensen and Hans Livbjerg (2007), Aerosol Formation during the Combustion of Straw with Addition of Sorbents, Energy & Fuels, 21 (2), 699-709.

4. 1   Introduction

The increased concern for reduction in CO_2 has urged Danish power companies to use straw as an alternative to coal. Straw and similar biomass fuels are used in many other countries. Straw is a CO_2 neutral and renewable fuel. The combustion of straw causes some specific problems including formation of corrosive deposits, aerosol formation, and difficult handling and storage of the fuel. The aerosol particles formed during straw combustion consist mainly of alkali salts and are formed during the condensation of the gas phase salts during cooling of the flue gas (Frandsen, 2005). The content of alkali salt in the fuel varies with fuel type and the extent of release during combustion depends on the combustion technology and boiler design. A high temperature will increase the release of alkali salts from the straw. The volatile inorganic content in straw is mainly chloride, potassium, and sulphur (Michelsen *et al*., 1998; Baxter *et al*., 1998; Christensen *et al*., 1998). The potassium is typically released as hydroxides and chlorides while the sulphur is released as sulphur dioxide (Christensen *et al*., 1998; Knudsen *et al*., 2004b). The sulphur dioxide can react with potassium by the following global reactions:

$$2KOH + SO_2 + ½O_2 \leftrightarrow K_2SO_4 + H_2O \tag{56}$$

$$2KCl + SO_2 + ½O_2 + H_2O \leftrightarrow K_2SO_4 + 2HCl \tag{57}$$

---
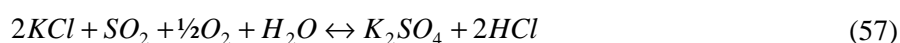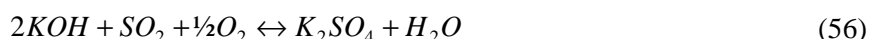
[6] The results are also described in the report: 'Aerosolmålinger under additivforsøg på AVV2', DTU, 2005.

The reactions are exothermic and the equilibrium will favor sulphation at low temperature. However, the reactions are very slow at temperatures below ~800°C (Christensen *et al.*, 1998) and the temperature interval for sulphation is limited to approximately 800-900°C. Sulphation of solid potassium chloride is very slow compared to the gas phase sulphation reaction (Iisa *et al.*, 1999). A detailed mechanism for the sulphation is given by Glarborg and Marshall (2005).

The particle size distribution of aerosols from biomass combustion is often bimodal. One peak results from particles formed from the gas phase by homogeneous nucleation and one results from entrained ash from the fuel. The content of inorganic volatile matter in biomass fuels varies considerably. The alkali content of wheat straw is high compared to most biomass fuels (>1 kg alkali/GJ) (Jenkins *et al.*, 1998; Turn *et al.*, 1997). Previous studies have shown that the alkali content of the fuel correlates well with the mass concentration of sub-micrometer particles (Christensen *et al.*, 1998). The content of salt in the straw varies with use of fertilizer and with weather conditions before harvesting (Sander, 1997; Olsson *et al.*, 1997). Washing of straw will reduce the salt content and minimize deposit and aerosol formation, but this is not practically feasible (Jenkins *et al.*, 1996; Dayton *et al.*, 1999).

The particle growth in aerosols from biomass combustion is mainly dominated by heterogeneous condensation of chlorides and only to a limited extent by coagulation of particles (Jensen *et al.*, 2000). Alkali can be captured from the gas phase by adding a solid sorbent. A sorbent that binds potassium to a mineral with a higher melting temperature while releasing chlorine to the gas phase will reduce deposit formation and corrosion. HCl needs to be removed from the flue gas. By binding potassium in components with higher melting points, sintering of the deposits is reduced and it is easier to remove deposits by soot-blowing. Some sorbents with the desired properties are Kaolin ($Al_2O_3 \cdot 2SiO_2 \cdot (OH)_4$) (Turn *et al.*, 1998; Tran *et al.*, 2004; Tran *et al.*, 2005; Wei *et al.*, 2005; Steenari and Lindqvist, 1998), dolomite (Steenari and Lindqvist, 1998), and alumina oxide (Chen *et al.*, 1999). Addition of limestone and dolomite addition has been proposed to capture sulphur emissions as a replacement of tail-end sulphur removal equipment during biomass combustion (Bain *et al.*, 1998; Ferrer *et al.*, 2005; Lang *et al.*, 2006), S and P will also bind alkali in sulphates and phosphates. Sulphur dioxide has been added to biomass combustion to minimize the chlorine content in deposits. The alkali chlorides may react with sulphur as in (61) and the chlorine will stay in the gas phase during cooling. Ammonium sulphate, when added as a sorbent, will decompose and form sulphur trioxide. Since the oxidation of sulphur dioxide is believed to be the rate limiting step in (61) this will give a direct sulphation of the alkali chloride by the reaction:

$$2KCl + H_2O + SO_3 \leftrightarrow K_2SO_4 + 2HCl \qquad (58)$$

By addition of ammonium sulphate the reaction might be further enhanced although some of the SO_3 may also be decomposed to SO_2 and O_2. The content of chlorine is important for the corrosive behavior of the deposits. Small amounts of chlorine will increase the corrosion rate significantly (Pedersen *et al.*, 1996).

The effect on particle size distributions when applying increased levels of SO_2 and HCl during combustion of biomass was reported by Lind *et al.* (2006). They found that when adding HCl to a circulating fluidized bed boiler the mass concentration of fine particles was considerably increased. When further adding SO_2 the fine particle concentration was reduced. They suggest that this is caused by reaction of the formed sulphate with the coarse ash particles. This will remove some of the potassium from the gas phase before nucleation and thus decrease the fine

74

particle mass concentration. A side effect of adding sorbents may be capture of toxic metals that would otherwise leave the stack as part of the fine particles (Biswas and Wu, 1998). Bentonite has been used to remove alkali metals from hot flue gases in gasification systems (Wolf *et al.*, 2004).

A two-week measuring campaign was done at a power plant. The purpose of the campaign was to find new sorbents suitable for combating formation of corrosive deposits and aerosols during combustion of straw. The sorbents were also tested in a laboratory setup to avoid effects of variations in fuel composition.

4. 2   Experimental

All aerosol measurements of the campaign were carried out during full-scale experiments at the Danish Avedøre-2 power plant in November-December 2004. Avedøre-2 is a modern multi-fuel plant with two boilers, of which the capacity on the biomass boiler is 100 MW. The plant combines power from a biomass steam cycle and a fossil fuel ultra-supercritical steam cycle with heat recovery steam generators (total capacity is 570 MW). The steam cycle of the biomass boiler operates with steam at 300 bars and is superheated to 580°C. Approximately 150,000 tons of straw is used per year (~25 tons per hour of operation). Bottom ash is recycled as fertilizer. The plant is equipped with baghouse filters. Straw is fed to the boiler on a vibrating grate; primary air is supplied through the grate and secondary air downstream from the grate. The temperature of the straw was measured by IR camera and varied from 900-1300°C depending on the position on the grate. The hottest part of the boiler is above the grate with a temperature of 1600°C. Aerosol measurements are carried out upstream from the baghouse filter. The temperature at the location of the measurements was 170°C. SO_2 and HCl concentrations in the boiler are measured continuously. Figure 56 shows schematically the bio-boiler and the sampling locations for of the aerosol measurements.
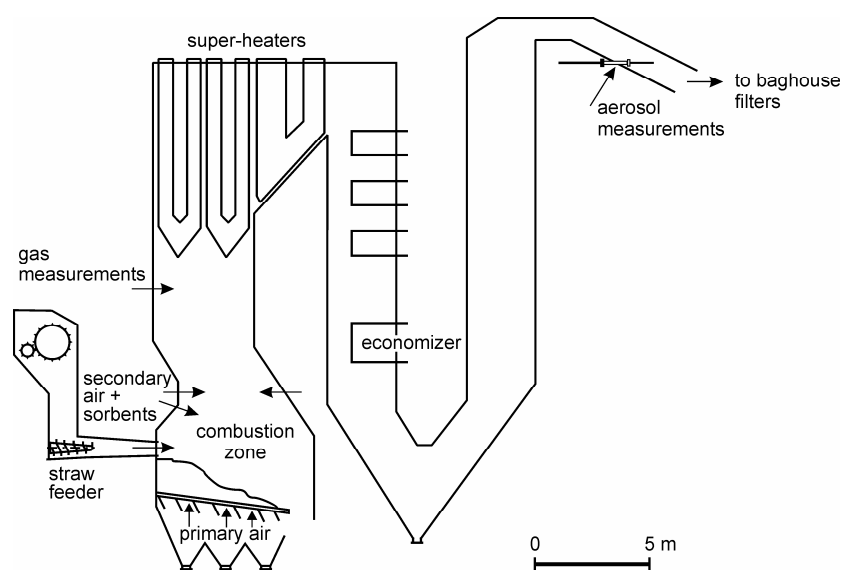
Figure 56. *Illustration of the boiler. The locations of combustion zone, air and sorbent injection, gas measurements, and aerosol measurements are shown.*

4. 2. 1   Full-scale experiments

Six sorbents were used during the measurements: ammonium sulphate, calcium phosphate, Bentonite, ICA5000, clay, and chalk. The choice of sorbents was based on the assumptions that: Bentonite and clay would bind alkali, while monocalcium phosphate would bind alkali in phosphates. Ammonium sulphate is expected to bind potassium as sulphates while adding ammonia to the reduction of NO_x by the selective non-catalytic removal (SNCR) process. ICA5000 is a commercial sorbent for waste incineration for the reduction of deposits and chalk is added in some small scale combustors to reduce the amount of slag from the combustion process. The chemical composition and mean diameter of Bentonite, ICA5000, and clay are shown in Table 7. Chalk ($CaCO_3$), monocalcium phosphate, and ammonium sulphate were of technical quality with a purity exceeding ~95%. The powder diameter given by the manufacturer is approximately 5 μm for chalk and approximately 500 μm for monocalcium phosphate. For ammonium sulphate, which vaporizes completely and decomposes shortly after entering the boiler the particle size was not been measured.

Table 7. *Chemical composition of Bentonite, ICA5000, and clay. Carbon is measured with a carbon analyzer. All other elements are measured by ICP-OES. Data for Bentonite is provided from the manufacturer. All elements, except water, are given on a dry basis*

Sorbent	Bentonite	ICA5000	Clay
Total water (%)	8.9	7.2	1.4
C (%)	-	0.2	1.3
Cl (%)	-	< 0.1	< 0.1
Al (%)	10.1	7.9	10.0
Ca (%)	0.87	0.75	1.7
Fe (%)	6.6	2.0	4.9
K (%)	2.3	1.4	2.3
Mg (%)	1.7	0.78	0.32
Na (%)	0.99	0.17	0.26
P (%)	-	0.020	0.080
S (%)	-	0.071	0.050
Si (%)	24	30	25
Mean diameter (μm)	20.7	43.7	47.9

The sorbent powders are injected continuously into the boiler together with the secondary air above the vibrating grate as shown in Figure 56. For the sorbents Bentonite and ammonium sulphate, two different feeding rates, marked 'high' and 'low' respectively, were used. For Bentonite, there were two different runs with the high feed rate: One with the load on the boiler reduced to 85% of full load marked 'high, reduced' and the other run with full load. There were two additional runs without sorbents, one with increased flow of primary air (marked 'Increased primary air') and one with seed grass instead of wheat straw. Table 8 shows operational data for all runs. The fuel analyses obtained by ISO standard methods are shown in Table 9. The fuel samples were collected during the measuring campaign. Representative samples from different bales of straw were taken and mixed for the analysis. The total mixed sample for chemical analysis varied in size with a total weight up to a few hundred grams.

76

Table 8. *List of runs during the campaign, number of measurements and the feeding rate of sorbents. Some selected stoichiometric ratios are given for the individual runs. They are calculated with the assumption that all sulphur in the fuel and 50% of all potassium is released to the gas phase from the grate combustion zone (estimated value based on values from Knudsen et al. (2004b; 2005a)). The element ratios include measured element content from sorbent and fuel ash*

Run	Date and time of run	Number of LPI measurements	Feeding rate of sorbent (kg/h)	Relevant element ratio (mol/mol)
Reference	11-23. 9-12 am	3	0	Si:K=2.3, S:K=0.23
Chalk	11-24. 9-12 am	3	216	Ca:K=0.5, Ca:S=4.5
Increased primary air	11-24. 3-5 pm	2	0	Si:K=2.3
ICA5000	11-25. 9-12 am	3	582	Al:K=0.49, Si:K=3.6
monocalcium phosphate	11-26. 9-12 am	2	351	P:K=0.71
Bentonit. 'Low'	12-01. 9-12 am	3	450	Al:K=0.37, Si:K=5.6
Bentonit. 'High. Reduced load'	12-01. 1-4 pm	2	900	Al:K=0.98, Si:K=6.1
Bentonit. 'High'	12-07. 9-11 am	2	900	Al:K=0.60, Si:K=2.1
Clay	12-02. 9-12 am	2	654	Al:K=0.67, Si:K=5.3
Seed grass	12-02. 1-4 pm	3	0	Si:K=1.6
Ammonium sulphate. 'High'	12-06. 9-12 am	2	360	S:K=0.83
Ammonium sulphate. 'Low'	12-06. 1-4 pm	3	180	S:K=0.44

The operating conditions of the boiler were adjusted at least one hour before a run, which lasted for approximately three hours. Occasionally, the first aerosol measurement deviated from the following ones indicating that the process conditions were not stable yet. In these cases the first aerosol measurement was discarded.

4. 2. 2   Aerosol measurements

For measuring the aerosol size distributions a 10-stage Berner low-pressure cascade impactor (LPI) with an aerodynamic diameter range: 0.03-12.7 μm was used. The LPI is operated with diluted flue gas withdrawn from the duct by a gas ejector. The ejector dilutes flue gas into a flow of dry, filtered air (Nielsen *et al.*, 2002). The dilution serves a three-fold purpose. Water condensation is prevented because the sample during dilution and cooling is held well above the water dew point. The coagulation rate is lowered by several orders of magnitude after dilution. The dilution also reduces the particle concentration to avoid overloading of the LPI. The dilution ratio varies with time due to changes in flow and pressure in the duct and clogging of the ejector capillary. The clogging of the ejector only happened in some runs. The data from these runs where not different from the runs without clogging (within the deviations between measurements

without blocking). The loss of large particles in the capillary is very low compared to the concentration of coarse particles in the gas and no correction is needed below the stated cut-diameter. To determine the correct dilution ratio during an LPI measurement (duration ~30 minutes) the dilution ratio is measured on-line by comparing the CO_2 concentration in the diluted flue gas with the concentration in the flue gas. Each sample line is dried and filtered continuously in gas-conditioners and fed into an IR CO_2-analyzer (Rosemount, NGA 2000). The dilution ratio can be changed by changing the length and internal diameter of the inlet capillary of the ejector.

Table 9. *Chemical analysis of fuel samples from different runs. All analyses except water are given on a dry basis. Water is determined by drying at 105°C in 20 hours and ash at 550°C in 20 hours. Heating values are determined by an ISO 1928 method. Cd is determined by GF-AAS, C, H, and N by ISO/TS 12902 and all other elements by ICP-OES*

Fuel	Reference	chalk	ICA5000	Increased primary air	MCP	Bent. low	Bent. high. red	Clay	Seed grass	Amm. high	Amm. low	Bent. high	Reference
Total water	13.0	16.6	14.8	15.3	16.3	13.9	14.1	14.0	21.5	15.7	25.2	15.3	17.3
Ash (%)	5.7	5.6	6.0	5.2	5.3	9.0	6.9	5.8	5.4	5.1	5.3	5.5	5.1
Upper heating value (kcal/kg)	18.90	18.69	18.56	18.86	18.93	18.19	18.58	18.60	18.99	18.96	18.90	18.76	18.69
Effective heating value (kcal/kg)	17.65	17.43	17.32	17.61	17.66	16.96	17.31	17.34	17.72	17.72	17.64	17.52	17.44
C (%)	46.5	46.7	46.2	46.2	47.4	45.6	47.0	46.9	47.2	47.2	47.3	46.7	46.6
H (%)	5.89	5.94	5.85	5.91	6.01	5.79	5.95	5.93	5.98	5.84	5.90	5.83	5.89
N (%)	0.98	0.75	0.60	0.80	0.79	0.78	0.75	0.79	1.17	0.63	0.67	0.55	0.58
Cl (%)	0.27	0.59	0.35	0.23	0.16	0.21	0.17	0.19	0.38	0.26	0.24	0.67	0.46
Al (%)	0.009	0.008	0.015	0.056	0.031	0.11	0.067	0.006	0.048	0.014	0.022	0.007	0.018
Ca (%)	0.43	0.43	0.34	0.45	0.37	0.39	0.43	0.28	0.37	0.42	0.45	0.33	0.45
Fe (%)	0.007	0.008	0.012	0.026	0.016	0.051	0.036	0.005	0.025	0.009	0.012	0.005	0.012
K (%)	0.84	1.5	0.88	0.84	0.84	0.72	0.65	0.60	0.96	0.79	0.76	1.4	1.1
Mg (%)	0.11	0.062	0.064	0.062	0.078	0.083	0.070	0.061	0.093	0.080	0.077	0.069	0.078
Na (%)	0.009	0.028	0.013	0.040	0.016	0.039	0.026	0.006	0.067	0.036	0.033	0.008	0.14
P (%)	0.11	0.072	0.076	0.086	0.079	0.093	0.085	0.082	0.18	0.12	0.12	0.077	0.088
S (%)	0.16	0.14	0.12	0.12	0.13	0.12	0.11	0.14	0.17	0.11	0.11	0.12	0.09
Si (%)	1.4	0.98	1.7	1.2	1.2	2.4	1.9	1.8	1.1	1.2	1.2	1.1	0.93
Cd (mg/kg)	0.26	0.14	0.17	0.11	0.16	0.20	0.15	0.24	0.047	0.10	0.097	0.20	0.097

The average dilution ratio during a measurement varied from 5 to 400. If the ejector capillary clogged too fast a smaller dilution was obtained by changing the ejector capillary. By inserting the ejector in the duct with the axis at an angle of ~ 130° to the direction of the gas flow, it is

ensured that the largest particles are filtered from the sample line by inertial forces while the sub-micrometer particles are sampled undisturbed (Vincent, 1989). This pre-filtering is necessary in order to avoid overloading of the impactor by large particles. With the conditions used in the experiments a cut-off diameter of ~2.5 μm for the pre-filtering is obtained (Nielsen *et al.*, 2002). The entire sampling setup is shown in Figure 57.
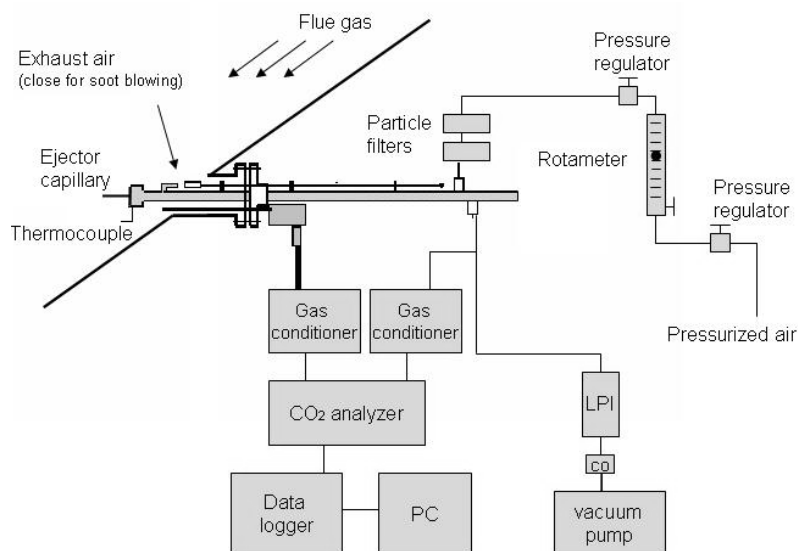
Figure 57. *Setup for aerosol measurements with ejector-diluter and low-pressure cascade impactor.*

Deposited particles in the impactor are collected on aluminum foils. To reduce rebounce of particles, the foils are coated with a thin film of Apiezon H grease using a dilute toluene solution of the grease. The weight gain from the deposited particles was determined with a Sartorius M5D-000V001 micro balance. The LPI is thermostated at 60ºC during measurements to avoid water condensation from the flue gas. The change in cut-diameters of the impactor stages affected by the temperature change is calculated assuming constant values of the Stokes number (cf. Valmari *et al.* (1998)). Tygon tubes were used between ejector and LPI to avoid deposition due to static electrical charges. The sampling time for a measurement was adjusted in order to achieve a suitable amount of deposits. In most cases 30 minutes proved adequate. In some runs plugging of the ejector capillary occurred quite rapidly. However, frequent soot-blowing of the capillary sufficed to keep the ejector functioning in all runs. In between runs the ejector was withdrawn from the flue gas duct and cleaned with water and ethanol. The CO_2 analyzer was calibrated daily (for every second run).

Deposits on impactor foils were analyzed by electron dispersive X-ray spectroscopy (EDS) and scanning electron microscopy (SEM) for chemical composition and particle morphology. In the first sample scan the analysis included all elements from Na and above. From this scan the elements of interest were chosen and later analysis did only include these. No problems with overlapping peaks from elements (Na-Pb etc.) were encountered. The light elements were not corrected for. Some content of C could influence the results, but to correct for this would require a carbon-analysis. The detector is a Li drifted silicon crystal detector.

4. 2. 3   Laboratory measurements

In an investigation run parallel to the field measurements, the six sorbents were tested in a bench scale tubular furnace in the laboratory. The furnace is called the laminar flow aerosol condenser and is described in more details in Chapter 2. The setup is shown in Figure 58.
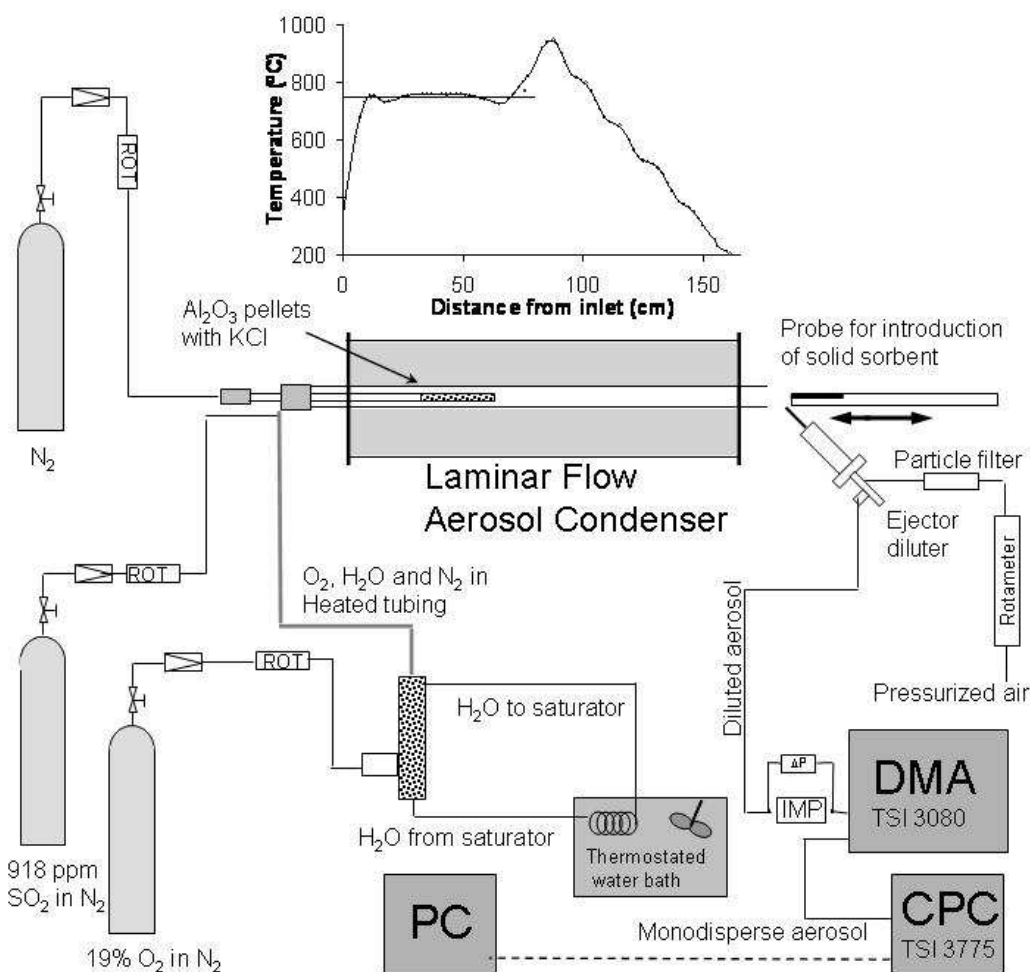
Figure 58. *Laminar flow aerosol condenser (LFAC) used to test the sorbents in the laboratory. Aerosols are sampled using an ejector-diluter and analyzed using a differential mobility analyzer (DMA) and a condensation particle counter (CPC). Above the furnace is shown the measured axial temperature profile used in the LFAC.*

The furnace is provided with a multi-zone temperature control, by means of which a predetermined axial temperature profile can be imposed on a cylindrical, ceramic tubular reactor.

A synthetic flue gas consisting of $KCl_{(g)}$ (200 ppm), SO_2 (50 ppm), H_2O (5%), and O_2 (5%) in nitrogen was passed through the reactor. By mean of the selected temperature profile (cf. Figure

58) the flue gas is heated to 950°C and then cooled with an average cooling rate of ~500°C/s decreasing to ~350°C/s when the gas is cooled to 500°C. KCl is fed by passing an inert gas through a packed bed of alumina pellets impregnated with the salt. The inlet concentration is controlled by adjusting the temperature of the saturator zone of the furnace. As the gas passes the reactor, an aerosol of small chloride and sulphate particles is formed by mechanisms similar to those forming the combustion aerosol of the field study. The size distribution of the nucleated particles in the effluent aerosol from the reactor is measured with a scanning mobility particle sizer (SMPS), which includes a differential mobility analyzer (TSI, Long DMA, model 3081) and a condensation particle counter (TSI, CPC, model 3775) with a size range from 14-800 nm.

To study the influence of the sorbents a specially designed probe[7] containing sorbent powder was inserted into the furnace. The furnace was kept in a horizontal position since the sorbent is placed in a long steel-cup to obtain a large contact area between powder and gas. The probe is placed centrally along the reactor axis and allows contact between gas and sorbent particles in the temperature range 900°C to 500°C. The sorbent probe was inserted cold into the hot furnace and particle size distributions were measured repeatedly after insertion. The temperature of the sorbent particles as measured by a thin thermocouple imbedded in the sorbent particles attains the temperature of the surrounding gas in 2-3 minutes. The size distribution stabilized after approximately 6 minutes except when ammonium sulphate was tested. Reference measurement were made with an empty probe inserted in the reactor to ensure that the conditions for sorbent and reference runs were the same. The particle size distribution is heavily affected by the presence of the probe. The steel surface of the probe seems to catalyze the oxidation of SO_2 and thereby increase the number of particles formed. All sorbents were tested using the same experimental conditions, i.e. residence time, temperature, flue gas composition etc.

4. 3   Results and discussion

Figure 59 shows the mass-based size distributions for all twelve runs of the field measurements. Each distribution curve is the mean of 2 or 3 measurements. As shown by the standard deviations, the reproducibility of the measured distributions is satisfactory. The mass concentrations of particles with an aerodynamic diameter less that 2.5 μm, i.e. $PM_{2.5}$ are computed from the distributions of Figure 59 and summarized in Table 10.

The main part of the particle size distribution lies below 2 μm. For this reason small variations in the cut-off diameter around 3 μm due to variations in dilution ratio have a minor importance for the results. The dilution ratio did evidently not have a considerable effect on the results. The numerous reference measurements are made with very different dilution ratios (5-180) and the results are very similar as seen by the error bars in Figure 59. The variation between the results does not correlate with the dilution ratio. For the field measurements the mass and number concentrations in Table 10 and the particle size distributions in Figure 59 clearly show that the addition of ammonium sulphate, monocalcium phosphate, clay, ICA5000, and Bentonite leads to

---

7 The probe was made of stainless steal by Henning Koldbech. It is basically just a long spoon, which is stabilized to withstand the mechanical strain at high temperatures.

a large reduction in the mass load of particles, whereas the addition of chalk increases the mass concentration of fine particles by more than 30%.
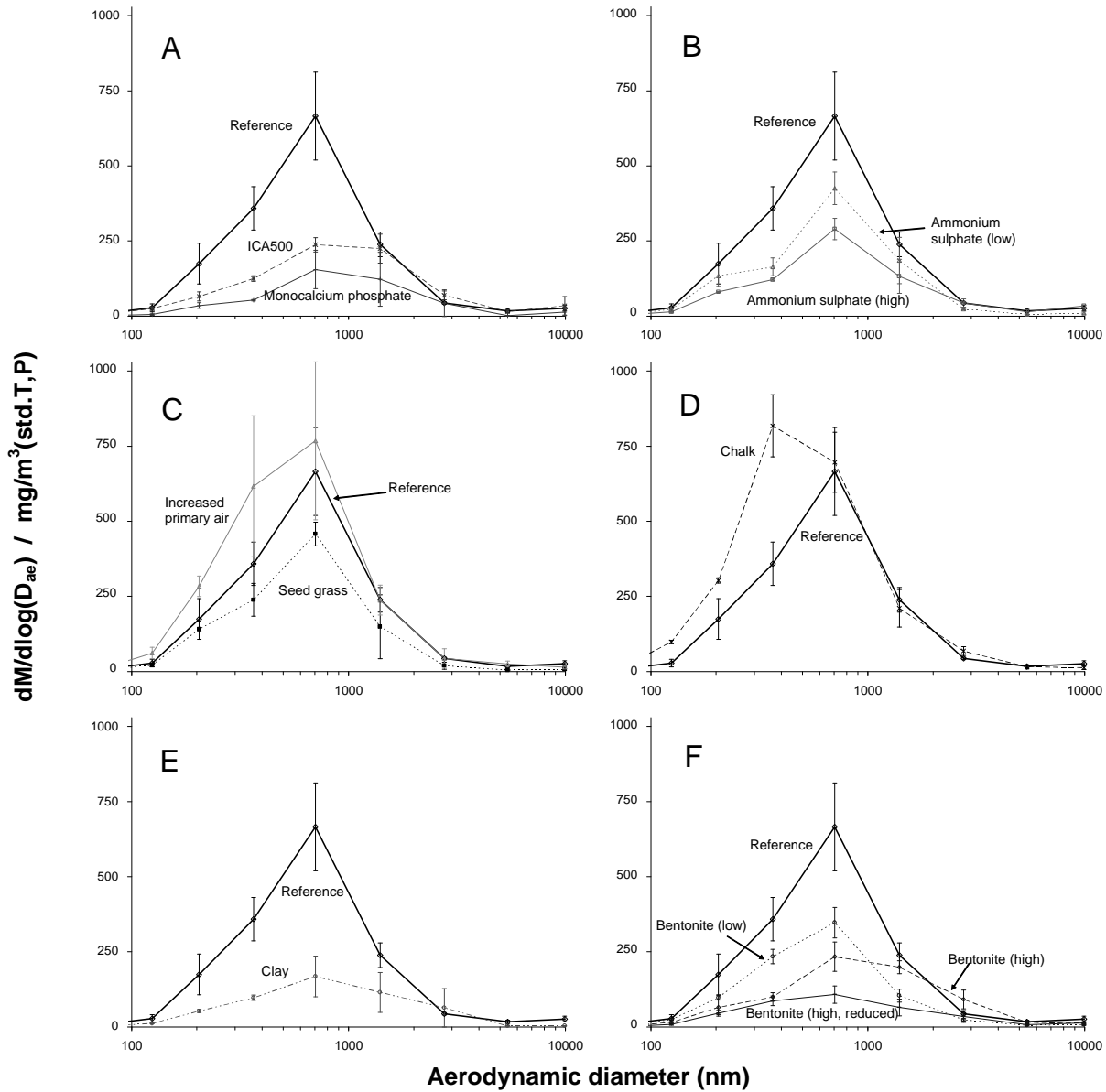
Figure 59. *Mass-based size distributions from measurements by cascade impactor. The reference run is show together with: A) the sorbents ICA5000 and monocalcium phosphate, B) the sorbent ammonium sulphate in high and low feeding rate, C) combustion of grass and run with increased primary air inlet, D) the sorbent chalk, E) the sorbent clay, and F) the sorbent Bentonite with high and low feeding rate and with reduced load on the boiler. The vertical bars show the standard deviations of repeated measurements. All flue gas concentrations are converted to a reference state of dry gas at atmospheric pressure, 0 °C, and 6% O_2. All the measured distributions are shown in Appendix E.*

Table 10. *PM$_{2.5}$ values from full-scale and laboratory measurements and number concentrations from the laboratory measurements*

	Run:	Reference	Seed grass	Incr.d primary air	ICA5000	Moncalc. Phosph.	Bentonite, low	Bentonite, high	Bentonite, high, red.	clay	Chalk	Amm. sulph., high	Amm. sulph., low
Full-scale	PM$_{2.5}$ (mg/m^3) ±std.dev.	390 ±66	260 ±38	510 ±34	204 ±27	110 ±56	211 ±26	192 ±40	91 ±29	134 ±25	482 ±60	121 ±27	165 ±50
	Relative to ref. (%)	100	67	131	52	28	54	49	23	34	123	31	42
LFAC mass	PM$_{2.5}$ (mg/m^3)	38.3			29.0	30.5		20.5		21.8	106	1400	
	Relative to ref. (%)	100			80	80		50		60	280	3660	
LFAC number	#conc. (10^7/cm^3)	0.33			0.38	4.5		5.2		0.48	6.8	10.6	
	Relative to ref. (%)	100			115	136		1580		145	2060	3200	

For ammonium sulphate, monocalcium phosphate, Bentonite, ICA5000, and clay the addition of sorbents reduces the PM$_{2.5}$ by 50% or more. For Bentonite and ammonium sulphate it is noteworthy that a doubling of the sorbent feed rate only leads to a 5-10% reduction in the PM$_{2.5}$ concentration. The chemical composition of the fine particles as a function of particle size is shown in Figure 60. The composition is determined in the range 0.12 – 10 μm. The mass of particles collected with diameters above 2 μm is very low due to the cut-diameter of the inlet to the ejector. The collected mass is assumed to represent the composition of particles in this diameter range. The deviations for the coarse particles are probably caused by single-particle analysis and because the electron beam only analyzes the top 1-2 μm of the sample. All analyzed particle deposits contain high amounts of potassium and chlorine. Phosphorous and sulphur are present in all runs, but in varying amounts. The content is distributed evenly on all particle sizes in most cases. For the individual runs the following specific observations are noted: The Bentonite run has a low level of sulphur and phosphorous. The monocalcium phosphate run has a high level of phosphorous and a low level of sulphur. The clay run has an increased level of phosphorous. The run with ICA5000 shows a surprisingly high level of silicium even in the

smallest particles. The composition of the particles from the reference run (wheat) and the seed grass run are quite similar except for the fact that the seed grass run has an increased level of phosphorous.
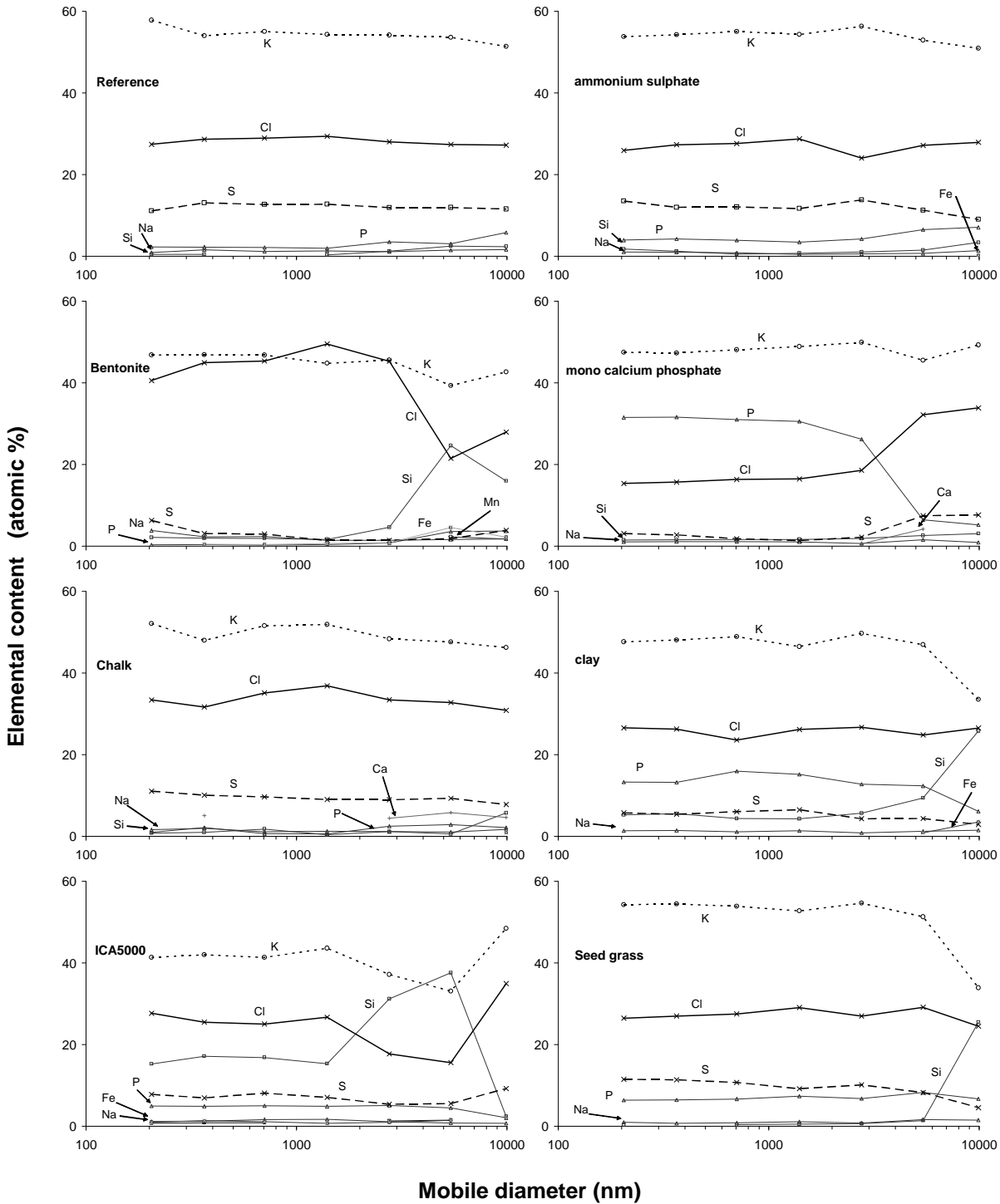
Figure 60. *Chemical composition of fine particles determined by EDS.*

The particle size distribution and the even size distribution of the elements allow us to conclude that the main components of the $PM_{2.5}$ fraction and in particular the elements potassium, chlorine, sulphur, and phosphorous primarily are formed by condensation of volatile species from the flue gas during passage through the heat exchangers from boiler to the sample point. The conclusion is supported by previous investigations of aerosols from straw combustion showing similar behavior of these four elements (e.g. Christensen *et al.*, 1998; Jimenez and Ballester, 2004). The variation of the phosphorous level in the particles is caused by variation in the content of volatile phosphorous species in fuel and/or sorbent, which is evident in the case of seed grass fuel (cf. Table 9) and the phosphate sorbent. While potassium and chlorine arises from the volatilization of the fuel ash component KCl at the high temperatures in the boiler, there is solid evidence to prove that sulphur in the particles originates from K_2SO_4 formed in the flue gas by the reversible gas phase sulphation reaction (2) (Glarborg and Marshall, 2005). Therefore, the variation of the sulphur level in the particles, is influenced by the extent of the chemical conversion of the sulphation reaction and is further analyzed below. The mass-based particle size distributions measured at the outlet of the reactor during the laboratory investigation are shown in Figure 61. The primary data from the SMPS-analyzer yields the number-based size distribution, which has been converted to the mass-based size distribution in Figure 61, assuming that all particles are spherical with a density of 2.0 g/cm³ (the value for pure KCl). The curves of Figure 61 show that the presence of sorbents in the laboratory reactor affects the effluent particle distribution. For monocalcium phosphate, Bentonite, ICA5000, and clay the particle mass concentration is clearly reduced and the particle size is shifted towards smaller particles.

The total dust content of the flue gas was sampled by filter methods. The filter probe was designed for iso-kinetic sampling and for traversing of flue gas ducts.[8] The experimental time schedule only allowed time for sampling at very few locations and the sampling of coarse particles was probably not representative for the flue gas due to the stratification of the coarse particles. However, the results from the chemical analysis of filter samples from the different runs are shown in Table 11. No sample was taken during the run with addition of chalk.

Comparison of the chemical composition of the total filter samples with the composition of the fine particles show that the elements K, Cl, and S are enriched in the fine particles. It is also interesting to se that the content of these elements in the reference sample is lower than in the runs with addition of sorbents. This suggests that the sorbents remove the main components of the aerosol particles from the gas phase and capture them in the coarse particles. This is very beneficial since the coarse particles can be removed by the use of gas cleaning of the flue gases. However, due to the lack of traversing during the measurements and due to the large deviations in the determined total dust contents the lower content in the reference sample could be caused by a difference in the sampling. The same is possible for the huge deviation for the clay run.

It is remarkable that chalk increases the mass concentration and indeed leads to a decrease in particle size, evidently due to the formation of many new particles. The total particle mass concentration for the laboratory runs are shown in Table 10. It is remarkably clear from Table 10 and Figure 61 that the laboratory study for the sorbents monocalcium phosphate, Bentonite, ICA5000, clay, and chalk qualitatively agrees with the tendencies of the field measurements. This is not the case for ammonium sulphate. This sorbent evaporates too fast for the used feeding technique to be adequate for this study.

---

[8] The probe was borrowed with permission from Morten Thellefsen Nielsen at Haldor Topsøe A/S.

Table 11. *Total dust concentrations and chemical composition of total dust deposits from filter samples. The dust is sampled at the entrance to the baghouse filter. The samples are analyzed with ICP-OES. Si is not included since this component is found in the filter material. The standard deviation between samples for runs with multiple samples are shown for the dust concentration. No value for the concentration of ICA5000 is shown since the gas flow was not determined correctly in this case*

Parameter	Reference	Monocalcium phosphate	Bentonite, high	Bentonite, low	Ammonium sulphate, high	Ammonium sulphate, low	ICA5000	Clay	Increased primary air	Seed grass
Total dust concentration										
± standard deviation (mg/m^3(std. T,P))	748± 199	577± 11	749± 165	274± 69	656± 85	569± 141	n.d.	483	583	469
% PM$_{2.5}$ in total dust	52	19	26	77	19	29	n.d.	28	88	55
Al (%)	-	-	-	-	-	-	0.3	7.6	-	-
Ca (%)	-	0.24	-	-	-	-	-	-	-	-
K (%)	21	41	20	31	41	41	41	11	42	27
Na (%)	0.41	0.63	1.4	0.56	0.4	0.64	1.5	1.4	0.74	1.2
P (%)	1.5	3.6	2.9	11	2.8	3.9	3.8	1.9	2.3	5.3
Cl (%)	9.3	20	8.4	15	12	18	25	1.9	20	20
S (%)	1.1	6.4	1.7	1.3	10	7.4	6.1	0.52	7.6	5.5
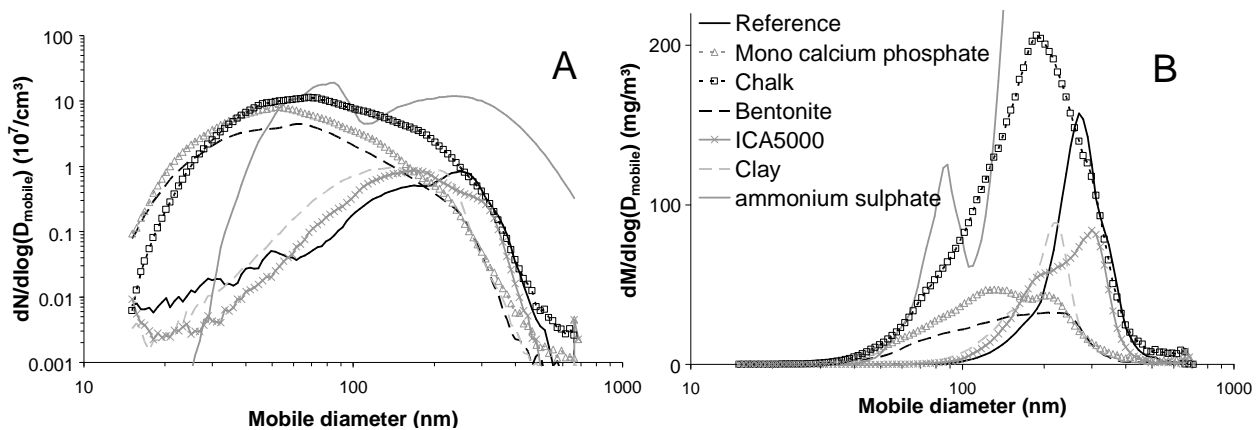
Figure 61. *Particle size distributions from experiments in a laboratory furnace. The data is collected when the probe temperature is steady (after 6 minutes). A: The number-based size distribution and B: The mass-based size distribution derived from the number-based ones. The mass-based size distribution for the ammonium sulphate run is out of scale above 200 nm.*

4. 3. 1 Effect of fuel ash composition

The concentration of PM$_{2.5}$-particles depends on the content of volatile species in the fuel ash, in particular the content of potassium (Wiinikka and Gebart, 2005; Christensen *et al.*, 1998). For practical reasons it is impossible to control the ash composition prior to combustion and part of

the variation of the $PM_{2.5}$ may therefore be explained by ash variations. Figure 62, which shows a plot of $PM_{2.5}$ versus potassium content for all runs of the field study, indicates a correlation between the two parameters, but the correlation is overshadowed by the particular influence of the addition of sorbents. The two fuel samples taken from reference runs vary considerably in composition, but are not correlated with $PM_{2.5}$. In the run with chalk addition the inorganic content is high and this could explain some of the increase in $PM_{2.5}$. Only one other run with sorbent addition is made with a high content of potassium. This is a run with Bentonite addition. $PM_{2.5}$ for this run is lowered compared to the reference runs. All other runs with sorbent addition show a lowered $PM_{2.5}$ value compared to the reference, but all are made during combustion with a low fuel content of potassium.

It is impossible to exclude the effect of fuel composition of the differences in $PM_{2.5}$ obtained from different runs. However, the effects of the sorbents observed in the laboratory measurements using the laminar flow aerosol condenser confirm the full-scale findings with strong effects of sorbent addition on the aerosol formation. The only exception is the sorbent ammonium sulphate where the feeding mechanism in the laboratory setup gives too high feeding rates of sorbent.
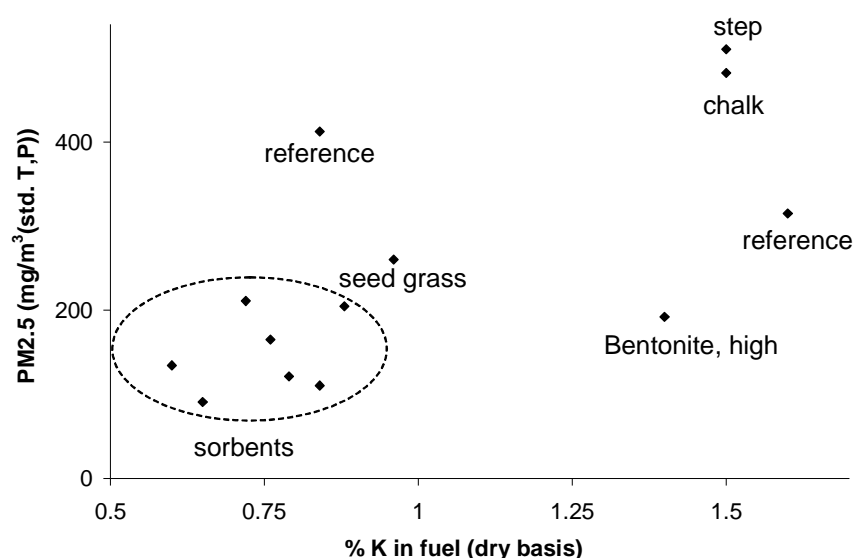
Figure 62. *$PM_{2.5}$ vs. fuel content of K. The fuel content of K, Cl, and S varies considerably. It is not possible to make a clear correlation between fuel composition and $PM_{2.5}$. In the two reference runs the largest $PM_{2.5}$ is found with the lower K content.*

The results from investigations of the six sorbents by field measurements and the laboratory investigation are discussed in the following sections.

4. 3. 2   Ammonium sulphate

Ammonium sulphate $(NH_4)_2SO_4$ is added to increase the sulphation of alkali chloride in order to minimize the chlorine content of the deposits. The sorbent dissociate and react with KCl to form sulphate (Henderson *et al.*, 2006).

$$(NH_4)_2SO_4 \rightarrow 2NH_3 + SO_3 + H_2O \tag{59}$$

$$2KCl + H_2O + SO_3 \leftrightarrow K_2SO_4 + 2HCl \tag{60}$$
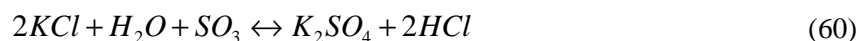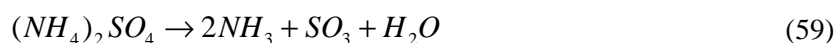
The effect of the ammonium sulphate addition is a reduction of the mass concentration of $PM_{2.5}$ to 42% of the reference level with the lowest feeding rate and 31% with the highest feeding rate. It is somewhat surprising that the addition of sulphate does not lead to an increased ratio of sulphate to chloride in the fine particles in agreement with the effect of an increased SO_2 concentration observed by Jimenez and Ballester (2005b). The effect of ammonium sulphate in the field measurements needs further investigation and the explanation offered here must be quite speculative: It is recognized that the rate limiting step for sulphation by reaction (61) is the oxidation of SO_2 (Glarborg and Marshall, 2005). The release of SO_3 to the gas phase at high temperature will cause a rapid formation of $K_2SO_{4(g)}$. The sulphate has a much lower vapor pressure than the chloride and hence forms small particles by nucleation much earlier in the process. Measurements by iso-kinetic sampling of the total dust load in the flue gas channel shows that the $PM_{2.5}$ fraction comprises in the order of 20-50% of the total dust load.

The formation of fine particles of sulphate at high temperatures allows longer time for transferring alkali to the coarse particles by scavenging of the fine particles and thus reduces the amount of alkali available for the fine particles. The scavenging effect of the coarse particles is absent in the laboratory measurements where ammonium sulphate yields a huge increase in the particle mass and number concentration, since no coarse particles are present. Also, the feeding technique of the sorbent in the laboratory cause high release of this sorbent due to its low vapor pressure. Ammonium sulphate is recognized to be a good sorbent for the reduction of corrosion and aerosol formation (Henderson *et al.*, 2006). However, its beneficial effects are obtained at the expense of an increased level of SO_2 emission. The increased level of P in the fine particles is probably caused by an increased content in the fuel during this run. The fuel-content of P was almost doubled in this run.

4. 3. 3   Monocalcium phosphate

Monocalcium phosphate (or calcium dihydrogen phosphate, $Ca(H_2PO_4)_2$) is added to the boiler to capture the alkali metals as phosphates and thus to reduce the content of chlorine in the deposits. The field measurements support this effect since the $PM_{2.5}$ is reduced to 28% of the reference value. However, the sorbent evidently releases volatile phosphorous species, which are transferred to the fine particles of which more than 30% consist of P. The laboratory measurements also show both effects of the phosphate. The mass concentration of aerosol particles decreases to 80% of the reference value, whereas the number concentration is considerably increased, which indicates a change in formation mechanism resulting in formation of new particles by homogeneous nucleation of phosphate.

4. 3. 4   Bentonite

Bentonite (containing mainly montmorillonite $(Na,Ca)_{0.33}(Al,Mg)_2Si_4O_{10}(OH)_2 \cdot nH_2O$) is added to the boiler to capture alkali and bind it into oxides with Al and Si. The observed reduction of the aerosol mass concentration is considerable. With the lowest feeding rate of sorbent a reduction to 54% is obtained and 49% with the highest. In the run with 85% load on the boiler and a high feeding rate of Bentonite ('Bentonite, high, reduced load') $PM_{2.5}$ is reduced to 23%. This is probably partly due to a lower combustion temperature when reducing the load on the boiler. The lower temperature decreases the degree of potassium release from the fuel. In some parts of the fuel bed the temperature measured by IR was below 900°C. At these low temperatures the release of potassium is dependent on the temperature (Knudsen *et al.*, 2004b). The sulphur concentration in the fine particles when adding Bentonite is very low. The particles are almost composed of pure KCl. The cubic shaped, crystalline particles observed on the SEM micrograph reflect this fact. These are compared to the particles sampled during a reference run in Figure 63. The particles from all the runs are shown in Appendix E.
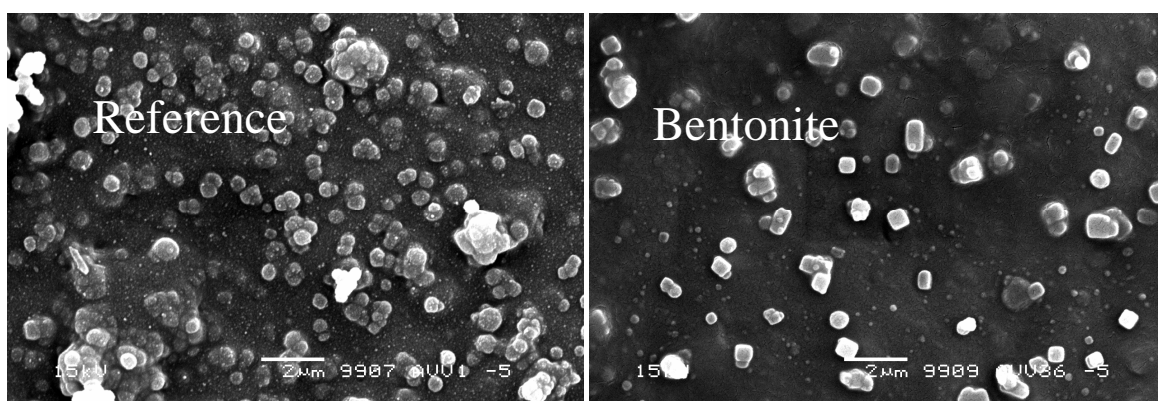
Figure 63. *SEM micrographs of particle deposits from reference run and run with Bentonite addition. The deposits are from the fifth stage of the impactor and thus their aerodynamic geometric mean diameter is 705 nm.*

The laboratory measurements show a reduction in the aerosol mass concentration by 45% while the number concentration increases by a factor of eight. The reduced mass concentration is caused by alkali capture from the gas phase, which causes the homogeneous nucleation to occur at a lower temperature. This might be the reason for the higher particle concentration and smaller particle diameters observed for this sorbent. The higher particle number concentrations when nucleation takes place at lower temperatures was also found for KCl in Chapter 2.

4. 3. 5   ICA5000

This sorbent (mainly composed of oxides of Si, Al and Fe) is added to the boiler to capture alkali metals in compounds with high melting points. The $PM_{2.5}$ concentration was reduced to 52%

when this sorbent was used. The chemical composition of the fine particles shows a small reduction in sulphur content, while the presence of 15-30% Si indicates that some fine sorbent particles are present in this size range. The content of Si in the fine particles must be due to release of Si to the gas phase from the sorbent. The laboratory measurements show a reduction in aerosol mass concentration (to 80%) and a small increase in number concentration (16%). The effect of this sorbent was weaker than for Bentonite and clay. This could possibly be due to the larger particle diameter for this sorbent, which provides a smaller contact area for gas phase adsorption of alkali.

4. 3. 6   Clay

As ICA5000, this sorbent (mainly composed of oxides of Si, Al and Fe) is added to the boiler to capture alkali metals in compounds with high melting points. $PM_{2.5}$ was reduced to 34% and the amount of sulphur in the fine particles is lowered while more than 10% P is observed. The laboratory test of the sorbent shows a reduction to 60% of fine particle mass concentration and a 48% increase in number concentration. The effect on particle diameter is less pronounced than for Bentonite. The results from all the runs with Si and Al rich sorbents (Bentonite, ICA500 and clay) show reduction of aerosol mass concentrations in both full-scale and in the laboratory reactor. In the laboratory reactor the number concentration increases as a result of the addition of these sorbents, probably because the homogeneous nucleation takes place at a lower temperature. As for the ammonium sulphate run the increased level of P in the fine particles is probably caused by an increased content of this element in the fuel. The fuel-content of P was more than doubled during this run.

4. 3. 7   Chalk

Chalk (limestone, $CaCO_3$) is added to some boilers to reduce the emissions of sulphur oxides. In this campaign the effect on aerosol formation was studied. The sorbent was entrained in the flue gas flow, since no considerable increase in Ca is seen in the slag during this run (from 7.2 to 8.2% (w/w)) while the amount of Ca in the baghouse filter was five doubled (from 0.7 to 3.7% (w/w)). $PM_{2.5}$ was increased by more than 30%. The sulphur content of the fine particles was slightly reduced compared to the reference run. The increase in $PM_{2.5}$ can not be explained by sampling fine sorbent particles. A small amount of Ca was observed only in the particles larger than 2 µm. The concentration of SO_2 in the flue gas was reduced from 39 ppm to 26 ppm. The increase in $PM_{2.5}$ could be caused by a capture of Si by Ca in $Ca_3Si_2O_7$. The Si from the fuel captures part of the alkali from the gas phase. When Si binds to Ca a larger amount of alkali is available for deposit and aerosol formation. This capture of Si is favored at high temperatures (Lang *et al*., 2006). However, a similar effect on the fine particle size distribution as found in the full-scale experiments is found when adding chalk to the synthetic flue gas free of particles and Si. The mass concentration in the laboratory investigation was increased almost 3 times while the number concentration increased 20 times and the average particle diameter was reduced considerably. The smaller particle diameter suggests that the sorbent changes the nucleation mechanism in this case. Chalk can not be recommended as a sorbent when considering the effects observed here on aerosol formation.

90

4. 3. 8   Chemical equilibrium

Due to the sulphation of chloride at high temperature by reaction (61) the concentrations of SO_2 and HCl are mutually dependent. If equilibrium is reached in the flue gas before it is cooled the two concentrations will be correlated by the equilibrium expression for the reaction. The measured concentrations of SO_2 are plotted against the measured concentrations of HCl in Figure 64.
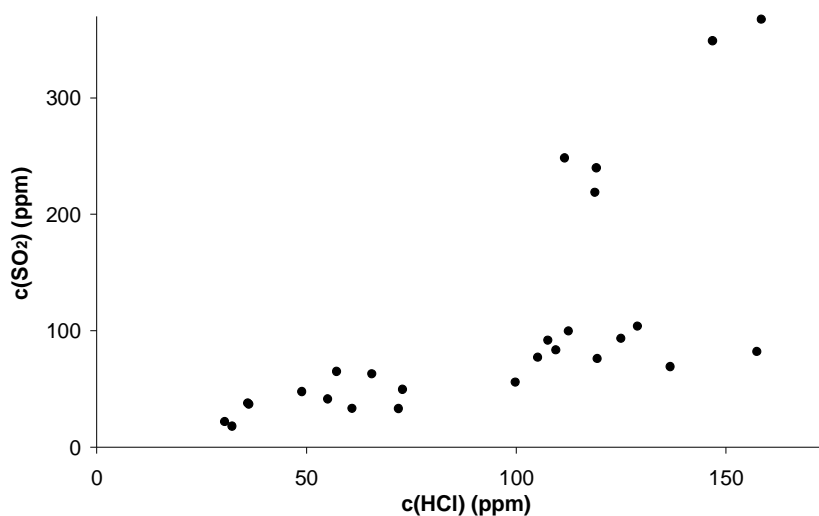
Figure 64. *The concentrations of SO_2 plotted versus the concentrations of HCl from the individual runs. The points with very high SO_2 concentrations are from runs with addition of ammonium sulphate.*

The composition of the fine particles has been determined by EDS. Most aerosols from biomass combustion are composed mainly of KCl and K_2SO_4. The molar ratio between S and Cl in the fine particles has been calculated at different aerodynamic diameters for all runs with sorbents (for Bentonite and Ammonium sulphate the runs with the highest feeding rates are used) and for the run with seed grass combustion. The ratios are shown in Figure 65.

It is seen that most sorbents lower the S/Cl ratio. The sorbents do not capture sulphur (the SO_2 concentration is increased during these runs) and the change of S/Cl ratio must be caused by a change in the equilibrium described by (61) when potassium is captured.

Reaction (60) is quenched when the flue gas is cooled. It is tested whether the composition of flue gas and particles follow the 'Quenched equilibrium theory' described by Christensen *et al.* (1998).
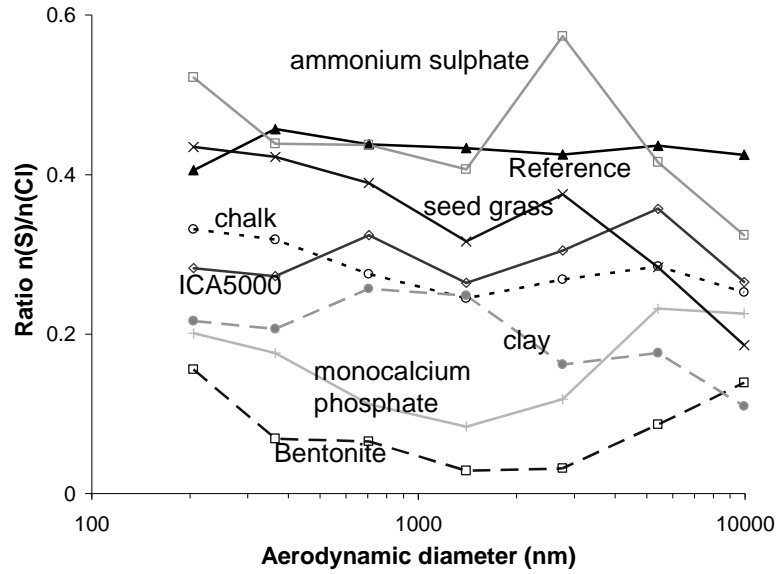
Figure 65. *Ratio between sulphur and chlorine content in the fine particles in different particle sizes.*

In this theory equilibrium between KCl and K_2SO_4 is reached at 812°C and subsequently quenched. The gas phase salts are then condensed, but the composition is described by the high temperature equilibrium. The equilibrium is given by

$$\frac{[K_2SO_4]_g \cdot [HCl]^2}{[SO_2] \cdot [KCl]_g^2} = K_{eq}[H_2O] \cdot [O_2]^{1\!/\!2} = K_{eq}^{'}$$ (61)

Since the activities of water and oxygen are almost constant the equilibrium constant $K_{eq}^{'}=0.25$ is used. Elemental balances are introduced

$$\begin{aligned} 2y_1 + y_3 &= e_K \\ y_3 + y_4 &= e_{Cl} \\ y_1 + y_2 &= e_S \end{aligned}$$ (62)

where $y_1 = [K_2SO_4]_g$, $y_2 = [SO_2]$, $y_3 = [KCl]_g$ and $y_1 = [HCl]$. Combining (61) and (62) gives:

$$y_2 = \frac{e_S}{K_{eq}^{'}\left(\frac{e_{Cl}}{y_4}\right)^2 - 2K_{eq}^{'}\left(\frac{e_{Cl}}{y_4}\right)+1+K_{eq}^{'}}$$ (63)

Values for the total chlorine and sulphur content are fitted to experimental data and the SO_2 concentrations calculated by the equilibrium are plotted together with the experimental data. In Figure 66 the calculated and experimental data are shown together. The calculated concentrations are shown with and without including the effect of fuel and additive composition. The calculation without inclusion of the fuel and sorbent composition is shown as a curve. This curve does totally fail to represent the run with addition of ammonium sulphate.
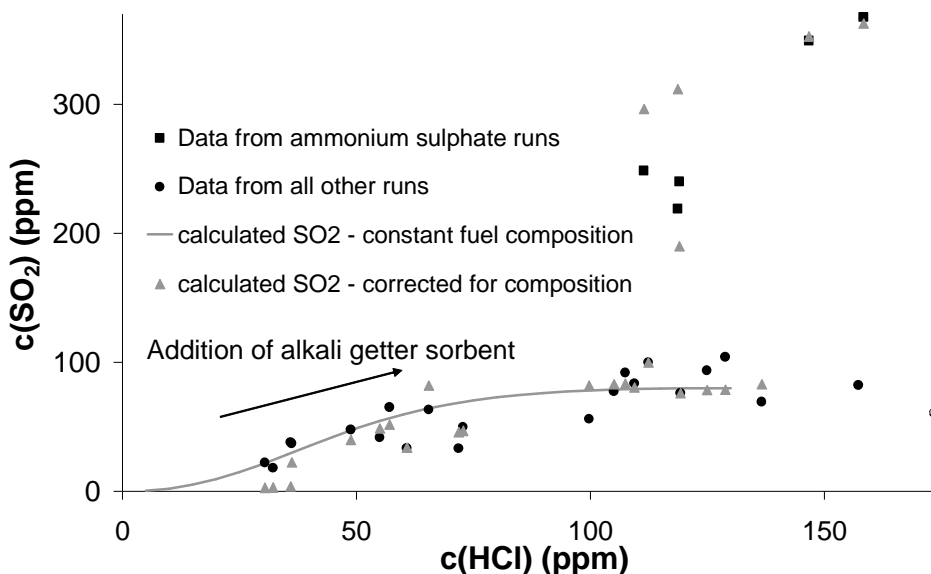
Figure 66. *Parity diagram depicting the measured versus the calculated concentrations of SO_2 from the individual runs. The experimental data are the same as shown in Figure 64.*

The agreement is very good when the composition of fuel and additive are taken into account. In Figure 67 the experimental data and the calculated values are compared for this case.
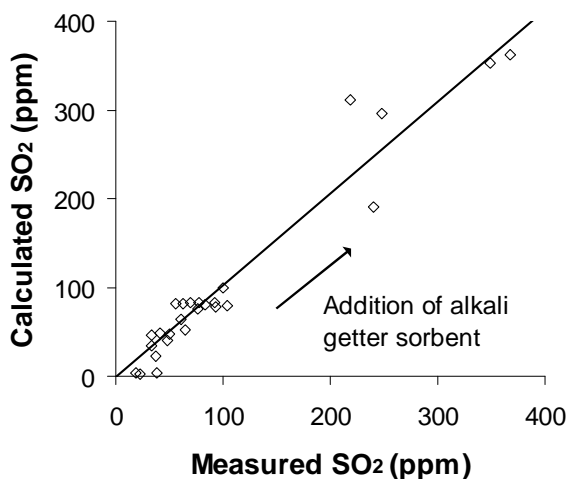
Figure 67. *Parity diagram depicting the measured versus the calculated concentrations of SO_2 from the individual runs.*

Average values of e_{Cl} and e_S are obtained by a least square fit of the calculated SO_2 concentrations to the experimental values. The total chlorine and sulphur amounts obtained by using this method are e_{Cl} =231 ppm and e_S =92 ppm. The fuel and sorbent contents of Cl and S in the individual runs are compared to the average content and e_{Cl} and e_S are multiplied by these ratios. The good agreement between calculated concentrations and experimental data suggest that equilibrium is reached in the gas phase before the formation of fine particles.

The particle compositions are analyzed in a similar way. Combining equation (59) and (60) to eliminate y_2, y_3, and y_4 gives:

$$K'_{eq} = \frac{\dfrac{y_1}{e_K}\left(\dfrac{e_{Cl}}{e_K}-1+\dfrac{2y_1}{e_K}\right)^2}{\left(\dfrac{e_S}{e_K}-\dfrac{y_1}{e_K}\right)\left(1-\dfrac{2y_1}{e_K}\right)^2} \tag{64}$$

The total amount of chlorine and sulphur determined from the reference run and the equilibrium constant suggested by Christensen *et al.* (1998) are now used. The ratio between S and Cl is calculated by solving equation (64). From the measured chemical compositions and the amounts of fine particles the reduction in potassium is determined. A plot of the molar chlorine to sulphur ratio as a function of the amount of potassium is given in Figure 68. The amount of potassium is scaled as the reduction in total potassium compared to the amount at the reference run:.

$$\% \text{ K-removal} = \left(1-\frac{e_K}{e_{K,\,reference}}\right)\cdot 100\% \tag{65}$$
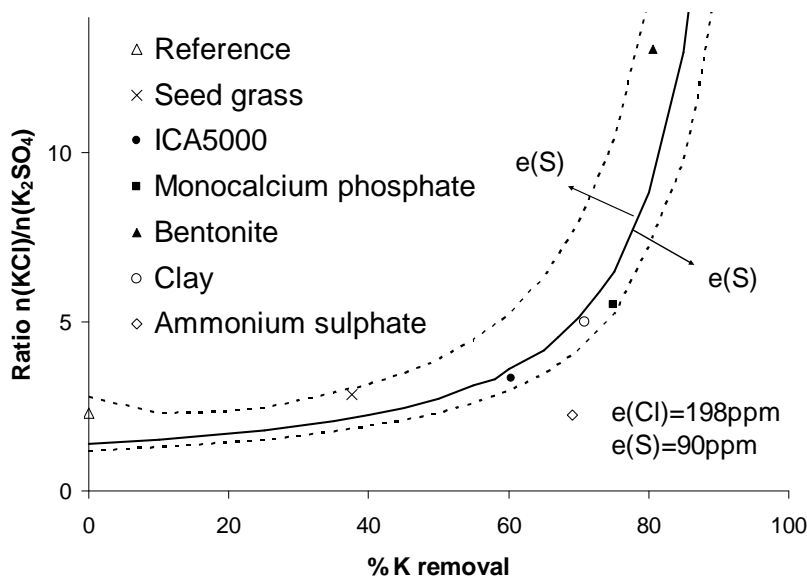
Figure 68. *The molar ratio between potassium chloride and potassium sulphate. The curves are calculated based on the gas phase equilibrium described by Christensen et al. (1998) at 812 °C. The points represent the experimentally found molar ratios measured in the fine particles from individual runs. For e(Cl) and e(S) the values from the reference run are used. The dotted lines represents the prediction when the value of e(S) is varied +/- 25%.*

A good agreement between the experimental values from particle compositions and the curves resulting from gas phase calculations using the 'Quenched equilibrium theory' is found. This suggests that the main influence on the particle formation from adding sorbent is an adjustment of the alkali concentration in the gas phase with a resulting change in the gas phase equilibrium at high temperatures. This calculation is not corrected for variations in chemical composition of fuel and sorbent.

4. 4   Conclusion

The observations in the field measurements show a large reduction in the aerosol formation for five of six studied sorbents. These findings are corroborated by a laboratory study of the fine particle formation during addition of the same sorbents. The laboratory study qualitatively supported the full-scale findings.

The mineral-based sorbents; Bentonite, ICA5000, and clay reduced the mass concentration of aerosol particles. These sorbents reduce the potassium content of the flue gas and thereby shifts the equilibrium between potassium chloride and sulphate toward more chloride. The depletion of alkali from the gas phase delay the homogeneous nucleation of sulphate particles to lower temperature and increases the particle number concentration. Addition of monocalcium phosphate also lowered aerosol mass concentrations. This sorbent evaporates in the boiler and the phosphate binds potassium. Some of this adsorbs to coarse particles before fine particles are formed. The fine particles have a high content of P indicating a changed formation mechanism with nucleation of potassium phosphate. Addition of ammonium sulphate decreases the aerosol mass concentration. The sorbent decomposes and increases the SO_2 and SO_3 concentration and thus the degree of sulphation. The decrease in fine particle mass load is probably caused by heterogeneous condensation of vapors on coarse particles similar to the case with monocalcium phosphate. Addition of chalk as a sorbent decreases the sulphur content of the flue gas slightly but increases the aerosol mass concentration considerably in both full-scale and laboratory experiments. It is not clear why this sorbent increases particle mass and number concentrations. In general the alkali-getter sorbents Bentonite, ICA5000, clay, monocalcium phosphate, and ammonium sulphate can be recommended from an aerosol-reduction viewpoint. They all reduce mass loads of fine particles. Ammonium sulphate increases the level of SO_2 that has to be removed to avoid emissions. Chalk is used to reduce sulphur emissions, but is not recommended when considering the negative effects on aerosol formation.

A considerable variation is observed from run to run for the gas concentrations of sulphur dioxide and hydrogen chloride and for the content of sulphate and chloride in the particles. A theoretical analysis of this variation indicates that a chemical equilibrium for the sulphation reaction is established at high temperatures. After cooling the flue gas composition can be described by an equilibrium established at 812°C.

CHAPTER 5   FULL–SCALE COMBUSTION OF WASTE

This chapter covers the results obtained during a full-scale measuring campaign at I/S FASAN waste-to-energy plant in Næstved from 21 August to 8 September 2006. The project was funded by PSO grant 5784. The chapter was used as a draft for the manuscript:

Jacob H. Zeuthen, Anne J. Pedersen, Christian Riber, Thomas Astrup, Jørn Hansen, Flemming Frandsen, and Hans Livbjerg, 'Combustion Aerosols from Municipal Waste Incineration – Effect of Fuel Feedstock and Plant Operation', Combustion Science and Technology, In press.

5. 1   Introduction

The environmental concerns related to waste incineration have increased the focus on stack emissions from municipal waste incinerators. The effects of fuel feedstock and plant operation on the aerosol formation are not well known. In this full-scale measuring campaign the effect of adding well defined waste fractions to a base of standard waste and of introducing changes to the operational conditions to a municipal waste incinerator were studied.

Only few studies on the generation of sub-micrometer particles from waste incineration have been published. Maguhn *et al*. (2003) have reported particle size distribution obtained by SMPS in a plant equipped with electrostatic precipitator, Yoo *et al*. (2002) have reported particle size distributions in stacks from plants with cyclone separators, and Chang *et al*. (2000) have reported mass-based size distributions measured by a cascade impactor in two incinerators.

In this study the particles are sampled with an ejector-diluter upstream from the flue gas cleaning and characterized with cascade impactor, scanning mobility particle sizer, electron microscopy, and energy dispersive X-ray spectroscopy. The stack-aerosol is sampled without dilution and characterized by scanning mobility particle sizer.

5. 2   Experimental

A three-weeks measuring campaign was performed in a 22 MW (thermal energy, 14 MW electric) grate-fired waste incinerator to investigate the effect of changes in the combustion conditions and from addition of different waste fractions to a base-load waste. The base-load waste was a mixture of 80% household waste and 20% small combustibles; a composition close to the mixed municipal solid waste that is incinerated during daily operation of the plant, but with the exclusion of industrial waste fractions. Measurements performed during experiments with the base-load waste at normal operational parameters are termed 'Reference' in this chapter. The special waste fractions all contain elevated concentrations of potential harmful elements, i.e. heavy metals and/or Cl, compared to the base-load waste. The fractions, which were obtained from different recycling facilities in Denmark, comprised the following:

- **PVC plastics**. PVC is the polymer poly(vinyl chloride) and contains large amounts of organically bound Cl. The PVC was collected at recycling stations for special treatment – the entire fraction was plastic but probably not all of this was PVC.

- **Automotive shredder waste**. Residual fraction from industrial shredding of cars for recycling. The residual fraction is normally land-filled as hazardous waste. Shredder waste consists of plastics (rigid and foam), rubber, glass, dirt, and fines that remain after metals and other recyclables have been removed from scrap cars (Boughton and Horvath, 2006). It contains high amounts of Cl (from PVC), alkali metals, and heavy metals. The concentration levels of metals in shredder waste are typically 10 times higher than in municipal solid waste (Zevenhoven and Saeed, 2003).

- **Batteries**. A mixture of different batteries (alkaline, Ni-Cd, Li-ion. etc.) originating from special collection of problematic waste sources separated in private households. Contain high concentrations of heavy metals such as Ni, Cd, Zn, and Hg. Car batteries are not included and no increase in the Pb-level is expected.

- **Impregnated wood**. CCA impregnated wood collected at recycling stations for special treatment. The wood is treated under pressure with solutions containing metal salts of boron, phosphorous, copper, chromium or arsenic. CCA (Chromated Cupper Arsenate) is to date the most widely used wood preservative worldwide, and when the impregnated wood turns into waste at the end of service, the content of Cu, Cr, and As is still high.

- **Shoes**. Sorted from clothes collected from private households for recycling. Leather shoes contain high amounts of Cr, which is added in the leather tanning process.

- **Salt**. Crystalline NaCl for ice control on roads delivered in 25 kg bags. This fraction was added to increase the content of inorganically bound Cl in the waste. Pure salt is obviously not incinerated during regular operation, but is added here to investigate the effect of changing the content of salt in the waste

The special fractions were added to the base-load waste in amounts ranging from 0.5 to 14.2% (w/w) of the total fuel; see
Table 12 for details on base-load waste composition, mixing ratios, and elements of interests for the individual runs. The respective mixing ratios were defined in order to obtain a substantial increase in heavy metal and/or Cl concentrations in the combustion residues, while at the same time ensuring an acceptable heating value of the mixed fuel.

Table 12. *The fraction of the special waste types in the fuel (total load ~9.5 tonnes/hour), the elements of interest in the individual runs, estimate of the chemical composition of the inorganic part of the base-load fuel, and the lower heating value of this. The estimate of the chemical composition is based on previous analysis of Danish household waste and small combustibles (Riber and Christensen, 200 The X-marks indicate which elements are expected to be increased when the fuel is mixed with the special waste fractions.*

Property	Base-load fuel	PVC	Imp. wood	Shoes	Salt	Shredder	Batteries
Content of special waste fraction (%w/w)	-	11	11	1.6	0.5	14	0.5
Lower heating value, wet basis (MJ/kg)	10.2						
S (mg/kg)	1800						
As (mg/kg)	11		X			X	
Cd (mg/kg)	8.1					X	X
Cr (mg/kg)	114		X	X		X	
Cu (mg/kg)	1200	X				X	
Hg (mg/kg)	2.6					X	X
Mn (mg/kg)	0.0						
Mo (mg/kg)	2.9						
Ni (mg/kg)	57						X
Pb (mg/kg)	440				X		
Zn (mg/kg)	1600					X	X
Al (mg/kg)	10000						
Fe (mg/kg)	12000					X	
Ca (mg/kg)	7900						
Na (mg/kg)	1800				X**	X	
Mg (mg/kg)	560						
N (mg/kg)	5600						
P (mg/kg)	960						
K (mg/kg)	1800						
F (mg/kg)	58						
Cl (mg/kg)	9000	X*			X	X	

   * : *organically bound*   ** : *inorganically bound*

Waste is an inhomogeneous fuel of complex physical structure and composition. Therefore, each run was carried out for several hours and sampling and measurements were made repeatedly during a run. For each run, the changes in fuel or operational conditions were made well before the measurements in order to ensure steady state.

The changes in the operational conditions were the following. In two runs the amounts of primary and secondary air were increased or decreased. These runs are called 'Maximum oxygen' and

'Minimum oxygen'. In another run the primary air was decreased, but the oxygen level in the stack gas was unchanged. This run is called 'Minimum primary air'. In the last run with changed operational conditions the combustion zone was extended. This run is called 'Extended combustion zone'.

Aerosol measurements were performed before and after the flue gas cleaning. Total dust measurements were also performed before the filter in the reference run. An overview of the plant and the location of the measuring points are shown in Figure 69.
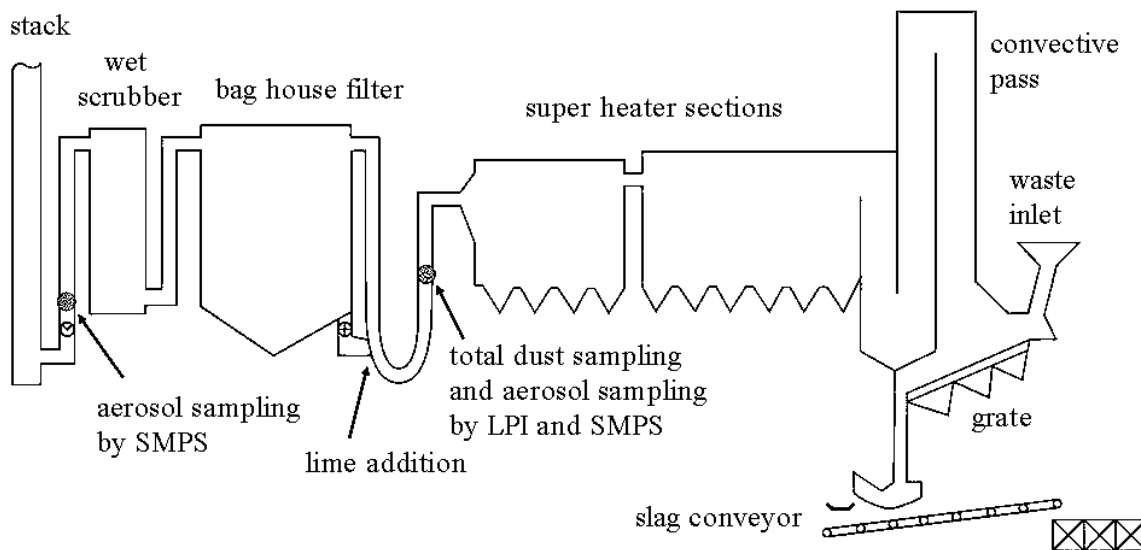
Figure 69. *Illustration of the 22 MW municipal waste incinerator FASAN. The two positions for aerosol sampling are marked on the figure.*

The oxygen and water content of the flue gas at the location of the ejector-diluter are 7.8±0.5% O_2 and 14.6±1.3% H_2O, the temperature is 176±3°C (standard deviations indicate the variation between runs), and the linear gas velocity is approximately 10 m/s. The average oxygen and water concentrations, the average temperatures of the combustion chamber (top and bottom), and the gas flows of air during the individual runs are given in

Table 13. The air flows are normalized to the average values of the flow throughout the entire measuring campaign. It is seen that the oxygen content in the post-combustion flue gas is rather stable during the different runs. Only in the run 'Maximum oxygen' the concentration is increased to 9.1% while the value is between 7.2 and 8.3 in all other runs. The water content deviates somewhat more and lies between 11.7% and 17.4%. The temperatures in the bottom of the combustion chamber and at the location of the aerosol sampling are very constant during the measuring campaign. In the top of the boiler an increase in temperature is found when decreasing the primary air and when adding PVC or shoes.

Table 13. *Average concentrations of O_2 and H_2O at the sampling point for the aerosol measurements during the individual runs. The temperatures in the bottom and the top of the combustion chamber and the temperatures at the sampling point are given. The gas flows of primary, secondary, and total air are given on a normalized basis (to the average values)*

Run:	Reference 1	Reference 2	Ext. comb. zone	Min. oxygen	Max. oxygen	Decr. prim. air	Salt	Batteries	Shredder	Imp. wood	PVC	Shoes
O_2 (vol. %, wet)	7.3	7.9	8.3	7.2	9.1	7.5	7.6	7.9	7.5	7.8	7.9	8.0
H_2O (vol. %)	14.9	15.3	15.3	17.4	13.6	15.0	14.9	14.3	14.7	14.2	11.7	13.8
T_{bottom} (°C)	1037	1010	985	1018	991	1011	1014	1017	1028	1018	1010	1011
T_{top} (°C)	865	912	928	912	890	1179	920	963	919	1024	1112	1124
$T_{sampling}$ (°C)	175	175	173	176	184	175	175	176	175	176	175	177
Primary Air	0.90	1.14	1.08	1.00	1.15	0.78	1.03	1.14	1.01	0.93	0.91	0.92
Secondary Air	1.09	0.73	0.79	0.61	1.44	1.22	1.02	0.93	1.05	1.00	1.12	0.99
Total air	0.96	1.01	1.00	0.88	1.24	0.91	1.03	1.07	1.02	0.95	0.98	0.94

5. 3   Particle Sampling

The measurements of mass-based size distributions were made using a 10-stage Berner Low-Pressure cascade Impactor (Hauke GmbH LPI). Number-based size distributions were obtained using a scanning mobility particle sizer (SMPS). The SMPS system consists of a differential mobility analyzer (TSI 3071 DMA) and a condensational particle counter (TSI 3010 CPC). The mass concentration of coarse particles was obtained by filter methods in the reference run and the particle size distribution for coarse particles was determined by laser diffraction using a Malvern Mastersizer S long bed. The measurements were obtained from a dry sample and the measuring range was 0.49-754 μm.

The LPI and the SMPS are operated with diluted flue gas withdrawn from the duct by a gas ejector. The ejector dilutes flue gas into a flow of dry, filtered air (Nielsen *et al*., 2002; Nielsen *et al*., 1996; Zeuthen *et al*., 2006), The dilution serves a three-fold purpose. Water condensation is prevented because the sample during dilution and cooling is held well above the water dew point. Coagulation in the sampling line becomes effectively quenched because its rate is lowered by several orders of magnitude due to the dilution. The dilution also reduces the particle concentration to avoid overloading of the LPI and more important to keep the concentration in the condensational particle counter of the SMPS system low to ensure counting of single particles. The overloading of the impactor can be avoided by reducing the time of sampling. However, a long sampling time reduces the influence of fluctuations in the operation of the plant. The dilution ratio varies with time due to changes in flow and pressure in the duct and clogging of the ejector capillary. To determine the precise dilution ratio during a measurement (up to 30 minutes) the dilution ratio is measured on-line by comparing the CO_2 concentration in the diluted flue gas with

the concentration in the flue gas. Each sampling line is dried and filtered continuously in gas-conditioners and fed into an IR CO_2-analyzer (Rosemount, NGA 2000). Changing the internal diameter of the inlet capillary of the ejector changes the dilution ratio. Dilution ratios in the range 5 to 200 can be chosen. By inserting the ejector in the duct with the capillary at an angle of 90° to the direction of the gas flow, it is ensured that the largest particles are filtered from the sampling line by inertial forces while the sub-micrometer particles are sampled undisturbed (Vincent, 1989). This pre-filtering is necessary in order to avoid overloading of the impactor by large particles. With the conditions used in the experiments a cut-off diameter of ~3 μm for the pre-filtering is obtained (Nielsen *et al*., 2002). The entire sampling setup is shown in Figure 70.
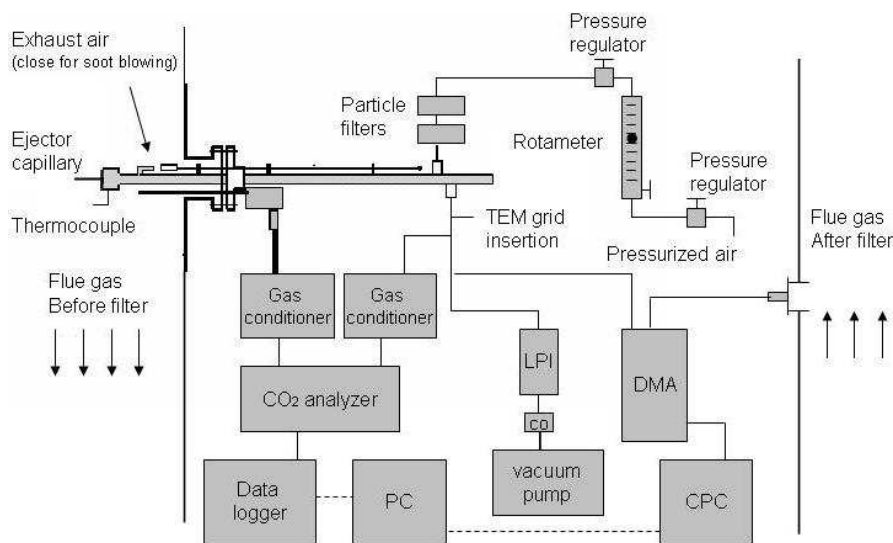
Figure 70. *Setup for aerosol measurements. A sample stream of flue gas is withdrawn from the duct by an ejector and diluted with dry, filtered air. Part of the diluted flue gas is fed to the low-pressure cascade impactor (LPI) another part to the scanning mobility particle sizer (SMPS) and a third part is filtered and dried for CO_2 analysis. A second stream of flue gas is withdrawn and filtered in a hot ceramic filter and its CO_2 concentration is determined by an IR gas analyzer. A gas stream to the SMPS is withdrawn from the cleaned gas in the stack (see Figure 69).*

The two CO_2 concentrations are stored by a data-logger and saved on a computer. The ejector capillary can be cleaned by 'soot-blowing', i.e. by blocking the gas exit and forcing pressurized air through the capillary.

The cascade impactor has an aerodynamic diameter range from 0.03 to 12.7 μm. Deposited particles in the impactor are collected on aluminum foils. To reduce re-bounce of the particles, the foils are coated with a thin film of Apiezon H grease using a dilute toluene solution of the grease. The weight gain from the deposited particles was determined with a Sartorius M5D-000V001 micro balance. The LPI is thermostated at 60ºC before measurements to avoid water condensation from the flue gas. The change in cut-diameters of the impactor stages caused by the temperature change is calculated assuming constant values of the Stokes number as suggested by Valmari *et al*. (1998). Tygon tubes were used to avoid deposition due to static electrical charges. The sampling time for a LPI measurement was adjusted in order to achieve a suitable amount of

102

deposits. In most cases 30 minutes proved adequate. In a few runs plugging of the ejector capillary occurred quite rapidly. However, frequent soot-blowing of the capillary sufficed to keep the ejector functioning in all runs. In between runs the ejector was withdrawn from the flue gas duct and cleaned with water and ethanol. The CO_2 analyzers were calibrated daily. Deposits on impactor foils were analyzed by energy dispersive X-ray spectroscopy (EDS) to obtain the chemical composition.

In the SMPS system the particles are classified by their mobile diameter in the DMA with a range from 14 to 800 nm. The particles are counted in the CPC with high accuracy giving a finely resolved number-based size distribution. The SMPS system is able to determine the size distributions for particles at very low concentrations. In this campaign it was possible to place the instrument in a way that allowed switching between measuring particles from the ejector probe (before the flue gas cleaning) and particles from the clean gas in the stack. The filtered gas is withdrawn through a 3 m Tygon tube. Due to the low number concentration of particles after the filter the coagulation in the tube is negligible.

Particles were collected for morphology studies by transmission electron microscopy (TEM). Cu-grids with carbon film were emerged in the diluted aerosol from the ejector exit for approximately three minutes to obtain an adequate density of particles by diffusional deposition.

5. 4   Results and discussion

5. 4. 1   Mass-based particle size distributions

The mass-based particle size distributions for the runs with changes in the operational conditions are shown in Figure 71, together with the reference measurements from three different reference runs. The references are based on two or three measurements from each of the three days, and a total of eight successful reference measurements are carried out. The average mass-based particle size distribution, based on all eight reference measurements, is used for comparison with runs with different operational conditions. The size distributions from runs with changes in the operational conditions are each based on three measurements.

The aerodynamic diameter of the particles are converted to a mobile diameter by assuming a particle density of 2 g/cm^3 (that of alkali chlorides) and using the interpolation formula given by (Baron and Willeke, 2005):

$$D_p(St) = \sqrt{\frac{\rho_{ae}}{\rho_p} \frac{C_c(D_p(ae))}{C_c(D_p(St))}} \cdot D_p(ae) \tag{66}$$

where C_c is the diameter-dependent Cunningham's slip correction factor. ρ_p is the particle density, and ρ_{ae} is the aerodynamic density defined as 1 g/cm^3. The diameter-dependent Cunningham slip correction is given by (Friedlander, 2000):

$$C_c = 1 + \frac{2\lambda}{D_p}\left(2.5140 + 0.800\exp\left\{\frac{-0.55D_p}{\lambda}\right\}\right) \qquad (67)$$

where λ is the mean free path of the gas. The changes in the operational conditions do not have a considerable effect on the mass-based particle size distribution. The results from the test-runs with addition of waste fractions, are shown in Figure 72, and the overall properties of the particle size distributions are summarized in Table 14.
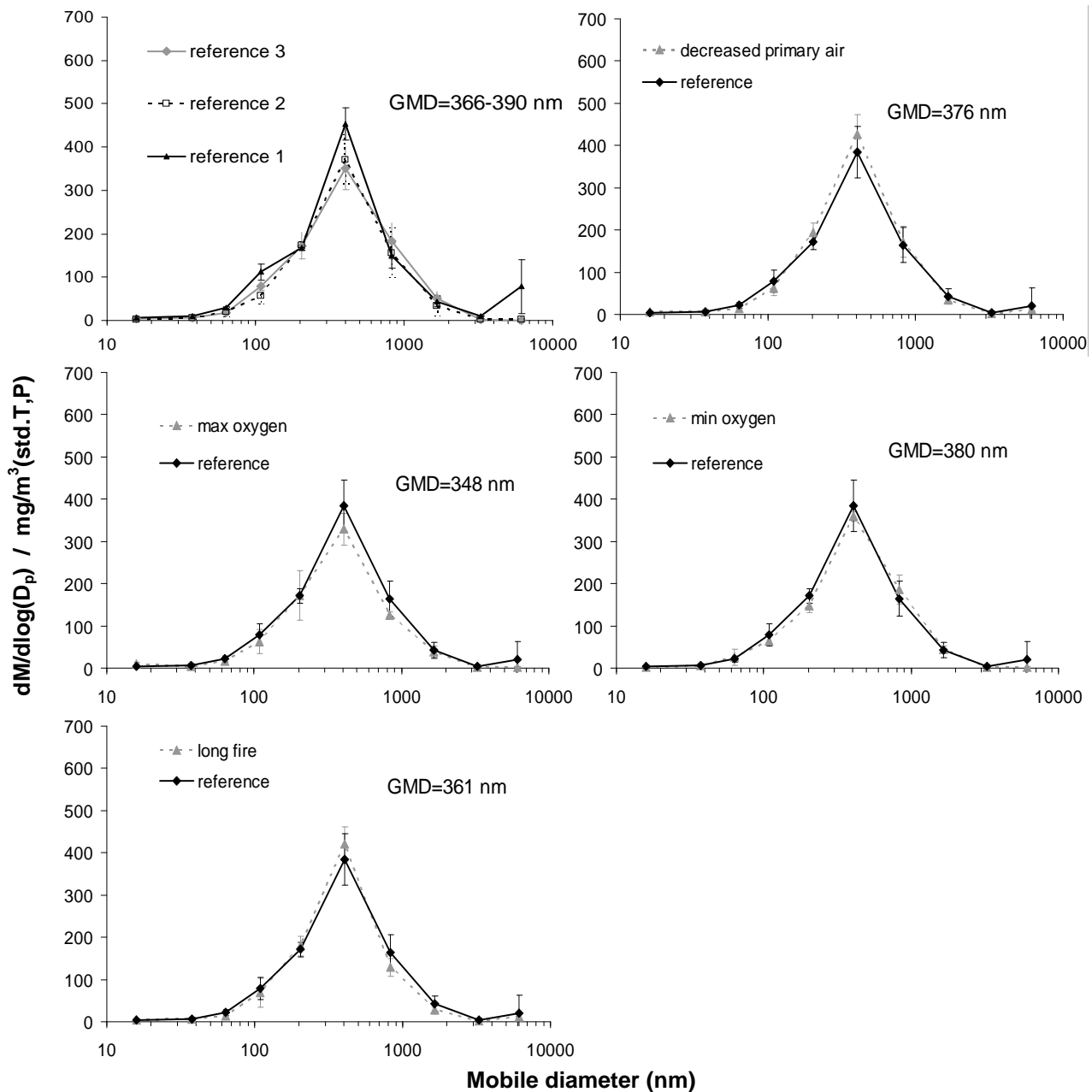
Figure 71. *Mass-based size distributions from runs with base-load waste measured with cascade impactor. The first plot show reference runs from 3 different days. Each day is based on 2-3 measurements with a total of 8 reference measurements. In the remaining plots, runs with different combustion conditions are shown together with an average reference distribution. The average reference distribution is based on 8*

104

measurements; the other distributions are each based on 3 measurements. The geometric mean diameter of the distributions are given in the figure (GMD).
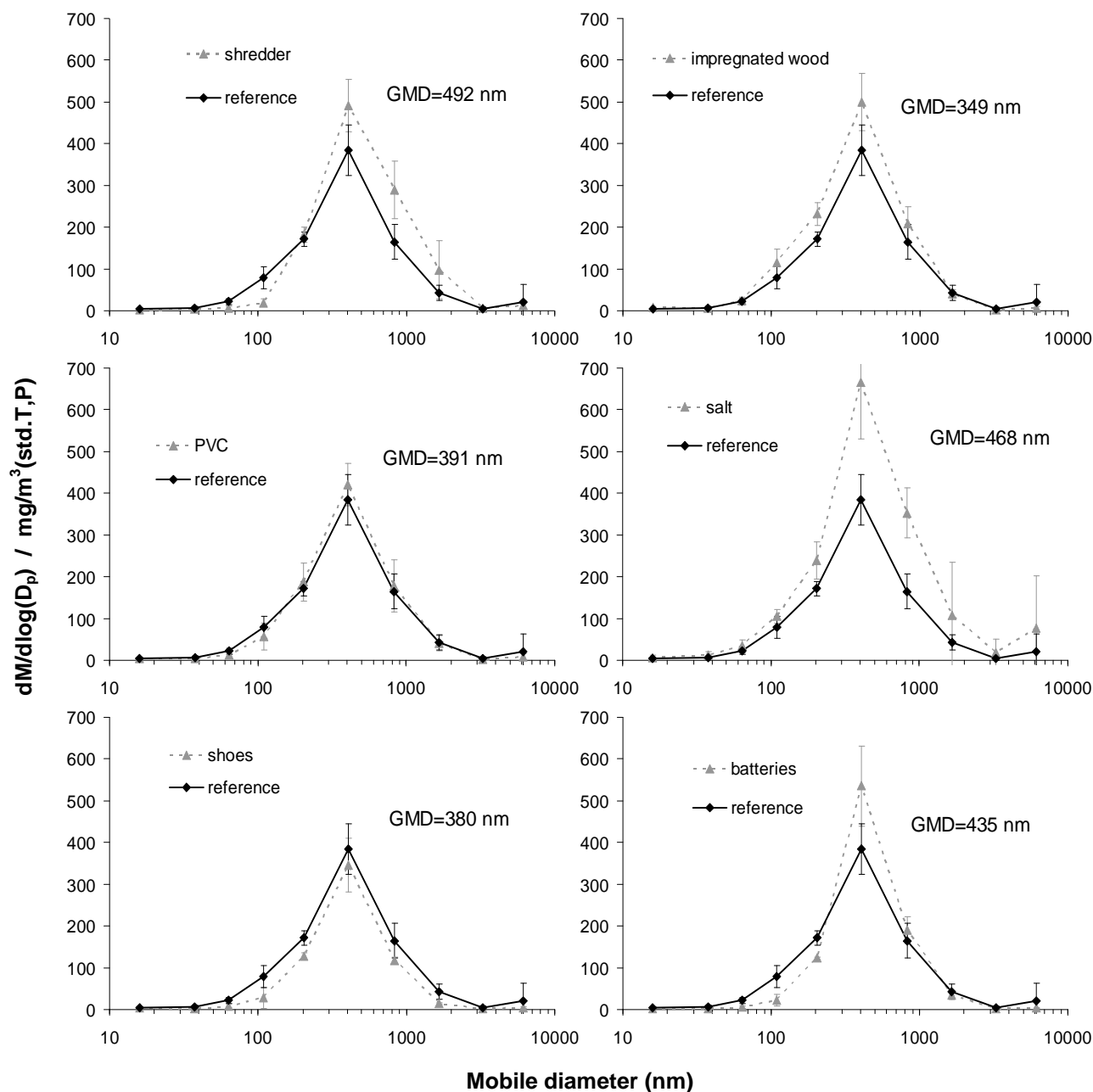
Figure 72. *Mass-based size distributions of the runs with combustion of waste with different waste fractions. The distributions are measured using cascade impactor. Six runs with addition of different waste types are shown in individual plots and compared to the reference runs. The particle size distribution for shredder waste is based on 4 measurements, the runs with shoes and batteries are based on 2 measurements and impregnated wood, PVC, and salt are each based on 3 measurements. The geometric mean diameter of the distributions are given in the figure (GMD).*

The number-based geometric mean diameter is defined as:

$$GMD = \exp\left\{\frac{\sum_i dN_i \ln(D_{p,i})}{\sum_i dN_i}\right\} \qquad (68)$$

For the mass-based GMD, dN_i is replaced by dM_i. The addition of salt, shredder waste, and impregnated wood increases the mass concentration and shredder waste, batteries, and salt increases the mass-based geometric mean diameter (GMD). The addition of batteries increases the GMD slightly. The total mass concentration is given by the area under each curve and is obtained by integration. The increase in mass load of fine particles when adding salt is not found when adding PVC-waste. In both cases high amounts of chlorine are added. However, the chlorine in PVC is not bound in the particles, probably due to lack of alkali metals or other condensable cations. The chlorine in this case is released as $HCl_{(g)}$.

The mass concentrations calculated here do not cover the total particulate concentration. A peak is found above the range of the cascade impactor (upper cut-diameter is 12.7 μm) and the peak is not seen in the LPI results. These particles probably originate from non-combustible inclusions in the fly ash. The pre-cutting diameter of the ejector sampler (~3 μm) is not responsible for this. In a few runs, the ejector capillary was turned against the flow direction to avoid pre-filtering and no changes in the particle size distribution were observed. Thipse *et al.* (2002) found that the peak of the coarse mode fraction of the total particle size distribution from waste incineration particles was ~600-700 μm.

The total particulate matter was determined in one of the reference runs ('reference 2') by traversing of the duct with a fibrous filter, and the mass concentration was 2.2 g/m³(std.T,P). The $PM_{2.5}$ in this run was 0.23 g/m³(std.T,P) and the $PM_{2.5}$ fraction of the total mass concentration is thus 10.5% (w/w) (all $PM_{2.5}$-values are summarized in Table 14). A similar total dust concentration for waste incineration (between 2.22 and 3.07 g/m³(std.T,P)) for waste incineration has been reported elsewhere (Chang *et al.*, 2000). A particle size distribution for the coarse particles from the reference run with total ash filtering was obtained using laser diffraction of the filter sample. The entire size spectrum from 0.03 to 754 μm is shown in Figure 73.

Table 14. *Properties for fine particles from runs with changes in operational conditions or with addition of different waste fractions.*

Operational conditions	Reference 1	Reference 2	Reference 3	Long comb. zone	Min. oxygen	Max. oxygen	Min. prim. air
$PM_{2.5}$ (mg/m³)	274.0±4.8	231.6±29.9	249.9±23.4	241.3±26.8	236.8±13.4	213.5±4.7	270.4±24.4
# Conc. (10^6/cm³)	44.4±8.6	58.7±10.8	47.3±12.0	86.7±5.0	62.1±18.3	61.3±7.9	50.7±2.0
Mass-GMD (nm)	439±67	385±63	393±25	380±34	404±28	368±21	363±16
Number-GMD(nm)	181±56	160±9	159±18	158±54	158±23	151±12	191±11

Waste fractions	Reference*	Salt	Batteries	Shredder	Imp. wood	PVC	Shoes
$PM_{2.5}$ (mg/m³)	251.8±21.3	437.1±44.0	267.0±46.0	312.7±19.8	319.7±21.8	257.2±9.9	185.9±9.6
# Conc. (10^6/cm³)	50.1±7.6	71.2±28.4	43.8±13.7	63.0±20.5	54.6±6.7	42.8±5.1	53.9±1
Mass-GMD (nm)	405±23	488±156	446±4	479±107	371±30	410±65	394±23
Number-GMD(nm)	167±12	213±44	222±30	176±74	151±16	188±18	191±6

*: Average of three average runs. The standard deviations for these data reflect the deviation between the different reference runs. All other standard deviations reflect the deviation during a single run.
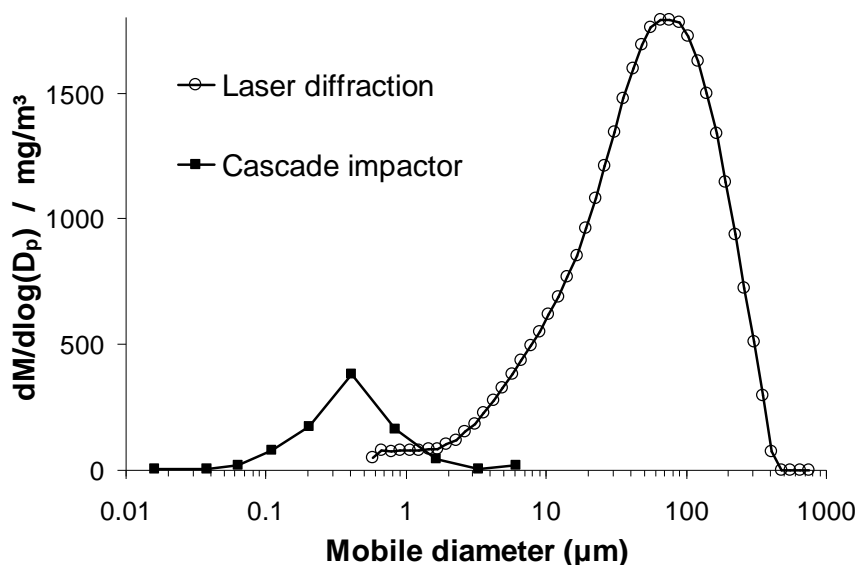
Figure 73. *Bimodal mass-based particle size distribution. The fine particles are measured using cascade impactor while the coarse particles are measured using laser diffraction on coarse particles re-suspended in a gas.*

5. 4. 2   Number–based particle size distributions

The size distributions for the aerosols before the flue gas cleaning, obtained by the SMPS system, are shown in Figure 74. The deviation between the measurements was larger than for the LPI-measurements. This is seen by the total number and mass concentrations plotted with standard deviations in Figure 75. This was probably due to the short measuring time for one scan (~5 min). The curves shown here are all average values of several scans during one day. A very large change in the number-based size distribution may cause only a minor change in the mass-based size distribution, because the mass of the smallest particles is so small that it only gives a vanishing contribution to the mass concentration of particles. The curves shown here are all average values of several scans during one day. The total number concentration is given by the area under each curve and is obtained by integration. The integrated properties of the mass- and number-based particle size distributions are given in Table 14.

The PM$_{2.5}$ value for the runs with base-load waste is very constant (213-274 mg/m^3) while the number concentration varies considerably (44 - 87·10^6 #/cm^3). For the runs with different waste fractions added to the base-load waste, the variation in both mass and number concentration is significant. The variations in number and mass concentrations between the different runs are not correlated (see Figure 75). This might indicate that different aerosol formation mechanisms take place during the different runs. However, the large variation in number concentration makes it difficult to draw this conclusion. The number-based geometric mean diameter (GMD) is only changed in a few runs. The reference value 167 nm (aerodynamic diameter) is increased to 188-222 nm when adding the waste fractions salt, batteries, PVC, and shoes. The geometric mean diameter is also increased to 191 nm for the run with minimal primary air. The particles are slightly larger than the ones reported by Maguhn *et al.* (2003).
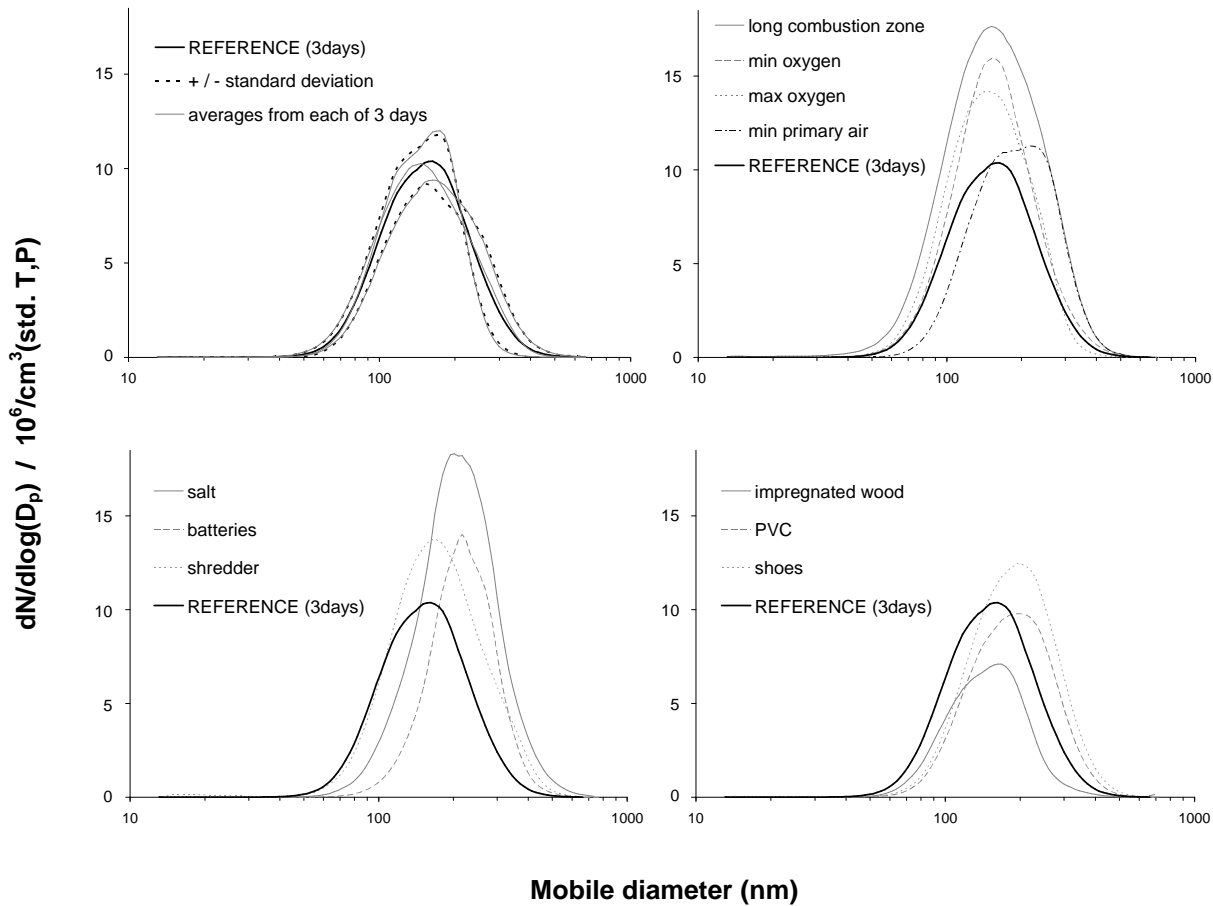
Figure 74. *Number-based particle size distributions. All curves shown represent a mean of several SMPS scans during one day of measurements. In the first figure the 3 daily average distributions from th e reference runs are shown together with the 3-day average. For this average a standard deviation between the reference runs is shown. On the upper-right figure the distributions from runs with changed operational conditions are shown and in the lower two figures the distributions from waste addition runs are shown. All distributions are shown together with the averaged reference distribution.*

The number-based size distributions can be converted to mass-based ones by assuming that all particles are spheres with a constant density. The resulting mass-based size distribution is shown for the reference case in Figure 76. The two curves are averages of all reference measurements from three different days. The effective density of the particles is found by integrating the curves in order to obtain the mass concentration of particles smaller than 800 nm (mobile diameter) and fit these concentrations by the effective particle density. The quality of the match for the other runs is similar to the reference case. The fitted densities range from 0.6 to 2.1. The rather poor fit and the fitted densities reflect the presence of aggregates, because the densities are rather low compared to the main components (~2 g/cm^3 for alkali chlorides) and suggest that aggregates are present in many of the particle size distributions. A lower density could also be caused by the presence of soot, because soot forms very large aggregates.
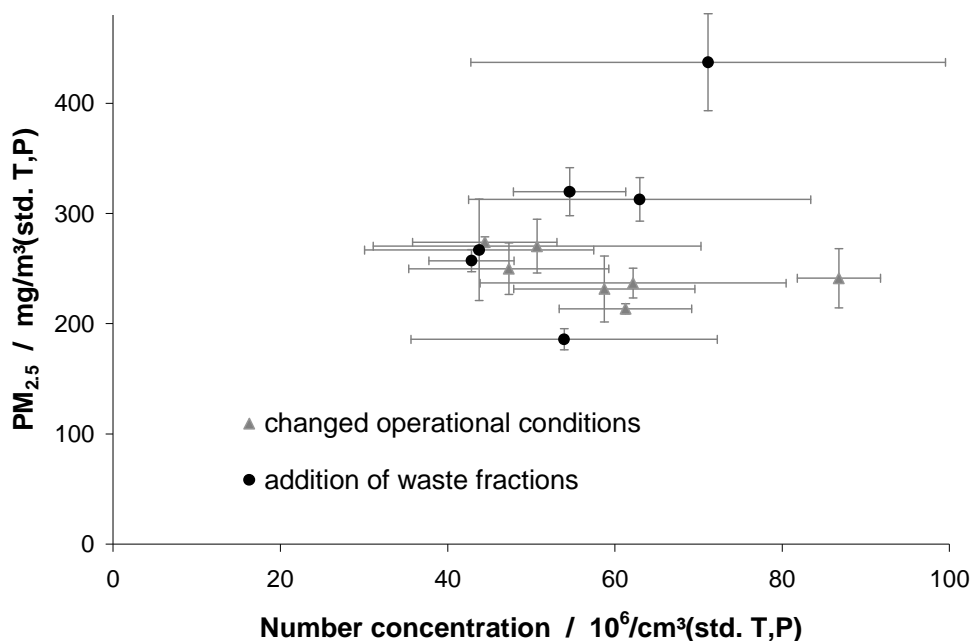
Figure 75. *Mass concentration versus number concentrations for all runs. The variation of these two concentrations are evidently uncorrelated. The standard deviations for the number concentrations are considerably higher than for the mass concentrations due, probably, to the short measurement time for the SMPS system and the unsteady release of nucleating components.*
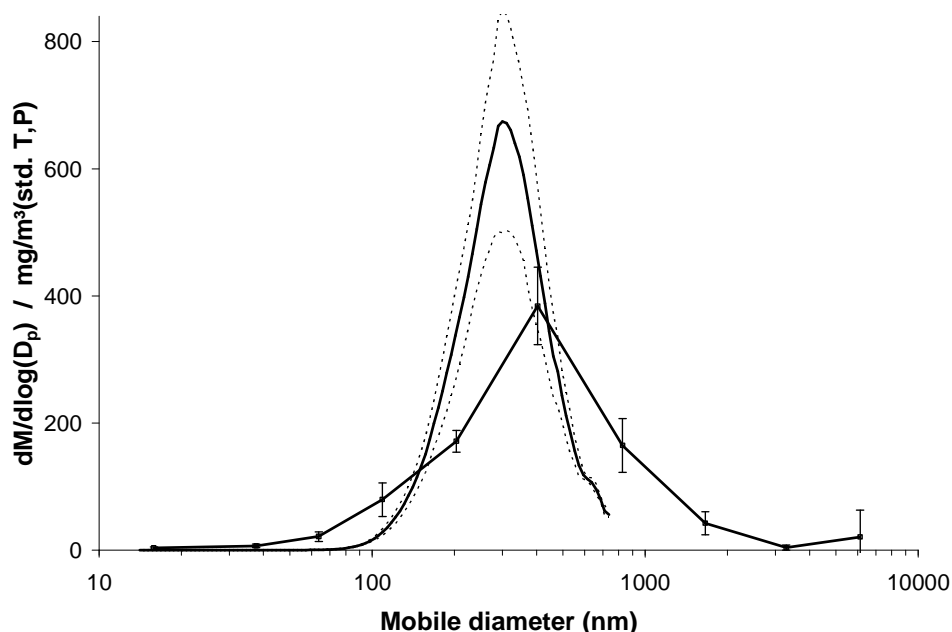
Figure 76. *Mass-based size distribution for reference runs obtained from SMPS and LPI measurements. Both curves are averages of all reference measurements from 3 different days. The dotted curves represent the standard deviation of the distribution based on SMPS data. The effective particle density for the conversion of the number-based distribution is found by fitting of the integrated mass concentration of particles smaller than 800 nm (Stokes diameter) corresponding to the upper limit of the SMPS instrument. The best fit is obtained for an effective density of 1.52 g/cm³.*

5. 4. 3 Penetration through flue gas cleaning

From the number-based size distributions before and after the flue gas cleaning a penetration curve is obtained. The penetration describes the fraction of the particles from the boiler that are emitted to the stack. That is, the penetration characterizes the flue gas cleaning of particles in the plant. Between the two measuring points hydrated lime is added to remove SO_2 and HCl, the gas is filtered in a baghouse filter, and the gas is wet-scrubbed to remove traces of HCl. Each of these operations may affect the particle size distribution. The addition of hydrated lime may increase the number of coarse particles. Baghouse filter removes particles very efficiently (Jiang et al., 2006). However, the minimum collection efficiency in the range 0.1-1.0 μm can result in a small amount of particles passing the filter. The wet-scrubber can create new particles. The mineral content of the droplets will create new particles as the droplets evaporate and these particles will stay in the gas when leaving the wet-scrubber.

The major part of the particles from the boiler is removed from the flue gas by the flue gas cleaning. The average number-based size distributions before and after the flue-gas cleaning are shown in Figure 77. No correlation was found between the number concentration of particles before and after the flue gas cleaning. The particle size distributions from the stack are shown in Appendix E. The distributions are averages over all runs and the dotted lines represent the standard deviations between runs. The average total number concentration is decreased from $6.2 \cdot 10^7$ #/cm^3 to $6.9 \cdot 10^4$ #/cm^3 corresponding to an overall number-based penetration of 0.11%. The total number concentrations for the individual runs, before and after the flue gas cleaning, are plotted together in Appendix E and the best linear correlation is obtained by regression. The slope of the regression line suggest a value of 0.12% penetration, which is in good agreement with the value found for the average concentrations.

The contribution to the total number concentration by coarse particles is small and can be neglected. The penetration maximum between 0.4 and 1.0 μm is caused by the minimum in collection efficiency of the fabric filter. The penetration maximum in the 0.01-0.1 range is not typical for fabric filters. The diffusional deposition of such small particles removes them from the gas very efficiently (Kim *et al.*, 2006). This maximum has to reflect a formation of new particles downstream from the baghouse filter. This formation is probably caused by evaporation of droplets in the wet-scrubber. Particles smaller than 40 nm formed in a wet-scrubber has been reported previously by Maguhn *et al.* (2003). The overall efficiency (although some of the particles are newly formed this term is used here) can be compared with the one reported by Chang *et al.* (2000) (0.07-0.48%) for two plants equipped with electrostatic precipitator. The penetration through an electrostatic precipitator is generally larger than for fibrous filters.
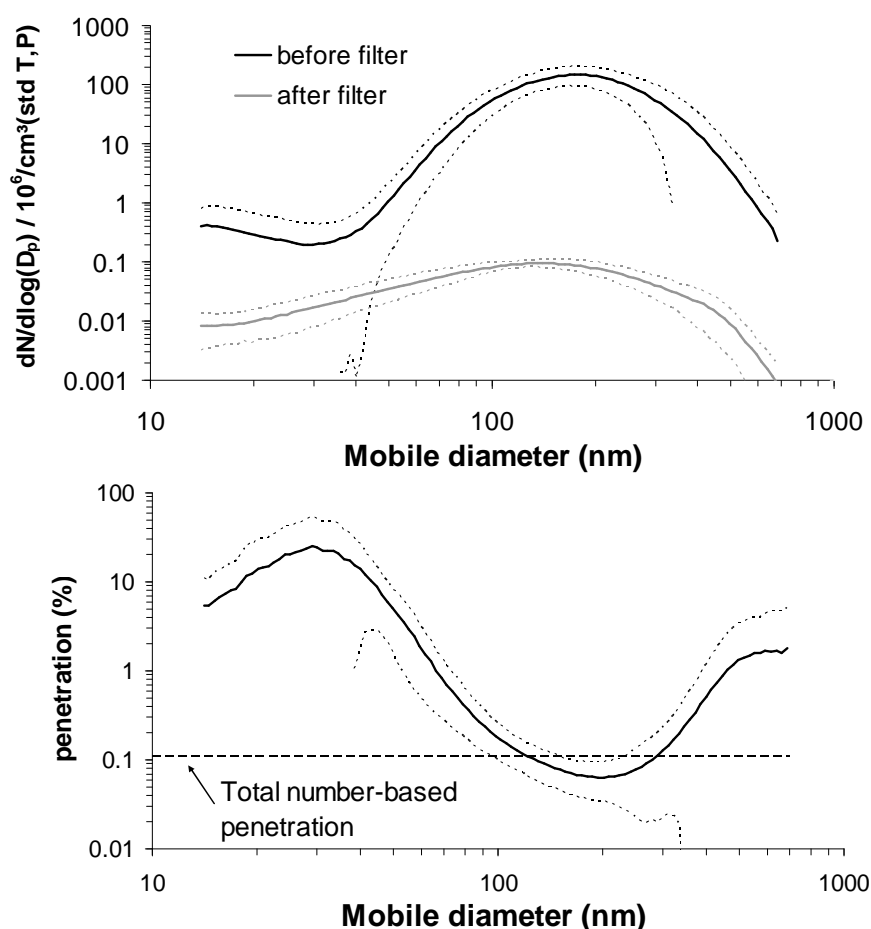
Figure 77. *Upper plot: The average number-based size distributions before and after the flue gas cleaning during all runs. The stack-distributions from the individual runs are shown in Appendix E. Lower plot: Penetration through the flue gas-cleaning system. This consists of CaO powder addition, baghouse filters and wet-scrubber. Standard deviations indicate variations between all the runs.*

5. 4. 4   Chemical composition

The chemical compositions of the fine particles, sampled at the end of the convective sections, from runs with different waste fractions are shown in Figure 78 and in Figure 79. Only the runs with different fuels were investigated. The operational conditions were not expected to influence the composition considerably. For each measured element the content is depicted for all six runs with changes in fuel composition together. The error bars on the reference contents indicate the standard deviation between 3 runs from 2 different days with reference measurements. The accuracy of EDS is ~ ±1% and measured concentrations below 1% are generally not reliable. The elements Cd and Ni were also measured but the content was below 1% (w/w) for all sizes in all runs and the results are not shown. In all runs the six major elements by weight are Na, S, Cl, K, Zn, and Pb. The chlorine content is increasing with the particle diameter. The content of alkali (Na+K) is rather constant for all runs. The molar Na/K ratio decreases with the particle diameter indicating that the sodium salts condenses at a higher temperature than those of potassium. The ratio is increased considerably when adding salt (+67%) or shredder waste (+112%) to the base-load waste. For shredder waste this increase is also due to very low potassium content in the

particles. The zinc content increases with particle diameter and for the runs with shredder waste, shoes and PVC the content is increased. For the shredder waste run the content by weight is increased more than seven times with respect to zink. The content of lead is rather constant as a function of particle diameter and throughout the series of runs. However, for the shredder waste combustion, a 40% increase is found.
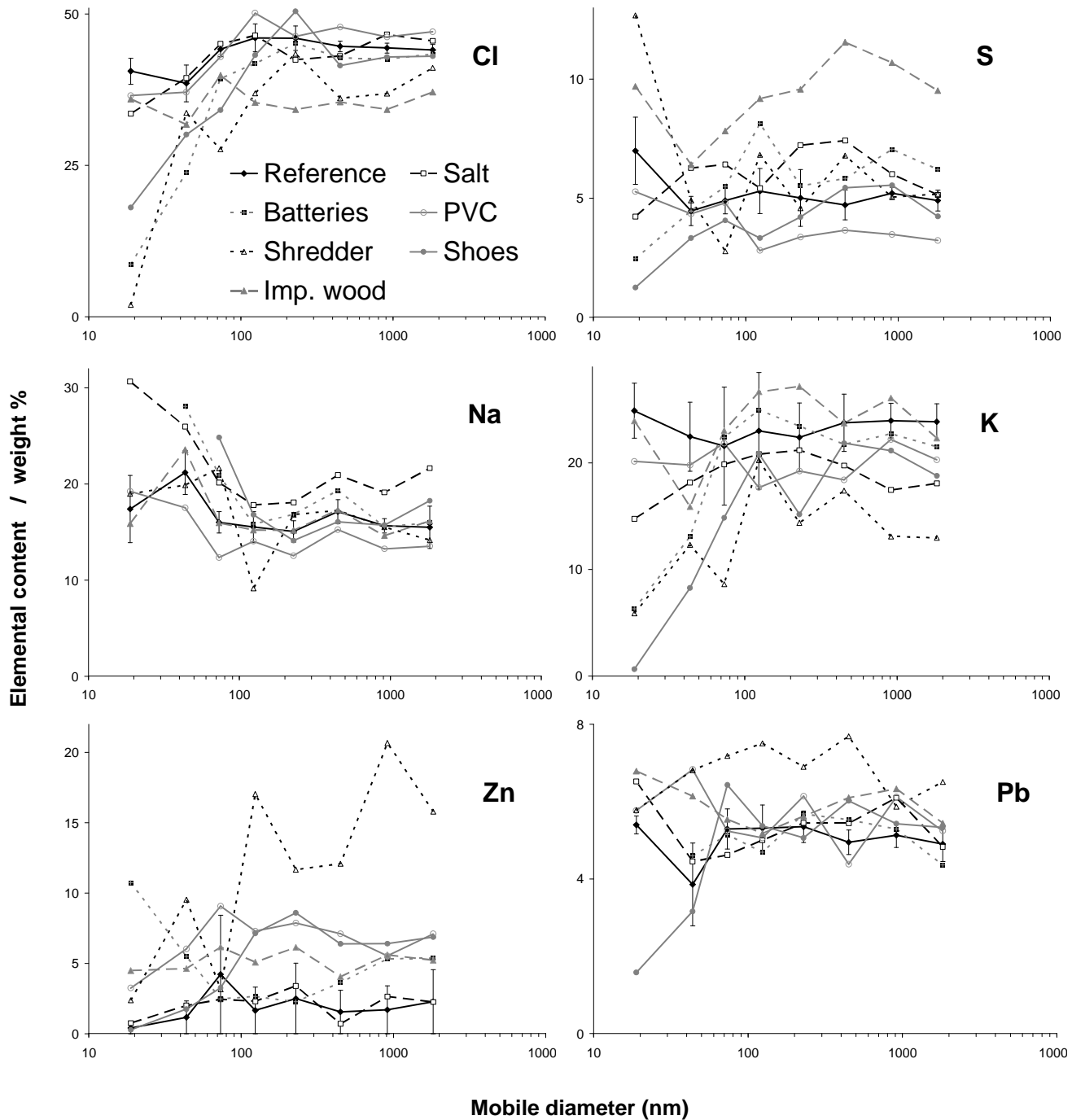
Figure 78. *Size dependent elemental content of main components of the combustion aerosols in runs with addition of various waste fractions. The composition is obtained by energy dispersive spectroscopy (EDS). The error bars on the reference composition represent the standard deviation between 3 reference runs.*
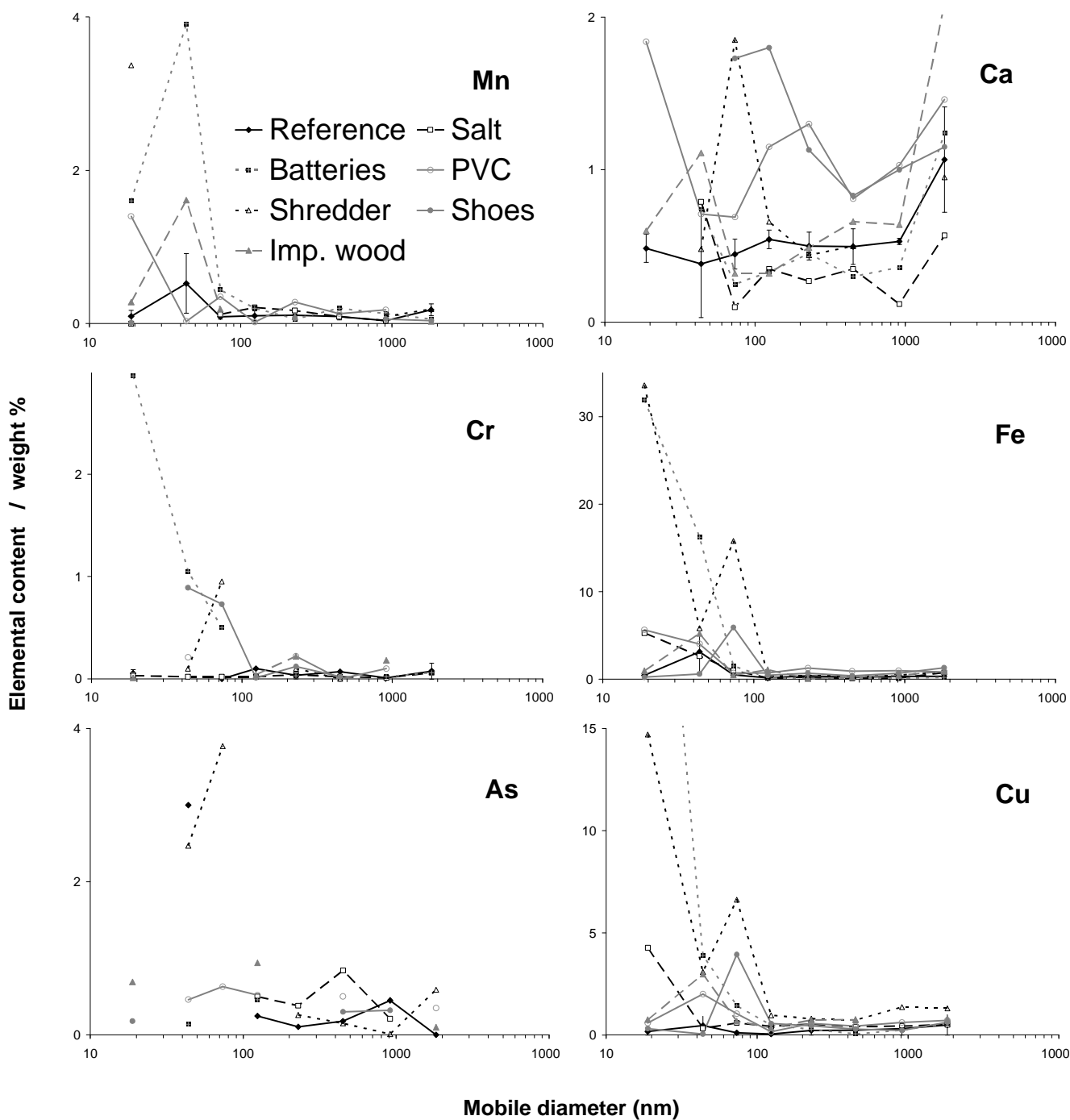
Figure 79. *Size dependent elemental content of minor components of the combustion aerosols in runs with addition of waste fractions. The composition is obtained by Energy Dispersive Spectroscopy. The error bars on the reference composition represent the standard deviation between 3 reference runs.*

The contents of Fe, Cu, Cr, As, and Mn are below the 1% accuracy limit for the large particles. However, for these elements a considerable amount is found for the very fine particles. Fe and Cu are found as major elements in the smallest particles during shredder waste and battery combustion and the two elements are found in the fine particles for all runs. Chromium is found in the smallest particles during battery, shoes, and shredder waste combustion while manganese is found mainly during shredder waste, battery, and PVC combustion. Arsenic is found in the smallest particles during combustion of shredder waste and during one of the reference runs. The content of Ca is above the accuracy limit in most cases, but no clear trends are found between particle diameter and content. The content is largest during combustion of shredder waste, PVC, and shoes. The Hg-content of the particles was only analyzed for the reference, battery, and shredder waste runs. For the reference run the mass content is below 0.5% at all stages. For the battery run 2.8% is found in the smallest particles and in the shredder waste run 4.6% is found in the smallest particles. The measurements of Ni (not shown) indicate that this element is concentrated in the finest particles. The Ni content is close to the accuracy limit during combustion of PVC, shredder waste, and batteries.

In general, the deviation between the three reference runs analyzed with EDS is quite low. Only the content of K, Zn, and S deviates considerably as seen on the depicted error bars.

For the reference experiments a total dust sample was analyzed for chemical composition by inductively coupled plasma-optical emission spectrometry (ICP-OES) for comparison of the elemental content in the fine particles and in the total fly ash. Two reference samples from two different runs were analyzed and compared to EDS data from the $PM_{2.5}$-fraction of the impactor samples.

Since the EDS analysis does not allow detection of oxygen, the ICP-OES data were corrected to an absence of oxygen by assuming that all the detected elements were present as their most important oxides, except for the alkali metals that are present as chlorides and sulphates. The data are listed in Table 15. The data shows an enrichment of the main elements in the fine particles: Na, K, S, and Cl. They also show a high enrichment of the heavy metals Cu, Cd, Hg, and Pb while Zn is enriched in one of the two runs. The elements S, Zn, Cu, Pb, and Cr are also enriched in fine particles from combustion of coal as reported by Nielsen *et al.* (2002).

Table 15. *Comparison of content in the PM$_{2.5}$-fraction of particles to the content of the same elements in the total fly ash dust from two reference runs. The fly ash is analyzed for the relevant elements by ICP-OES. The EDS measurements are normalized to the elemental content without oxygen, since oxygen is not detectable. To enable comparison, this has been corrected for in the ICP-OES data. The standard deviation shown for the total dust is based on multiple measurements of the same sample. The standard deviation shown for the PM$_{2.5}$ particles is between deposits from different impactor stages in a single series. The enrichment is the ratio of the composition of PM$_{2.5}$ and of the total dust*

Parameter	Total dust - element content (%w/w)		PM$_{2.5}$ - element content (%w/w)		Enrichment	
Element	Reference 2	Reference 3	Reference 2	Reference 3	Reference 2	Reference 3
Na	8.24±0.04	10.3±0.01	17.5±2.4	15.1±1.6	2.1	1.5
S	3.80±0.02	4.57±0.01	5.47±1.2	5.51±0.3	1.4	1.2
Cl	22.6±0.07	29.3±0.07	43.2±4.2	43.1±1.2	1.9	1.5
K	9.45±0.2	12.7±0.07	20.0±2.7	27.8±0.8	2.1	2.2
Ca	19.4±0.007	15.1±0.07	0.581±0.2	0.529±0.4	0.030	0.035
Cr	0.0691 ±0.02	0.0521±0.1	0.0480±0.1	0.0300±0.04	0.70	0.58
Fe	0.942±0.001	0.663±0.004	1.10±1.9	0.378±0.3	1.17	0.57
Cu	0.133±0.007	0.194±0.000	0.493±0.5	0.653±0.3	37	34
Zn	2.45±0.007	2.484±0.000	5.75±2.2	2.76±0.8	2.4	1.1
Cd	0.0248±0.001	0.0214±0.001	0.496±0.3	0.650±0.2	20	30
Hg	0.000285±0.0003	0.000109±0.000	n.d.	0.210±0.2	n.d.	1900
Pb	0.418 ±0.001	0.667±0.001	4.80±0.3	5.41±0.4	12	8.1

5. 4. 5   Morphology

The morphology of the particles found by TEM-imaging of particles deposited on a grid reveals a broad variety of shapes and structures. Some particles are polyhedral and probably crystalline, while most are close to a spherical shape with smaller particles attached to their edges. Micrographs showing particles from a reference run are shown in Figure 80. Most of the particles are a few hundred nanometers in diameter as expected from the number-based particle size distribution. The cubic structures are generally found only in the larger particles. This suggests that chlorides are condensed at a lower temperature than the one where particles are formed. EDS on single particles with cubic structures showed an increased content of alkali chlorides but also high amounts of heavier elements reflecting that the chlorides are condensed on other particles. As seen on the particle size distributions the average size of particles does not change much between the different runs. It is difficult to explain the low effective particle densities, found when fitting the number-based particle size distributions to mass-based ones, from the TEM micrographs. For the runs with addition of waste fractions the particle morphology is very similar to the reference case. Only in the runs with addition of salt, batteries, and shoes, and when reducing the primary air, the particle size is increased. The size-increase in these runs is probably due to increased heterogeneous condensation after the particle formation. This is also reflected in the PM-values measured by the LPI for these runs. In the run with reduced primary air, the morphology is changed. More and larger aggregates are formed. The aggregates have a different structure with single particles glued together. When looking at the surface of some of the

particles, a layer-structure is observed. The structure looks like graphite. The aggregates and the layer structure are shown in Figure 81. The PM$_{2.5}$ values for this run are similar to the ones for all reference runs. The chemical compositions of the single particles observed by the TEM were determined using EDS. The particle compositions were very close to the compositions determined from the LPI-foils on similar particle sizes. This means that the elements are distributed evenly on all particle sizes.
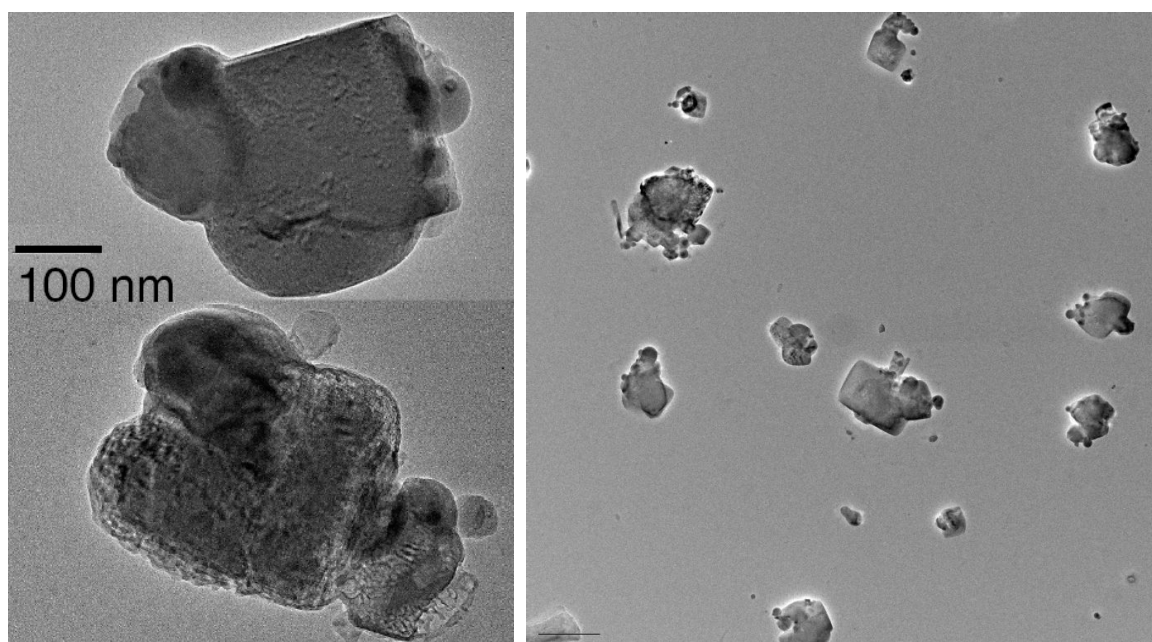
Figure 80. *TEM images of particles from a reference run. The particles vary in size and morphology. Cubic shapes are seen and also some aggregates are found. In the left picture, examples of large particles with cubic-like structures and aggregate-like structures are shown.*
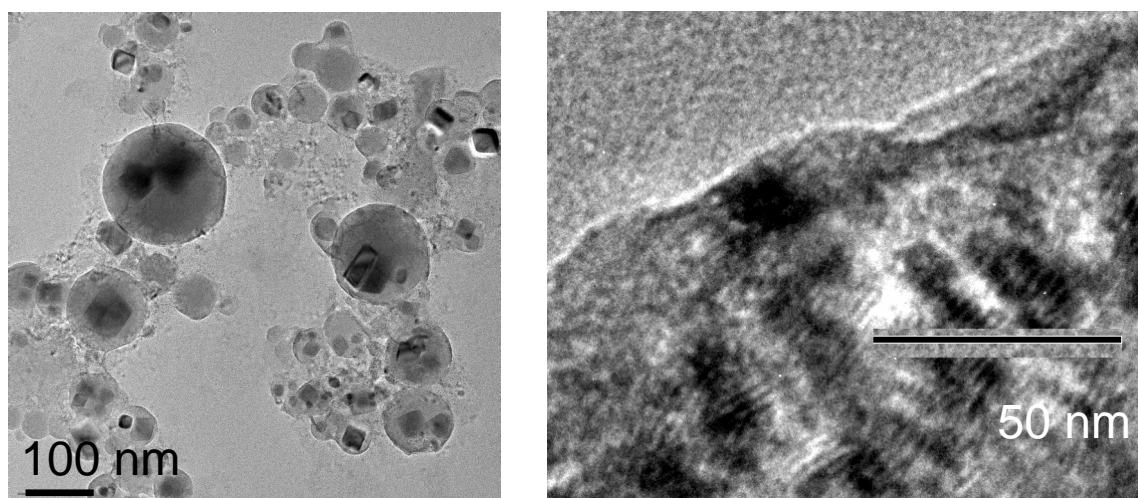
Figure 81. *TEM images of particles from run with minimum primary air. Left: Aggregates much larger than those found for other runs. Right: Graphite like structures are found on the surface of the particles in this run. This could indicate that soot is formed and that the soot glues the aerosol particles together.*

116

The compositions are compared for the reference run in Figure 82. The chlorine content of all particles, measured with EDS in the TEM microscope, is slightly lower than when the SEM-microscope is used. This is due to the fact that the electron beam evaporates some of the chlorine while measuring the composition. Since the electron beam is more intense in the TEM microscope the evaporation is more pronounced and a larger evaporation results. This may also explain the lower chlorine content measured at the smallest particles, because the evaporation is facilitated by the large surface area. The variation in the Zn content of single particles vary considerably more than the other elements.

5. 4. 6　　Particle formation

The formation of fine particles during waste combustion is caused by homogeneous nucleation of volatile matter during cooling of the flue gas. The particle number concentration during the experiments described here varies considerably with time. This could be due to a non-steady release of the nucleating components of the fuel. Maguhn *et al*. (2003) also found that the number concentration varied considerably with time. In their measurements, the number concentration correlates well with the SO_2-concentration of the flue gas, suggesting that sulphur containing compounds are responsible for nucleation. This correlation is not evident from the data from these field measurements. The high content of Cu and Fe, and to some extent Cr and Mn suggests that these heavy metals are involved in the nucleation process. The metals could condense as oxides, carbonates, phosphates, sulfides or sulfates. The content of carbonates and phosphates are unfortunately not known. The sulphur content is not increased for the smallest particles and since the SO_2-concentration is not correlated to the number of particles the nucleation of sulfates is not the dominating mechanism for particle formation. In biomass combustion, the particle formation is probably caused by nucleation of potassium sulfate. The number concentrations found in biomass combustion span from $6 \cdot 10^6$ to $35 \cdot 10^6$ #/cm^3 (Nielsen, 2001) and are lower than the ones found here.
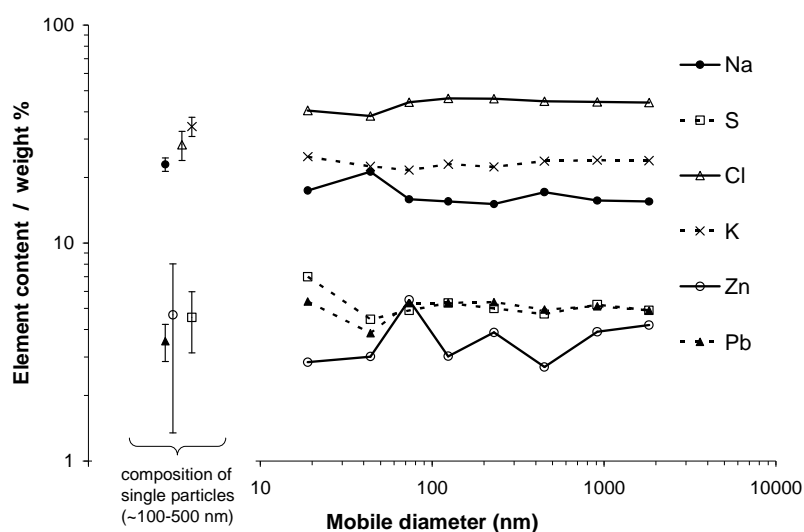
Figure 82. *Comparison of elemental composition of single particles (100-500 nm) on the impactor foils. The composition is from the run 'reference 2' and particles from LPI and TEM deposits are sampled at the same time. Only the major elements are shown corresponding to those shown in Figure 78.*

5. 5   Aerosols from waste and biomass combustion

The measured size distributions from full-scale combustion of waste are quite similar to the ones found during full-scale combustion of straw presented in Chapter 4. The mass-based particle size distributions for the 'reference' runs are monomodal with a mass-based geometric mean diameter or 354 or 384 nm. The particles from both types of combustion are mainly composed of alkali salts. The mass-based particle size distributions for the aerosols sampled from waste combustion and straw combustion are also very similar to the ones observed in the laminar flow aerosol condenser in the experiments with condensation of 300 ppm KCl and 50 ppm SO_2 (the so-called 'high KCl' experiment in Chapter 2). The mass-based particle size distribution from the three aerosols are shown in Figure 83 and some selected properties are shown in Table 16. The particle size distributions are very similar while the sulphur content of the particles is much higher in the particles sampled from combustion sources.

Table 16. *Selected properties for aerosols from straw combustion, from waste combustion, and from the LFAC.*

	$PM_{2.5}$ (mg/m^3)	Mass-based GMD (nm)	Number concentration (10^6/cm^3)	Main composition alkali/chloride/sulphur (normalized to n_{alkali})
LFAC (300 ppm KCl)	275	319	18.3	1 : 1.0 : 0.02
Straw combustion	390	353	Not measured	1 : 0.60 : 0.29
Waste combustion	252	384	43	1 : 1.3 : 0.18
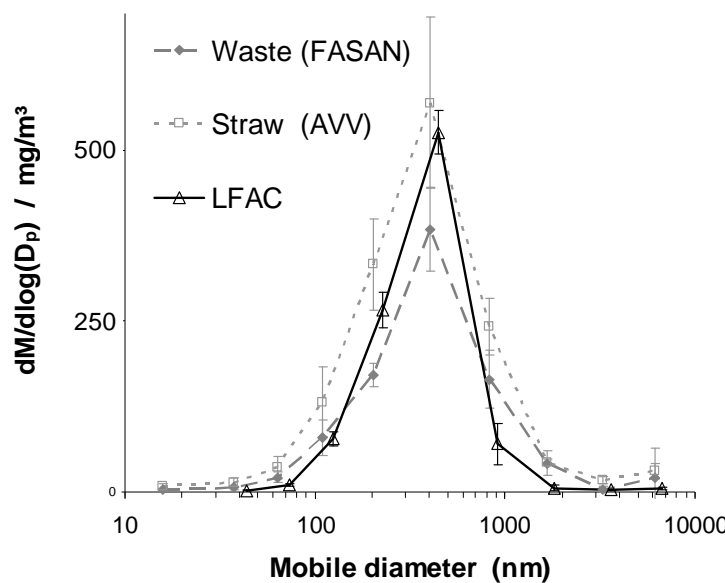
Figure 83. *The mass-based size distributions of aerosols sampled during full-scale combustion of waste and straw and from the LFAC. The feed in the LFAC contained 300 ppm KCl, 50 ppm SO_2, 5% O_2, and 5% H_2O.*

5. 6   Conclusion

Combustion aerosols from a 22 MW municipal waste incinerator were characterized during runs with different waste inputs and operational conditions. The aerosol mass load was very stable when no changes in fuel composition were introduced ($PM_{2.5}$: 252 ± 21 mg/m^3) and increased considerably during combustion of waste when including automotive shredder waste, impregnated wood, and NaCl ($PM_{2.5}$: 313, 320, and 431 mg/m^3). The particle size distribution is bimodal with approximately 10% (w/w) of the total particle mass in the $PM_{2.5}$ fraction. The number concentrations of particles varied during combustion and between varying operational conditions and waste mixes (from $43\cdot10^6$ to $87\cdot10^6$ #/cm^3). The number-based geometric mean diameters of the particles were in the range 151 to 222 nm, and the morphology was complex with a mixture of small aggregates and cubic-like structures. The particles were mainly composed of alkali chlorides and sulphates. A high content of zinc and lead was found in all runs, while smaller amounts of iron, copper, manganese, chromium, and mercury were found in some runs with waste containing these elements. Only the heavy metals Cu, Cd, Hg, Pb, and Zn were enriched in the fine particles. The increased content of heavy metals Fe and Cu in the smallest particles could indicate that these elements nucleate to form new particles. The particle penetration through the flue gas cleaning was characterized by two penetration peaks: one for particles ~500 nm with less than 2% penetration and one for particles ~30 nm with a 25% penetration maximum. The former one is probably caused by penetration of combustion generated particles through the fabric filter, while the later is caused by formation of new particles in the wet-scrubber.

The mass-based particle size distribution from the combustion of base-load waste was very similar to the distribution from the combustion of straw in a 100 MW unit described in Chapter 4. It was also very similar to the size distribution for the aerosol formed in the laminar flow aerosol condenser when 300 ppm KCl and 50 ppm SO_2 is introduced in the feed gas as described in Chapter 2.

CONCLUSIONS

The formation mechanism for aerosol particles in biomass combustion processes has been investigated. Post-combustion gasses from biomass combustion contain gaseous alkali chlorides, sulphur dioxide, oxygen, and water. The results from this study support the theory that gaseous alkali sulphate is formed and causes homogeneous nucleation of new particles to occur well above the condensation temperature of the chlorides. The existence of pure alkali sulphate particles at high temperatures has been proved by direct sampling at 800°C and 850°C with a specially designed single-step impactor. It was shown that alkali sulphate can be formed by reaction with alkali from either alkali chlorides or hydroxides.

Computer simulations supports the hypothesis that particles are formed by condensation of new particles by sulphate. The model included a chemical reaction of sulphur dioxide to form gaseous alkali sulphate. The reaction rate was based on experimental data from experiments with homogeneous gas phase reactions. The nucleation front of sulphate, predicted by the model, is located well before the nucleation front for nucleation of chloride found under similar conditions when no sulphur is present. The model was used in a two-step simulation to simulate the particle size distribution from an experiment with formation of particles in a tubular furnace. In the first step of the simulation the condensation of chloride was neglected and a particle size distribution of pure sulphate particles was obtained. The number of particles was fitted to the experimental data by adjusting the curvature dependence of the surface tension. The resulting fitted value of this so-called Tolman length was in good agreement with the value suggested by molecular dynamics simulations in the literature. In the second step of the simulation the particle size distribution from the first step was used as seed particles and a vapor pressure of chloride was applied to simulate the heterogeneous nucleation of alkali chloride on the particles. The resulting particle size distribution is very similar to the experimental results. This strongly supports the theory that the formation of gaseous sulphate initiates the homogeneous nucleation of new particles.

The limiting step in the formation of gaseous sulphate is the oxidation of sulphur dioxide. The homogeneous gas phase reaction is too slow to account for the sulphate formation found in this study as well as in other studies. In experiments with addition of seed particles during aerosol formation in a reacting gas containing alkali chloride, sulphur dioxide, oxygen, and water, the added seeds were unable to suppress the homogeneous nucleation. However, the results indicate an increased formation of sulphate. This suggests that the surface of the added seeds of alkali sulphate act as a catalyst for the oxidation of sulphur dioxide. Computer simulations show that a seed concentration of $2.2 \cdot 10^6$ #/cm^3 will suppress the homogeneous nucleation of alkali sulphate under the conditions typically found in biomass combustion. It was not possible to verify this by the experimental methods applied here.

Experiments with sulphation of alkali hydroxide in the tubular furnace showed a unexpected behavior. The mass concentration of the formed aerosol drifted over time. If sulphur is present the

mass of particles increase with time while pure hydroxide shows the opposite behavior. The number concentration was rather stable and in some runs it is very similar to the number concentration found when alkali was introduced as chloride under similar conditions. This supports the theory that the oxidation of sulphur dioxide is the rate limiting step. When sulphur trioxide is formed it reacts immediately with the alkali metal, regardless of the concentration of the alkali and the form of the alkali compound. Computational fluid dynamics (CFD) simulations suggested that the mass of hydroxide leaving the furnace is limited by an extremely fast reaction with the reactor walls at all temperatures.

Experiments with different peak temperatures in the furnace and with different residence times at the peak temperature showed that the sulphate content in the particles increases with increasing peak temperature until a maximum is reached at 875°C. After this point the content decreased with increasing temperature with a limitation corresponding well to the one suggested by gas phase equilibrium calculations. The particle size distribution was only dependent of the residence time at the peak temperature when the peak temperature was below 850°C. This also suggests that the sulphation is thermodynamically limited at high temperatures.

Aerosol measurements were carried out during full-scale combustion experiments in a 100 MW straw-fired unit. The particle size distribution was nearly stable during operation at standard conditions. Addition of six different sorbents to the boiler showed a considerable effect on the particle size distribution and on the chemical composition of the particles. The sorbents ammonium sulphate, monocalcium phosphate, Bentonite, ICA5000, and clay all reduced the mass concentration of fine particles, while chalk increased the mass concentration considerably. The full-scale findings were verified by measurements in a laboratory furnace. The composition of flue gas and aerosol particles during the full-scale runs was in good agreement with the composition proposed by equilibrium calculations using an equilibrium constant for the sulphation reaction at 812°C. The sorbents affected the amount of alkali available to formation of fine particles in the gas phase and thereby shifted the equilibrium between chloride and sulphate. The chemical equilibrium composition of the gas phase at high temperatures was fixed when the sulphation reaction became kinetically limited. The particle composition measured at low temperatures also suggested that this 'fixed equilibrium' corresponded to the gas phase equilibrium observed at 812°C.

Full-scale experiments with waste incineration in a 22 MW unit were carried out with addition of various waste fractions and with variation in the operational parameters. Aerosol measurements with cascade impactor and scanning mobility particle sizer showed a very stable mass-based particle size distribution while a higher deviation of the number concentration was observed. The added waste fractions were automotive shredder, impregnated wood, sodium chloride, batteries, PVC-plastic, and shoes. The applied changes of the operational parameters did not affect the particle formation much, while the addition of automotive shredder waste, impregnated wood, and NaCl increased the mass concentration of particles considerably. The chemical composition of the fine particles did show a large variation when adding various waste fractions. Heavy metals were enriched in the finest particles. The main part of the fine particle mass is composed of alkali salts as in biomass combustion. The large variations in particle number concentration during a single run could indicate that particles were formed by nucleation of copper or iron. The waste incinerator was equipped with lime addition, a baghouse filter, and a wet-scrubber unit. The penetration through the gas cleaning devises was very low overall (0.11% by number). However, the penetration profile showed a maximum at ~30 nm, which is not expected for baghouse filters. This indicates that new particles are formed in the scrubber unit.

The aim of the work in this thesis was to gain further understanding of the processes leading to formation of fine particles in biomass and waste combustion processes. Once the particles are formed it is difficult to remove them completely from the carrier gas. The aerosol particles cause adverse health effects by their mere presence, and they can also carry poisonous trace metals from the combustion process through the gas cleaning devices. For this reason the minimization of particle formation is important and should be considered in the design of new combustion facilities. The increasing usage of biomass and waste in the energy production and the increasing concern for public health will require a continued focus on the formation processes in the future. Since the fine particles act as carriers of corrosive chlorides to super heater tubes the limitation of particle formation is also important from an economic point of view.

It is not possible to avoid the particle formation completely. However, the formation can be reduced considerably by using the following guidelines:

- Using fuels with a low content of alkali metals. This will reduce aerosol formation as well as deposit build up. In most cases the fuel is chosen by other measures. The content of alkali salts can be reduced to some extent by washing of the fuel. High precipitation will cause a natural washing of light biomass fuels like straw.

- Reducing the temperature of the combustion zone. Low temperatures will limit the release of alkali from the fuel.

- Slow cooling of post-combustion gases. This will cause the alkali components to condense heterogeneously on coarse particles and other surfaces to a larger extent.

- Addition of sorbents. The use of 'alkali-getter' sorbents will capture the alkali metals from the gas phase and reduce the amount of fine particles formed when the gas is cooled. Some sorbents are mentioned above. These sorbents are also added to decrease the formation of deposits.

- The formation of soot particles is minimized by using a sufficient surplus of oxidant in the combustion process.

By understanding how particles are formed it is hoped that the formation of particles during combustion of biomass and waste can be minimized.

REFERENCES

Anderson, H.R., Ponce de Leon, A., Bland, J.M., Bower, J.S., and Strachan, D.P. (**1996**). Air pollution and daily mortality in London: 1987-92. *British Medical Journal (Clinical research edition)* 312**,** 665-669.

Appl, M. and Neth, N. (**1979**). The Catalytic Oxidation of Sulphur Dioxide. *Sulphur* 145**,** 26.9-38.9.

Atkins, P.W. (**1998**). Physical Chemistry. *Oxford University Press*.

Bain, R.L., Overend, R.P., and Craig, K.R. (**1998**). Biomass-fired power generation. *Fuel Processing Technology* 54**,** 1-16.

Baron, P.A. and Willeke, K. (**2005**). Aerosol Measurements - Principles, Techniques and Applications. *John Wiley & Sons*.

Baxter, L.L. (**1993**). Ash deposition during biomass and coal combustion: A mechanistic approach. *Biomass & Bioenergy* 4**,** 85-102.

Baxter, L.L., Miles, T.R., Miles, T.R.J., Jenkins, B.M., Milne, T., Dayton, D.C., Bryers, R.W., and Pagels, J. (**1998**). The behavior of inorganic material in biomass-fired power boilers: field and laboratory experiences. *Fuel Processing Technology* 54**,** 47-78.

Bird, R.B., Stewart, W.E., and Lightfoot, E.N. (**1960**). Transport Phenomena. *John Wiley & Sons*.

Biswas, P. and Wu, C.Y. (**1998**). Control of toxic metal emissions from combustors using sorbents: A review. *Journal of the Air & Waste Management Association* 48**,** 113-127.

Bockhorn, H. (**1994**). Soot formation in combustion, mechanisms and models. *Springer-Verlag, Berlin*.

Boughton, B. and Horvath, A. (**2006**). Environmental assessment of shredder residue management. *Resources, Conservation and Recycling* 47**,** 1-25.

Brunekreef, B., Dockery, D.W., and Krzyzanowski, M. (**1995**). Epidemiologic Studies on Short-Term Effects of Low-Levels of Major Ambient Air-Pollution Components. *Environmental Health Perspectives* 103**,** 3-13.

Bryers, R.W. (**1996**). Fireside slagging, fouling, and high-temperature corrosion of heat-transfer surface die to impurities in steam-raising fuels. *Progress in Energy and Combustion Science* 22**,** 29-120.

Chang, M.B., Huang, C.K., Wu, H.T., Lin, J.J., and Chang, S.H. (**2000**). Characteristics of heavy metals on particles with different sizes from municipal solid waste incineration. *Journal of Hazardous Materials* 79**,** 229-239.

Charlson, R.J., Schwartz, S.E., Hales, J.M., Cess, R.D., Coakley, J.A., Hansen, J.E., and Hofmann, D.J. (**1992**). Climate Forcing by Anthropogenic Aerosols. *Science* 255**,** 423-430.

Charlson, R.J. and Wigley, T.M.L. (**1994**). Sulfate Aerosol and Climatic-Change. *Scientific American* 270**,** 48.

Chen, J.-C., Wey, M.-Y., and Ou, W.-Y. (**1999**). Capture of heavy metals by sorbents in incineration flue gas. *The Science of the Total Environment* 228**,** 67-77.

Christensen, K.A. (**1995**). The Formation of Submicron Particles from the Combustion of straw. *PhD dissertation, Department of Chemical Engineering, Technical University of Denmark.*

Christensen, K.A. and Livbjerg, H. (**1996**). A field study of submicron particles from the combustion of straw. *Aerosol Science and Technology* 25**,** 185-199.

Christensen, K.A. and Livbjerg, H. (**2000**). A plug flow model for chemical reactions and aerosol nucleation and growth in an alkali-containing flue gas. *Aerosol Science and Technology* 33**,** 470-489.

Christensen, K.A., Stenholm, M., and Livbjerg, H. (**1998**). The formation of submicron aerosol particles, HCl and SO_2 in straw-fired boilers. *Journal of Aerosol Science* 29**,** 421-444.

Danish Energy Authority (**2006**). Kommissionen: EU bør fordoble anvendelsen af biomasse frem til 2010. *'www.ens.dk/sw33126. asp'.*

Danish Ministry of the Environment (**2006a**). Råd til forbrugerne vedrørende levende lys. *Report 02051808 (also at www.mst.dk).*

Danish Ministry of the Environment (**2006b**). Waste Statistics 2004. *Environmental Review No. 1.*

Dayton, D.C., Jenkins, B.M., Turn, S.Q., Bakker, R.R., Williams, R.B., Belle-Oudry, D., and Hill, L.M. (**1999**). Release of inorganic constituents from leached biomass during thermal conversion. *Energy & Fuels* 13**,** 860-870.

Dayton, D.C. and Milne, T. (**1996**). Laboratory Measurements of Alkali Metal Containing Vapors Released During Biomass Combustion. *New York: In: Applications of Advanced Technology to Ash-Related Problems in Boilers, Plenum Press.*

Delfino, R.J., Sioutas, C., and Malik, S. (**2005**). Potential role of ultrafine particles in associations between airborne particle mass and cardiovascular health. *Environmental Health Perspectives* 113**,** 934-946.

Diesel Particulate Filter Manufacturers Task Force (**2000**). Lexikon Verbrennungsmotor Partikel. *AKPF.*

Dockery, D.W., Pope III, C.A., Xu, X., Spengler, J.D., Ware, J.H., Fay, M.E., Ferris Jr, B.G., and Speizer, F.E. (**1993**). An association between air pollution and mortality in six U.S. cities. *The New England Journal of Medicine,* 329**,** 1753-1759.

Ewing, G.W. (**1985**). Instrumental Methods of Chemical Analysis. *McGraw-Hill International Editions.*

Fernandez, A., Wendt, J.O.L., and Witten, M.L. (**2005**). Health effects engineering of coal and biomass combustion particulates: influence of zinc, sulfur and process changes on potential lung injury from inhaled ash. *Fuel* 84**,** 1320-1327.

Ferrer, E., Aho, M., Silvennoinen, J., and Nurminen, R.V. (**2005**). Fluidized bed combustion of refuse-derived fuel in presence of protective coal ash. *Fuel Processing Technology* 87**,** 33-44.

126

Flagan, R.C. and Taylor, D.D. (**1981**). Laboratory studies of submicron particles from coal combustion. *Symposium (Int) on Combustion* 18**,** 1227-1237.

Frandsen, F.J. (**2005**). Utilizing biomass and waste for power production - a decade of contributing to the understanding, interpretation and analysis of deposits and corrosion products. *Fuel* 84**,** 1277-1294.

Friedlander, S.K. (**2000**). Smoke, Dust, and Haze. *Oxford University Press*.

Gelbard, F. (**1990**). Modelling multicomponent aerosol particle growth by vapor condensation. *Aerosol Science and Technology* 12**,** 399-412.

Glarborg, P. and Marshall, P. (**2005**). Mechanism and modeling of the formation of gaseous alkali sulfates. *Combustion and Flame* 141**,** 22-39.

Harrison, R.M. and Yin, J.X. (**2000**). Particulate matter in the atmosphere: which particle properties are important for its effects on health? *Science of the Total Environment* 249**,** 85-101.

Haye, M.J. and Bruin, C. (**1994**). Molecular Dynamics Study of the Curvature Correction to the Surface Tension. *Journal of Chemical Physics* 100**,** 556-559.

Heinzel, T., Siegle, V., Spliethoff, H., and Hein, K.R.G. (**1998**). Investigation of slagging in pulverized fuel co-combustion of biomass and coal at a pilot-scale test facility. *Fuel Processing Technology* 54**,** 109-125.

Henderson, P., Szakalos, P., Pettersson, R., Andersson, C., and Hogberg, J. (**2006**). Reducing superheater corrosion in wood-fired boilers. *Materials and Corrosion-Werkstoffe und Korrosion* 57**,** 128-134.

Hillamo, R.E. and Kauppinen, E.I. (**1991**). On the Performance of the Berner Low-Pressure Impactor. *Aerosol Science and Technology* 14**,** 33-47.

Hindiyarti, L. (**2007**). Gas Phase Sulphur, Chlorine, and Alkali Metal Chemistry in Biomass Combustion. *PhD dissertation, Department of Chemical Engineering, Technical University of Denmark*.

Huang, S.H. and Chen, C.C. (**2002**). Ultrafine aerosol penetration through electrostatic precipitators. *Environmental Science & Technology* 36**,** 4625-4632.

Iisa, K., Lu, Y., and Salmenoja, K. (**1999**). Sulfation of potassium chloride at combustion conditions. *Energy & Fuels* 13**,** 1184-1190.

Incropera, F.P. and DeWitt, D.P. (**1996**). Fundamentals of Heat and Mass Transfer. *Wiley*.

Jenkins, B.M., Bakker, R.R., and Wei, J.B. (**1996**). On the properties of washed straw. *Biomass & Bioenergy* 10**,** 177-200.

Jenkins, B.M., Baxter, L.L., Miles, T.R., and Miles, T.R. (**1998**). Combustion properties of biomass. *Fuel Processing Technology* 54**,** 17-46.

Jensen, J.R., Nielsen, L.B., Schultz-Møller, Wedel, S., and Livbjerg, H. (**2000**). The nucleation of aerosols in flue gases with a high content of alkali - A laboratory study. *Aerosol Science and Technology* 33**,** 490-509.

Jiang, W., Cheung, C.S., Chan, C.K., and Zhu, C. (**2006**). The aerosol penetration through an electret fibrous filter. *Chinese Physics* 15**,** 1864-1870.

Jimenez, S. and Ballester, J. (**2005b**). Influence of operating conditions and the role of sulfur in the formation of aerosols from biomass combustion. *Combustion and Flame* 140**,** 346-358.

Jimenez, S. and Ballester, J. (**2004**). Formation and emission of submicron particles in pulverized olive residue (orujillo) combustion. *Aerosol Science and Technology* 38**,** 707-723.

Jimenez, S. and Ballester, J. (**2005a**). Effect of co-firing on the properties of submicron aerosols from biomass combustion. *Proceedings of the Combustion Institute* 30**,** 2965-2972.

Jimenez, S. and Ballester, J. (**2006**). Particulate matter formation and emission in the combustion of different pulverized biomass fuels. *Combustion Science and Technology* 178**,** 655-683.

Johansson, L.S., Tullin, C., Leckner, B., and Sjovall, P. (**2003**). Particle emissions from biomass combustion in small combustors. *Biomass & Bioenergy* 25**,** 435-446.

Jokiniemi, J.K., Lazaridis, M., Lehtinen, K.E.J., and Kauppinen, E.I. (**1994**). Numerical-Simulation of Vapor Aerosol Dynamics in Combustion Processes. *Journal of Aerosol Science* 25**,** 429-446.

Joller, M., Brunner, T., and Obernberger, I. (**2005**). Modeling of aerosol formation during biomass combustion in grate furnaces and comparison with measurements. *Energy & Fuels* 19**,** 311-323.

Kauppinen, E., Pakkanen, T., and . (**1990**). Coal combustion aerosols: A field study. *Environmental Science & Technology* 24**,** 1811-1818.

Kawahara, S. (**1977**). Description of Aerosol Release Associated with Sodium Burning. *Journal of Nuclear Science and Technology* 14**,** 343-350.

Kim, C.S., Bao, L., Okuyama, K., Shimada, M., and Niinuma, H. (**2006**). Filtration efficiency of a fibrous filter for nanoparticles. *Journal of Nanoparticle Research* 8**,** 215-221.

Knacke, O., Kubaschewski, O., and Hesselmann, K. (**1991**). Thermochemical Properties of Inorganic Substances. *Springer, Berlin.*

Knudsen, J.N., Jensen, J.P., Biede, O., Montgomery, M., Larsen, O.H., Zeuthen, J., Hansen, J., Jensen, P.A., and Clausen, S. (**2005a**). Full-Scale Evaluation of Additives for the Reduction of Chlorine-Rich Deposits in a 100 MW Straw-Fired Boiler. *European Conference and Exhibition: Biomass for Energy, Industry and Climate Protection, Paris, 17-21 October.*

Knudsen,J.N., Jensen,P.A., Lin,W., Frandsen,F., and Dam-Johansen,K. (**2004a**). Sulfur Transformations during Thermal Conversion of Herbaceous Biomass. *Energy & Fuels* 18**,** 810-819.

Knudsen,J.N., Jensen,P.A., and Dam-Johansen,K. (**2004b**). Transformation and Release to the Gas Phase of Cl, K, and S during Combustion of Annual Biomass. *Energy & Fuels* 18**,** 1385-1399.

Knudsen, J.N., Jensen, P.A., Lin, W.G., and Dam-Johansen, K. (**2005b**). Secondary capture of chlorine and sulfur during thermal conversion of biomass. *Energy & Fuels* 19**,** 606-617.

Knudsen,N.O., Jensen,P.A., Sander,B., and Dam-Johansen,K. (**1998**). Possibilities and Evaluations of Straw Pretreatment. *Proceedings from the 10th European Conference on Biomass for Energy and Industry, Würxburg, Germany, 8-11 June* 224.

Lang,T., Jensen,P.A., and Knudsen,J.N. (**2006**). The effects of Ca-based sorbents on sulfur retention in bottom ash from grate-fired annual biomass. *Energy & Fuels* 20**,** 796-806.

Lighty, J., Veranth, J., and Sarofim, A.F. (**2000a**). Introduction to the air & waste management association's 30th annual critical review. *Journal of the Air & Waste Management Association* 50**,** 1562-1564.

Lighty, J.S., Veranth, J.M., and Sarofim, A.F. (**2000b**). Combustion aerosols: Factors governing their size and composition and implications to human health. *Journal of the Air & Waste Management Association* 50**,** 1565-1618.

Lind, T., Kauppinen, E.I., Hokkinen, J., Jokiniemi, J.K., Orjala, M., Aurela, M., and Hillamo, R. (**2006**). Effect of chlorine and sulfur on fine particle formation in pilot-scale CFBC of biomass. *Energy & Fuels* 20**,** 61-68.

Lind, T., Valmari, T., Kauppinen, E.I., Sfiris, G., Nilsson, K., and Maenhaut, W. (**1999**). Volatilization of the heavy metals during circulating fluidized bed combustion of forest residue. *Environmental Science & Technology* 33**,** 496-502.

LMNO Engineering (**2003**). Gas Viscosity Calculator. *'www.lmnoeng.com/Flow/GasViscosity.htm'*.

Maguhn, J., Karg, E., Kettrup, A., and Zimmermann, R. (**2003**). On-line Analysis of the Size Distribution of Fine and Ultrafine Aerosol Particles in Flue and Stack Gas of a Municipal Waste Incineration Plant: Effects of Dynamic Process Control Measures and Emission Reduction Devices. *Environmental Science & Technology* 37**,** 4761-4770.

Mateu, J., de Mirabo, F.B., Forteza, R., Cerda, V., Colom, M., and Oms, M. (**1999**). Heavy metals in the aerosols collected at two stations in Mallorca (Spain). *Water Air and Soil Pollution* 112**,** 349-363.

Maynard, A.D. and Maynard, R.L. (**2002**). A derived association between ambient aerosol surface area and excess mortality using historic time series data. *Atmospheric Environment* 36**,** 5561-5567.

McCain, J.D., Gooch, J.P., and Smith, W.M. (**1975**). Results of field measurements of industrial particulate sources and electrostatic precipitator performance. *Journal of Air Pollution Control Association* 25**,** 117-121.

McElroy, M.W., Carr, R.C., Ensor, D.S., and Markowski, G.R. (**1982**). Size Distribution of Fine Particles from Coal Combustion. *Science* 215**,** 13-19.

Michelsen, H.P., Frandsen, F., Dam-Johansen, K., and Larsen, O.H. (**1998**). Deposition and high temperature corrosion in a 10 MW straw fired boiler. *Fuel Processing Technology* 54**,** 95-108.

Michelsen, M.L. (**1989**). Calculation of Multiphase Ideal Solution Chemical-Equilibrium. *Fluid Phase Equilibria* 53**,** 73-80.

Mikkanen, P., Jokiniemi, J.K., Kauppinen, E.I., and Vakkilainen, E.K. (**2001**). Coarse ash particle characteristics in a pulp and paper industry chemical recovery boiler. *Fuel* 80**,** 987-999.

Miles, T.R., Miles, T.R., Baxter, L.L., Bryers, R.W., Jenkins, B.M., and Oden, L.L. (**1996**). Boiler deposits from firing biomass fuels. *Biomass & Bioenergy* 10**,** 125-138.

Miller, B., Dugwell, D.R., and Kandiyoti, R. (**2003**). The influence of injected HCl and SO_2 on the behavior of trace elements during wood-bark combustion. *Energy & Fuels* 17**,** 1382-1391.

Miltner, A., Beckmann, G., and Friedl, A. (**2006**). Preventing the chlorine-induced high temperature corrosion in power boilers without loss of electrical efficiency in steam cycles. *Applied Thermal Engineering* 26**,** 2005-2011.

Ministry of Transport and Energy (**2006**). Sustainable Energy. *'www.energistyrelsen.dk/sw11370.asp'*.

Muller, H. (**1994**). Sulfuric Acid and Sulfur Trioxide. *Ullmann's Encyclopedia of Industrial Chemistry* A25**,** 635-702.

Nielsen, H.P. (**1998a**). Deposition and High-Temperature Corrosion in Biomass-Fired Boilers. *PhD dissertation, Department of Chemical Engineering, Technical University of Denmark*.

Nielsen, L.B. (**1998b**). Combustion aerosols from potassium-containing fuels. *PhD dissertation, Department of Chemical Engineering, Technical University of Denmark*.

Nielsen, L.B., Jensen, L.S., Pedersen, C., Røkke, M., and Livbjerg, H. (**1996**). Field measurements of combustion aerosols from co-firing of coal and straw. *Journal of Aerosol Science* 27**,** S365-S366.

Nielsen, M.T. (**2001**). Field Study of Combustion Aerosols. *PhD dissertation, Department of Chemical Engineering, Technical University of Denmark*.

Nielsen, M.T., Livbjerg, H., Fogh, C.L., Jensen, J.N., Simonsen, P., Lund, C., Poulsen, K., and Sander, B. (**2002**). Formation and emission of fine particles from two coal-fired power plants. *Combustion Science and Technology* 174**,** 79-113.

Ntziachristos, L., Samaras, Z., Zervas, E., and Dorlhene, P. (**2005**). Effects of a catalysed and an additized particle filter on the emissions of a diesel passenger car operating on low sulphur fuels. *Atmospheric Environment* 39**,** 4925-4936.

Nussbaumer, T. (**2003**). Combustion and co-combustion of biomass: fundamentals, technologies, and primary measures for emission reduction. *Energy & Fuels* 17**,** 1510-1521.

Nussbaumer, T. and Hasler, P. (**1999**). Formation and behavior of aerosols from wood combustion. *Holz Als Roh-und Werkstoff* 57**,** 13-22.

Obernberger, I. (**1998**). Ashes and Particulate Emissions from Biomass Combustion - Formation, Characterisation, Evaluation, Treatment. *dbv-Verlag der Technischen Universität Graz*.

Obernberger, I., Biedermann, F., Widmann, W., and Riedl, R. (**1997**). Concentrations of inorganic elements in biomass fuels and recovery in the different ash fractions. *Biomass & Bioenergy* 12**,** 211-224.

Obernberger, I., Brunner, T., and Bärnthaler, G. (**2006**). Chemical properties of solid biofuels—significance and impact. *Biomass & Bioenergy* 30**,** 973-982.

Oh, J.E., Choi, S.D., Lee, S.J., and Chang, Y.S. (**2006**). Influence of a municipal solid waste incinerator on ambient air and soil PCDD/Fs levels. *Chemosphere* 64**,** 579-587.

Olsson, J.G., Jägild, U., Petterson, J.B.C., and Hald, P. (**1997**). Alkali Metal Emission during Pyrolysis of Biomass. *Energy & Fuels* 11**,** 779-784.

Pagels, J. (**2005**). Fine and Ultrafine Particles from Combustion Sources. *Doctoral Thesis, Department of Design Sciences, Lund University*.

Pagels, J., Strand, M., Rissler, J., Szpila, A., Gudmundsson, A., Bohgard, M., Lillieblad, L., Sanati, M., and Swietlicki, E. (**2003**). Characteristics of aerosol particles formed during grate combustion of moist forest residue. *Journal of Aerosol Science* 34**,** 1043-1059.

Parker, R., Calvert, S., Drehmel, D., and Abbott, J. (**1981**). Inertial Impaction of Fine Particles at High-Temperature and High-Pressure. *Journal of Aerosol Science* 12**,** 297-306.

Pedersen, A.J., Ottosen, L.M., and Villumsen, A. (**2005**). Electrodialytic removal of heavy metals from municipal solid waste incineration fly ash using ammonium citrate as assisting agent. *Journal of Hazardous Materials* 122**,** 103-109.

Pedersen, L.S., Nielsen, H.P., Kiil, S., Hansen, L.A., Dam-Johansen, K., Kildsig, F., Christensen, J., and Jespersen, P. (**1996**). Full-scale co-firing of straw and coal. *Fuel* 75**,** 1584-1590.

Pope, C.A., Burnett, R.T., Thun, M.J., Calle, E.E., Krewski, D., Ito, K., and Thurston, G.D. (**2002**). Lung cancer, cardiopulmonary mortality, and long-term exposure to fine particulate air pollution. *Jama-Journal of the American Medical Association* 287**,** 1132-1141.

Pope, C.A., Verrier, R.L., Lovett, E.G., Larson, A.C., Raizenne, M.E., Kanner, R.E., Schwartz, J., Villegas, M., Gold, D.R., and Dockery, D.W. (**1999**). Heart rate variability associated with particulate air pollution. *American Heart Journal* 138**,** 890-899.

Pyykönen, J. (**2002**). Computational simulation of aerosol behavior. *PhD dissertation, Technical Research Center of Finland (VTT).*

Pyykönen, J. and Jokiniemi, J. (**2000**). Computational fluid dynamics based sectional aerosol modelling schemes. *Journal of Aerosol Science* 31**,** 531-550.

Quann, R.J., Neville, M., and Sarofim, A.F. (**1990**). A laboratory study of the effect of coal selection on the amount and composition generated submicron particles. *Combustion Science and Technology* 74**,** 245-265.

Quann, R.J. and Sarofim, A.F. (**1982**). Vaporization of Refractory Oxides During Coal Combustion. *Proceedings of the Combustion Institute* 19**,** 1429-1440.

Ramanathan, V., Crutzen, P.J., Kiehl, J.T., and Rosenfeld, D. (**2001**). Atmosphere - Aerosols, climate, and the hydrological cycle. *Science* 294**,** 2119-2124.

Reid, R.C., Prausnitz, J.M., and Poling, B.E. (**1987**). The Properties of Gases and Liquids. *New York: McGraw-Hill.*

Riber, C., Fredriksen, G.S., and Christensen, T.H. (**2005**). Heavy metal content of combustible municipal solid waste in Denmark. *Waste Management & Research* 23**,** 126-132.

Sabbas, T., Polettini, A., Pomi, R., Astrup, T., Hjelmar, O., Mostbauer, P., Cappai, G., Magel, G., Salhofer, S., Speiser, C., Heuss-Assbichler, S., Klein, R., and Lechner, P. (**2003**). Management of municipal solid waste incineration residues. *Waste Management* 23**,** 61-88.

Sander, B. (**1997**). Properties of Danish biofuels and the requirements for power production. *Biomass & Bioenergy* 12**,** 177-183.

Sarofim, A.F., Howard, J.B., and Padia, A. (**1977**). The Physical Transformation of the Mineral Matter in Pulverized Coal Under Simulated Combustion Conditions. *Combustion Science and Technology* 16**,** 187-204.

Schofield, K. (**2003**). A new method for the direct flame calibration of nebulized additive concentrations. *Combustion and Flame* 133**,** 147-156.

Seinfeld, J.H. (**1986**). Atmospheric Chemistry and Physics of Air Pollution. *New York: Wiley*.

Seinfeld, J.H. and Pandis, S.N. (**1998**). Athmospheric Chemistry and Physics - From Air Pollution to Climate Change. *New York: Wiley*.

Simonsen, O. (**1993**). Condensation of Sulfuric Acid Vapors - Dynamics of Binary Aerosol Condensation. *PhD dissertation, Department of Chemical Engineering, Technical University of Denmark*.

Simonsen, O. and Livbjerg, H. (**1992**). The Influence of Seed Nuclei on Aerosol Condensation. *Computers & chemical engineering* 16**,** S379-386.

Skjøth-Rasmussen, M.S., Glarborg, P., Østberg, M., Johannessen, J.T., Livbjerg, H., Jensen, A.D., and Christensen, T.S. (**2004**). Formation of polycyclic aromatic hydrocarbons and soot in fuel-rich oxidation of methane in a laminar flow reactor. *Combustion and Flame* 136**,** 91-128.

Skrifvars, B.J., Backman, R., Hupa, M., Sfiris, G., Abyhammar, T., and Lyngfelt, A. (**1998**). Ash behaviour in a CFB boiler during combustion of coal, peat or wood. *Fuel* 77**,** 65-70.

Spencer, M.T., Shields, L.G., Sodeman, D.A., Toner, S.M., and Prather, K.A. (**2006**). Comparison of oil and fuel particle chemical signatures with particle emissions from heavy and light duty vehicles. *Atmospheric Environment* 40**,** 5224-5235.

Steenari, B.M. and Lindqvist, O. (**1998**). High-temperature reactions of straw ash and the anti-sintering additives kaolin and dolomite. *Biomass & Bioenergy* 14**,** 67-76.

Steffensen, E. (**1998**). Bestemmelse af aerosolers størrelsesfordeling ved brug af en Berner-impaktor. *Master dissertation, Department of Chemical Engineering, Technical University of Denmark*.

Steinberg, M. and Schofield, K. (**1990**). The Chemistry of Sodium with Sulfur in Flames. *Progress in Energy and Combustion Science* 16**,** 311-317.

Steinberg, M. and Schofield, K. (**1996**). Controlling chemistry in flame generated surface deposition of Na_2SO_4 and the effects of chlorine. *Proceedings of the Combustion Institute* 26**,** 1835-1843.

Steinberg, M. and Schofield, K. (**2002**). The controlling chemistry of surface deposition from sodium and potassium seeded flames free of sulfur or chlorine impurities. *Combustion and Flame* 129**,** 453-470.

The Danish Environmental Protection Agency (**2004**). Waste Strategy 2005-2008. *www.mst.dk*.

Thipse, S.S., Schoenitz, M., and Dreizin, E.L. (**2002**). Morphology and composition of the fly ash particles produced in incineration of municipal solid waste. *Fuel Processing Technology* 75**,** 173-184.

Tran, K.Q., Iisa, K., Steenari, B.M., and Lindqvist, O. (**2005**). A kinetic study of gaseous alkali capture by kaolin in the fixed bed reactor equipped with an alkali detector. *Fuel* 84**,** 169-175.

Tran, Q.K., Steenari, B.M., Iisa, K., and Lindqvist, O. (**2004**). Capture of potassium and cadmium by kaolin in oxidizing and reducing atmospheres. *Energy & Fuels* 18**,** 1870-1876.

Turn, S.Q., Jenkins, B.M., chow, J.C., Pritchett, L.C., Campbell, D., Cahill, T., and Walen, S.A. (**1997**). Elemental characterization of particulate matter emitted from biomass burning: Wind tunnel source profiles for herbaceous and wood fuels. *Journal of geophysical research* 102**,** 3683-3699.

Turn, S.Q., Kinoshita, C.M., Ishimura, D.M., Zhou, J., Hiraki, T.T., and Masutani, S.M. (**1998**). A review of sorbent materials for fixed bed alkali getter systems in biomass gasifier combined cycle power generation applications. *Journal of the Institute of Energy* 71**,** 163-177.

U.S.Environmental Protection Agency (**2006**). National Ambient Air Quality Standards (NAAQS). *'www.epa.gov/air/criteria. html'*.

Valmari, T. (**2000**). Potassium Behaviour during Combustion of Wood in Circulating Fluidised Bed Power Plants. *PhD dissertation, Technical Research Center of Finland (VTT)*.

Valmari, T., Kauppinen, E.I., Kurkela, J., Jokiniemi, J.K., Sfiris, G., and Revitzer, H. (**1998**). Fly ash formation and deposition during fluidized bed combustion of willow. *Journal of Aerosol Science* 29**,** 445-459.

Valmari, T., Lind, T.M., Kauppinen, E.I., Sfiris, G., Nilsson, K., and Maenhaut, W. (**1999**). Field study on ash behavior during circulating fluidized-bed combustion of biomass. 1. Ash formation. *Energy & Fuels* 13**,** 379-389.

van Loo, S. and Koopejan, J. (**2002**). Handbook of biomass combustion and co-firing. *Twente University Press, Enschede*.

Villadsen, J. and Michelsen, M.L. (**1978**). Solution of differential equations by polynomial approximation. *New Jersey: Prentice-Hall*.

Vincent, J.H. (**1989**). Aerosol Sampling. *John Willey Sons Ltd*.

Vogelsberger, W. (**1980**). Influence of Curvature-dependent Surface Tension of the Free Energy of Formation of Microclusters. *Chemical Physical Letters* 74**,** 143-146.

Wang, Y., Zhuang, G., Xu, C., and An, Z. (**2007**). The air pollution caused by the burning of fireworks during the lantern festival in Beijing. *Atmospheric Environment* 41**,** 417-431.

Wei, X.L., Schnell, U., and Hein, K.R.G. (**2005**). Behaviour of gaseous chlorine and alkali metals during biomass thermal utilisation. *Fuel* 84**,** 841-848.

Wiinikka, H. and Gebart, R. (**2005**). The influence of fuel type on particle emissions in combustion of biomass pellets. *Combustion Science and Technology* 177**,** 741-763.

Willeke, K. (**1976**). Temperature Dependence of Particle Slip in a Gaseous Medium. *Journal of Aerosol Science* 7**,** 381-387.

Wolf, K.J., Muller, M., Hilpert, K., and Singheiser, L. (**2004**). Alkali sorption in second-generation pressurized fluidized-bed combustion. *Energy & Fuels* 18**,** 1841-1850.

Yamasoe, M.A., Artaxo, P., Miguel, A.H., and Allen, A.G. (**2000**). Chemical composition of aerosol particles from direct emissions of vegetation fires in the Amazon Basin: water-soluble species and trace elements. *Atmospheric Environment* 34**,** 1641-1653.

Yilmaz, A., Hindiyarti, L., Jensen, A.D., Glarborg, P., and Marshall, P. (**2006**). Thermal Dissociation of SO_3 at 1000-1400 K. *Journal of Physical Chemistry A* 110**,** 6654-6659.

Yoo, J.I., Kim, K.H., Jang, H.N., Seo, Y.C., Seok, K.S., Hong, J.H., and Jang, M. (**2002**). Emission characteristics of particulate matter and heavy metals from small incinerators and boilers. *Atmospheric Environment* 36**,** 5057-5066.

Zeuthen, J.H., Jensen, P.A., Jensen, J.P., and Livbjerg, H. (**2007**). Aerosol formation during combustion of straw with addition of sorbents. Energy & Fuels, 21 (2), 699-709.

Zevenhoven, R., and Saeed, L. (**2003**). Automotive shredder residue (ASR) and compact disc (CD) waste: options for recovery of materials and energy. *Report TKK-ENY-14, Helsinki University of Technology, Energy Engineering and Environmental Protection. Espoo.*

Zimmermann, R., Heger, H.J., Kettrup, A., and Nikolai, U. (**2000**). Direct observation of the formation of aromatic pollutants in waste incineration flue gases by on-line REMPI-TOFMS laser mass spectrometry. *Fresenius Journal of Analytical Chemistry* 366**,** 368-374.

Appendix A   Experimental laboratory data

Mass-based particle size distributions from LPI measurements described in Chapter 2 and experimental data for the homogeneous oxidation of SO₂ used in Chapter 3 as basis for a kinetic model.
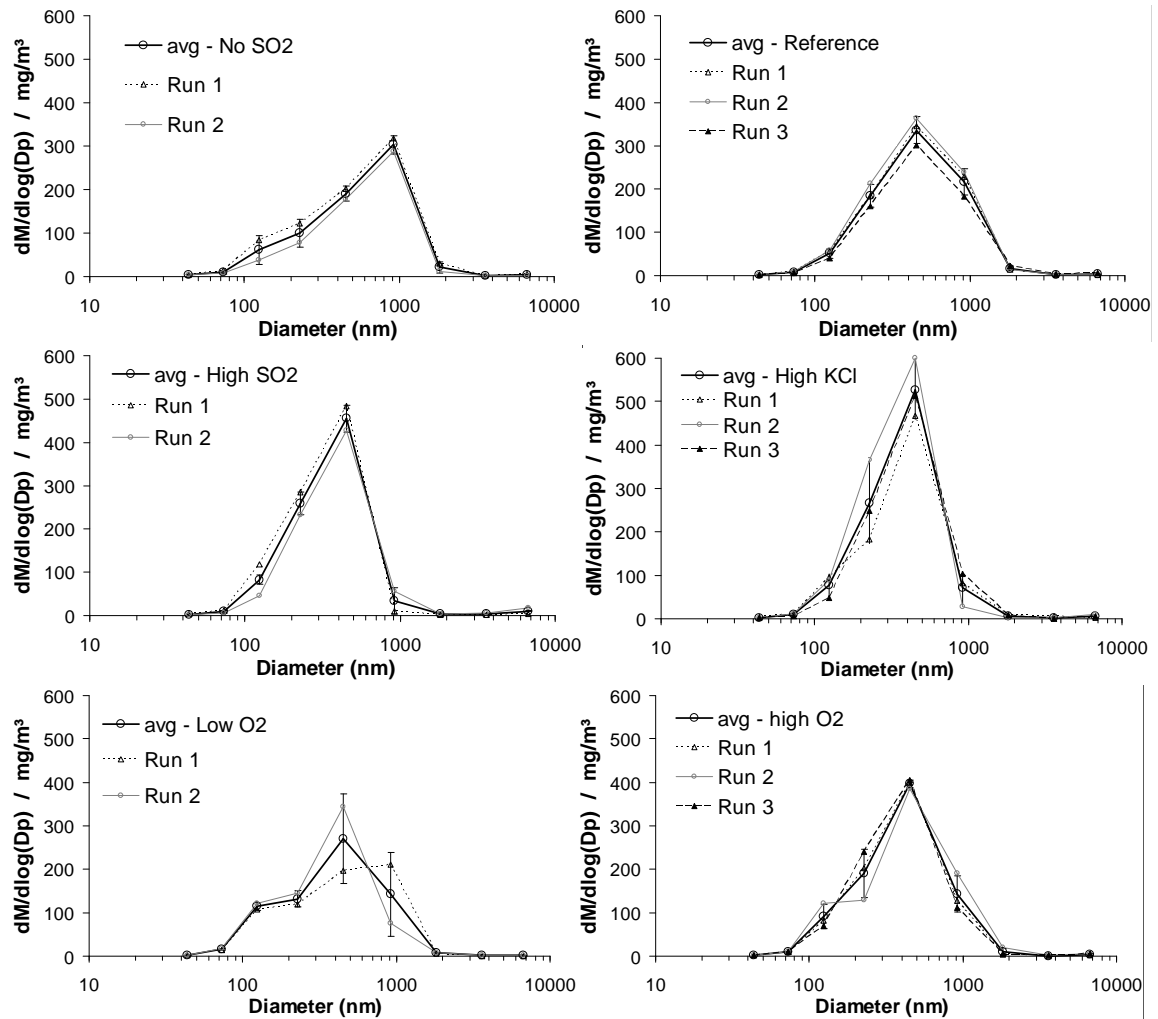
Figure A1. *Mass-based size distributions from experiments with varying chemistry in the laminar flow aerosol condenser. 2-3 measurements are made with the cascade impactor for each run and the individual particle size distributions are shown together with the average value.*

Total Flow : 910 mL/min			
Inlet to catalytic reactor			
SO_2	920	Ppm	
O_2	2,6%	**Res Time :**	2123/T
N_2	balance	SO_3	**420 ppm**
SO_2 inlet to homogeneous reactor : 500 ppm			
T,°C	**T,K**	**SO2 out, ppm**	**t (s)**
825	1098	501	1.93
850	1123	500	1.89
875	1148	501	1.85
900	1173	504	1.81
925	1198	510	1.77
950	1223	527	1.74
975	1248	578	1.70
1000	1273	633	1.67
1025	1298	706	1.64
1050	1323	778	1.60
1075	1348	831	1.57
1100	1373	854	1.55

Total Flow : 800 mL /min (STP)			
Inlet to catalytic reactor			
SO_2	946	ppm	
O_2	4,7%	**Res Time :**	2415/ (K)
N_2	balance	SO_3	406 ppm
SO_2 inlet to homogeneous reactor : 540 ppm			
T, °C	**T,K**	**SO_2 out, ppm**	**t (s)**
850	1123	540	2.15
875	1148	551	2.10
900	1173	568	2.06
925	1198	580	2.02
950	1223	605	1.97
975	1248	623	1.94
1000	1273	641	1.90
1025	1298	694	1.86
1050	1323	765	1.83
1075	1348	833	1.79
1100	1373	851	1.76

Total Flow : 800 mL /min (STP)			
Inlet to catalytic reactor			
SO_2	1010	ppm	
O_2	4.60%	**Res Time :**	2415/T
N_2	balance	SO_3	469 ppm
SO_2 inlet to homogeneous reactor : 541 ppm			
T, °C	**T,K**	**SO_2 out, ppm**	**t (s)**
800	1073	541	2.25
825	1098	541	2.20
850	1123	545	2.15
875	1148	550	2.10
900	1173	548	2.06
925	1198	561	2.02
950	1223	572	1.97
975	1248	595	1.94
1000	1273	651	1.90
1025	1298	718	1.86
1050	1323	800	1.83
1075	1348	831	1.79
1100	1373	877	1.76
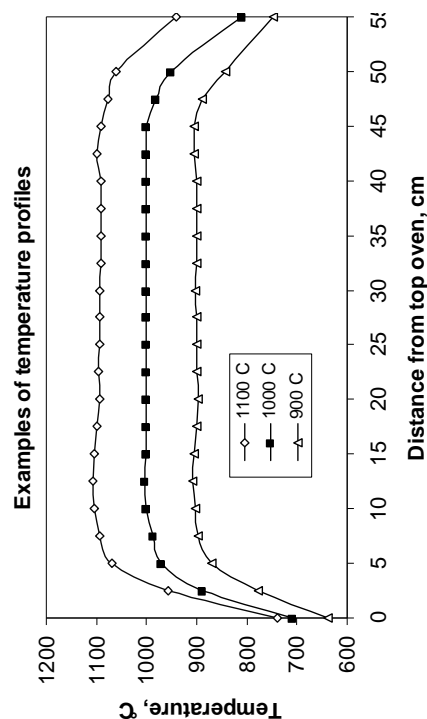
Figure A2. *Experimental data from homogeneous gas phase reactions of oxidation of SO_2 and dissociation of SO_3. The data are used in Chapter 3. Examples on the temperature profiles applied to the reactor are shown.*

Appendix B   COMPARING TWO 1D MODELS

This appendix compares two models for aerosol simulations. Experimental data from a tubular furnace is modeled by 1D-simulations. Thus, radial diffusion is neglected, which is a great simplification in a tubular furnace. A few examples of flow and aerosol dynamics from 2D-simulations are given for illustrative purposes.[9]

The Plug Flow Aerosol Condenser (PFAC) model developed by Christensen (1995) is applied to experimental data from the LFAC. Also the Stream tube model developed by Pyykönen (2002) is reduced to a 1D model and applied to the same data. The two models are very similar. The same equations are used for the nucleation and the particle sizes are divided into sections in both models. If two sections get too similar they are lumped into one bigger section. A few differences are that they use different routines for the condensation and that the PFAC model can include gravitational settling and turbulent shear. The Brownian motion is calculated by the same equations in the two models. The turbulent shear and gravitational settling are given by:

$$\beta_{Turbulent\,shear} = 0.162 \left(\frac{\varepsilon_d \rho}{\mu} \right)^{1/2} \left(d_{p1} + d_{p2} \right)^3$$

$$\beta_{Turbulent\,shear} = \eta_c \left(d_{p1}, d_{p2} \right) \frac{\pi}{4} \left(d_{p1} + d_{p2} \right)^2 \left(v_{s1} + v_{s2} \right), \qquad v_{s1} \geq v_{s2}$$

$$v_s = \frac{\rho_p g d_p^{\,2}}{18\mu} \left(1 - \frac{\rho}{\rho_p} \right) \approx \frac{\rho_p g d_p^{\,2}}{18\mu}$$

where ε_d is the energy dissipitation by turbulence, η_c is the collision efficiency and v_{is} the settling velocity. For submicron particles gravitation is of minor importance and since the flow in the LFAC is non-turbulent the two contributions to the collision frequency are neglected. The heterogeneous nucleation is calculated by:

---

[9] The results in this appendix are also described in the report: 'Simulation of Aerosol Dynamics in a Computational Fluid Dynamics-based Model', DTU/VTT, 2006.

$$I_i = \frac{dm_i}{dt} = \frac{2\pi d_p D_i M_i}{R_g T} F_D(Kn_{Di})(p_i - p_{iS}{}^*)$$

$$F_D(Kn_{Di}) = \frac{1 + Kn_{Di}}{1 + 2Kn_{Di}(1 + Kn_D)/\eta_i}$$

where F_D is a correction factor to the continuum growth and Kn_D is the Knudsen number. The PFAC can also include chemical equilibrium by using the CREAC2 routine developed by Michelsen (1989). The model can simulate the gas phase equilibrium between potassium chloride, sulphur, oxygen, and water. It assumes that the oxidation of sulphur dioxide is the only kinetically limitation of sulphatisation. However, no chemistry is included in the model in this comparison. The temperature profiles applied are mass-averaged flows calculated by FLUENT. Wall deposition is not included in the models and the inlet concentrations are calculated as the fraction of the experimental concentrations that are not deposited:

$$c(KCl_g)_{in,1D\,simulations} = (1 - F_{wall\,condensation}) \cdot c(KCl_g)_{in}$$

Results from the 1D simulations are shown in Table A1. The inlet concentrations found by subtracting the deposited amount of salt is given in brackets.

Table B1. *Results from 1D simulations of experiments from Jensen et al. (2000) using the 1D stream tube model and the PFAC model*

Input			Experiment		1D-stream tube		PFAC model	
case	Temp. Profile **	Inlet conc. initial (1D) /ppm	number conc. / $\cdot 10^7 \frac{\#}{Ncm^3}$	GMD (number) / nm	number conc. / $\cdot 10^7 \frac{\#}{Ncm^3}$	GMD (number) / nm	number conc. / $\cdot 10^7 \frac{\#}{Ncm^3}$	GMD (number) / nm
4	1-av	124 (49.6)	2.7	132	1.58	189	1.82	181
5	1-av	259 (93.2)	0.44	313	0.64	334	0.75	319
6	1-av	368 (132.5)	0.33	356	0.42	437	0.47	425
7	2-av	124 (44.6)	1.7	152	1.61	223	1.87	224
8	*2-av*	*176 (61.6)**	*1.6*	*192*	*1.49*	*192*		
9	2-av	368 (128.8)	0.99	252	0.44	411	0.53	392
10	3-av	124 (43.4)	3	117	1.5	184	1.69	178
11	3-av	176 (61.6)	2.4	162	0.97	242	1.11	233
12	3-av	368 (106.7)	0.83	263	0.50	370	0.58	354

* In case 8 the wall deposition deviates very much from all other cases. The results obtained when using the inlet concentration based on the experimental wall deposition are also deviates highly. Thus, a 65% wall deposition is assumed in this case.
** The wall temperature profiles are shown in Jensen et al. (2000). Here the mass-averaged temperatures of the gas are used to calculate the profiles used for the 1D simulation.

It is seen that both 1D models predict too low number concentrations (in all cases except 5 and 6 + 7 for PFAC) and too large GMD (all cases for both models). For the 1D stream tube model the predicted number concentrations are 58±66% too low and the GMD 27±11% too large. For the

PFAC model the predicted number concentrations are 37±58% too low and the GMD 25±11% too large. A difference between the experimental results and the two 1D models is expected. No parameters are fitted to the results and the 1D simulation is a simplification of the system. What is interesting is that the two models predict very similar results in all cases. On average the PFAC model predicts 16.8±4.7% higher number concentrations than the 1D stream tube model and -1.7±7.1% smaller (/larger) GMD.
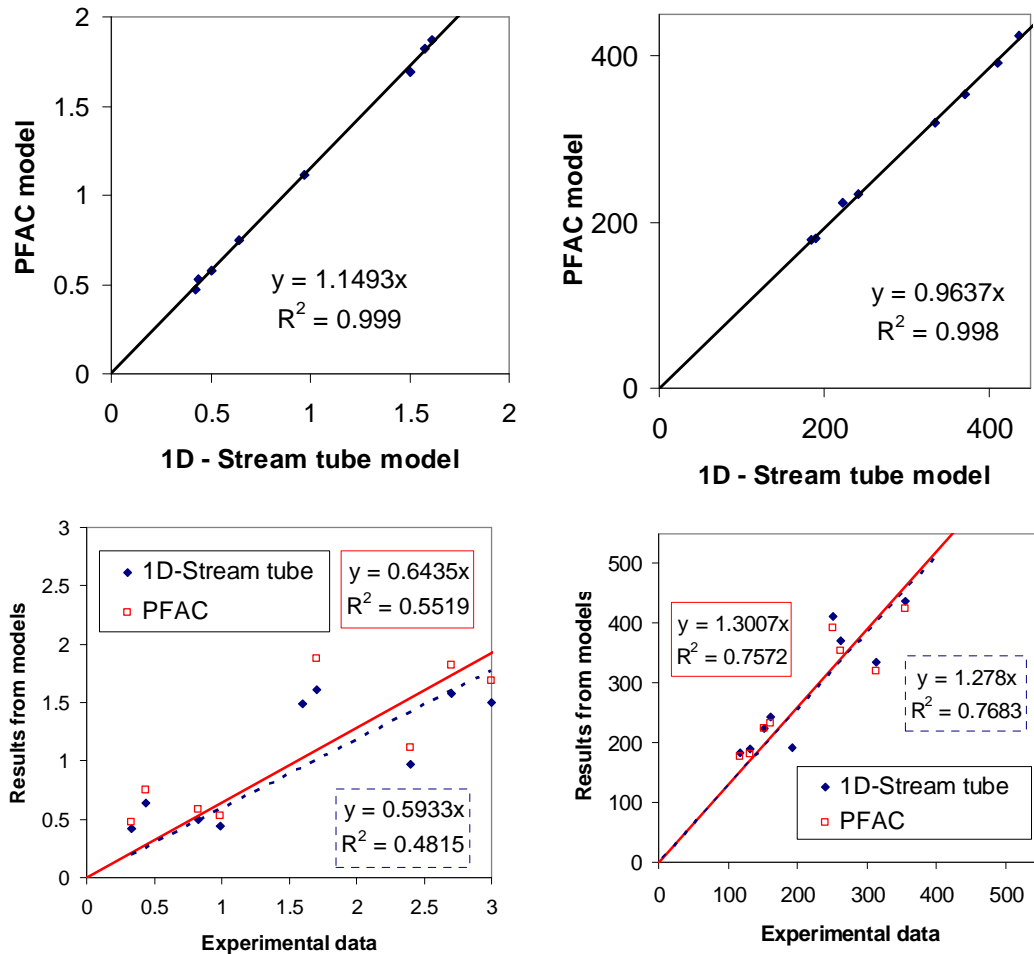
Figure B1. *Comparison of experimental data with the simulations by 1D-models. Upper-left: Number concentrations from the two models against each other. A very good regression is obtained and it is seen that the PFAC model predicts 15% higher concentrations. Concentrations are in given $10^7 \#/Ncm^3$. Upper-right: GMD from the two models against each other. A very nice regression is obtained and it is seen that the PFAC model predicts 3.5% lower diameters than the Stream tube model. Diameters are given in nm. Lower-left: 1D model predictions against experimental data for number concentrations. The regression is quite poor and concentrations are under predicted by 35%. Concentrations are given in $10^7 \#/Ncm^3$. Lower-right: 1D model predictions against experimental data for GMD. The regression is quite poor and concentrations are over-predicted by 30%. Diameters are given in nm.*

It is difficult to compare the 1D models with the 2D stream tube model. The main problem in the 2D simulations has been to get the deposition of vapor correct. The deposition is not included in the 1D models and the apparent input concentration to the 1D models is different from the vapor concentration in the 2D model when nucleation takes place. This means that the aerosol dynamics

are different and the different bulk results can not be taken only as a result of different geometry but more as a difference in aerosol dynamics.

2D-simulation with CFD and the Stream Tube model

No satisfactory prediction of experimental data from homogeneous nucleation of alkali chlorides in the laminar flow aerosol condenser were obtained in this study when using the 2D Stream tube model. However, the contour plots of the nucleation rate and the saturation ratio in the furnace during the simulations provides a good qualitative illustration of the nucleation burst in the furnace. In Figure B2 these properties are shown for the simulation of cooling of 176 ppm KCl in the LFAC.
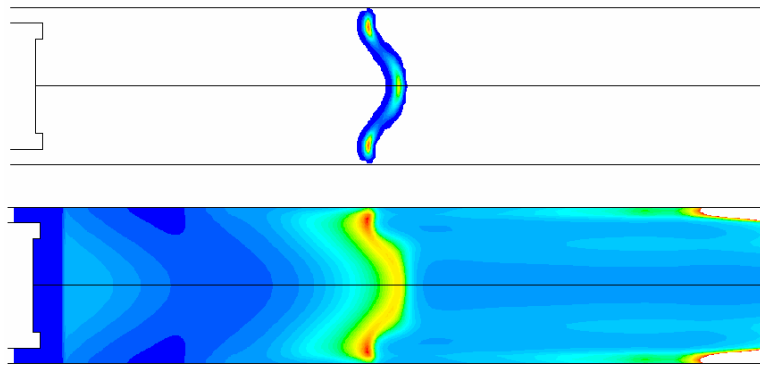
Figure B2. *Contour plots for the nucleation rate (upper) and saturation ratio (lower) for KCl during the cooling of 176 ppm KCl in the LFAC. Two separate locations zones with high nucleation rates are found in this case – one in the center line and one close to the reactor wall. The maximum nucleation (red) rate in this case is $5.5 \cdot 10^9/(cm^3 s)$ and the maximum saturation (red) ratio is 8.7. Close to the outlet the saturation ratio increases again. This is due to numerical inaccuracies at low temperature, where saturation vapor pressure and vapor concentrations are very low.*

The flow field of the furnace after the mixing of the gasses downstream from the saturator is illustrated by CFD simulations. In Figure B3 the flow field is shown for the case of a total flow rate of 3500 mL/min (as used in Chapter 2) – with the volumetric flow equally distributed between the two inlets.
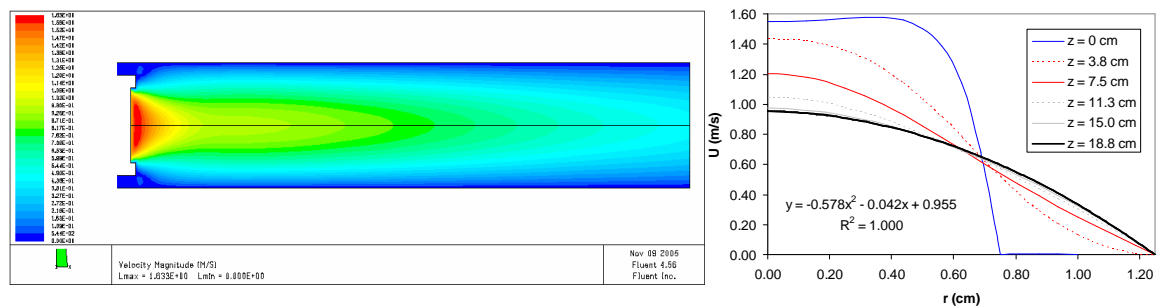
Figure B3. *Left: Contour plot of the flow field in the LFAC after the mixing of the gasses from the saturator and the parallel gas inlet. Right: Radial flow profiles at different distances from the saturator outlet when all the gas is introduced through the saturator. After approximately 10 cm a perfect parabolic profile is obtained.*

Appendix C   Physical constants

The method and source data for obtaining the physical constants used for simulation of aerosol formation in Chapter 3 and the parameters used for simulating the equilibrium composition in Chapter 2 are given here.

Diffusion constants

The diffusion coefficient for the vapor species are given by the Chapmann-Enskog theory (Bird *et al.*, 1960). This is given by:

$$D_{AB} = 0.018829 \frac{\sqrt{T^3 \left(M_A^{-1} + M_B^{-1} \right)}}{P_t \sigma_{AB}^2 \Omega_{D,AB}}$$

where D_{AB} is the binary diffusion coefficient for the molecular pair A and B [m^2/s], T is the temperature [K], M the molecular weight [g/mole], P_t is total pressure [Pa], σ_{AB} is the characteristic length [Å], and Ω_D is the dimensionless diffusion collision integral. The following mixing rules are used:

$$\sigma_{AB} = \frac{\sigma_A + \sigma_B}{2}, \quad \varepsilon_{AB} = \left(\varepsilon_A \cdot \varepsilon_B \right)^{1/2}$$

The Lennart-Jones parameters for pure components are used for the characteristic lengths. These are given in Table C1. The Lennart-Jones parameters are obtained from the properties of the pure solids at their melting temperature:

$$\varepsilon_{LJ} = 1.92 \cdot k_B \cdot T_m, \quad \sigma_{LJ} = 1.222 \cdot v_m^{\frac{1}{3}}$$

v_m is the molecular volume of the solid at the melting point [cm^3/mole]. The diffusion collision integral is given by Reid *et al.* (1987):

$$\Omega_D = \frac{A}{\left(T^* \right)^B} + \frac{C}{\exp\{ DT^* \}} + \frac{E}{\exp\{ FT^* \}} + \frac{G}{\exp\{ HT^* \}}, \quad T^* = \frac{T \cdot k_B}{\varepsilon_{LJ}}$$

A=1.06036,   *B*=0.15610,   *C*=0.19300,   *D*=0.47635,   *E*=1.03587,   *F*=1.52996,   *G*=1.76474,
H=3.89411

In the work by Jensen *et al*. (2000) the binary diffusion coefficient is obtained by averaging the diffusion coefficient for the monomer and the dimmer of a salt obtained by a modified Chapmann-Enskog equation (Bird *et al*., 1960):

$$D_A^{\#} = Q \cdot A \cdot T^B$$

Q is an empirical constant obtained by fitting the model to experimental values of number concentration, the wall deposition, and the average geometric mean diameter. *A* and *B* are Chapmann-Enskog parameters. In Figure C1 the diffusion coefficients obtained by Jensen *et al*. are shown together with values of pure monomers and dimers obtained by using the Chapmann-Enskog theory. Values are also shown for a weighted average of the monomer and dimer values. This is obtained by:

$$D_{salt} = \left(\frac{p_{mono}^{sat}}{p_{mono}^{sat} + 2 \cdot p_{di}^{sat}} \right) \cdot D_{mon} + 2 \cdot \left(\frac{p_{di}^{sat}}{p_{mono}^{sat} + 2 \cdot p_{di}^{sat}} \right) \cdot D_{di}$$

Table C1: *Properties of KCl, (KCl)$_2$, K$_2$SO$_4$, NaCl, (NaCl)$_2$, and N$_2$*

Species	M g/mole	T_m K	v_m cm^3/mole	σ_{LJ} Å	ε_{LJ} / k_B K
KCl	74.55	1045	49.05	4.47	2006
(KCl)$_2$	149.10	1045	98.05	5.64	2006
K$_2$SO$_4$	174.25	1342	93.18	5.54	2577
NaCl		1074			
(NaCl)$_2$		1074			
N$_2$	28	-		3.62	97.0

In Figure C1 the Chapmann-Enskog values for D_{AB} are plotted together with the values used by Jensen *et al. (*2000).
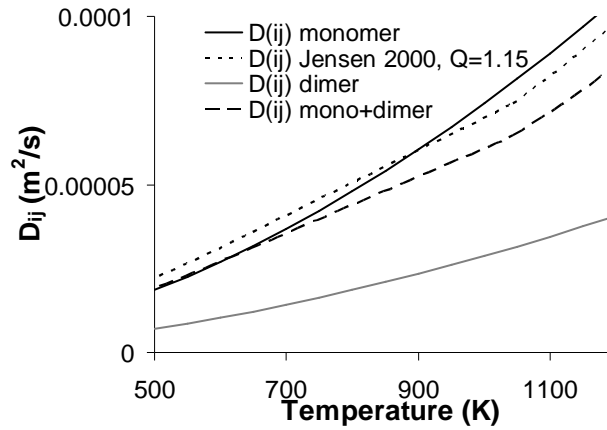
Figure C1. *Binary diffusion coefficient for KCl and (KCl)$_2$ in N$_2$ obtained by the Chapman-Enskog equation. A weighted average based on the vapor pressures of monomers and dimers is shown. These data are used by Jensen et al. (2000) with an additional fitted constant.*

For K$_2$SO$_4$ the Chapman-Enskog values are used. The data are fitted with a two-parameter expression.
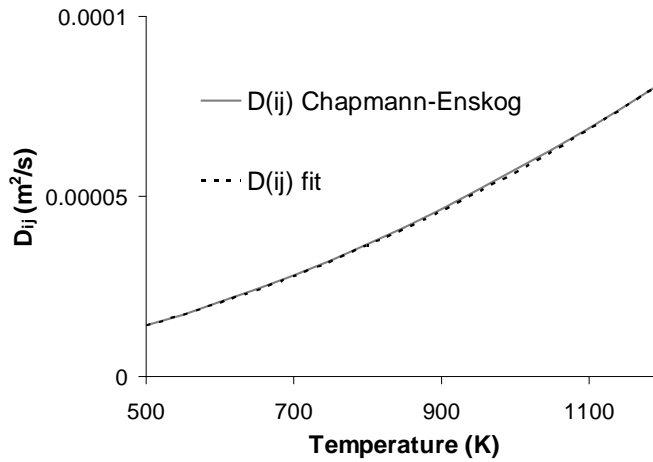
Figure C2. *Binary diffusion coefficient for K$_2$SO$_4$ in N$_2$ obtained by the Chapman-Enskog equation. The data are fitted with the two-parameter expression $D_{ij}=A\cdot(T/K)^B$ with a least-square method. The values of the fitted parameters are $A=5.66\cdot10^{-11} m^2/s$ and $B=2.00$.*

Molecular weights:

$M_w(NaCl) = 0.05844\, kg/mol$ $\qquad$ $M_w(KCl) = 0.07454\, kg/mol$,

$M_w(N_2) = 0.02800\, kg/mol$ $\qquad$ $M_w(K_2SO_4) = 0.15619\, kg/mol$

$M_w(KOH) = 0.05611\, kg/mol$

Viscosity of fluid:

It is assumed that the fluid has the viscosity and thermal conductivity of pure nitrogen.

A polynomial is fitted to data from Incropera and DeWitt (1996) to estimate the viscosity:

$$\mu_{N_2}(T) = -4.290 \cdot 10^{-8} + 6.290 \cdot 10^{-8} \cdot \left(\frac{T}{K}\right) - 3.068 \cdot 10^{-11} \cdot \left(\frac{T}{K}\right)^2 + 7.985 \cdot 10^{-15} \cdot \left(\frac{T}{K}\right)^3$$

A polynomial is fitted to data from Incropera and DeWitt (1996) to estimate the thermal conductivity:

$$k_{N_2}(T) = 5.464 \cdot 10^{-4} + 9.959 \cdot 10^{-5} \cdot \left(\frac{T}{K}\right) - 5.674 \cdot 10^{-8} \cdot \left(\frac{T}{K}\right)^2 + 2.144 \cdot 10^{-11} \cdot \left(\frac{T}{K}\right)^3$$

Data and fits of the thermal conductivity and the viscosity of pure nitrogen are shown in Figure C3.
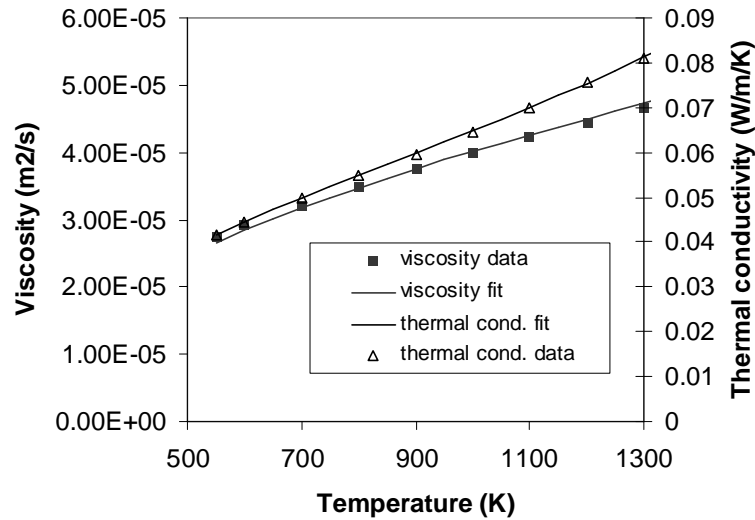
Figure C3: *Viscosity and thermal conductivity for N₂.*

Pressure:
The operating pressure used in all simulations is 101325 Pa. This is a reasonable assumption for the LFAC because the pressure drop is very small.

Chemical potentials:
The chemical potentials are calculated by the formula:

$$\mu_i^o = 10^3 \left[H_i^+ - S_i^+ y - a_i y \left(\ln\left(\frac{T}{K}\right) - 1 \right) - \frac{b_i}{2} y^2 - \frac{c_i}{2} y^{-1} - \frac{d_i}{6} y^3 \right] \frac{J}{mole}, \quad y = 10^{-3} \frac{T}{K}$$

The parameters used in the equilibrium calculations in Chapter 2 are given in Table C2:

Table C2. *Coefficients for standard chemical potential from Knacke et al. (1991).*

Component	a	b	c	d	H+	S+
1: KCl	37.154	0.962	-0.084	0	-225.998	26.653
2: K_2SO_4	145.432	6.489	-3.753	0	-1150.357	-485.497
3: $(KCl)_2$	83.119	0.013	-0.201	0	-640.856	-124.329
4: K	20.610	0.146	0.021	0	83.101	42.984
5: KOH	51.241	3.920	-0.389	0	-249.781	-58.931
6: $(KOH)_2$	97.613	14.284	-1.954	0	-696.443	-243.411
7: KH	35.330	1.992	-0.460	0	110.844	-6.448
8: SO_2	49.936	4.766	-1.046	0	-315.442	-43.725
9: SO_3	69.998	6.611	-1.937	0	-423.384	-154.578
10: H_2SO_4	117.596	17.184	-3.845	0	-783.850	-398.067
11: HS	28.995	3.598	0.201	0	131.200	30.465
12: H_2S	34.911	10.686	-0.448	0	-32.887	1.142
13: Cl	23.736	-1.284	-0.126	0	113.853	29.624
14: Cl_2	36.610	1.079	-0.272	0	-11.875	12.638
15: HCl	26.527	4.602	0.109	0	-100.056	35.010
16: H	20.786	0	0	0	211.768	-3.714
17: H_2	26.882	3.586	0.105	0	-7.823	-22.966
18: O	21.008	-0.247	0.088	0.071	243.211	41.929
19: O_2	29.154	6.477	-0.184	-1.017	-9.589	36.116
20: OH	0	0	0	0	60.0	220.0
21: H_2O	34.376	7.841	-0.423	0	-253.871	-11.750
22: N_2	30.418	2.544	-0.238	0	-9.982	16.203

Vapor pressure:
Vapor pressures are calculated by the method given by Knacke *et al.* (1991) and plotted in Figure C4.
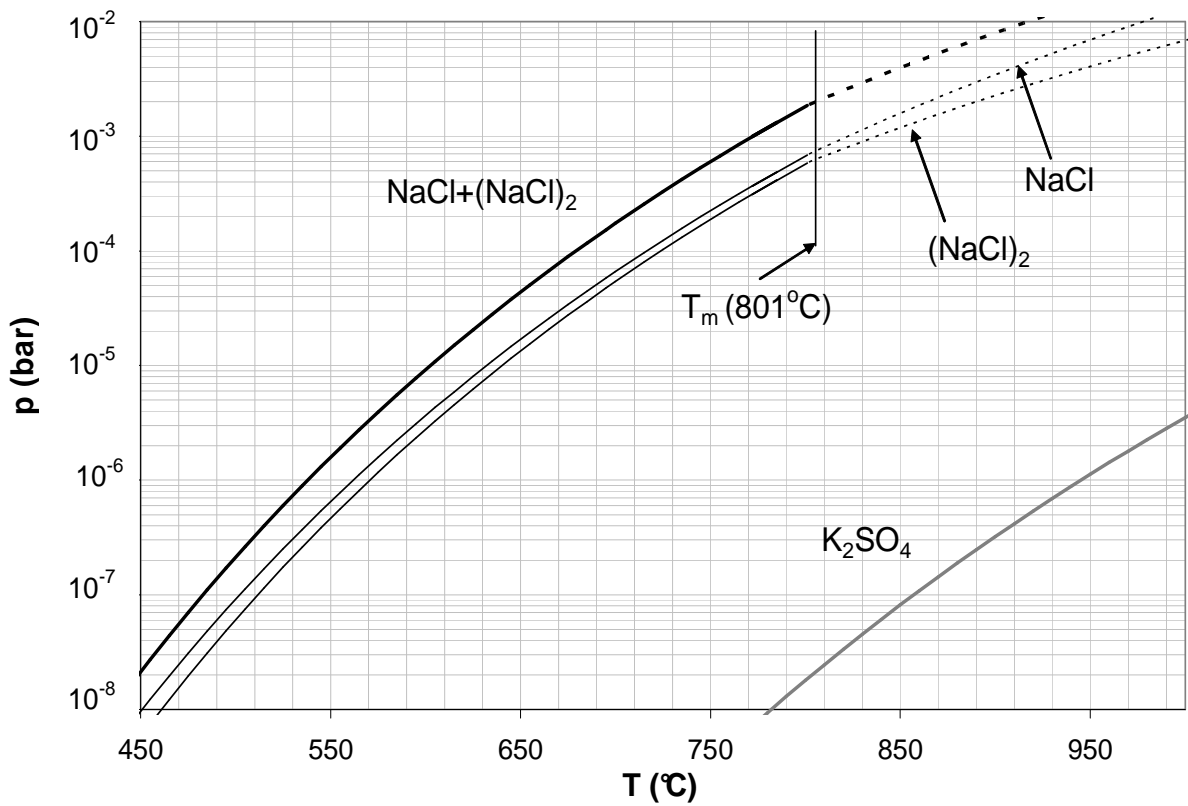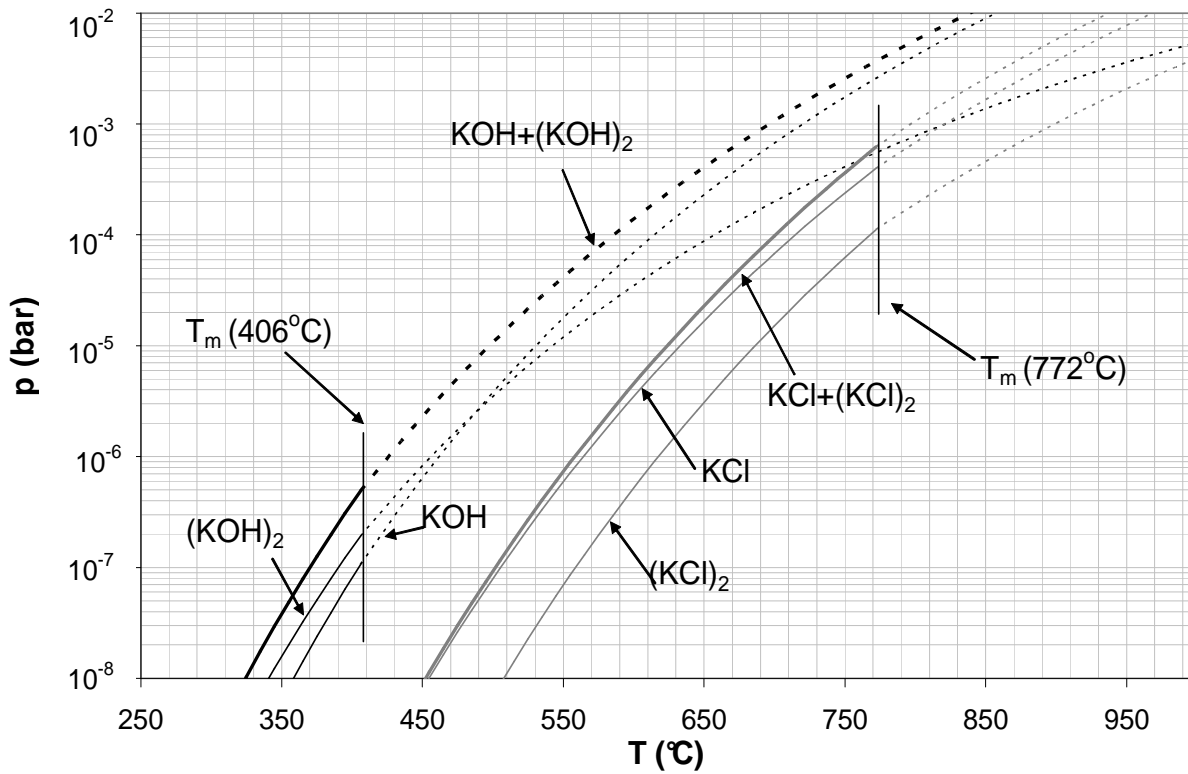
Figure C4. *Vapor pressure of alkali components. Based on Knacke et al. (1991).*

Appendix D   Program for K₂SO₄ nucleation

*The simulation of aerosol formation by a 2-step procedure as described in Chapter 3 was done with 2 different FORTRAN codes. The first code, shown in the following, calculates the formation of K₂SO₄ by a first order reaction of SO₂, and the homogeneous nucleation of this compound. The most important changes to the MONAERO-code are marked with **bold**. An example of an input file is given first.*

Input file is shown on this page and the rest of the program on the following pages:

750.0D0
NUMBER OF LINEAR TEMPERATURE ZONES NZON
7
LOCATION OF THE NZON+1 TEMPERATURE ELEMENTS (MM)
0.1 157 277 422 572 712 862 1012
LOCATION OF THE NZON ZONE ENDPOINTS (MM)
157 277 422 572 712 862 1012
THE NZON+1 MEASURED TEMPERATURES (øC):
750 750 950 800 650 500 350 200 200
TOTAL TUBE LENGTH (MM):
1012
TUBE DIAMETER (MM):
25
SATURATED GASFLOW (L/MIN AT 20 C):
0
SEED GASFLOW (L/MIN AT 20 C):
3.5
NUMBER OF COLLOCATION POINTS:
20
NUMBER OF SIZE SECTIONS ON EACH COLLOCATION LINE:
1
TOTAL PARTICLE CONCENTRATION IN MIXED GAS AT 20 C (#/CM**3):
0.0D-5
PERCENTAGE AT EACH SIZE SECTION:
100
DIAMETER OF SEED NUCLEI FOR EACH SIZE SECTION (UM)
0.001
FILE NAME OF PENETRATION FILE AND DISTFIT FORMAT SEED NUCLEI INLET DIST. FILE
'pen1.dat' '@220498.S02' 1.d0
INDICATOR MUST BE SET TO 1 IF EXPERIMENTAL SEED NUCLEI DIST. IS TO BE READ
0
INITIAL DIMENSIONLESS STEP LENGTH FOR INTEGRATION:
1.D-4
INTEGRATION TOLERANCE:
5.D-4
MINIMUM STEP LENGTH DZSMAL:
2.0D-4

```
C******************************************************************
C  K2SO4_AERO_reaction
C******************************************************************
C  PROGRAM FOR SIMULATION OF A LAMINAR FLOW AEROSOL CONDENSER
C  WITH ONE COMPONENT (MONOMER) CONDENSATION
C   Kinetics for K2SO4 formation from SO2 has been added and the physical
C   properties and relevant nucleation parameters for K2SO4 are included
C
C  COMPONENT: Potassium sulphate (K2SO4)
C
C MADE BY OLE SIMONSEN, DEPT. OF CHEM. ENG., TECHN. UNIV. OF DK
C LAST REVISION: DECEMBER 1992
C
C ADDITIONAL CHANGES BY LARS BALZER NIELSEN, JANUARY 1995, AND
C SEPT. 1996
C
C ADDITIONAL CHANGES BY JOAKIM REIMER JENSEN, APRIL 1998
C
C  ADDITIONAL CHANGES BY Jacob H. Zeuthen, June 2006
C

      PROGRAM K2SO4_AERO_reaction

      IMPLICIT DOUBLE PRECISION(A-H,O-Z)
      CHARACTER *60 PENFILE,INFILE
C---DIMENSIONS: ICAR=MAX. NUMBER OF SIZE SECTIONS, ICOL=MAX. NUMBER
C         OF COLLOCATION POINTS:---
      PARAMETER (ICAR=20000,ICOL=20,IZON=25)
      DIMENSION XNO(ICAR),Y(ICAR),NCAR(ICOL),RAD(ICOL),GR(ICOL)
      DIMENSION TRN(ICAR),Y4(ICAR)
      DIMENSION W(4*ICOL*(2*ICAR-2*ICOL-3)+16*ICAR+2)
      DIMENSION CMAT(ICOL,ICOL),CBOUND(ICOL),SUMF(ICOL),GV(ICOL+2)
      DIMENSION XR0(120),XNSEED(120),PLOT(ICOL,1000)
      DIMENSION ALOGPLOT(ICOL,1000)
      DIMENSION AMAT(ICOL,ICOL),ABOUND(ICOL),ASUM(ICOL),ROOT(ICOL)
      DIMENSION SUMT1(ICOL),SUMT2(ICOL),SUMP1(ICOL),SUMP2(ICOL)
      DIMENSION FACP(ICOL),FACT(ICOL),BIG(ICOL),BIGAP(ICOL)
      DIMENSION BIGAT(ICOL),DLIQ(ICAR),IDFO(ICAR),XMINI(ICAR)
      DIMENSION XNUC(ICOL),XHOLD(ICOL),IDHOM(ICOL),RHOM(ICOL)
      DIMENSION DN(ICOL,ICAR),DLDP(ICOL,ICAR),CONC(ICOL,ICAR)
      DIMENSION RAHOM(ICOL,ICAR),XRHOM(ICOL,ICAR),NHOM(ICOL),NSEED(ICOL)
      DIMENSION RSEED(ICOL,ICAR),XRSEED(ICOL,ICAR),AX(10000),
     &    ABSRAD(ICOL)
      COMMON/UDS/ZOLD
      COMMON/GAUSS/GV
      COMMON/NNNN/NCOL,NCAR
      COMMON/YI4/Y4
```

```
      COMMON/XKON/XK1,XK2,XKDG,XK4,XK5,XK6,XK7,XK8,XK9,XK11
      COMMON/XTEAFH/XKE1,XKE2,XKE3,XBE1
      COMMON/XTAFH/XB2,XB3,XB4,XB5,XB6,XB7,XB8,XB9,XB10,XB11,XCOND
      COMMON/DXTAFH/DXB8,DXB9,DXB10
      COMMON/GAS/XMGAS
      COMMON/PT/XOP,TOP,T1,CKON
      COMMON/ANTAL/XNO,TRN,GR
      COMMON/FOVER/O1,O2,O3
      COMMON/FCONDU/C1,C2,C3,C4
      COMMON/FDAMP/T0,P0
      COMMON/FDENS/D1,D2
      COMMON/FDIFF/DI1,XMYD
      COMMON/FVISCO/V1,V2,V3
      COMMON/FVARME/VA1,VA2,VA3
      COMMON/FVARMH/VS1,VS2,VS3
      COMMON/STICK/SA
      COMMON/UNDIM/AMAX,XTUBE
      COMMON/COLLOK/CMAT,CBOUND,AMAT,ABOUND,ASUM,ROOT
      COMMON/RADIUS/RAD
      COMMON/WALL/PW,TW,PP,SUMAM,SUMAMT
      COMMON/SUMMA/SUMF
      COMMON/DIVDF/SUMT1,SUMT2,SUMP1,SUMP2,FACP,FACT,BIG,BIGAP,BIGAT
      COMMON/DIV2/DLIQ
      COMMON/PDIV/PPP
      COMMON/IDFOR/IDFO,XMINI
      COMMON/WALLCO/ZW(IZON+1),EQMAT(IZON,2),TWW(IZON+1)
      COMMON/ZONE/NZON,ZEND(IZON)
      COMMON/ACID/XMOLEA,XMASSA
      COMMON/LARS/ADDS,EPS1,NFUN,CONT(ICAR)
      COMMON/SIZEDIS/DLDP,DN
C     COMMON/ARAD/ABSRAD,AX,IPCOUNT,PLOT,ALOGPLOT
C-----JRJ D. 10/6-98
      COMMON/ARAD/ABSRAD,AX,IPCOUNT,PLOT,ALOGPLOT,AXOLD,AXOLD2
      COMMON/SEED/NSECT,XNTOT,XNSEED,XR0,PENFILE,INFILE,FACTSIM
C-----JRJ D.3/4-98 (BENYTTES TIL UDSKRIVNING AF OVERM'TNINGSGRAD)
      COMMON/MAX/SMAX,HOMMAXOLD,POSIMAX,TEMMAX,HOMMAX
C
C  IDFO(I) = I ORIGINAL CHACTERISTIC (HET. NUCL.) CAN ONLY EVAPORATE
C         TO RADIUS = XR0(I) (SET IN XMINI(NN)).
C  IDFO(I) = 0 HOM. NUCL. CHARACTERISTIC, CAN EVAPORATE COMPLETELY
C  IDFO(I) =-1 THIS CHARACTERISTIC IS REMOVED IN NEXT INTEGRATION STEP
C         (SEE SUBROUTINE REMCAR).
C  I RUNS OVER ALL CHARACTERISTICS
C
      COMMON/CONC/XTOT
      COMMON/HOMOG/XH1,XH2,XH3
      COMMON/HNTEST/XNUC,XHOLD,RHOM,VALUE,IDHOM,IDTOT
```

```
      COMMON/ADDCA/XAD1,XAD2
      COMMON/WALLOS/AMWAL(ICOL+2),CWALL,XKOLD
      COMMON/CAROUT/ICARUT
      COMMON/WALTEM/WC(6),WK(6),TFIN,TEPS,ZD1,ZD2,ZD3,ZD4,TWC(2)
      COMMON/DIVKUL/WALCON,GASIND
      COMMON/OUTNO/IUD
      COMMON/DIAM/XDIAM
      COMMON/HEATCO/XLCON
C=====================================================
C     CALL CONDUP
C=====================================================
C---MAXIMUM TOTAL NUMBER OF EQUATIONS:---
      NTOTAL=4*ICOL*(2*ICAR-2*ICOL-3)+16*ICAR+2
C---IN- AND OUTPUT DEVICE NUMBERS:---
      IUD=2
      IND=3
      IND2=3
C---FILE NAMES:---
C=========================================================
C     OPEN(20,FILE='VAR2.DAT')
C=========================================================
      OPEN(IUD,FILE='DATA1.out')
      OPEN(IND,FILE='C:\Fortran\laminar\INPUT2.DAT')
      OPEN(10,FILE='HOM1.dat')
      OPEN(11,FILE='SEED1.dat')
      OPEN(12,FILE='TEMPERATURE.DAT')
      OPEN(13,FILE='OVER.DAT')
      OPEN(8,FILE='NUK.dat')
      OPEN(9,FILE='NUK_log.dat')
      OPEN(7,FILE='FORDELING.dat')
C---INPUT DATA:---
c     READ(IND2,*)
c     READ(IND2,*)
      READ(IND,*)THOT
      WRITE(IUD,*)'T (SATURATOR)=',THOT,' C'
      WRITE(6,*)'SATURATOR TEMPERATURE (C):',THOT
      THOT=THOT+273.15D0
      READ(IND2,*)
      READ(IND,*)NZON
      WRITE(IUD,*)'NUMBER OF ZONES: ',NZON
      WRITE(6,*)'NUMBER OF ZONES: ',NZON
      READ(IND2,*)
      READ(IND,*)(ZW(I),I=1,NZON+1)
      READ(IND2,*)
      READ(IND,*)(ZEND(I),I=1,NZON)
      READ(IND2,*)
      READ(IND,*)(TWW(I),I=1,NZON+1)
```

```
      READ(IND2,*)
      TEND=TWW(NZON+1)+273.15D0
      READ(IND,*)XTUBE
      WRITE(IUD,*)'TUBE LENGTH=',XTUBE,' MM'
      WRITE(6,*)'TOTAL TUBE LENGTH (MM):',XTUBE
      XTUBE=XTUBE/1.D3
      READ(IND2,*)
      READ(IND,*)XDIAM
      WRITE(IUD,*)'TUBE DIAMETER=',XDIAM,' MM'
      WRITE(6,*)'TUBE DIAMETER (MM):',XDIAM
      XDIAM=XDIAM/1.D1
      READ(IND2,*)
      READ(IND,*)XFLOWH
      WRITE(IUD,*)'SATURATED GAS FLOW=',XFLOWH,' L/MIN AT 20 C'
      WRITE(6,*)'SATURATED GAS FLOW (L/MIN AT 20 C):',XFLOWH
C---FLOW AT THOT:---
      XFLOWH=XFLOWH*THOT/293.15D0
      READ(IND2,*)
      READ(IND,*)XFLOWK
      WRITE(IUD,*)'SEED-GASFLOW=',XFLOWK,' L/MIN AT 20 C'
      WRITE(6,*)'SEED-GASFLOW (L/MIN AT 20 C):',XFLOWK
C---FLOW AT THOT:---
      XFLOWK=XFLOWK*THOT/293.15D0
      XFLOW=XFLOWH+XFLOWK
      READ(IND2,*)
      READ(IND,*)NCOL
      WRITE(IUD,*)'NUMBER OF COLLOCATION POINTS:',NCOL
      WRITE(6,*)'NUMBER OF COLLOCATION POINTS:',NCOL
      READ(IND2,*)
      READ(IND,*)NSECT
      WRITE(IUD,*)'NUMBER OF SIZE SECTIONS=',NSECT
      WRITE(6,*)'NUMBER OF SIZE SECTIONS:',NSECT
      READ(IND2,*)
      READ(IND,*)XNTOT
      WRITE(IUD,*)'TOTAL CONC. IN MIXED GAS AT 20 C=',XNTOT,' CM*-3'
      WRITE(6,*)'TOTAL PARTICLE CONCENTRATION IN MIXED GAS AT 20 C:',
     !XNTOT
C     WRITE(6,*)'PERCENTAGE AT EACH SIZE SECTION:'
      READ(IND2,*)
      READ(IND,*)(XNSEED(I),I=1,NSECT)
C     WRITE(IUD,*)'PERCENTAGE AT EACH SIZE SECTION:'
C     WRITE(IUD,*)(XNSEED(I),I=1,NSECT)
C     WRITE(6,*)(XNSEED(I),I=1,NSECT)
C     WRITE(6,*)'DIAMETER OF SEED NUCLEI FOR EACH SIZE SECTION (UM)'
      READ(IND2,*)
      READ(IND,*)(XR0(I),I=1,NSECT)
C     WRITE(IUD,*)'DIAMETER OF SEED NUCLEI FOR EACH SIZE SECTION (UM)'
```

```
C     WRITE(IUD,*)(XR0(I),I=1,NSECT)
C     WRITE(6,*)(XR0(I),I=1,NSECT)
      READ(IND2,*)
      READ(IND,*)PENFILE,INFILE,FACTSIM
      READ(IND2,*)
      WRITE(6,*)PENFILE,INFILE
      WRITE(IUD,*)PENFILE,INFILE
      READ(IND,*)INDIC
      IF(INDIC.EQ.1)CALL SEED_READ
      DO 10 I=1,NSECT
C---CONCENTRATION AT THOT:---
      XNSEED(I)=XNTOT*XNSEED(I)/100.D0*293.15D0/THOT
C---CONVERSION TO RADIUS:---
      XR0(I)=XR0(I)/2.D0
   10 CONTINUE
      WRITE(6,*)'TOTAL SEED CONCENTRATION (CM**-3)',XNTOT
      WRITE(IUD,*)'TOTAL SEED CONCENTRATION (CM**-3)',XNTOT
      WRITE(IUD,*)'SEED CONC. (CM**-3 AT THOT) FOR EACH SIZE SECTION:'
      WRITE(6,*)'SEED CONC. (CM**-3 AT THOT) FOR EACH SIZE SECTION:'
      DO 12 I=1,NSECT
      WRITE(IUD,*)XNSEED(I)
      WRITE(6,*)XNSEED(I), 'seed'
   12 CONTINUE
C---TOTAL NUMBER OF EQUATIONS:---
      N=NCOL*NSECT+2*NCOL+2
      READ(IND2,*)
      READ(IND,*)STEP
      WRITE(IUD,*)'INITIAL STEP LENGTH FOR INTEGRATION=',STEP
      WRITE(6,*)'INITIAL STEP LENGTH FOR INTEGRATION (DIM.LESS):',STEP
      READ(IND2,*)
      READ(IND,*)EPS
      WRITE(IUD,*)'INTEGRATION TOLERANCE=',EPS
      WRITE(6,*)'INTEGRATION TOLERANCE',EPS
      READ(IND,*)
      READ(IND,*)DZSMAL
      WRITE(IUD,*)'MINIMUM STEP LENGTH=',EPS
      WRITE(6,*)'MINIMUM STEP LENGTH=',EPS
      AMAX=1.D0
      AMAX=AMAX*1.D-6
      DO 876 I=1,NZON+1
      TWW(I)=(TWW(I)+273.15D0)/THOT
      ZW(I)=ZW(I)/(XDIAM*1.D-2)*2.D0/1.D3
  876 CONTINUE
      DO 877 I=1,NZON
      ZEND(I)=ZEND(I)/(XTUBE*1.D3)
  877 CONTINUE
      IPCOUNT=1
```

```
C---NUMERICAL CONSTANTS:---
      ADDS=1.D0
      EPS1=1.D-6
C---PHYSICAL CONSTANTS:---
      PI=3.141592654D0
      R=8.314D0
      XKB=1.38D-23
      XNA=6.02D23
C---INITIALIZING:---
      CWALL=0.D0
      XTOT=0.D0
      ZOLD=0.D0
C---TOTAL PRESSURE:---
      PT=1.D5
C
C COMPONENT-SPECIFIC PARAMETERS
*******************************************
C
C---MOLEWEIGHT CONDENSING COMPONENT (KG/MOLE)
      XM=174.25E-3
C---HEAT OF CONDENSATION, CONDENSING COMPONENT (J/MOL):---
      XLCON=1.243D5
C*******************************************
C
C
C---MOLEWEIGHT  CARRIER GAS (N2) (Kg/mol):---
      XMGAS=2.8D-2
C---CONSTANTS:---
      T0=THOT
      P0=1.D0
      P0=DAMP(1.D0)
C        write(*,*)P0
878      CONTINUE
         Write(6,*)P0, THOT,
      PPP=PT/P0
      WALCON=-4.D0*PI*P0*XTUBE/(R*T0)
C--- INLET FLOW CONDENSING COMPONENT MOL/S:---
      GASIND=(XFLOWH/6.D4)*P0/(R*T0)
C---INITIALIZE CONSTANT FOR PHYSICAL PROPERTIES:---
      CALL INITPP(T0,XM,XMGAS)
C---FLOW-TEST:---
      AREA=PI*(XDIAM/200.D0)**2
      VOLUM=XTUBE*AREA
      VZA=XFLOW/6.D4/AREA
      DN2=PT*XMGAS/(R*TEND)
      RE=VZA*(XDIAM/100.D0)*DN2/(VISCOS(TEND/THOT))
      SC=VISCOS(TEND/THOT)/(DN2*DIFF(TEND/THOT))
```

```
      PE=SC*RE
      WRITE(IUD,*)'REYNOLD=',RE
      WRITE(IUD,*)'PECLET =',PE
      WRITE(IUD,*)'L/dt=',XTUBE*100.D0/XDIAM
      WRITE(6,*)'L/dt=',XTUBE*100.D0/XDIAM
      LCON=1
      LCON2=1
      LAM=1
      IF (RE.GT.2100.D0) LAM=0
      IF (PE.LT.100.D0) LCON=0
      IF (PE.GE.100.D0.AND.XTUBE/XDIAM.LT.PE*1.5D-3) LCON2=0
      IF (LAM.EQ.0) WRITE(IUD,*)'TURBULENT FLOW !!! (RE>2100)'
      IF (LCON.EQ.0) WRITE(IUD,*)'AXIAL DIFF. SIGNIFICANT !(PE SMALL)'
      IF (LCON2.EQ.0) THEN
        WRITE(IUD,*)'FIGURE 19, CHAP.9 IN LEVENSPIEL IS NOT VALID SINCE'
        WRITE(IUD,*)'L/dt IS NOT >> ',PE/33.D0
      ENDIF
C---CONSTANTS FOR VARIOS ROUTINES:---
      DG0=PT*XM/(R*T0)
      XKE1=P0*DSQRT(XMGAS/(2.D0*PI*R*T0))
      XKE2=P0*DSQRT(XM/(2.D0*PI*R*T0))
      XKE3=2.D0*AMAX
      XK1=2.D0*XM/(R*T0*AMAX)
      XK2=XTUBE*XM/(XMGAS*AMAX*AMAX)
      XKDG=XMGAS*PT/(R*T0)
      XK4=2.D0*AMAX*AMAX/(XM*XTUBE*T0)
      XK5=-4.D0*PI/XM
C---XK6 NEGATIVE, BECAUSE XK5 IS USED FOR CALCULATION OF XB6:---
      XK6=-1.D0/T0
      XR2=(XDIAM/200.D0)**2
      XK7=4.D0*XTUBE*XMGAS/XR2
      XK8=4.D0*XTUBE/XR2
      XK9=PT/(R*T0)
      XK11=2.D0*DSQRT(PI*XM/(8.D0*R*T0))/AMAX
      XOP=2.D0-XMYD
      TOP=XMYD-1.D0
C---CONSTANTS FOR CALCULATION OF HOMOGENEOUS NUCLEATION:---
      XH1=2.D0*P0*P0*XM/(XKB*R*T0*T0*DSQRT(2*PI*XM/XNA))
      XH2=-16.D0*PI*XM*XM/(3.D0*XKB*R*R*T0*T0*T0)
      XH3=2.D0*XM/(R*T0)
      XAD1=4.D0*PI*R*T0/(3.D0*XM*P0)
      XAD2=AMAX*AMAX*AMAX*XTUBE*XKDG/2.D0
C---INITIALIZING HOM.NUCL. CHECK VARIABLE:---
      DO 40 I=1,NCOL
        RHOM(I)=1.D10
 40   CONTINUE
C---MINIMUM NUCLEATION RATE:---

C      VALUE=1.D4
       VALUE=1.D5
C---MINIMUM DELTA-Z SECTION (DIM.LESS):---
       DZSMAL=DZSMAL/XTUBE
       WRITE(6,*)'MINIMUM SKRIDTL'NGDE ',DZSMAL
C---MAXIMUM STEP:---
       DZBIG=5.D-2
C---
       IDADD=0
       IDTOT=0
       DO 50 J=1,NCOL
         IDHOM(J)=0
         XNUC(J)=0.D0
         XHOLD(J)=0.D0
 50   CONTINUE
      TTDIM=THOT/T0
      PP=XFLOWH*DAMP(TTDIM)/XFLOW
C---BOUNDARY CONDITIONS:---
      TW=THOT/T0
      PW=DAMP(TW)
      IF (PW.GT.PP) PW=PP
C---CALCULATION OF COLLOCATION PARAMETERS:---
      CALL INITCO(NCOL)


C*******                        *******
C*******                        *******
C******* START OF NEW WALL TEMPERATURE CALCULATIONS   *******
C*******                        *******
C*******                        *******
      CALL INIW(EQMAT)
C     DO 68 I=1,1000
C     ZT=DBLE(I)/1000.D0
C     CALL WFUN(ZT)
C     WRITE(4,*)ZT,TW*THOT-273.15,PW
C 68 CONTINUE
C---G(R) AFTER BIRD P. 46:---
      RHOGAS=XMGAS*PT/(R*THOT)
      R2=(XDIAM/200)**2
      RIL=0.D0
      DO 60 I=1,NCOL
      AI=GV(I)*AREA
      RIR=DSQRT( (AI+PI*RIL*RIL)/PI )
      ABSRAD(I)=RIR
      WRITE(6,*)ABSRAD(I)*1000.D0, 'hej1'
      VZI=2.D0*PI*VZA*(RIR**2-RIL**2-(RIR**4-RIL**4)/(2.D0*R2))/AI
      GR(I)=RHOGAS*VZI
```

```
      RIL=RIR
      Y(I)=0.0D0
      Y(I+NCOL)=1.D0
 60   CONTINUE
      Y(2*NCOL+1)=0.D0
      IREF=2*NCOL+2
      DO 70 I=1,NCOL
      DO 70 J=1,NSECT
        Y(IREF)=XR0(J)*1.D-6/AMAX
        XMINI(IREF)=XR0(J)
        XNO(IREF)=XNSEED(J)*1.D6*AMAX*AMAX*AMAX
        TRN(IREF)=(THOT+1.D0)/T0
        IDFO(IREF)=J
        IREF=IREF+1
 70   CONTINUE
      Y(N)=0.D0
      DO 80 I=1,NCOL
      NCAR(I)=NSECT
 80   CONTINUE
      ZFINE=0.D0
      DZ=DZBIG
      NPR=1
      K=1
C===============================================================
      LLLL=0
      HOMNUCOLD=0.D0
      AXOLD=0.D0
      HOMMAXOLD=0.D0
C===============================================================
C---START INTEGRATION:---
 100  CONTINUE
C===============================================================
C-----------------------------------------------------------
C   Write the dependent parameters
C-----------------------------------------------------------
C     WRITE(20,*) NSECT
C     DO 344 I=1,2*NCOL+1+NSECT*NCOL
C     DO 344 I=1,2*NCOL+1
C     WRITE(20,*) Y(I)
C     WRITE(6,766) (Y(I),I=1,NCOL)
C     WRITE(6,766) (Y(I),I=NCOL+1,2*NCOL)
C     WRITE(12,766) (Y(I),I=1,NCOL)
C     WRITE(12,766) (Y(I)*THOT,I=NCOL+1,2*NCOL)
C 766 FORMAT(20E10.3)
C 344 CONTINUE
C     ENDIF
C===============================================================
      DO 110 I=1,N
      W(I)=1.D0
 110  CONTINUE
      W(N+1)=ZFINE
      W(N+2)=ZFINE+DZ
      IF (W(N+2).GT.ZEND(K))W(N+2)=ZEND(K)
      W(N+3)=STEP
      W(N+4)=EPS
      W(N+5)=0
      ICARUT=0
C        AX2=AX(IPCOUNT)
      CALL SIRUKE(N,NPR,Y,W,P_SO2,P_SO2_0)
      ZFINE=W(N+2)
      IF (ICARUT.EQ.1) CALL REMCAR(N,Y)
      IF (IDADD.EQ.1) THEN
       CALL NEWCAR(N,Y)
       IDTOT=0
       IDADD=0
       DZ=DZBIG
       DO 120 J=1,NCOL
        IDHOM(J)=0
        XNUC(J)=0.D0
        XHOLD(J)=0.D0
 120    CONTINUE
      ELSE
       IF(IDTOT.EQ.1) THEN
        DZ=DZSMAL
        IDADD=1
       ELSE
        DZ=DZBIG
       ENDIF
      ENDIF
      IF (ZFINE.LT.ZEND(K)) GOTO 100
      K=K+1
      IF(K.LE.NZON)GOTO 100
C---END OF INTEGRATION:---
      AM3=1.D6*AMAX**3
      NN=2*NCOL+2
      XTOT=0.D0
      XTOT1=0.D0
      CDROP=0.D0
      TCOR=THOT/293.15D0
      XA1=0.D0
C--- SUMMATION OVER COLLOCATION POINTS---
      DO 200 J=1,NCOL
      NHOM(J)=0
      NSEED(J)=0
```

```
      XTLOK=0.D0
      XTL1=0.D0
      DGE=PT*XMGAS/(R*Y(J+NCOL)*T0)
      VZE=GR(J)/DGE
      FLOW=VZE*AREA*GV(J)
C--- SUMMATION OVER CHARACTERISTICS---
C---LISTING OF TOTAL CONCENTRATION---
C
      DO 210 I=NN,NN+NCAR(J)-1
      IF(IDFO(I).EQ.0)THEN
C         IF(0.EQ.0)THEN
        NHOM(J)=NHOM(J)+1
        RAHOM(J,NHOM(J))=Y(I)
        XRHOM(J,NHOM(J))=XNO(I)*GV(J)
      ELSE
        NSEED(J)=NSEED(J)+1
        RSEED(J,NSEED(J))=Y(I)
        XRSEED(J,NSEED(J))=XNO(I)*GV(J)
      ENDIF
      XTLOK=XTLOK+XNO(I)
      IF (IDFO(I).GT.0) THEN
        SVOL=4.D0*PI*((Y(I)*AMAX*1.D2)**3-(XR0(IDFO(I))*1.D-4)**3)/3.D0
        XA1=XA1+Y(I)*AMAX*XNO(I)*FLOW
        XTL1=XTL1+XNO(I)
      ELSE
        SVOL=4.D0*PI*((Y(I)*AMAX*1.D2)**3)/3.D0
      ENDIF
      CDR=SVOL*DENS(TRN(I))*XNO(I)/XM/AM3/Y(J+NCOL)
      CDROP=CDROP+CDR*FLOW
 210  CONTINUE
      NN=NN+NCAR(J)
      WRITE(IUD,201)J,XTLOK/AM3*TCOR
 201  FORMAT('ON COLL. NO.',I2,'THE CONC IS ',E15.8)
      XTOT=XTOT+XTLOK*GV(J)
      XTOT1=XTOT1+XTL1*FLOW
 200  CONTINUE
      XTOT=XTOT/AM3
      CWALL=100.D0*Y(N)*WALCON/GASIND
      PC=DAMP(TEND/T0)*P0
      GASOUT=0.D0
      DO 220 I=1,NCOL
      DGE=PT*XMGAS/(R*Y(I+NCOL)*T0)
      VZE=GR(I)/DGE
      FLOW=VZE*AREA*GV(I)
      GASOUT=GASOUT+FLOW*Y(I)*P0/(R*Y(NCOL+I)*T0)
 220  CONTINUE
      COUT=100.D0*GASOUT/GASIND
```

```
      CDROP=100.D0*CDROP/GASIND
      WRITE(IUD,9920)
      WRITE(IUD,9930)CWALL,COUT,CDROP
      XNTOT=0.D0
      DO 230 I=1,NSECT
      XNTOT=XNTOT+XNSEED(I)*TCOR
 230  CONTINUE
      XA1=1.D6*XA1/XTOT1*2.D0*DSQRT(DENS(5.D0)/1.D3)
 9920 FORMAT(34X,'WALL      GAS      AEROSOL')
 9930 FORMAT(30X,F11.5,F11.5,2X,F11.5)
 9910 FORMAT (2F14.0,3F14.5)
       WRITE(IUD,*)'TOTAL %=',CWALL+COUT+CDROP
       WRITE(IUD,9940)XTOT*TCOR
 9940 FORMAT(2X,'TOTAL CONCENTRATION =',E12.6,' AT 20øC')
      CIALT=COUT+CDROP+CWALL
C    WRITE(7,*)XNTOT,XTOT*TCOR,CWALL,CIALT,XA1,N
C---OUTPUT OF SIZE DIST TO FILE ---
      WRITE(10,*)(NHOM(I),I=1,NCOL)
C        WRITE(7,*)(NHOM(I),I=1,NCOL)
      CHKSUM=0.D0
      DO 433 J=1,NCOL
      DO 434 I=1,NCAR(J)-NSECT
      IF(XRHOM(J,I)/AM3*TCOR.LT.1.D-2)XRHOM(J,I)=1.D-2*AM3/TCOR
      WRITE(10,*)RAHOM(J,I),XRHOM(J,I)/AM3*TCOR

      CHKSUM=CHKSUM+XRHOM(J,I)/AM3*TCOR
 434  CONTINUE
      DO 435 I=1,NSECT
      IF(XRSEED(J,I)/AM3*TCOR.LT.1.D-2)XRSEED(J,I)=1.D-2*AM3/TCOR
      WRITE(11,*)RSEED(J,I),XRSEED(J,I)/AM3*TCOR
      CHKSUM=CHKSUM+XRSEED(J,I)/AM3*TCOR
 435  CONTINUE
 433  CONTINUE
C    WRITE(10,*)CHKSUM
C---OUTPUT OF HOM. NUCLEATION RATES TO FILE---
      DO 460 I=1,IPCOUNT
      DO 465 J=1,NCOL
      WRITE(8,470)AX(I),1.D3*ABSRAD(J),PLOT(J,I)
      WRITE(9,470)AX(I),1.D3*ABSRAD(J),RAHOM(J,I)
       IF (J .EQ. 1) THEN
              WRITE(8,470) AX(I),0.0D0 ,PLOT(J,I)
              WRITE(9,470) AX(I),0.0D0 ,RAHOM(J,I)
           ENDIF
 465  CONTINUE
 460  CONTINUE
      DO 480 I=1,IPCOUNT
      DO 485 J=1,NCOL
```

```
      WRITE(8,470)AX(I),-1.D3*ABSRAD(J),PLOT(J,I)
      WRITE(9,470)AX(I),-1.D3*ABSRAD(J),RAHOM(J,I)
            IF (J .EQ. 1) THEN
                  WRITE(8,470) AX(I),0.0D0 ,PLOT(J,I)
                  WRITE(9,470) AX(I),0.0D0 ,ALOGPLOT(J,I)
            ENDIF
  485 CONTINUE
  480 CONTINUE
  470 FORMAT(3(1X,E10.3))
C---UDSKRIVNING AF MAX-V'RDIER
      WRITE(2,*) SMAX,POSIMAX,TEMMAX,HOMMAX
C---CLOSE FILES:---
      CLOSE(2)
      CLOSE(3)
      CLOSE(10)
      CLOSE(11)
      CLOSE(12)
      CLOSE(8)
      CLOSE(9)
      CLOSE(13)
C====================================================================
C     CLOSE(20)
C====================================================================
      STOP
      END
C++++++++++++++++++++++++++++++++++++++++++++++++++++++++++++++++++++
      SUBROUTINE SEED_READ
      IMPLICIT DOUBLE PRECISION (A-H,O-Z)
      CHARACTER *60 PENFILE,INFILE
      PARAMETER(NDA=120)
      DIMENSION FCOR(NDA),DP(NDA),ANUM(NDA),XNSEED(NDA),XR0(NDA)
      DIMENSION D_TEMP(NDA),TEMP(NDA),DT(NDA),XORI(NDA)
      DIMENSION FORD1(NDA),FORD2(NDA)
      COMMON/SEED/NSECT,XNTOT,XNSEED,XR0,PENFILE,INFILE,FACTSIM
      XNTOT=0.D0
      OPEN(12,FILE=PENFILE)
      OPEN(13,FILE=INFILE)
c     OPEN(14,FILE='TESTSEED.DAT')
      READ(13,*)
      READ(13,*)NSECT
      DO 10 I=1,6
   10 READ(13,*)
      DO 20 I=1,NSECT
      READ(12,*)FCOR(I)
      READ(13,*)DP(I),ANUM(I)
      ANUM(I)=ANUM(I)*FCOR(I)*FACTSIM
      XNTOT=XNTOT+ANUM(I)
   20 CONTINUE
      READ(13,*)DP(I)
      DHMIN=DP(1)
      DHMAX=DP(I)
C---THE NUMBER OF DISCRETE SEED NUCLEI SECTIONS IS REDUCED TO N_SEED
C     WRITE(6,*)'INPUT #SECTIONS IN SEED DIST'
C     READ(6,*)N_SEED
      N_SEED=23
      D_TEMP(1)=DHMIN
      D_TEMP(N_SEED+1)=DHMAX
      DO 25 I=1,N_SEED
      TEMP(I)=0.D0
C---CALCULATE INTERVAL DIAMETERS IN REDUCED DISCRETE DISTRIBUTION
      D_TEMP(I+1)=(D_TEMP(I)**N_SEED*DHMAX/DHMIN)**(1.D0/N_SEED)
   25 CONTINUE
C---CALCULATE CONCENTRATIONS IN REDUCED SIZE INTERVALS
      DO 70 I=1,NSECT
      XORI(I)=DSQRT(DP(I)*DP(I+1))
      FORD1(I)=ANUM(I)/(DLOG(DP(I+1)/DP(I)))
      DO 80 K=1,N_SEED
      IF(DP(I).GT.D_TEMP(K).AND.DP(I).LT.D_TEMP(K+1))THEN
       TEMP(K)=TEMP(K)+ANUM(I)
       GOTO 70
      ENDIF
   80 CONTINUE
   70 CONTINUE
      DO 30 I=1,N_SEED
      XR0(I)=DSQRT(D_TEMP(I)*D_TEMP(I+1))/1.D3
      XNSEED(I)=1.D2*TEMP(I)/XNTOT
      FORD2(I)=TEMP(I)/(DLOG(D_TEMP(I+1)/D_TEMP(I)))
      DT(I)=DSQRT(D_TEMP(I)*D_TEMP(I+1))
c     WRITE(14,*)XORI(I),FORD1(I),DT(I),FORD2(I)
   30 CONTINUE
c     DO 21 I=N_SEED+1,NSECT
c     WRITE(14,*)XORI(I),FORD1(I)
c  21 CONTINUE
      NSECT=N_SEED
      RETURN
      END
C++++++++++++++++++++++++++++++++++++++++++++++++++++++++++++++++++++
      SUBROUTINE INITPP(T0,XM,XMGAS)
C
C CONSTANTS FOR CALCULATION OF PHYSICAL PROPERTIES
c SOME PARAMETERS ARE COMPONENT-SPECIFIC
C
      IMPLICIT DOUBLE PRECISION (A-H,O-Z)
      COMMON/FOVER/O1,O2,O3
```

```
      COMMON/FCONDU/C1,C2,C3,C4
      COMMON/FDENS/D1,D2
      COMMON/FDIFF/DI1,XMYD
      COMMON/FVISCO/V1,V2,V3
      COMMON/FVARME/VA1,VA2,VA3
      COMMON/FVARMH/VS1,VS2,VS3
      COMMON/STICK/SA
      COMMON/STICK2/SAS1
C---CONSTANTS FOR CONDUCTIVITY OF GAS (N2):---
      C1=3.919D-4
      C2=9.816D-5
      C3=-5.067D-8
      C4=1.504D-11
C---CONSTANTS FOR VISCOSITY OF GAS (N2):---
      V1=4.8652D-6
      V2=4.7826D-8
      V3=1.1763D-11
C---CONSTANTS FOR HEAT CAPACITY OF GAS (N2):---
      VA1=2.727D1
      VA2=4.93D-3
      VA3=3.326D4
C
C     COMPONENT-SPECIFIC PARAMETERS
C***************************************************************
C---CONSTANTS FOR DENSITY OF DROPLETS (CONDENSING COMPONENT):---
      D1=DENSIT(293.15D0/T0)
      D2=0.D0

C---CONSTANTS FOR DIFFUSION COEFFICIENT OF CONDENSING COMPONENT
C   THE DIFFUSION COEFICIENT EXPRESSION MUST BE OF THE FORM
C     A*T**B
      DI1=0.566D-10
      XMYD=2.00
C---CONSTANTS FOR HEAT CAPACITY OF CONDENSING COMPONENT:---
      VS1=39.940D0
      VS2=2.5468D-2
      VS3=3.64D+5
C***************************************************************
C---2/STICKING COEFFICIENT CONDENSING COMPONENT (value is assumed):
      SAS1=1.d0
      SA=2.D0/SAS1
C---DIMENSIONLESS CONSTANTS:---
      C2=C2*T0
      C3=C3*T0*T0
      C4=C4*T0*T0*T0
      DI1=DI1*T0**XMYD
      V2=V2*T0
```

```
      V3=V3*T0*T0
C---SPECIFIC HEAT CAPACITY:---
      VA1=VA1/XMGAS
      VA2=VA2*T0/XMGAS
      VA3=VA3/(T0*T0)/XMGAS
      RETURN
      END
C++++++++++++++++++++++++++++++++++++++++++++++++++++++++++++++++
      SUBROUTINE WFUN(DZZ)
C
C CALCULATES THE WALL TEMPERATURE AND THE PARTIAL PRESSURES
C
C NOTE! LINEAR TEMPERATURE PROFILES
      IMPLICIT DOUBLE PRECISION (A-H,O-Z)
      PARAMETER(IZON=25)
      COMMON/START/Y10,Y20,PT
      COMMON/WALL/PW,TW,PP,SUMAM,SUMAMT
      COMMON/DIAM/XDIAM
      COMMON/UNDIM/AMAX,XTUBE
      COMMON/ZONE/NZON,ZEND(IZON)
      COMMON/WALLCO/ZW(IZON+1),EQMAT(IZON,2),TWW(IZON+1)
      ZZ=DZZ*XTUBE/(XDIAM*1.D-2)*2.D0
      DO 10 I=NZON,2,-1
            IF(DZZ.GT.ZEND(I-1))THEN
      TW=EQMAT(I,1)*ZZ+EQMAT(I,2)
      GOTO 20
      ELSE
      ENDIF
   10 CONTINUE
      TW=EQMAT(1,1)*ZZ+EQMAT(1,2)
   20 CONTINUE
C---MOLEFRACTIONS WALL FILM:---
      PW=DAMP(TW)
      IF (PW.GT.PP) PW=PP
      RETURN
      END
C++++++++++++++++++++++++++++++++++++++++++++++++++++++++++++++++
      SUBROUTINE WDFUN(DZZ,DTDZ,DPDZ)
C
C CALCULATES THE DERIVATIVES OF THE WALL TEMPERATURE AND
C THE PARTIAL PRESSURE
C
C NOTE! LINEAR TEMPERATURE PROFILES
      IMPLICIT DOUBLE PRECISION (A-H,O-Z)
      PARAMETER(IZON=25,ICAR=20000)
      COMMON/START/Y10,Y20,PT
      COMMON/WALL/PW,TW,PP,SUMAM,SUMAMT
```

D–9

```
      COMMON/DIAM/XDIAM
      COMMON/UNDIM/AMAX,XTUBE
      COMMON/ZONE/NZON,ZEND(IZON)
      COMMON/WALLCO/ZW(IZON+1),EQMAT(IZON,2),TWW(IZON+1)
      COMMON/LARS/ADDS,EPS1,NFUN,CONT(ICAR)
      TEPS=1.D-4
      IZ=1
      Z=DZZ*XTUBE/(XDIAM*1.D-2)*2.D0
      DO 10 I=NZON,2,-1
      IF(DZZ.GT.ZEND(I-1))THEN
      DTWZ=EQMAT(I,1)
      GOTO 20
      ELSE
      ENDIF
   10 CONTINUE
      DTWZ=EQMAT(1,1)
   20 CONTINUE
      DTDZ=DTWZ*XTUBE/(XDIAM*1.D-2)*2.D0
C    DT=(TW+ADDS)*EPS1
      DT=(TW)*EPS1
      DP=DAMP(TW+DT)
      IF (DP.GT.PP)THEN
       DPDZ=0.D0
      ELSE
       DPDZ=DTDZ*(DP-PW)/DT
      ENDIF
      RETURN
      END
C++++++++++++++++++++++++++++++++++++++++++++++++++++++++++++++++++++
      SUBROUTINE INIW(WMAT)
C
C CALCULATES SLOPES AND INTERSECTIONS OF THE NZON LINEAR
TEMPERATURE
C PROFILES
C
      IMPLICIT DOUBLE PRECISION(A-H,O-Z)
      PARAMETER(IZON=25)
      COMMON/ZONE/NZON,ZEND(IZON)
      COMMON/WALLCO/ZW(IZON+1),EQMAT(IZON,2),TWW(IZON+1)
      DIMENSION WMAT(IZON,2)
      DO 10 N=1,NZON
      Z1=ZW(N+1)
      Z2=ZW(N)
      TW1=TWW(N+1)
      TW2=TWW(N)
      WMAT(N,1)=(TW1-TW2)/(Z1-Z2)
      WMAT(N,2)=TW1-WMAT(N,1)*Z1
```

```
   10 CONTINUE
      RETURN
      END


C++++++++++++++++++++++++++++++++++++++++++++++++++++++++++++++++++++
      SUBROUTINE NEWCAR(N,Y)
C
C CHECKS IF NEW SIZE SECTIONS SHOULD BE ADDED
C
      IMPLICIT DOUBLE PRECISION(A-H,O-Z)
      PARAMETER (ICAR=20000,ICOL=20)
      DIMENSION NCAR(ICOL),Y(*)
      DIMENSION XNUC(ICOL),XHOLD(ICOL),IDHOM(ICOL),RHOM(ICOL)
      COMMON/NNNN/NCOL,NCAR
      COMMON/HNTEST/XNUC,XHOLD,RHOM,VALUE,IDHOM,IDTOT
      DO 10 J=1,NCOL
      IF (IDHOM(J).EQ.1) CALL ADDCAR(J,N,Y)
   10 CONTINUE
      RETURN
      END
C++++++++++++++++++++++++++++++++++++++++++++++++++++++++++++++++++++
      SUBROUTINE ADDCAR(ID,N,Y)
C
C ADDS NEW SIZE SECTIONS
C
      IMPLICIT DOUBLE PRECISION(A-H,O-Z)
      PARAMETER (ICAR=20000,ICOL=20)
      DIMENSION NCAR(ICOL),Y(*)
      DIMENSION XNO(ICAR),TRN(ICAR),GR(ICOL),IDFO(ICAR),XMINI(ICAR)
      DIMENSION XNUC(ICOL),XHOLD(ICOL),IDHOM(ICOL),RHOM(ICOL)
      COMMON/NNNN/NCOL,NCAR
      COMMON/ANTAL/XNO,TRN,GR
      COMMON/UNDIM/AMAX,XTUBE
      COMMON/IDFOR/IDFO,XMINI
      COMMON/HNTEST/XNUC,XHOLD,RHOM,VALUE,IDHOM,IDTOT
      COMMON/ADDCA/XAD1,XAD2
      NCAR(ID)=NCAR(ID)+1
      N=N+1
C    WRITE(6,*)'NEW N:',N
      Y(N)=Y(N-1)
      JJ=N-1
      DO 10 I=NCOL,ID+1,-1
      DO 10 J=NCAR(I),1,-1
      JJ1=JJ-1
      TRN(JJ)=TRN(JJ1)
      XNO(JJ)=XNO(JJ1)
```

```
      Y(JJ)=Y(JJ1)
      IDFO(JJ)=IDFO(JJ1)
      XMINI(JJ)=XMINI(JJ1)
      JJ=JJ1
   10 CONTINUE
      TRN(JJ)=1.01D0*Y(ID+NCOL)
C     WRITE(6,*)XNUC(ID)
      XNO(JJ)=XNUC(ID)*XAD2/GR(ID)
C---THE CRITICAL SIZE IS INCREASED WITH 25% TO INITIALIZE GROWTH:---
      Y(JJ)=1.25D0*RHOM(ID)/AMAX
      IDFO(JJ)=0
      XMINI(JJ)=0.D0
      NT=ID+NCOL
      Y(ID)=Y(ID)-XAD1*XNUC(ID)*((1.25D0*RHOM(ID))**3)*DENS(Y(NT))
      RETURN
      END
C++++++++++++++++++++++++++++++++++++++++++++++++++++++++++++++++++++
      SUBROUTINE REMCAR(N,Y)
C
C CHECKS IF SIZE SECTIONS SHOULD BE REMOVED
C
      IMPLICIT DOUBLE PRECISION(A-H,O-Z)
      PARAMETER (ICAR=20000,ICOL=20)
      DIMENSION NCAR(ICOL),Y(*),IDFO(ICAR),XMINI(ICAR)
      COMMON/IDFOR/IDFO,XMINI
      COMMON/NNNN/NCOL,NCAR
      NM=0
      I=2*NCOL+2
      DO 20 J=1,NCOL
      IC=0
   10 CONTINUE
      IF (IDFO(I).EQ.-1) THEN
        CALL MOVCAR(I,N,Y)
        NCAR(J)=NCAR(J)-1
        NM=NM+1
      ELSE
        IC=IC+1
        I=I+1
      ENDIF
      IF (IC.LT.NCAR(J)) GOTO 10
   20 CONTINUE
      N=N-NM
C     IF (NM.NE.0) WRITE(6,*)'NY N KUN:',N
      RETURN
      END
C++++++++++++++++++++++++++++++++++++++++++++++++++++++++++++++++++++
      SUBROUTINE MOVCAR(ID,N,Y)
```

```
C
C REMOVES SIZE SECTIONS
C
      IMPLICIT DOUBLE PRECISION(A-H,O-Z)
      PARAMETER (ICAR=20000,ICOL=20)
      DIMENSION Y(*)
      DIMENSION XNO(ICAR),TRN(ICAR),GR(ICOL),IDFO(ICAR),XMINI(ICAR)
      COMMON/ANTAL/XNO,TRN,GR
      COMMON/IDFOR/IDFO,XMINI
C     TRN(N)=0.D0
C     XNO(N)=0.D0
C     IDFO(N)=0.D0
C     XMINI(N)=0.D0
      DO 10 I=ID,N-1
      TRN(I)=TRN(I+1)
      XNO(I)=XNO(I+1)
      Y(I)=Y(I+1)
      IDFO(I)=IDFO(I+1)
      XMINI(I)=XMINI(I+1)
   10 CONTINUE
      RETURN
      END
C++++++++++++++++++++++++++++++++++++++++++++++++++++++++++++++++++++++
      SUBROUTINE INITCO(N)
C
C CALCULATES WEIGHTS FOR ORTHOGONAL COLLOCATION
C
      IMPLICIT DOUBLE PRECISION (A-H,O-Z)
      PARAMETER (ICAR=20000,ICOL=20)
      PARAMETER (IC=ICOL+2)
      DIMENSION CMAT(ICOL,ICOL),CBOUND(ICOL),RAD(ICOL)
      DIMENSION R(IC),D1(IC),D2(IC),D3(IC),V1(IC),V2(IC),A(IC,IC)
      DIMENSION B(IC,IC),GV(IC)
      DIMENSION AMAT(ICOL,ICOL),ABOUND(ICOL),ASUM(ICOL),ROOT(ICOL)
      COMMON/COLLOK/CMAT,CBOUND,AMAT,ABOUND,ASUM,ROOT
      COMMON/RADIUS/RAD
      COMMON/GAUSS/GV
      COMMON/WALLOS/AMWAL(ICOL+2),CWALL,XKOLD
      COMMON/OUTNO/IUD
      ALFA=0.D0
      BETA=0.D0
      N1=N+1
C---ROOTS OF THE JACOBI POLYNOMIAL:---
      CALL XJCOBI(IC,N,0,1,ALFA,BETA,D1,D2,D3,R)
C---GAUSSIAN WEIGHTS:---
      CALL DFOPR(IC,N,0,1,IDUM,3,D1,D2,D3,R,GV)
C---WEIGHTS FOR FIRST DERIVATIVE AT WALL:---
```

```
      CALL DFOPR(IC,N,0,1,N+1,1,D1,D2,D3,R,AMWAL)
      DO 10 I=1,N
C---WEIGHTS FOR FIRST DERIVATIVE:---
      CALL DFOPR(IC,N,0,1,I,1,D1,D2,D3,R,V1)
C---WEIGHTS FOR SECOND DERIVATIVE:---
      CALL DFOPR(IC,N,0,1,I,2,D1,D2,D3,R,V2)
      DO 10 J=1,N1
      A(I,J)=V1(J)
      B(I,J)=V2(J)
   10 CONTINUE
      DO 20 I=1,N
      ROOT(I)=R(I)
      RAD(I)=DSQRT(R(I))
      CBOUND(I)=A(I,N+1)+B(I,N+1)*R(I)
      ABOUND(I)=A(I,N+1)
      DO 20 J=1,N
      CMAT(I,J)=A(I,J)+B(I,J)*R(I)
      AMAT(I,J)=A(I,J)
   20 CONTINUE
C     WRITE(IUD,*)
C     WRITE(IUD,*)'COLLOCATION POINTS DIMENSIONLESS:'
C     WRITE(IUD,9910)(RAD(I),I=1,N)
C     WRITE(IUD,*)
 9910 FORMAT(7F10.4)
      RETURN
      END
C+++++++++++++++++++++++++++++++++++++++++++++++++++++++++++++++++++++
      SUBROUTINE NEWTP(T,P,X,GR)
C
C CALCULATES PRESSURE AND TEMPERATURE DEPENDENT PARAMETERS FOR
C THE GROWTH FUNCTION
C
C CONTAINS SOME COMPONENT-SPECIFIC PARAMETERS
C
      IMPLICIT DOUBLE PRECISION (A-H,O-Z)
      COMMON/XKON/XK1,XK2,XKDG,XK4,XK5,XK6,XK7,XK8,XK9,XK11
      COMMON/XTEAFH/XKE1,XKE2,XKE3,XBE1
      COMMON/XTAFH/XB2,XB3,XB4,XB5,XB6,XB7,XB8,XB9,XB10,XB11,XCOND
      COMMON/DXTAFH/DXB8,DXB9,DXB10
      COMMON/PT/XOP,TOP,T1,CKON
      COMMON/GAS/XMGAS
      COMMON/FVARME/VA1,VA2,VA3
      COMMON/FCONDU/C1,C2,C3,C4
      COMMON/PDIV/PPP
      COMMON/FDIFF/DI1,XMYD
      COMMON/HEATCO/XLCON
C---DENSITY OF GAS:---
      DG=XKDG/T
C---THERMAL CONDUCTIVITY AT T---
      XCOND=CONDUC(T)
C---DIFFUSION COEFFICIENT:---
      D=DIFF(T)
C---HEATCAPACITY:---
      CP=VARMEK(T,X)
C COMPONENT-SPECIFIC PARAMETERS
*******************************************
C
C---MOLEWEIGHT CONDENSING COMPONENT (KG/MOLE)
      XM=174.25D-3
C---HEAT OF CONDENSATION, CONDENSING COMPONENT (J/MOL):---
      XL=1.243D5
C*******************************************
C
C---PARAMETERS:---
      PIN=PPP-P
      XBE1=DSQRT(T)/(XKE1*CP*PIN+XKE2*VARMEH(T)*P)
      XB2=XK2*D*DG*DG/GR
      XB4=XLCON*GR*XK4/DG
      XB3=-DLOG(PIN)
      XX=XK5/DG
      XB5=XMGAS*XX*PPP
      XB6=XL*XX*XK6/CP
      XB7=XK7/GR
      XB8=XK8/(GR*CP)
      XB9=XK9*D/T
      XB10=XCOND
      XB11=XK11*D/DSQRT(T)
      CKON=XOP/T**TOP
      T1=T**XOP
      T2=T*T
      T3=T2*T
      DXB8=(XK8*T*(2.D0*VA3*T-VA2*T3)/(VA1*T2+VA2*T3+VA3)**2)/GR
      DXB9=(XMYD-1.D0)*XB9/T
      DXB10=C2+2.D0*C3*T+3.D0*C4*T*T
      RETURN
      END
C+++++++++++++++++++++++++++++++++++++++++++++++++++++++++++++++++++++
      DOUBLE PRECISION FUNCTION GROWTH(Y,T,X,TRN,DL,IDF,YMIN)
C
C GROWTH FUNCTION. CALCULATES DA/DZ
C
      IMPLICIT DOUBLE PRECISION(A-H,O-Z)
      COMMON/XKON/XK1,XK2,XKDG,XK4,XK5,XK6,XK7,XK8,XK9,XK11
      COMMON/XTEAFH/XKE1,XKE2,XKE3,XBE1
```

```
      COMMON/XTAFH/XB2,XB3,XB4,XB5,XB6,XB7,XB8,XB9,XB10,XB11,XCOND
      COMMON/PT/XOP,TOP,T1,CKON
      COMMON/PDIV/PPP
      COMMON/CAROUT/ICARUT
      COMMON/STICK/SA
C---CORRECTION FACTOR BY DAHNEKE-EXPRESSION:---
C     TRN=0.9D0
C     TRN=T
      IF (Y.LE.1.D-40) GOTO 20
      XKN=XB11/Y
      XKN1=XKN+1
      FKN=XKN1/(1.D0+SA*XKN*XKN1)
C---KULMALA GROWTH EQUATION:---
      NITER=0
      DL=DENS(T)
C Write DENS(T)
      XI1=XK1/Y/DL
      XI2=XB2*FKN/Y
      XI3=XKE3*Y
C---DROPLET TEMPERATURE ITERATION:---
   10 CONTINUE
      TR=TRN
C----------------------------------------------------
C FAK can be set to zero to investigate the effect of the Kelvin effect
C on the simulations
C----------------------------------------------------
C     FAK=0.D0
      FAK=XI1*OVER(TR)/TR
C     IF (FAK.GT.700.D0) GOTO 20
C     IF (FAK.GT.1.D1) GOTO 20

      PR=DAMP(TR)*DEXP(FAK)
C        write(6,*)TR, DAMP(TR)
C     C=CKON*(T-TR)/(T1-TR**XOP)
      IF (PR.GT.PPP) GOTO 20
C     G=C*XI2*(DLOG(PPP-PR)+XB3)
      G=XI2*(DLOG(PPP-PR)+XB3)
C---XHD=1/HD=1/HC+1/HKN:---
      XHD=XI3/(XCOND+CONDUC(TR))+XBE1
      TRN=T+XB4*G*XHD
      NITER=NITER+1
      IF (NITER.GT.10) THEN
       TRN=(TR+TRN)/2.D0
      ENDIF
      IF ((DABS(TRN-TR))/TR.GT.1.D-16) GOTO 10
      IF (G.LT.0.D0) THEN
       IF (IDF.GT.0.AND.Y.LE.YMIN) G=0.D0
```

```
      ENDIF
      GOTO 30
   20 CONTINUE
      G=0.D0
      IF (IDF.LT.1) THEN
C---SIZE SECTION SHOULD BE REMOVED:---
       ICARUT=1
       IDF=-1
      ENDIF
   30 CONTINUE
      GROWTH=G/DL
C       GROWTH=1.5D0
C       write(6,*) growth
      RETURN
      END
C++++++++++++++++++++++++++++++++++++++++++++++++++++++++++++++++++++
      DOUBLE PRECISION FUNCTION HOMNUC(P,T,RHOM,S)
C
C CALCULATES HOMOGENEOUS NUCLEATION RATE FOR H2SO4 (M**-3 S**-1)
C EXPRESSION FROM SEINFELD:ATM. CHEM. & PHYS. OF AIR POLLUTION 1986
C P.362
C
      IMPLICIT DOUBLE PRECISION (A-H,O-Z)
      DOUBLE PRECISION K1,K2,K3,NGE
      COMMON/HOMOG/XH1,XH2,XH3
      COMMON/STICK2/SAS1
C-----JRJ D. 1/4-98 (XK6 BENYTTES I BEREGNINGERNE I FUNKTIONEN)
      COMMON/XKON/XK1,XK2,XKDG,XK4,XK5,XK6,XK7,XK8,XK9,XK11
C-------------------------------------------------------------
C    KORREKTION AF DET HOMOGENE NUKLEERINGSUDTRYK JRJ D. 1/4-98
C-------------------------------------------------------------
C     WRITE (2,*) P,T
      E1=-19.286
      F1=-7.15
      G1=31.895
      E2=-16.549
      F2=-5.62
      G2=25.071

      TT0=-1/XK6
      IF (T*TT0 .LT. 1342) THEN
      PS=10**(E1*1.D3/(T*TT0) + F1*DLOG10(T*TT0) + G1)*1.0D5
      ELSE
      PS=10**(E2*1.D3/(T*TT0) + F2*DLOG10(T*TT0) + G2)*1.0D5
      ENDIF

      PP0=10**(E1*1.D3/TT0 + F1*DLOG10(TT0) + G1)*1.0D5
```

```
      P1=P*PP0
    S=P*PP0/(PS)


    TOLMAN=1.20E-10
C---S MUST BE GREATER THAN 1.5:---
C JZ: Nucleation at low temperatures can be suppressed:
    IF (S.GT.1.5D0.AND. T*TT0 .GT. 600) THEN
      XLOGS=DLOG(S)
      SIGMA=OVER(T)
C JZ: Density of liquid K2SO4:
      DL=1870
C JZ - component specific parameters!!!
      VM=(174.25)*0.001/DL/6.022E23
      K1=(3*VM/4.D0/3.141593)**(1/3.D0)
      K2=3*SIGMA*VM
      K3=1.38E-23*T*TT0*DLOG(S)/2.D0/SIGMA/VM
      DP=1/K3*(1-4*K3*TOLMAN+(4*K3*TOLMAN+1)**(0.5))
      IF (DP.LT.0.D0) THEN
      WRITE (6,*) ('TOLMAN CORRECTION IS TOO LARGER')
      STOP
C      DP=1.D-12
      ENDIF
      RHOM=DP/2.D0
      QHOM=3.141593/6.D0/VM*(DP**3.D0)
C JZ: KC p 61 (12.27):
          DELTAG=-QHOM*1.38E-
23*TT0*T*LOG(S)+(K2*QHOM)/(K1*QHOM**(1/3.D0)
    &+2*TOLMAN)
C JZ: KC phd-thesis p 61 (12.29)
      NGE=(P1)*100000/1.38E-23/T/TT0*DEXP(-DELTAG/1.38E-23/T/TT0)
C JZ: KC phd- thesis  p 62 (12.34)
      Z=(K1*K2/9.D0/3.141593/1.38E-23/T/TT0*(K1*QHOM**(-1/3.D0)+
    &4.D0*TOLMAN*QHOM**(-2/3.D0))/(K1*QHOM**(-1/3.D0)+2*TOLMAN)**3.D0
    &)**(0.5)
C JZ: KC phd- thesis p 65
      C=(P1)*100000*3.141593*DP**2.D0/1.38E-23/T/TT0
    &*(8.314*T*TT0/2.D0/3.141593/(174.25)/0.001)**(0.5)
      HOMNUC=C*Z*NGE

    ELSE
      HOMNUC=0.D0
      RHOM=0.D0
    ENDIF
    RETURN
    END
```

C+++

```
      SUBROUTINE DXB(T,DXB5,DXB6,DDXB9,DDXB10)
C
C CALCULATES THE DERIVATIVE OF XB6, XB9 AND XB10
C
      IMPLICIT DOUBLE PRECISION(A-H,O-Z)
      COMMON/XKON/XK1,XK2,XKDG,XK4,XK5,XK6,XK7,XK8,XK9,XK11
      COMMON/XTAFH/XB2,XB3,XB4,XB5,XB6,XB7,XB8,XB9,XB10,XB11,XCOND
      COMMON/DXTAFH/DXB8,DXB9,DXB10
      COMMON/FVARME/VA1,VA2,VA3
      COMMON/GAS/XMGAS
      COMMON/FCONDU/C1,C2,C3,C4
      COMMON/PDIV/PPP
      COMMON/FDIFF/DI1,XMYD
      DXB5=XMGAS*XK5*PPP/T
      T2=T*T
      T3=T2*T
      DXB6=XK6*T*(2.D0*VA3*T-VA2*T3)/(VA1*T2+VA2*T3+VA3)**2
      DXB6=XB5*DXB6/XMGAS+XB6*DXB5/XB5
      DDXB9=(XMYD-2.D0)*DXB9/T
      DDXB10=2.D0*C3+6.D0*C4*T
      RETURN
      END
```

C+++

```
      SUBROUTINE OUT(N,X,Y,ICON, SULPHATE)
C
C CALCULATES THE INTERMEDIATE HOMOGENEOUS NUCLEATION RATE IN
C A Z INTERVAL
C
      IMPLICIT DOUBLE PRECISION (A-H,O-Z)
      PARAMETER (ICAR=20000,ICOL=20)
      DIMENSION Y(*),NCAR(ICOL),GV(ICOL+2),AX(10000),ABSRAD(ICOL)
      DIMENSION XNO(ICAR),TRN(ICAR),GR(ICOL),PLOT(ICOL,10000)
      DIMENSION ALOGPLOT(ICOL,10000)
      DIMENSION XNUC(ICOL),XHOLD(ICOL),IDHOM(ICOL),RHOM(ICOL)
      COMMON/NNNN/NCOL,NCAR
      COMMON/ANTAL/XNO,TRN,GR
      COMMON/UNDIM/AMAX,XTUBE
      COMMON/FDAMP/T0,P0
      COMMON/UDS/ZOLD
      COMMON/HNTEST/XNUC,XHOLD,RHOM,VALUE,IDHOM,IDTOT
      COMMON/WALLOS/AMWAL(ICOL+2),CWALL,XKOLD
      COMMON/GAUSS/GV
      COMMON/DIVKUL/WALCON,GASIND
      COMMON/OUTNO/IUD
      COMMON/WALL/PW,TW,PP,SUMAM,SUMAMT
      COMMON/DIAM/XDIAM
      COMMON/ARAD/ABSRAD,AX,IPCOUNT,PLOT,ALOGPLOT,AXOLD,AXOLD2
```

```
      COMMON/MAX/SMAX,HOMMAXOLD,POSIMAX,TEMMAX,HOMMAX
         COMMON/XKON/XK1,XK2,XKDG,XK4,XK5,XK6,XK7,XK8,XK9,XK11
 3333 FORMAT(5F14.4)
C---CHECK FOR HOMOGENEOUS NUCLEATION:---
      DO 10 J=1,NCOL
      NT=J+NCOL

      XHOM=HOMNUC(Y(J),Y(NT),RH,S)
      IF (IDHOM(J).EQ.1) THEN
       XNUC(J)=XNUC(J)+(X-ZOLD)*(XHOM+XHOLD(J))
       XHOLD(J)=XHOM
C---SAVE LARGEST J:---
       IF (RHOM(J).LT.RH) RHOM(J)=RH
      ELSE
       IF (XHOM.GT.VALUE) THEN
        XHOLD(J)=XHOM
        RHOM(J)=RH
        IDHOM(J)=1
        IF (IDTOT.EQ.0) THEN
         ICON=1
         IDTOT=1
        ENDIF
       ENDIF
      ENDIF
C---WRITE THE NUCLEATION RATE
      IF(DABS(1000.D0*Y(2*NCOL+1)).GT.IPCOUNT)THEN
       DUM=XHOM
       IF(DUM.LT.1.D-10)DUM=1.D-10
       AX(IPCOUNT)=X*XTUBE*1000.D0
       PLOT(J,IPCOUNT)=(DUM/1.D6)
       ALOGPLOT(J,IPCOUNT)=DLOG10(DUM/1.D6)
       WRITE(13,111) AX(IPCOUNT),1.D3*ABSRAD(J),S
       WRITE(13,111) AX(IPCOUNT),-1.D3*ABSRAD(J),S

       IF (J .EQ. 1) THEN
                WRITE(13,111) AX(IPCOUNT),0.0D0,S
          ENDIF

          IF (AXOLD.EQ.0.D0) THEN
       AXOLD=AX(IPCOUNT)
       AXOLD2=AX(IPCOUNT)
       ENDIF
          E1=-19.286
          F1=-7.15
          G1=31.895
          TT0=-1/XK6
          PP0=10**(E1*1.D3/TT0 + F1*DLOG10(TT0) + G1)*1.0D5
```

```
       WRITE(7,111) AX(IPCOUNT),-1.D3*ABSRAD(J), Y(J)*PP0
       WRITE(7,111) AX(IPCOUNT),1.D3*ABSRAD(J), Y(J)*PP0

      IF (J .EQ. 1) THEN
                WRITE(7,111) AX(IPCOUNT),0.0D0,Y(J)*PP0
         ENDIF

         WRITE(928,111) AX(IPCOUNT),-1.D3*ABSRAD(J), XHOM

      IF (AX(IPCOUNT).GT.(AXOLD2+10.D0).OR.ABS(AX(IPCOUNT)-AXOLD).LT.
     &0.00000001) THEN
       WRITE(12,111) AX(IPCOUNT),1.D3*ABSRAD(J),((Y(J+NCOL))*966.D0)-
     &273.D0
       WRITE(12,111) AX(IPCOUNT),-1.D3*ABSRAD(J),((Y(J+NCOL))*966.D0)-
     &273.D0

C     WRITE (20,*) AX(IPCOUNT),AXOLD,AX(IPCOUNT)-AXOLD,AXOLD2
       AXOLD2=AX(IPCOUNT)
       AXOLD=AX(IPCOUNT)
      ENDIF

      IF (XHOM.GT.HOMMAXOLD) THEN
       SMAX=S
       HOMMAXOLD=XHOM
       POSIMAX=AX(IPCOUNT)
       TEMMAX=(((Y(J+NCOL))*966.D0)-273.D0)
       HOMMAX=XHOM
      ENDIF

      IF(J.EQ.NCOL)IPCOUNT=IPCOUNT+1
      ENDIF
   10 CONTINUE
  111 FORMAT(3(1X,E10.3))
      ZOLD=X
      RETURN
      END
C++++++++++++++++++++++++++++++++++++++++++++++++++++++++++++++++++++
C     SUBROUTINE RES(N,Y)
C
C OUTPUT ROUTINE
C     IMPLICIT DOUBLE PRECISION (A-H,O-Z)
C     PARAMETER (ICAR=20000,ICOL=20)
C     DIMENSION Y(*),S(ICOL),NCAR(ICOL)
C     DIMENSION XNO(ICAR),TRN(ICAR),GR(ICOL)
C     COMMON/WALL/PW,TW,PP,SUMAM,SUMAMT
C     COMMON/NNNN/NCOL,NCAR
C     COMMON/ANTAL/XNO,TRN,GR
```

```
C      COMMON/UNDIM/AMAX,XTUBE
C      COMMON/FDAMP/T0,P0
C      COMMON/OUTNO/IUD
C      AM3=1.D6*AMAX**3
C      WRITE(IUD,*)Y(2*NCOL+1)*XTUBE,TW*T0-273.15D0
C      WRITE(6,77)Y(2*NCOL+1)*XTUBE,TW*T0-273.15D0
C  77 FORMAT(2F12.2)
C      WRITE(IUD,9910)(Y(I)*P0,I=1,NCOL)
C      WRITE(IUD,9910)(Y(I+NCOL)*T0,I=1,NCOL)
C      WRITE(IUD,*)
C      DO 10 I=2*NCOL+2,N-1
C      WRITE(IUD,9910)XNO(I)/AM3,1.D6*Y(I)*AMAX
C  10 CONTINUE
C      WRITE(IUD,*)
C      WRITE(IUD,9910)(XNO(I)/AM3,I=2*NCOL+2,N-1)
C      WRITE(IUD,*)
C      DO 20 J=1,NCOL
C      S(J)=Y(J)/DAMP(Y(J+NCOL))

CC      DO 11 I=1,J
CC      WRITE (6,*) S(J)
CC   11 CONTINUE

CC   20 CONTINUE
CC      WRITE(IUD,9920)(S(J),J=1,NCOL)
C 9910 FORMAT(7F10.4)
C 9920 FORMAT(5F10.5)
C      RETURN
C      END


C++++++++++++++++++++++++++++++++++++++++++++++++++++++++++++++++++++
      SUBROUTINE FUN(N,NC21,Y,F, SULPHATE)
C
C CALCULATES THE RIGHT-HAND SIDE OF THE EQUATIONS DV/DZ=
      IMPLICIT DOUBLE PRECISION (A-H,O-Z)
      PARAMETER (ICAR=20000,ICOL=20)
      DIMENSION Y(*),F(*),XNO(ICAR),TRN(ICAR),Y4(ICAR),NCAR(ICOL)
      DIMENSION CMAT(ICOL,ICOL),CBOUND(ICOL),SUMF(ICOL),GR(ICOL)
      DIMENSION AMAT(ICOL,ICOL),ABOUND(ICOL),ASUM(ICOL),ROOT(ICOL)
      DIMENSION SUMT1(ICOL),SUMT2(ICOL),SUMP1(ICOL),SUMP2(ICOL)
      DIMENSION FACP(ICOL),FACT(ICOL),BIG(ICOL),BIGAP(ICOL)
      DIMENSION BIGAT(ICOL),DLIQ(ICAR),IDFO(ICAR),XMINI(ICAR)
      COMMON/NNNN/NCOL,NCAR
      COMMON/XTAFH/XB2,XB3,XB4,XB5,XB6,XB7,XB8,XB9,XB10,XB11,XCOND
      COMMON/DXTAFH/DXB8,DXB9,DXB10
      COMMON/YI4/Y4
      COMMON/ANTAL/XNO,TRN,GR
      COMMON/COLLOK/CMAT,CBOUND,AMAT,ABOUND,ASUM,ROOT
      COMMON/NDIV/NC2,NC22
      COMMON/WALL/PW,TW,PP,SUMAM,SUMAMT
      COMMON/SUMMA/SUMF
      COMMON/DIVDF/SUMT1,SUMT2,SUMP1,SUMP2,FACP,FACT,BIG,BIGAP,BIGAT
      COMMON/DIV2/DLIQ
      COMMON/PDIV/PPP
      COMMON/IDFOR/IDFO,XMINI
      COMMON/WALLOS/AMWAL(ICOL+2),CWALL,XKOLD
      COMMON/LARS/ADDS,EPS1,NFUN,CONT(ICAR)
      COMMON/LARS1/PWALL
         COMMON/XKON/XK1,XK2,XKDG,XK4,XK5,XK6,XK7,XK8,XK9,XK11
      NN=NC22
      CALL WFUN(Y(NC21))
      DO 20 J=1,NCOL
      NT=J+NCOL
      CALL NEWTP(Y(NT),Y(J),XDUM,GR(J))
      PWALL=PW
      SUM=0.D0
C---SUMMATION OVER NUMBER OF CHARACTERISTICS:---
      DO 10 I=NN,NN+NCAR(J)-1
C---GROWTH (da/dz):---
      G=GROWTH(Y(I),Y(NT),X,TRN(I),DL,IDFO(I),XMINI(I))
      F(I)=G
C---Y4 IS USED IN DFUN:---
      Y4(I)=XNO(I)*Y(I)*Y(I)/Y(NT)
      DLIQ(I)=DL*G
C    IF(NFUN.EQ.1)CONT(I+J-1)=DLIQ(I)*Y4(I)
      SUM=SUM+DLIQ(I)*Y4(I)
   10 CONTINUE
      SUMF(J)=SUM
      NN=NN+NCAR(J)
      FACP(J)=ABOUND(J)*PW
      FACT(J)=ABOUND(J)*TW
      SUMP1(J)=CBOUND(J)*PW
      SUMT1(J)=CBOUND(J)*TW
      SUMP2(J)=0.D0
      SUMT2(J)=0.D0
C---SUMMATION OVER NUMBER OF COLLOCATION POINTS:---
      DO 30 I=1,NCOL
      NTI=I+NCOL
      SUMP1(J)=SUMP1(J)+CMAT(J,I)*Y(I)
      SUMT1(J)=SUMT1(J)+CMAT(J,I)*Y(NTI)
      SUMP2(J)=SUMP2(J)+AMAT(J,I)*Y(I)
      SUMT2(J)=SUMT2(J)+AMAT(J,I)*Y(NTI)
   30 CONTINUE
```

```
C---MASS BALANCE (dp/dz):---

C----------------------- REACTION WITH SO2------------------

C PRESSURES ARE  IN Pa, EXCEPT p(O2) AND KEQ IN Bar
C Temperature from reduced temperature
        T=Y(J+ICOL)*(THOT +273.15D0)
C Pressure of SO2 in [Pa]
        P_SO2=50.0D0
C Equilibrium constant:
        KEQ=10** (4956.0D0/T-4.678 0D0)
C Parameters for kinetic expression:
C [1/s]
        k=69
C [J/mole]
        Ea=63000

C        IF (KEQ .LT. 0.1D0) THEN
C        KEQ=1.0D-2
C        ENDIF
C        IF (KEQ .GT. 1.0D7) THEN
C        KEQ=1.0D7
C        ENDIF
C        IF (T .LT. 1000) THEN
C        KEQ=1.0D7
C        k=0.0D0
        ENDIF
     E1=-19.286
     F1=-7.15
     G1=31.895
        TT0=-1/XK6
        PP0=10**(E1*1.D3/TT0 + F1*DLOG10(TT0) + G1)*1.0D5

C [r_K2SO4]=Pa/s
        P_K2SO4=Y(J)*PP0
        r_K2SO4=k*exp(-Ea/8.314/T)*P_SO2*(1-
     & (P_K2SO4/(0.05**0.5*P_SO2*KEQ)))

        IF (r_K2SO4 .LT. 0.00) THEN
        r_K2SO4=0.0D0
        ENDIF

C conversion to dimensionles variable

        SULPHATE=r_K2SO4/PP0*3.5

     BIGAP(J)=ROOT(J)*(SUMP2(J)*SUMT2(J)+
```

```
     & FACP(J)*SUMT2(J)+FACT(J)*SUMP2(J)+FACP(J)*FACT(J))

        F(J)=XB5*SUM+XB7*(XB9*SUMP1(J)+DXB9*BIGAP(J))+SULPHATE

C No changes in the energy balance due to reaction are introduced.
C---ENERGY BALANCE (dT/dz):---
     BIGAT(J)=ROOT(J)*(SUMT2(J)*SUMT2(J)+
     &    2.D0*FACT(J)*SUMT2(J)+FACT(J)*FACT(J))
     BIG(J)=XB10*SUMT1(J)+DXB10*BIGAT(J)
     F(NT)=XB6*SUM+XB8*BIG(J)
 20 CONTINUE
     SUMAM=0.D0
     DO 40 I=1,NCOL
     SUMAM=SUMAM+AMWAL(I)*Y(I)
 40 CONTINUE
     SUMAMT=SUMAM+AMWAL(NCOL+1)*PW
C---WALL CONDENSATION:---
     F(N)=SUMAMT*DIFF(TW)/TW
C---Z-VARIABEL:---
     F(NC21)=1.D0
     RETURN
     END
C++++++++++++++++++++++++++++++++++++++++++++++++++++++++++++++++++++++++
     SUBROUTINE DFUN(N,NC21,NM,Y,DF1,DF2,DF3,DF4,F)
C
C CALCULATES THE JACOBIAN OF FUN
     IMPLICIT DOUBLE PRECISION (A-H,O-Z)
     PARAMETER (ICAR=20000,ICOL=20)
     DIMENSION DF1(NC21,*),DF2(NM,*),DF3(NC21,*),DF4(*)
     DIMENSION Y(*),F(*),XNO(ICAR),TRN(ICAR),Y4(ICAR)
     DIMENSION NCAR(ICOL),SUMF(ICOL),GR(ICOL)
     DIMENSION CMAT(ICOL,ICOL),CBOUND(ICOL)
     DIMENSION AMAT(ICOL,ICOL),ABOUND(ICOL),ASUM(ICOL),ROOT(ICOL)
     DIMENSION SUMT1(ICOL),SUMT2(ICOL),SUMP1(ICOL),SUMP2(ICOL)
     DIMENSION FACP(ICOL),FACT(ICOL),BIG(ICOL),BIGAP(ICOL)
     DIMENSION BIGAT(ICOL),DLIQ(ICAR),IDFO(ICAR),XMINI(ICAR)
     COMMON/NNNN/NCOL,NCAR
     COMMON/XTAFH/XB2,XB3,XB4,XB5,XB6,XB7,XB8,XB9,XB10,XB11,XCOND
     COMMON/DXTAFH/DXB8,DXB9,DXB10
     COMMON/YI4/Y4
     COMMON/ANTAL/XNO,TRN,GR
     COMMON/COLLOK/CMAT,CBOUND,AMAT,ABOUND,ASUM,ROOT
     COMMON/NDIV/NC2,NC22
     COMMON/SUMMA/SUMF
     COMMON/DIVDF/SUMT1,SUMT2,SUMP1,SUMP2,FACP,FACT,BIG,BIGAP,BIGAT
     COMMON/DIV2/DLIQ
     COMMON/IDFOR/IDFO,XMINI
```

```
      COMMON/WALLOS/AMWAL(ICOL+2),CWALL,XKOLD
      COMMON/WALL/PW,TW,PP,SUMAM,SUMAMT
      COMMON/FDIFF/DI1,XMYD
      COMMON/LARS/ADDS,EPS1,NFUN,CONT(ICAR)
C---ZEROING VALUES:---
      DO 10 I=1,NC21
      DO 10 J=1,N-NC21
      DF2(J,I)=0.D0
      DF3(I,J)=0.D0
   10 CONTINUE
      DO 20 I=1,NC21
      DO 20 J=1,NC21
   20 DF1(I,J)=0.D0
      DO 30 I=1,NM
   30 DF4(I)=0.D0
      EPS=EPS1
      NN=NC22
      CALL WDFUN(Y(NC21),DTDZ,DPDZ)
      DO 40 J=1,NCOL
      NT=J+NCOL
      CALL NEWTP(Y(NT),Y(J),X,GR(J))
      DO 50 JJ=1,NCOL
C---NB ! XB7 AND XB8 ARE TEMPERATURE DEPENDENT:---
       NTJJ=JJ+NCOL
      DF1(J,JJ)=XB7*(XB9*CMAT(J,JJ)+DXB9*ROOT(J)*AMAT(J,JJ)*
     &       (SUMT2(J)+FACT(J)))
      DF1(J,NTJJ)=XB7*DXB9*ROOT(J)*AMAT(J,JJ)*(SUMP2(J)+FACP(J))
      DF1(NT,NTJJ)=XB8*(XB10*CMAT(J,JJ)+DXB10*ROOT(J)*2.D0*
     &           AMAT(J,JJ)*(SUMT2(J)+FACT(J)))
   50 CONTINUE
C---DERIVATIVE WITH RESPECT TO PW OG TW:---
      DF1(J,NC21)=XB7*(XB9*CBOUND(J)*DPDZ+ROOT(J)*DXB9*ABOUND(J)*
     &      (SUMP2(J)*DTDZ+SUMT2(J)*DPDZ+ABOUND(J)*(PW*DTDZ+TW*DPDZ)))
      DF1(NT,NC21)=XB8*DTDZ*(XB10*CBOUND(J)+2.D0*ROOT(J)*DXB10*ABOUND(J)
     &      *(SUMT2(J)+ABOUND(J)*TW))
      NEND=NN+NCAR(J)-1
      SUM=0.D0
      DO 60 I=NN,NEND
C---DERIVATIVES WITH RESPECT TO RADIUS (Y(I), I=2*NCOL+1,........):---
      DAI=(DABS(Y(I))+ADDS)*EPS
      G=GROWTH(Y(I)+DAI,Y(NT),X,TRN(I),DL,IDFO(I),XMINI(I))
      DG=(G-F(I))/DAI
      DGS=(G*DL-DLIQ(I))/DAI
      DF4(I-NC21)=DG
      XX=Y4(I)*DGS+2.D0*F(I)*Y(I)*DL*XNO(I)/Y(NT)
      DF3(J,I-NC21)=XB5*XX
      DF3(NT,I-NC21)=XB6*XX
```

```
   60 CONTINUE
C---DERIVATIVES WITH RESPECT TO PRESSURE P (Y(I), I=1,...,NCOL):---
      DP=(DABS(Y(J))+ADDS)*EPS
      YP=Y(J)+DP
      CALL NEWTP(Y(NT),YP,X,GR(J))
      SUM=0.D0
      DO 70 I=NN,NEND
      G=GROWTH(Y(I),Y(NT),X,TRN(I),DL,IDFO(I),XMINI(I))
      DG=(G-F(I))/DP
      DGS=(G*DL-DLIQ(I))/DP
      DF2(I-NC21,J)=DG
      SUM=SUM+DGS*Y4(I)
   70 CONTINUE
      DF1(J,J)=DF1(J,J)+XB5*SUM
      DF1(NT,J)=XB6*SUM
C---DERIVATIVE WITH RESPECT TO T (Y(I), I=NCOL+1,....,2*NCOL):---
      DT=(DABS(Y(NT))+ADDS)*EPS
      YT=Y(NT)-DT
      XB5G=XB5
      XB6G=XB6
      CALL DXB(Y(NT),DXB5,DXB6,DDXB9,DDXB10)
      CALL NEWTP(YT,Y(J),X,GR(J))
      SUM=0.D0
      DO 80 I=NN,NEND
      G=GROWTH(Y(I),YT,X,TRN(I),DL,IDFO(I),XMINI(I))
      DG=-(G-F(I))/DT
      DGS=-(G*DL-DLIQ(I))/DT
      DF2(I-NC21,NT)=DG
      SUM=SUM+DGS*Y4(I)
   80 CONTINUE
      DF1(J,NT)=DF1(J,NT)+XB5G*SUM+XB7*(DXB9*SUMP1(J)+DDXB9*BIGAP(J))
      DF1(NT,NT)=DF1(NT,NT)+XB6G*SUM+DXB6*SUMF(J)+DXB8*BIG(J)+
     &      XB8*(DXB10*SUMT1(J)+DDXB10*BIGAT(J))
      NN=NN+NCAR(J)
   40 CONTINUE
      DO 90 I=1,NCOL
      DF2(N-NC21,I)=DIFF(TW)*AMWAL(I)/TW
   90 CONTINUE
C---DER. WITH RESP. TO Z (REM: DEP. ON DIFFUSIONS COEFF. EXPRESS.):---
      DF2(N-NC21,NC21)=DI1*((XMYD-1.D0)*TW**(XMYD-2.D0)*SUMAMT*DTDZ+
     &      TW**(XMYD-1.D0)*AMWAL(NCOL+1)*DPDZ)
      RETURN
      END
C
C  R O U T I N E S   W I T H   P H Y S I C A L   P R O P E R T I E S
C SOME ROUTINES ARE COMPONENT-SPECIFIC
C
```

```
C++++++++++++++++++++++++++++++++++++++++++++++++++++++++++++++++
      DOUBLE PRECISION FUNCTION OVER(TT)
C
C    COMPONENT-SPECIFIC FUNCTION
C------ THE BULK SURFACE TENSION OF PURE K2SO4 [N/m]
      IMPLICIT DOUBLE PRECISION (A-H,O-Z)
      COMMON/FDAMP/T0,P0
C    MELTING POINT OF K2SO4
C----------------------------------------------------------------
C  FIT OF SURFACE TENSION
C----------------------------------------------------------------
      TM=1342.15D0
          FAKT=1.D0
      T=TT*T0
      IF(T.LT.TM) THEN
        OVER=0.6557-2.942E-4*T
        ELSE
        OVER=0.212D0 - 6.5D-5*(T-273.15)
        ENDIF
      OVER=OVER*FAKT
      RETURN
      END
C++++++++++++++++++++++++++++++++++++++++++++++++++++++++++++++++
      DOUBLE PRECISION FUNCTION CONDUC(T)
      IMPLICIT DOUBLE PRECISION (A-H,O-Z)
C
C CONDUCTANCE (N2) J/MSK
C FROM PROPERTIES OF LIQUID AND GASES
C
      COMMON/FCONDU/C1,C2,C3,C4
      CONDUC=C1+(C2+(C3+C4*T)*T)*T
      RETURN
      END
C++++++++++++++++++++++++++++++++++++++++++++++++++++++++++++++++
      DOUBLE PRECISION FUNCTION DAMP(TT)
C
C    COMPONENT-SPECIFIC FUNCTION
C------ Equilibrium vapor pressure of pure component I [Pa], T [K]
      IMPLICIT DOUBLE PRECISION (A-H,O-Z)
      COMMON/FDAMP/T0,P0
      T=TT*T0
      TM=1342.15D0
C-----JRJ D. 31/3-98
C JZ 6-2006
      E1=-19.286
      F1=-7.15
      G1=31.895
```

```
      IF(T.LT.TM) THEN
        DAMP=10**(E1*1.D3/T + F1*DLOG10(T) + G1)*1.D5
      ELSE
        DAMP=10**(E2*1.D3/T + F2*DLOG10(T) + G2)*1.D5
      ENDIF
      DAMP=DAMP/P0
      RETURN
      END
C++++++++++++++++++++++++++++++++++++++++++++++++++++++++++++++++
      DOUBLE PRECISION FUNCTION DENSIT(TT)
C
C    COMPONENT-SPECIFIC FUNCTION
C
C------ The density of pure condensed component I [kg/m3]
      IMPLICIT DOUBLE PRECISION (A-H,O-Z)
      COMMON/FDAMP/T0,P0
      T=TT*T0
      TM=1342.15D0
      RHOL=1870.D0
      RHOS=2660.D0
      IF(T.GT.TM) THEN
        DENSIT=RHOL
      ELSE
        DENSIT=RHOS
      ENDIF
      RETURN
      END
C++++++++++++++++++++++++++++++++++++++++++++++++++++++++++++++++
      DOUBLE PRECISION FUNCTION DENS(T)
C
C DENSITY (KG/M**3)
C
      IMPLICIT DOUBLE PRECISION (A-H,O-Z)
      COMMON/FDENS/D1,D2
      DENS=D1+D2
      RETURN
      END
C++++++++++++++++++++++++++++++++++++++++++++++++++++++++++++++++
      DOUBLE PRECISION FUNCTION DIFF(T)
C
C    COMPONENT-SPECIFIC FUNCTION
C
C DIFFUSION COEFFICIENT K2SO4 IN NITROGEN (M**2/S) AT 1 BAR
C DATA FROM CHRISTENSEN, KURT
      IMPLICIT DOUBLE PRECISION (A-H,O-Z)
      COMMON/FDIFF/DI1,XMYD
```

```
      DIFF=DI1*(T**(XMYD))
      dd=diff
      RETURN
      END
C++++++++++++++++++++++++++++++++++++++++++++++++++++++++++++++++++
      DOUBLE PRECISION FUNCTION VISCOS(T)
C
C VISCOSITY N2 (NS/M**2)
C LINEAR INTERPOLATION OF DATA FROM RUBBER CO.
       IMPLICIT DOUBLE PRECISION (A-H,O-Z)
      COMMON/FVISCO/V1,V2,V3
      VISCOS=V1+V2*T+V3*T*T
      RETURN
      END
C++++++++++++++++++++++++++++++++++++++++++++++++++++++++++++++++++
      DOUBLE PRECISION FUNCTION VARMEK(T,Y)
      IMPLICIT DOUBLE PRECISION (A-H,O-Z)
C
C HEAT CAPACITY (CP) OF N2 (J/K/MOL)
C AFTER SMITH & VAN NESS
C
      COMMON/FVARME/VA1,VA2,VA3
      VARMEK=VA1+VA2*T+VA3/(T*T)
      RETURN
      END
C++++++++++++++++++++++++++++++++++++++++++++++++++++++++++++++++++
      DOUBLE PRECISION FUNCTION VARMEH(T)
      IMPLICIT DOUBLE PRECISION (A-H,O-Z)
C     COMPONENT-SPECIFIC FUNCTION
C
C HEAT CAPACITY OF SOLID K2SO4(J/K/MOL)
C FROM KNACKE AT AL., 1982
C
      COMMON/FVARMH/VS1,VS2,VS3
      COMMON/FDAMP/T0,P0
      VARMEH=VS1+VS2*T*T0+VS3*(T*T0)**(-2.D0)
      RETURN
      END
C++++++++++++++++++++++++++++++++++++++++++++++++++++++++++++++++++
C
C---ROUTINES FROM VILLADSEN AND MICHELSEN:---
C
C   SUBROUTINE SIRUKE IS AN ADAPTION OF THE SIRUK-3 PROGRAMS FROM VIL-
C   LADSEN AND MICHELSEN,  SOLUTION OF DIFFERENTIAL EQUATION MODELS
C   BY POLYNOMIAL APPROXIMATION.
C
C   THIS VERSION IS REVISED BY OLE SIMONSEN TO DEAL WITH A JACOBIAN
```

```
C   OF TYPE:
C
C       s s e e e e
C       s s e e e e     S  E    WHERE D IS A N*N DIAGONAL
C   J = h h d 0 0 0   =       , AND E M*N, H M*N AND
C       h h 0 d 0 0       H  E    S M*M MATRIX
C       h h 0 0 d 0
C       h h 0 0 0 d
C   IN DFUN S=DF1, H=DF2, E=DF3 AND D=DF4 (VECTOR)
C
C   THE PROGRAM SOLVES DIFFERENTIAL EQUATIONS OF THE FORM
C
C   DY/DX = F(Y),   Y(X=X0) =Y0 , WHERE Y IS AN N-VECTOR,
C
C   OR, TO A LIMITID EXTENT, DIFFERENTIAL-ALGEBRAIC EQUATIONS,
C   DY/DX = F(Y,Z),   WHERE N-M EQUATIONS ARE DIFFERENTIAL EQUATIONS
C
C     0 = G(Y,Z),   AND M EQUATIONS ARE ALGEBRACI EQUATIONS
C
C   THE CALLING PARAMETERS ARE:
C
C   N:   TOTAL NUMBER OF EQUATIONS
C   NPR: PRINT FREQUENCY, AND INDICATOR FOR NUMERICAL JACOBIAN
C   NPR>0 : PRINT EVERY NPR STEPS, ANALYTIC JACOBIAN
C   NPR<0 : PRINT EVERY |NPR| STEPS, NUMERICAL JACOBIAN
C
C   Y:    VECTOR OF LENGTH AT LEAST N, CONTAINIUG THE INITIAL Y-VALUES
C         RETURNS: Y-VALUES AT THE ENDPOINT FOR THE INTEGRATION
C
C   W:    A ONE-DIMENSIONAL WORK VECTOR OF LENGTH AT LEAST
C         NTOTAL (SEE ROUTINE), INITIALIZED AS SHOWN BELOW
C   CALL FUN(N,Y,F)
C   WITH TYPE DECLARATION:   DOUBLE PRECISION Y(*),F(*)
C   WHERE Y (INPUT) IS THE VECTOR OF DEPENDENT VARIABLES
C   AND  F (OUTPUT) IS THE VECTOR OF CALCULATED RHS-VALUES
C   N IS THE NUMBER OF EQUATIONS
C   CALL DFUN(N,Y,DF)
C   WITH TYPE DECLARATION:   DOUBLE PRECISION Y(*),DF(N,*)
C
C   WHERE Y (INPUT) IS THE VECTOR OF DEPENDENT VARIABLES
C   AND  DF (OUTPUT) IS THE JACOBIAN MATRIX, DF(I,J) = DF(I)/DY(J)
C   N IS THE NUMBER OF EQUATIONS
C   CALL OUT(N,X,Y)
C
C   WITH TYPE DECLARATION:   DOUBLE PRECISION X,Y(*)
C   WITH X (INPUT): CURRENT VALUE OF THE INDEPENDENT VARIABLE
C      Y (INPUT): CURRENT VALUE OF THE DEPENDENT VARIABLES
```

```fortran
C       N (INPUT):   NUMBER OF EQUATIONS
C
C    NOTE:  NONE OF THESE FUNCTIONS MAY MODIFY INPUT VARIABLES
C
C    LANGUAGE: ANSI FORTRAN 77
C
      SUBROUTINE SIRUKE(N,NPR,Y,W,P_SO2,P_SO2_0)
      PARAMETER (ICAR=20000,ICOL=20)
      IMPLICIT DOUBLE PRECISION(A-H,O-Z)
      COMMON/NDIV/NC2,NC22
      COMMON/NNNN/NCOL,NCAR
      DIMENSION Y(*) , W(*)
      DIMENSION IP(ICAR*ICOL*2),NCAR(ICOL)
          DIMENSION P_SO2(ICOL)
      NC2=2*NCOL
      NC21=NC2+1
      NC22=NC21+1
      NM=N-NC21
C------ REQUIRED AREA :
      NTOTAL=4*ICOL*(2*ICAR-2*ICOL-3)+16*ICAR+2
      IF ( N.GT.NTOTAL ) THEN
        WRITE (*,*) ' SET OF EQUATIONS IS TOO LARGE '
        WRITE (*,*)
     &            ' PAUSING;  RECOMPILE WITH LARGER DIMENSION FOR IP '
        STOP
      ENDIF
      NAL = W(N+5)
      IR = 1
      IF ( NAL.LT.0 ) THEN
        NAL = -NAL
        IR = -1
      ENDIF
      N1 = N + 6
      N2 = N1 + N
      N4 = N2 + N
      N5 = N4 + N
      N6 = N5 + N
C    NN = INT(DBLE(N)**2)
      NN = N*N
      N7 = N6 + N
      N8 = N7 + N
      N9 = N8 + N
      NNCC=NC21*NC21
      NNC2=NC21*NM
      N10 = N9 + NNCC
      N11 = N10 + NNC2
      N12 = N11 + NNC2

      N13 = N12 + NM
      N14 = N13 + NNCC
      N15 = N14 + NNC2
      N16 = N15 + NNC2
C
      CALL STIFFE(N,IR,NAL,NPR,W(N+1),W(N+2),W(N+3),W(N+4),
     &       W,Y,W(N1),IP,W(N4),W(N5),W(N6),W(N7),W(N8),W(N9),
     &       W(N10),W(N11),W(N12),W(N13),W(N14),W(N15),W(N16),
     &       NM,NC21,P_SO2,P_SO2_0)
      RETURN
      END
      SUBROUTINE STIFFE(N,IR,NAL,NPR,X0,X1,H0,EPS,W,Y,DELY,
     &          IP,YK1,YK2,YK3,F,FOLD,DF1,DF2,DF3,DF4,DFO1,DFO2,
     &          DFO3,DFO4,NM,NC21, P_SO2,P_SO2_0)
      IMPLICIT DOUBLE PRECISION(A-H,O-Z)
      PARAMETER (ICAR=20000,ICOL=20)
      DIMENSION IP(*) , Y(*) , DELY(*) , YK1(*) , YK2(*)
      DIMENSION YK3(*) , W(*) , F(*) , FOLD(*)
      DIMENSION DF1(*) , DF2(*) , DF3(*), DF4(*)
      DIMENSION DFO1(*) , DFO2(*) , DFO3(*), DFO4(*)
      DIMENSION NCAR(ICOL)
          DIMENSION P_SO2(ICOL)
          COMMON/FDAMP/T0,P0
      COMMON/NNNN/NCOL,NCAR
      COMMON/NDIV/NC2,NC22
      COMMON/LARS/ADDS,EPS1,NFUN,CONT(ICAR)
      COMMON/LARS1/PWALL
      NPRINT = NPR
      WRITE(6,122)Y(2*NCOL+1)
          WRITE(6,*) 'Y(2*NCOL+1)'
  122 FORMAT(E15.8)
      IF ( NPRINT.LT.0 ) NPRINT = -NPRINT
      ICON = 0
C    NN = INT(DBLE(N)**2)
      NN = N*N
      NOUT = 0
      X = X0
      H = H0
C---DOES STEP EXCEED RANGE ?
      IF ( X0+H.LT.X1 ) GOTO 200
C---YES; SET TERMINAL STEP
  100  H = (X1-X)
      ICON = 1
  200  IF ( ICON.EQ.0 .AND. X+2.D0*H.GT.X1 ) H = (X1-X)/2.D0

          CALL FUN(N,NC21,Y,F, SULPHATE)
C----ANALYTIC
```

```
      CALL DFUN(N,NC21,NM,Y,DF1,DF2,DF3,DF4,F)
C----SAVE FOR REUSE IN CASE OF FAILURE
      DO 300 I = 1 , N
        FOLD(I) = F(I)
 300  CONTINUE
      NN1=0
      NN2=0
      DO 400 I = 1 , NC21
        DO 401 J = 1 , NM
          NO = NN1 + J
          DFO2(NO) = DF2(NO)
          DFO3(NO) = DF3(NO)
 401    CONTINUE
        NN1=NN1+NM
        DO 402 J = 1 , NC21
          NO = NN2 + J
          DFO1(NO) = DF1(NO)
 402    CONTINUE
        NN2=NN2+NC21
 400  CONTINUE
      DO 403 I = 1 , NM
        DFO4(I) = DF4(I)
 403  CONTINUE
 500  CALL SIRKE(N,IR,NAL,IP,F,Y,DELY,YK1,YK2,YK3,
     &         DF1,DF2,DF3,DF4,H,NC21,NM)
      E = 0.
      DO 600 I = 1 , N
        ES = W(I)*DABS(YK3(I))/(1.D0+DABS(Y(I)))
        IF ( ES.GT.E ) E = ES
 600  CONTINUE
      Q = E/EPS
      IF ( Q.GT.1. ) THEN
        DO 650 I = 1 , N
          F(I) = FOLD(I)
 650    CONTINUE
        NN1=0
        NN2=0
        DO 700 I = 1 , NC21
          DO 701 J = 1 , NM
            NO = NN1 + J
            DF2(NO) = DFO2(NO)
            DF3(NO) = DFO3(NO)
 701      CONTINUE
          NN1=NN1+NM
          DO 702 J = 1 , NC21
            NO = NN2 + J
            DF1(NO) = DFO1(NO)
```

```
 702      CONTINUE
          NN2=NN2+NC21
 700    CONTINUE
        DO 703 I = 1 , NM
          DF4(I) = DFO4(I)
 703    CONTINUE
        H = H/2
        ICON = 0
        GOTO 500
      ENDIF
C---ACCEPTED; CALCULATE NEW STEP
      DO 800 I = 1 , NC21
        Y(I) = Y(I) + DELY(I)
 800  CONTINUE
      DO 801 I = NC22 , N
        Y(I) = Y(I) + DELY(I)
 801  CONTINUE

 802      CONTINUE
      X = X + H
      Q = (3.D0*Q)**(-.33D0)
      IF ( Q.GT.3.D0 ) Q = 3.D0
      H = Q*H
      NOUT = NOUT + 1
      IF ( ( NOUT/NPRINT)*NPRINT.EQ.NOUT .OR. ICON.EQ.1 )
     & CALL OUT(N,X,Y,ICON, SULPHATE)

      IF ( ICON.EQ.1 ) THEN
        X1 = X
        RETURN
      ENDIF
      H0 = H
      IF ( X+H.GE.X1 ) GOTO 100
      GOTO 200
      END
C
      SUBROUTINE SIRKE(N,IR,NAL,IPIV,F,Y,DELY,YK1,YK2,YK3,
     &         DF1,DF2,DF3,DF4,H,NC21,NM)
      IMPLICIT DOUBLE PRECISION(A-H,O-Z)
      PARAMETER (ICAR=20000,ICOL=20)
      DIMENSION F(*) , Y(*) , DELY(*) , YK1(*) , YK2(*) , YK3(*) ,
     &      IPIV(*) , DF1(*) , DF2(*) , DF3(*) , DF4(*) , NCAR(ICOL)
      COMMON/NNNN/NCOL,NCAR
      COMMON/NDIV/NC2,NC22
      COMMON/LARS/ADDS,EPS1,NFUN,CONT(ICAR)
      DATA A , R1 , R2 , R3 , R4/.4358665215084589D0 ,
     &   1.037609496131859D0 , .8349304838526377D0 ,
```

```
     &    -.6302020887244523D0 , -.2423378912600452/
      DATA RN1 , RN2 , RN3/.7903283090535D0 , .491822861692D0 ,
     &    .3233676131956D0/
C     Y AND F IS DEFINED ON ENTRANCE
C
      HA = -H*A
      NN1=0
      NN2=0
      DO 100 J = 1 , NC21
        DO 101 I = 1 , NC21
          NO = NN2+I
          DF1(NO) = HA*DF1(NO)
          IF (I.EQ.J) DF1(NO) = DF1(NO) + 1.D0
 101    CONTINUE
        NN2=NN2+NC21
        DO 102 I = 1 , NM
          NO = NN1+I
          DF2(NO) = HA*DF2(NO)
          DF3(NO) = HA*DF3(NO)
 102    CONTINUE
        NN1=NN1+NM
 100  CONTINUE
      DO 103 I = 1 , NM
        DF4(I) = 1.D0 + HA*DF4(I)
 103  CONTINUE
C
      CALL LU(N,NC21,NM,DF1,DF2,DF3,DF4,IPIV)
      CALL BACK(N,NC21,NM,DF1,DF2,DF3,DF4,F,IPIV)
      DO 200 I = 1 , N
        YK1(I) = H*F(I)
        YK2(I) = Y(I) + .75D0*YK1(I)
 200  CONTINUE
      CALL FUN(N,NC21,YK2,F, SULPHATE)
      CALL BACK(N,NC21,NM,DF1,DF2,DF3,DF4,F,IPIV)
      DO 300 I = 1 , N
        SS = H*F(I)
        YK2(I) = SS
        DELY(I) = R1*YK1(I) + R2*SS
        ST = 0.
        IF ( IR*(I-NAL).GT.0 ) ST = R3*YK1(I) + R4*SS
        YK3(I) = ST
 300  CONTINUE
      CALL BACK(N,NC21,NM,DF1,DF2,DF3,DF4,YK3,IPIV)
      DO 400 I = 1 , N
        DELY(I) = DELY(I) + YK3(I)
 400  CONTINUE
C
```

```
C     CALCULATE RESULT OF EMBEDDED FORMULA
      DO 500 I = 1 , N
        IF ( IR*(I-NAL).LE.0 ) YK3(I) = 0.D0
 500  CONTINUE
      CALL BACK(N,NC21,NM,DF1,DF2,DF3,DF4,YK3,IPIV)
      DO 600 I = 1 , N
        YK3(I) = -DELY(I) + RN3*YK3(I) + RN1*YK1(I) + RN2*YK2(I)
 600  CONTINUE
      RETURN
      END
C
      SUBROUTINE LU(N,NC21,NM,A1,A2,A3,A4,INDX)
      IMPLICIT DOUBLE PRECISION (A-H,O-Z)
      PARAMETER (ICAR=20000,ICOL=20)
      DIMENSION A1(NC21,*),INDX(*),NCAR(ICOL),A2(NM,*),A3(NC21,*),A4(*)
      COMMON/NNNN/NCOL,NCAR
      DO 10 I=1,NM
C---D(INVERS):---
      A4(I)=1.D0/A4(I)
      DO 10 J=1,NC21
C---E*D(INVERS):---
      A3(J,I)=A4(I)*A3(J,I)
 10   CONTINUE
C---S-E*D(INVERS)*H:---
      DO 20 I=1,NC21
      DO 20 J=1,NC21
      DO 20 K=1,NM
      A1(I,J)=A1(I,J)-A3(I,K)*A2(K,J)
 20   CONTINUE
      DO 40 I=1,NM
      DO 40 J=1,NC21
C---D(INVERS)*H:---
      A2(I,J)=A4(I)*A2(I,J)
 40   CONTINUE
      CALL LUO(NC21,NC21,INDX,A1)
      RETURN
      END
C
      SUBROUTINE BACK(N,NC21,NM,A1,A2,A3,A4,B,INDX)
      IMPLICIT DOUBLE PRECISION (A-H,O-Z)
      PARAMETER (ICAR=20000,ICOL=20)
      DIMENSION A1(NC21,*),A2(NM,*),A3(NC21,*),A4(*)
      DIMENSION B(*),INDX(*),NCAR(ICOL)
      COMMON/NNNN/NCOL,NCAR
C---FIRST X IS FOUND:---
      DO 5 I=1,NC21
      SUM=0.D0
```

```
      DO 10 J=1,NM
      SUM=SUM+B(J+NC21)*A3(I,J)
   10 CONTINUE
      B(I)=B(I)-SUM
    5 CONTINUE
      CALL BACKO(NC21,NC21,INDX,A1,B)
      DO 20 I=1,NM
C---X(I),I=NN,N IS FOUND:---
      SUM=0.D0
      NI=I+NC21
      DO 30 J=1,NC21
      SUM=SUM+A2(I,J)*B(J)
   30 CONTINUE
      B(NI)=A4(I)*B(NI)-SUM
   20 CONTINUE
      RETURN
      END
C
      SUBROUTINE LUO(ND,N,INDX,A)
C
C    PLAIN FORTRAN VERSION
C
C  LU-DECOMPOSITION OF MATRIX A BY CROUT'S METHOD
C
C  ND:  ROW DIMENSION OF A IN CALLING PROGRAM
C  N:   ACTUAL SIZE OF A
C  INDX: PIVOT VECTOR FOR ROW INTERCHANGE DURING FACTORIZATION
C  A:   MATRIX TO FACTORIZE; ON EXIT: FACTORIZED MATRIX
C
      IMPLICIT DOUBLE PRECISION(A-H,O-Z) ON A(ND,*) , INDX(*)
C    SET INDX-VECTOR
C
      DO 200 I = 1 , N
        IM=I-1
        IP=I+1
        INDX(I) = I
        IF ( I.GT.1 ) THEN
          DO 20 K = I , N
            XX = A(K,I)
            DO 10 J = 1 , IM
              XX = XX - A(J,I)*A(K,J)
   10         CONTINUE
            A(K,I) = XX
   20       CONTINUE
        ENDIF
C   PIVOT
      XMAX = DABS(A(I,I))
```

```
      IPIV = I
      DO 50 K = IP , N
        Y = DABS(A(K,I))
        IF ( Y.GT.XMAX ) THEN
          IPIV = K
          XMAX = Y
        ENDIF
   50    CONTINUE
      IF ( IPIV.NE.I ) THEN
        INDX(I) = IPIV
        DO 60 K = 1 , N
          X = A(I,K)
          A(I,K) = A(IPIV,K)
          A(IPIV,K) = X
   60     CONTINUE
      ENDIF
      FACT = 1.D0/A(I,I)
      DO 100 K = IP , N
        A(K,I) = A(K,I)*FACT
  100    CONTINUE
      IF ( I.GT.1 .AND. I.LT.N ) THEN
        DO 120 K = IP , N
          XX = A(I,K)
          DO 110 J = 1 , IM
            XX = XX - A(J,K)*A(I,J)
  110       CONTINUE
          A(I,K) = XX
  120     CONTINUE
      ENDIF
  200 CONTINUE
      RETURN
      END
C
      SUBROUTINE BACKO(ND,N,INDX,A,V)
C
C   BACK-SUBSTITUTION FOR CROUT-BASED LU-ROUTINE
C   PLAIN FORTRAN VERSION
C
C   ND:    ROW DIMENSION OF A
C   N:     ACTUAL SIZE OF A
C   INDX:   PIVOT VECTOR CALCULATED IN LU
C   A:     FACTORIZED MATRIX
C   V:     RHS-VECTOR, ON EXIT SOLN. TO LINEAR EQNS.
C
      IMPLICIT DOUBLE PRECISION(A-H,O-Z)
      DIMENSION A(ND,*) , V(*) , INDX(*)
C   REORDER
```

```
      DO 100 I = 1 , N - 1
        IPIV = INDX(I)
        IF ( IPIV.NE.I ) THEN
          X = V(I)
          V(I) = V(IPIV)
          V(IPIV) = X
        ENDIF
 100  CONTINUE
C
C     L-INVERS
      DO 200 I = 2 , N
        XX = V(I)
        DO 150 J = 1 , I - 1
          XX = XX - V(J)*A(I,J)
 150    CONTINUE
        V(I) = XX
 200  CONTINUE
C
C     U-INVERS
C
      DO 300 I = N , 1 , -1
        X = V(I)
        IF ( I.NE.N ) THEN
          DO 220 J = I + 1 , N
            X = X - V(J)*A(I,J)
 220      CONTINUE
        ENDIF
        V(I) = X/A(I,I)
 300  CONTINUE
      RETURN
      END
C
      SUBROUTINE XJCOBI(ND,N,N0,N1,AL,BE,FA,FB,FC,ROOT)
      DOUBLEPRECISIONAL,BE,FA(*),FB(*),FC(*),ROOT(*),X,Y,Z,AB,
     *AD,AP,XD,XN,XP,XD1,XP1,XN1
      DOUBLEPRECISIONDABS
      AB=AL+BE
      AD=BE-AL
      AP=BE*AL
      FA(1)=(AD/(AB+2.)+1.)/2.
      FB(1)=0.
      DO10I=2,N
      K=2*I-2
      Z=AB+K
      FA(I)=(AB/Z*AD/(Z+2.)+1.)/2.
      K=I-1
      IF(I.NE.2)GOTO11
```

```
      FB(I)=(AB+AP+K)/Z/Z/(Z+1.)
      GOTO10
 11   Z=Z*Z
      Y=K*(AB+K)
      Y=Y*(AP+Y)
      FB(I)=Y/Z/(Z-1.)
 10   CONTINUE
      X=0.
      DO20I=1,N
 26   XD=0.
      XD1=0.
      XN=1.
      XN1=0.
      DO30J=1,N
      XP=(FA(J)-X)*XN-FB(J)*XD
      XP1=(FA(J)-X)*XN1-FB(J)*XD1-XN
      XD=XN
      XD1=XN1
      XN=XP
 30   XN1=XP1
      Y=1.
      Z=XN/XN1
      IF(I.EQ.1)GOTO21
      DO23J=2,I
 23   Y=Y-Z/(X-ROOT(J-1))
 21   Z=Z/Y
      X=X-Z
      IF(DABS(Z).GT..1D-9)GOTO26
      ROOT(I)=X
      X=X+0.0005
 20   CONTINUE
      NT=N0+N1+N
      IF (N0.EQ.1) ROOT(NT)=0.
      IF(N1.EQ.1)ROOT(N+1)=1.
      DO40I=1,NT
      X=ROOT(I)
      FA(I)=1.
      FB(I)=0.
      FC(I)=0.
      DO40J=1,NT
      IF(J.EQ.I)GOTO40
      Y=X-ROOT(J)
      FC(I)=Y*FC(I)+3.*FB(I)
      FB(I)=Y*FB(I)+2.*FA(I)
      FA(I)=Y*FA(I)
 40   CONTINUE
      RETURN
```

```
      END
      SUBROUTINE DFOPR(ND,N,N0,N1,I,ID,FA,FB,FC,ROOT,VECT)
      DOUBLE PRECISION FA(*),FB(*),FC(*),ROOT(*),VECT(*),X,Y,AX
      NT=N+N0+N1
      IF(ID.GE.3)GOTO10
      DO20J=1,NT
      IF(J.NE.I)GOTO21
      IF(ID.EQ.1)VECT(I)=FB(I)/FA(I)/2.
      IF(ID.EQ.2)VECT(I)=FC(I)/FA(I)/3.
      GOTO20
21    Y=ROOT(I)-ROOT(J)
      VECT(J)=FA(I)/FA(J)/Y
      IF(ID.EQ.2)VECT(J)=VECT(J)*(FB(I)/FA(I)-2./Y)
20    CONTINUE
      GOTO50
10    Y=0.
      IF(ID.EQ.4)GOTO30
      DO25J=1,NT
      X=ROOT(J)
      AX=X*(1.-X)
      IF(N0.EQ.0)AX=AX/X/X
      IF(N1.EQ.0)AX=AX/(1.-X)/(1.-X)
      VECT(J)=AX/FA(J)/FA(J)
25    Y=Y+VECT(J)
      GOTO60
30    DO35J=1,NT
      X=ROOT(J)
      IF(N0.EQ.0)AX=1./X
      IF(N1.EQ.0)AX=1./(1.-X)
      VECT(J)=AX/FA(J)/FA(J)
35    Y=Y+VECT(J)
60    DO61J=1,NT
61    VECT(J)=VECT(J)/Y
50    RETURN
      END
      SUBROUTINE GAUSL(ND,NC,N,NS,A)
C     NC IS NOT USED; ONLY INCLUDED FOR CONSISTENCY W. OLDER VERSIONS
C
      IMPLICIT REAL*8 (A-H,O-Z)
      DIMENSION A(ND,*),IP(100)
C     THIS ROUTINE IS ONLY PROVIDED TO YIELD AN INTERFACE CONSISTENT
C     WITH THE OLD GAUSL-ROUTINE
C     THE ACTUAL CALLS ARE REROUTED TO LU AND BACK
C     ASM-ROUTINES USED ARE: TRAN AND VMUL
      CALL LUO(ND,N,IP,A)
      DO 100 J=1,NS
      JPOS=N+J
      CALL BACKO(ND,N,IP,A,A(1,JPOS))
100   CONTINUE
      RETURN
      END
C ------------------------------------END OF PROGRAM---------------------------------

      PROGRAM DISTRIBUTION
C     CALCULATES THE PARTICLE SIZE DISTRIBUTION FROM THE DATA FROM
C     MONAERO. THE SIZE DISTRIBUTION OF SEED PARTICLES AND
C     HOMOGENEOUSLY FORMED PARTICLES ARE OBTAINED.
      IMPLICIT DOUBLE PRECISION(A-H,O-Z)
      CHARACTER*60 FILIN
C-----NSECT IS THE NUMBER OS SIZE CLASSES IN SEED PSD
      PARAMETER(ICAR=5000,NCOL=20,NSECT=1,NSMAX=200)
      DIMENSION HOMDIAM(NCOL,ICAR),HOMNUM(NCOL,ICAR)
      DIMENSION SEEDDIAM(NCOL,ICAR),SEEDNUM(NCOL,NSECT)
      DIMENSION NHOM(NCOL),DH(NSMAX+2),DS(NSMAX+2)
      DIMENSION HOMSUM(NSMAX+2),SEEDSUM(NSMAX+2)
      DIMENSION DMEAN_H(NSMAX+2),DMEAN_S(NSMAX+2)
      OPEN(8,FILE='KCLh1.DAT')
      OPEN(9,FILE='KCls1.DAT')
      OPEN(10,FILE='homogen.DAT')
      OPEN(11,FILE='seeds.DAT')
      YMIN=1.D-2
      DSMAX=0.D0
      DSMIN=1.D2
      DHMAX=0.D0
      DHMIN=1.D2
      READ(8,*)(NHOM(I),I=1,NCOL)
      DO 10 J=1,NCOL
      DO 20 I=1,NHOM(J)
      READ(8,*)HOMDIAM(J,I),HOMNUM(J,I)
C---MULTIPLICATION WITH 2 TO CONVERT TO DIAMETERS
      HOMDIAM(J,I)=2.D0*HOMDIAM(J,I)
C---FIND MAX AND MIN DIAMETERS IN THE J´TE COLLOCATION POINT
      IF(HOMDIAM(J,I).LT.DHMIN)DHMIN=HOMDIAM(J,I)
      IF(HOMDIAM(J,I).GT.DHMAX)DHMAX=HOMDIAM(J,I)
C---SIMILAR FOR SEED PARTICLES
20    CONTINUE
10    CONTINUE
      DO 30 J=1,NCOL
      DO 40 I=1,NSECT
      READ(9,*)SEEDDIAM(J,I),SEEDNUM(J,I)
      SEEDDIAM(J,I)=2.D0*SEEDDIAM(J,I)
      IF(SEEDDIAM(J,I).LT.DSMIN)DSMIN=SEEDDIAM(J,I)
      IF(SEEDDIAM(J,I).GT.DSMAX)DSMAX=SEEDDIAM(J,I)
40    CONTINUE
```

```
   30 CONTINUE
C---ASKS HOW MANY INTERVALS THE PSD SHOULD BE BASED ON
     WRITE(6,*)'INPUT NUMBER OF INTERVALS FOR HOM. NUC. PSD:'
         NSEC_H=40
     WRITE(6,*)' INPUT NUMBER OF INTERVALS FOR SEED PSD:'
         NSEC_S=16
C---DH IS THE VECTOR OF DIAMETERS IN HOM. NUC. PSD.
     DH(1)=DHMIN
     DH(NSEC_H+1)=DHMAX
     DO 55 I=1,NSEC_H
C---FIND AVG. DIAMETER IN N´TH INTERVAL WITH AN INTERVAL
C--- WIDTH DIVIDED EQUALLY ON A LOG AXIS
     DH(I+1)=(DH(I)**NSEC_H*DHMAX/DHMIN)**(1.D0/NSEC_H)
C---WRITE THE INTERVAL END POINT ON THE SCREEN
     WRITE(6,*)DH(I+1)
     HOMSUM(I)=0.D0
   55 CONTINUE
C---PUT THE COUNT NUMBERS FOR THE COLLOCATION POINT
C---J IN THE CORRECT INTERVALS
     DO 60 J=1,NCOL
     DO 70 I=1,NHOM(J)
     DO 80 K=1,NSEC_H
     IF(HOMDIAM(J,I).GT.DH(K).AND.HOMDIAM(J,I).LT.DH(K+1))THEN
      HOMSUM(K)=HOMSUM(K)+HOMNUM(J,I)
C        GOTO 70
     ENDIF
   80 CONTINUE
   70 CONTINUE
   60 CONTINUE
C---CORRESPONDINGLY FOR THE SEED PSD
     DS(1)=DSMIN
     DS(NSEC_S+1)=DSMAX
     DO 85 I=1,NSEC_S
     DS(I+1)=(DS(I)**NSEC_S*DSMAX/DSMIN)**(1.D0/NSEC_S)
     SEEDSUM(I)=0.D0
   85 CONTINUE
     DO 90 J=1,NCOL
     DO 100 I=1,NSECT
     DO 110 K=1,NSEC_S
     IF(SEEDDIAM(J,I).GT.DS(K).AND.SEEDDIAM(J,I).LT.DS(K+1))THEN
      SEEDSUM(K)=SEEDSUM(K)+SEEDNUM(J,I)
C        GOTO 100
     ENDIF
  110 CONTINUE
  100 CONTINUE
   90 CONTINUE
C---OUTPUT TO FILE
```

```
C     DO 120 I=1,NSEC_H
C     HOMSUM(I)=HOMSUM(I)/DLOG10(DH(I+1)/DH(I))
C     WRITE(10,*)DH(I),YMIN
C     WRITE(10,*)DH(I),HOMSUM(I)
CC     WRITE(10,*)DH(I+1),HOMSUM(I)
  120 CONTINUE
C   CALCULATION OF AVERAGE DIAMETER FOR HOM. FORMED PARTICLES
     SUMD_H=0.D0
     SUMN_H=1.D-20
     DO 140 K=1,NSEC_H
C   AVERAGE DIAMETER IN INTERVAL K
     DMEAN_H(K)=DSQRT(DH(K)*DH(K+1))
C---SUMMATION
     IF(HOMSUM(K).EQ.0)GOTO 199
     SUMD_H=SUMD_H+DLOG(DMEAN_H(K))*HOMSUM(K)*DLOG10(DH(K+1)/DH(K))
     SUMN_H=SUMN_H+HOMSUM(K)*DLOG10(DH(K+1)/DH(K))
  140 CONTINUE
C   OUTPUT FOR CONTINOUS FORMAT
     DO 122 I=1,NSEC_H
     HOMSUM(I)=HOMSUM(I)/DLOG10(DH(I+1)/DH(I))
     WRITE(10,*)DMEAN_H(I),HOMSUM(I)
  122 CONTINUE
  199 CONTINUE
C   CALCULATION OF MEAN DIAMETER FOR SEED PARTCLES
     SUMD_S=0.D0
     SUMN_S=0.D0
     DO 160 K=1,NSEC_S
C   AVERAGE DIAMETER FOR SEED PARTICLES
     DMEAN_S(K)=DSQRT(DS(K)*DS(K+1))
C---SUMMATION
     SUMD_S=SUMD_S+DLOG(DMEAN_S(K))*SEEDSUM(K)*DLOG10(DS(K+1)/DS(K))
     SUMN_S=SUMN_S+SEEDSUM(K)*DLOG10(DS(K+1)/DS(K))
  160 CONTINUE
C   OUTPUT IN CONTINUOUS FORMAT
     SUM=0.D0
     DO 161 I=1,NSEC_S
     SUM=SEEDSUM(I)+SUM
     SEEDSUM(I)=SEEDSUM(I)/DLOG10(DS(I+1)/DS(I))
     WRITE(11,*)DMEAN_S(I),SEEDSUM(I)
  161 CONTINUE
     WRITE (*,*) SUM
     GMM_H=DEXP(SUMD_H/SUMN_H)
     GMM_S=DEXP(SUMD_S/SUMN_S)
     WRITE (6,*)'MIDDELDIAMETER, F  DEKIM',GMM_S
     WRITE (6,*)'MIDDELDIAMETER, HOM_NUK',GMM_H
     END
C-------------------------------------------------------------------------
```

Appendix E   FIELD MEASUREMENTS

This appendix contains pictures and additional experimental data from the field measurements described in Chapter 4 and 5.

Straw-combustion at Avedøre Power Plant

The full-scale investigation of straw combustion described in Chapter 4 was made at the Avedøre Power Plant. The plant and the sampling location for aerosol measurements are shown in Figure E1
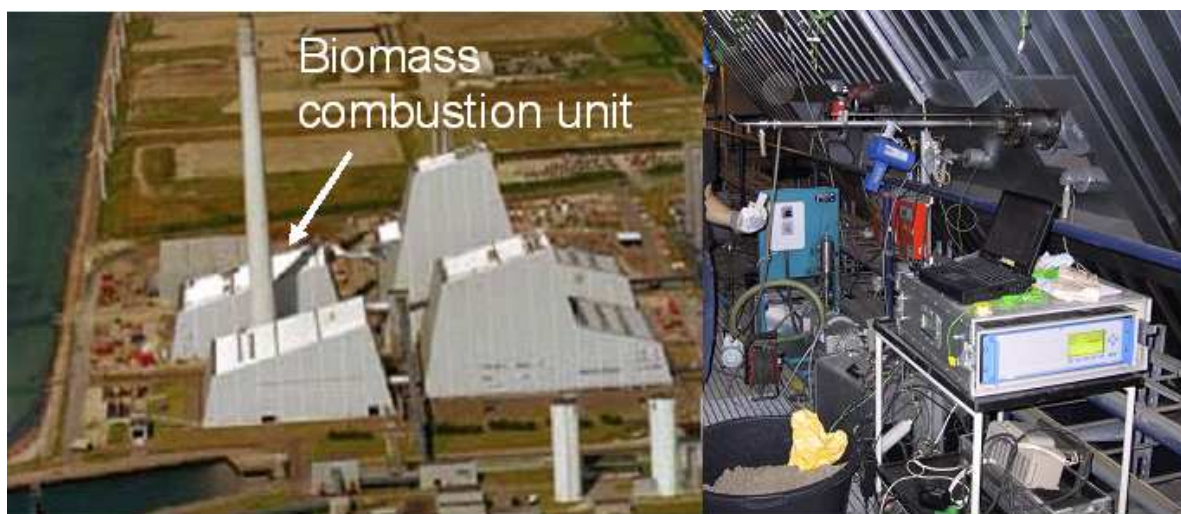

Figure E1. *Pictures from the Avedøre Power Plant (AVV). Left: Avedøre Power Plant. One of the four boilers is used for straw combustion. Right: the setup of the equipment for hot flue gas sampling at AVV: the ejector-diluter probe is inserted in the flue gas duct. In the back the cascade impactor is seen and in the from the gas analyzer and the computer for data collection are seen. The bucket in the lower left corner is used for cooling of the data logger with cold sand. The temperature was 40-45℃ and the logger turned of if no cooling was applied.*

The SEM images of the particle deposits in the low-pressure cascade impactor for all runs are shown in Figure E2. Two of the pictures are also shown in Figure 63.

The particles from the Bentonite run are cubic, while the particles from all other cases are dense spheres. The particles on the pictures are almost monodisperse, because they are all deposited on the same stage of the cascade impactor.
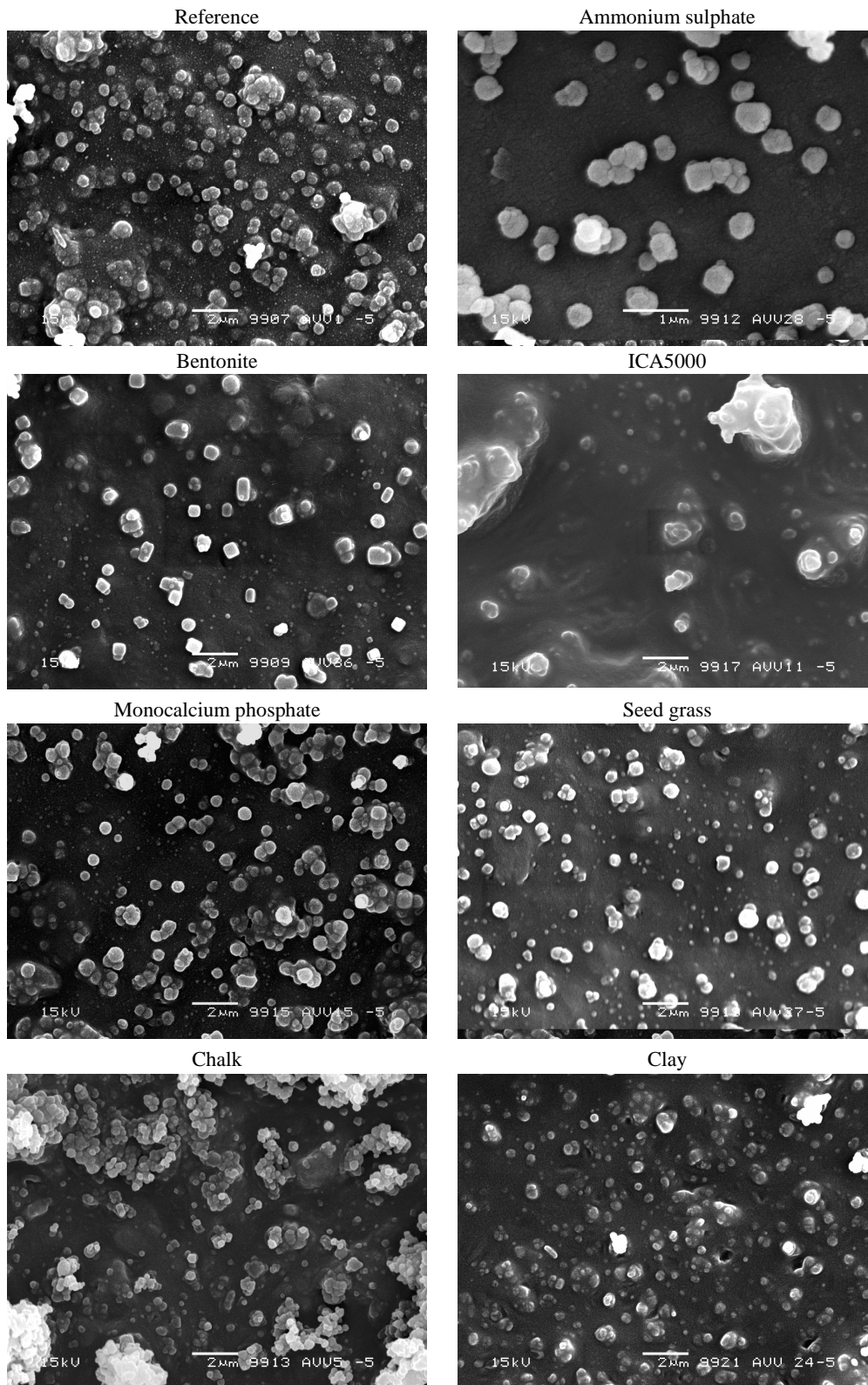
Reference

Ammonium sulphate

Bentonite

ICA5000

Monocalcium phosphate

Seed grass

Chalk

Clay

Figure E2. *SEM micrographs from impactor foils in stage 5 of the LPI during straw combustion with different sorbents and during combustion of seed grass. The images for the reference run and the Bentonite run are shown in Figure 63. Note the different scale used in the image for the ammonium sulphate run.*

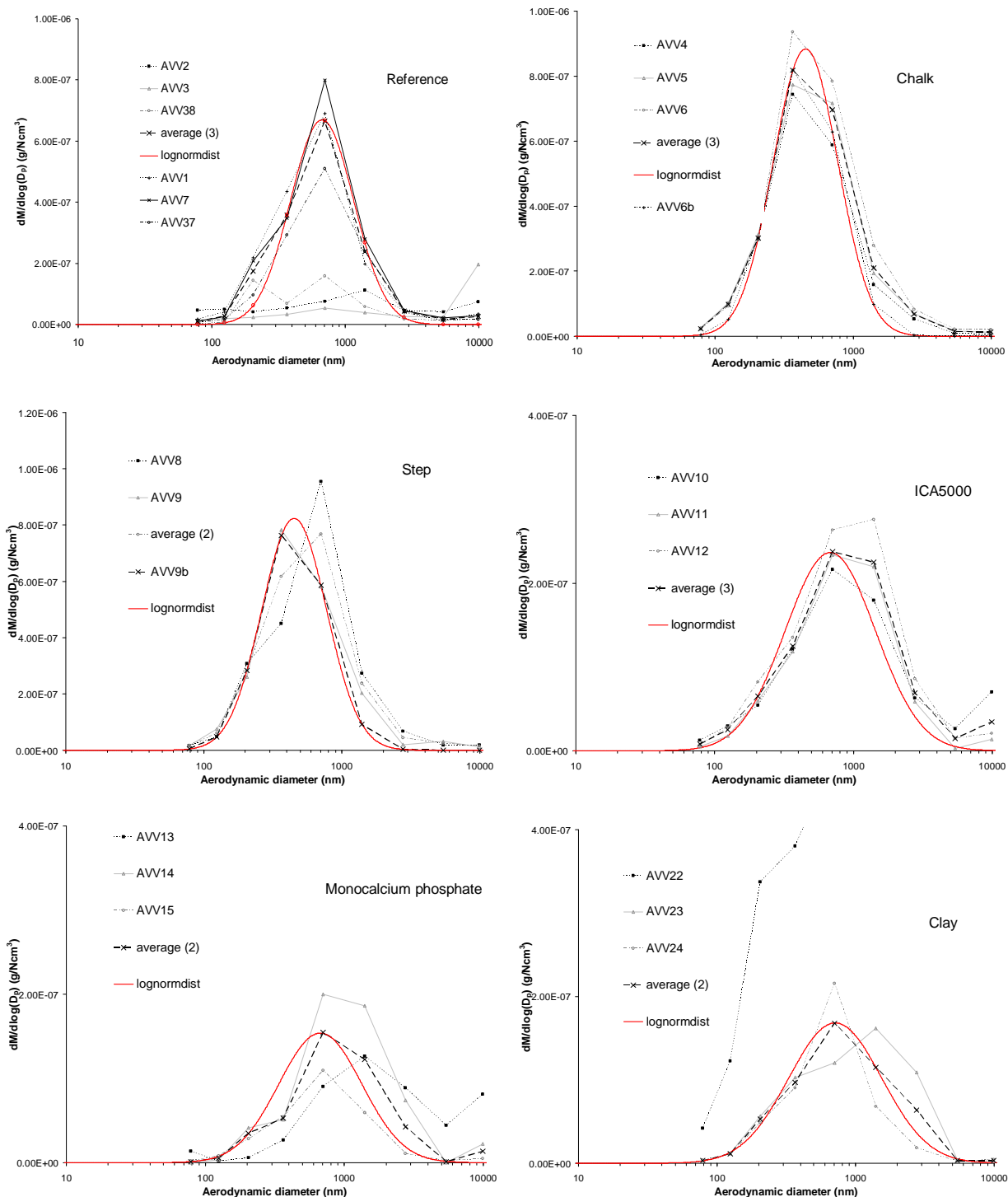All the particle size distributions obtained with the cascade impactor are shown in Figure E3 and E4.
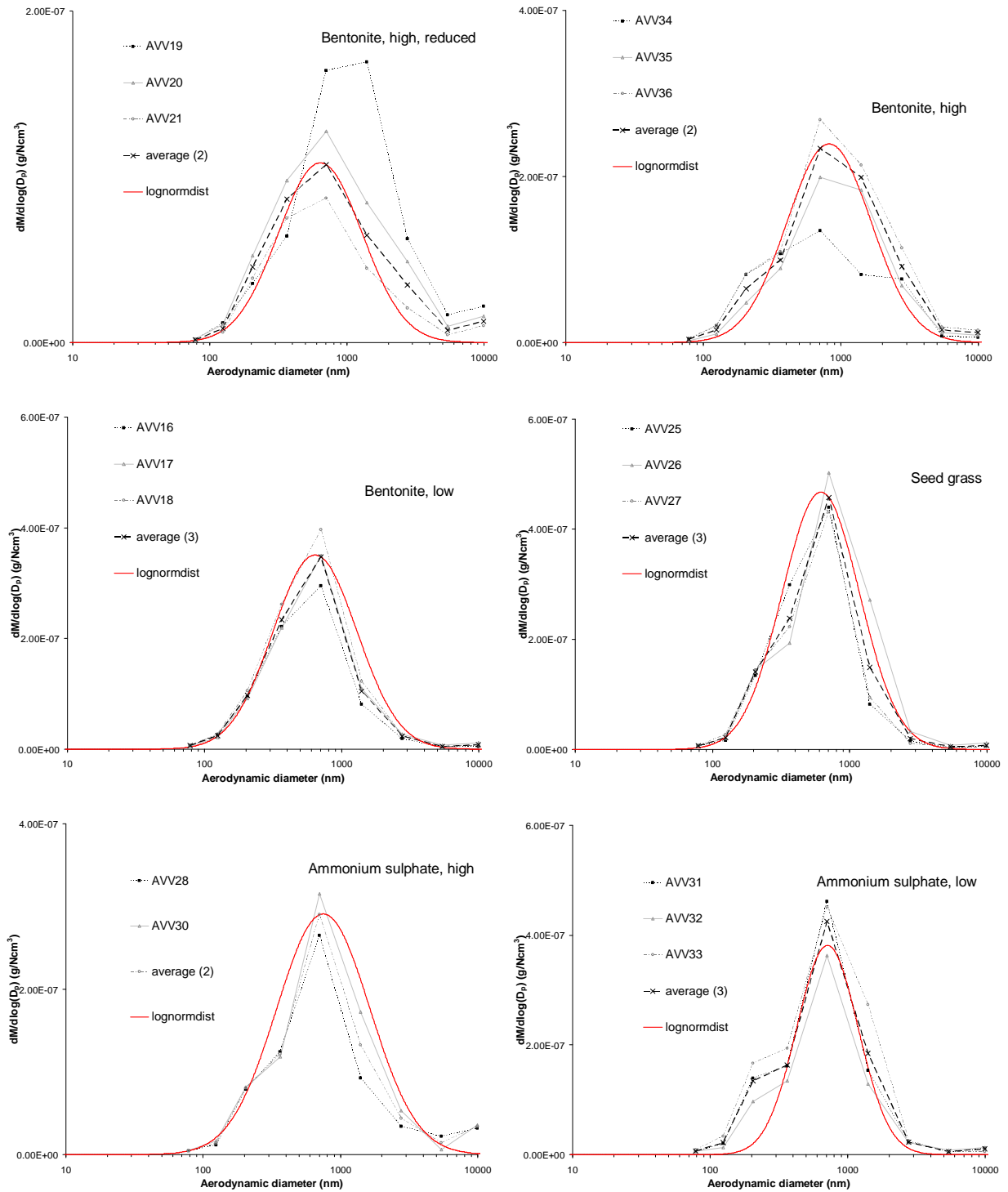

Figure E3. *The mass-based particle size distributions obtained with the low-pressure cascade impactor during the field measurements in a straw-fired power plant described in Chapter 4. The legends for the average distributions state the number of measurements used to calculate the average values. Fitted log-normal distributions fitted to the average distributions are shown. The average values are shown in Figure 59.*

Figure E4. *The mass-based particle size distributions obtained with the low-pressure cascade impactor during the field measurements in a straw-fired power plant described in Chapter 4. The legends for the average distributions state the number of measurements used to calculate the average values. Fitted log-normal distributions fitted to the average distributions are shown. The average values are shown in Figure 59.*

Waste-incineration at Fasan Waste-To-Energy Plant

The full-scale investigation of waste combustion described in Chapter 5 was made at the Fasan Waste-to-Energy Plant. The plant and the sampling location for aerosol measurements are shown in Figure E5
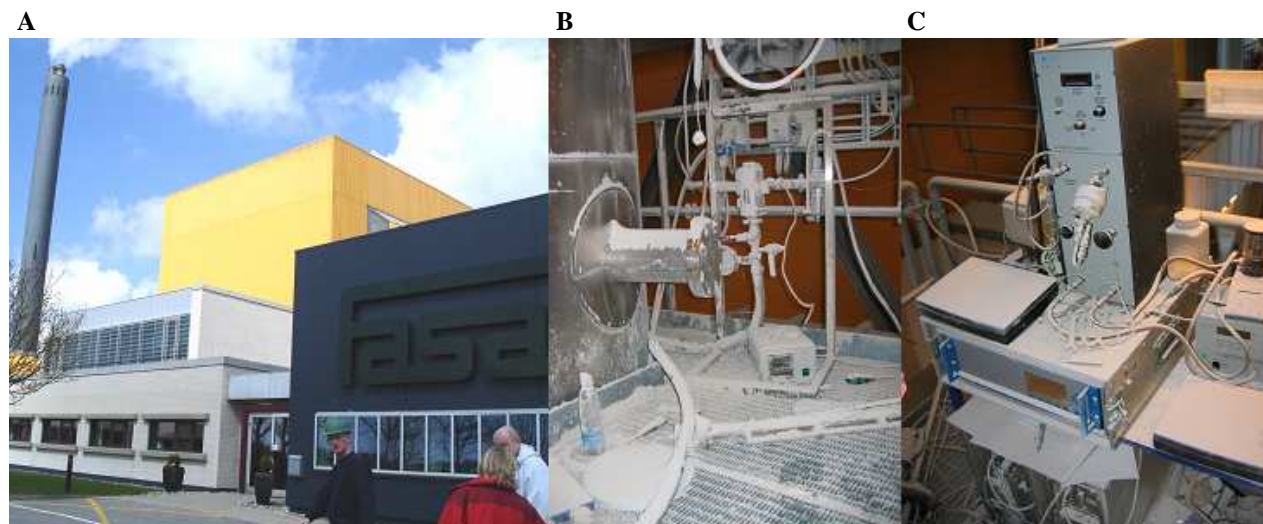
A   **B**   **C**

Figure E5. *I/S Fasan Waste-To-Energy Plant. A: Picture of the plant. B: Closed sampling port at FASAN. An accident with the lime powder for the flue gas cleaning delayed the campaign for a day. On the picture the dilution probe on the floor and the impactor setup in the back are seen covered with CaO powder. C: SMPS setup at FASAN. The setup is also covered with powder at the picture. Below the SMPS the gas analyzer and the gas conditioners are placed.*
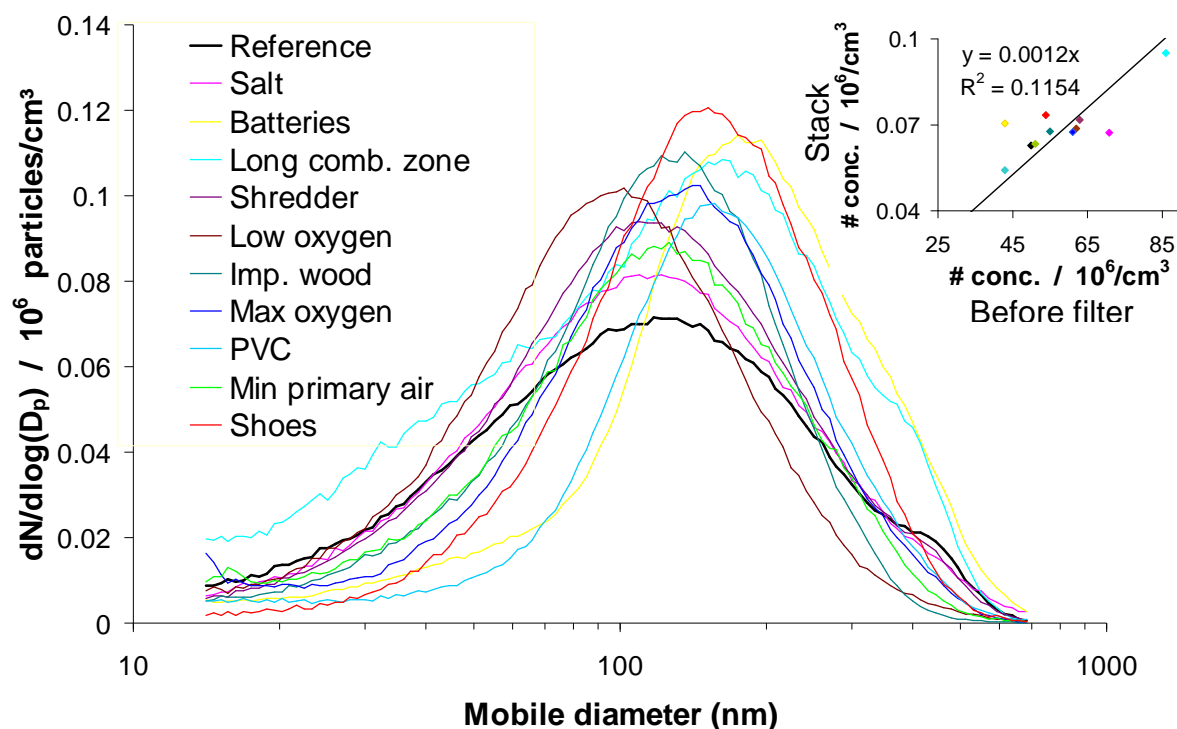

Figure E6. *Number-based particle size distributions in the stack. The best possible linear correlation between the total number of particles before and after the flue gas cleaning is shown.*
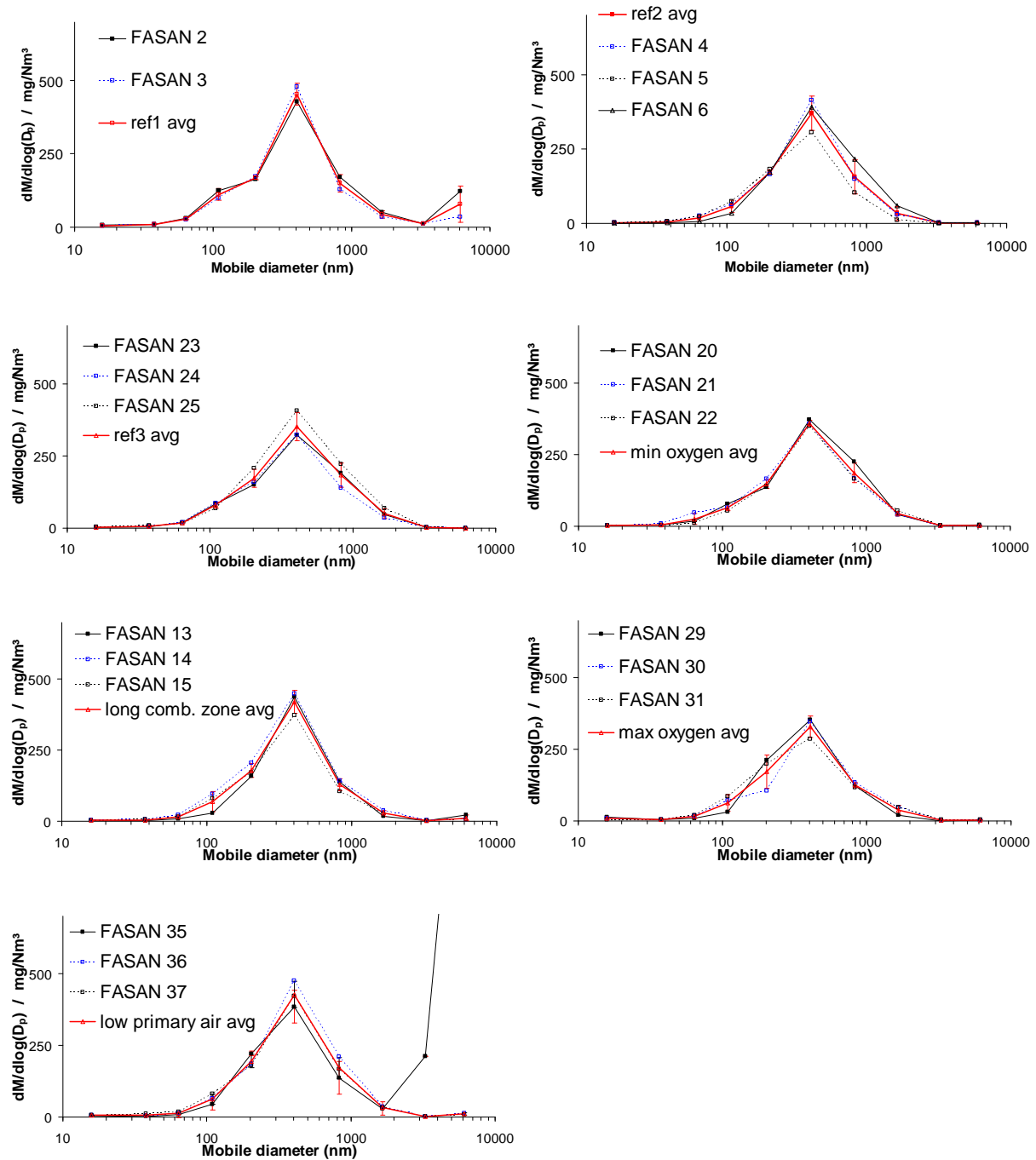
Figure E7. *The mass-based particle size distributions obtained with the low-pressure cascade impactor during the field measurements in the waste-to-energy plant described in Chapter5. The average values are shown in Figure 71. The aerodynamic cut diameters are converted to mobile diameters assuming a constant particle density of 2.2 g/cm³*
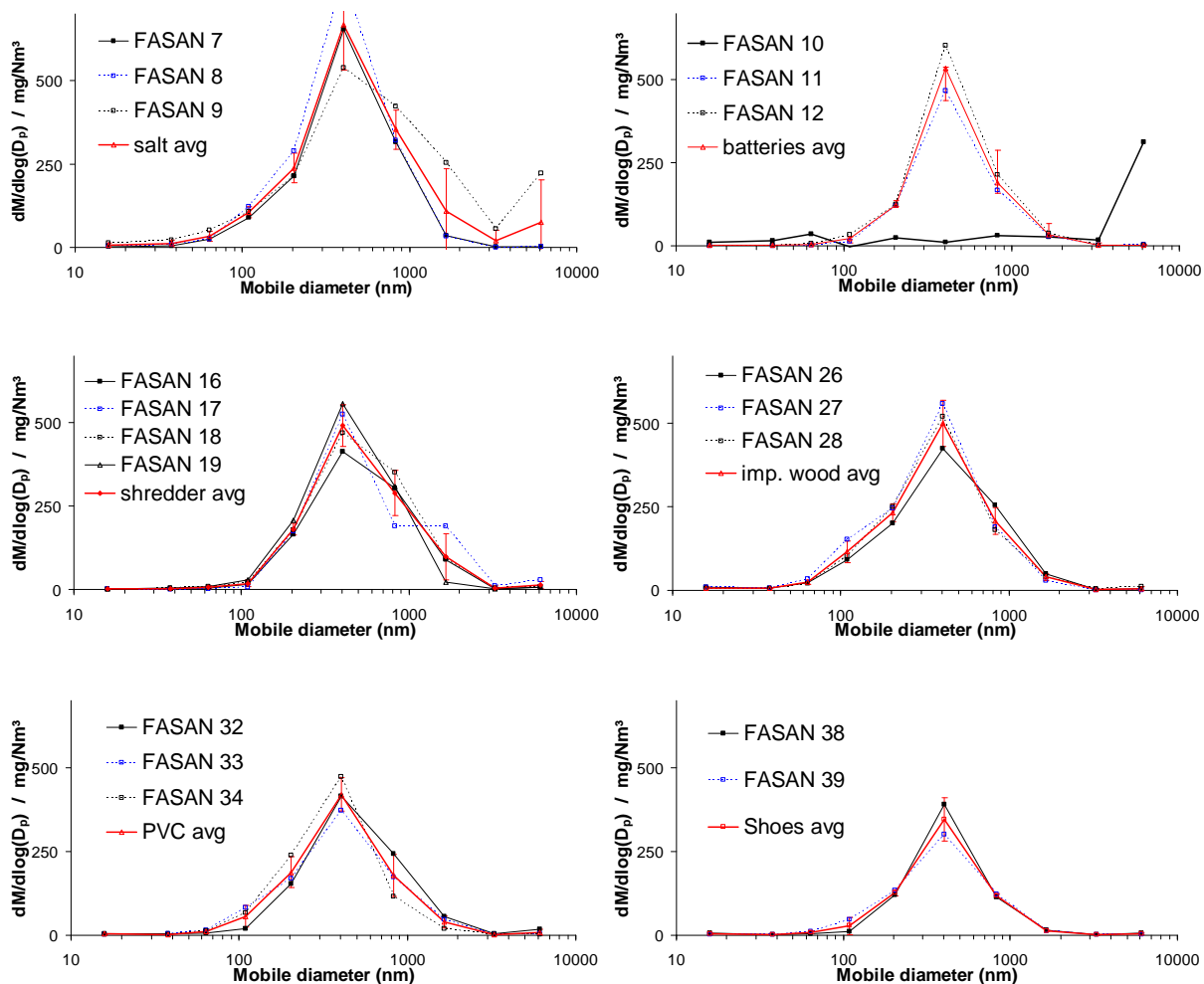
Figure E8. *The mass-based particle size distributions obtained with the low-pressure cascade impactor during the field measurements in the waste-to-energy plant described in Chapter5. The average values are shown in Figure 72. The aerodynamic cut-diameters are converted to mobile diameters assuming a constant particle density of 2.2 g/cm³*

Some of the measurements show clear deviations from the other distributions from the same runs (e.g. FASAN 10 and 35). These are not used to calculate the average size distributions. In general the reproducibility of the mass-based size distributions is very good.